UNIVERSITE DE BLIDA 1

Faculté de Technologie

Département d'Electronique

THESE DE DOCTORAT

en Génie Electrique

CONTRIBUTION TO THE DEVELOPMENT OF REAL-TIME CONTROL OF PHOTOVOLTAIC GRID CONNECTED INVERTER

Par

Abou soufyane BENYOUCEF

Devant le jury composé de :

A. Aissat	Professeur, U. de Blida 1	Président
H. Salhi	Professeur, U. de Blida 1	Examinateur
A. Mellit	Professeur, U. de Jijel	Examinateur
K. Kara	Professeur, U. de Blida 1	Rapporteur
A. Chouder	MCA, U. de M'sila	Co-Rapporteur

Blida, Le 16 décembre 2015

ACKNOWLEDGEMENTS

Je remercie Dieu le compassion et le miséricordieux de m'avoir aidé et donné patience et courage pour accomplir ce modeste travail.

Je tiens à exprimer ma reconnaissance à mes directeurs de thèse, le professeur Kamel KARA et le docteur Aissa CHOUDER, qui m'ont donné courage et motivation à aller jusqu'au bout du chemin et je suis reconnaissant pour leurs présences à mes côtés aux moments de doutes, pour leurs précieux conseils, aide et soutient.

Mes appréciations est également étendues au professeur Santiago SILVESTRE de l'Universitat Politecnica de Catalunya pour ses précieuses observations et suggestions.

Je remercie vivement le professeur Hassan SALHI pour toutes les corrections qu'il a apporté au manuscrit, d'avoir accepté d'examiner ce travail et de faire partie du jury.

Je tiens à remercier le professeur Abdelkader AISSAT pour avoir accepté de juger ce travail et d'en être le président de jury.

J'exprime toute ma gratitude au professeur Adel MELLIT d'avoir accepté de faire partie du jury.

J'exprime mes vifs remerciements à monsieur Amar HADJARAB, d'avoir examiné mon travail et émis un avis favorable pour sa soutenance.

Je tiens aussi a remercié mon collègue le doctorant Oussama AITSAHED pour son aide et pour l'atmosphère de fraternité et le confort que j'ai senti durant mes travaux dans le laboratoire d'automatique à son côté.

Je remercie tout le staff et toute l'équipe du laboratoire des systèmes électriques et de télécommande (LabSET), en particulier monsieur Omar NEDJEMI.

Je remercie aussi tout le staff du département d'électronique de l'université de Blida1 ainsi que mes collègues et mes amis, pour leur aide et soutient tout au long de ce travail.

A la fin, je remercie mes parents, ainsi que toute ma famille, pour leur amour, soutient et encouragement. Ils m'ont toujours donné confiance en soi et m'ont motivé pour toujours marcher en avant.

ABSTRACT

Photovoltaic systems are gaining more and more visibility, while the world power demand is increasing. Unconditional availability of the power source and the environmental friendliness of these systems are their major advantage. Nonetheless, their efficiency and difficult controllability stand as the major drawbacks. Furthermore, when PV system is connected to the utility grid, the transmission system operators are imposing tough standards and many requirements, such as the limits on total harmonic distortion (THD) and the power factor (PF) of the injected current.

To improve the grid connected photovoltaic systems behaviour, two main axes are explored by the researchers. In the first one, several researchers have addressed the issue of low yields and power losses in PV systems facilities and all have approved the use of a power optimizer known as maximum power point tracking (MPPT) to improve the overall efficiency of systems. In the second one, great research efforts are devoted to develop robust control strategies, which could ensure the imposed power quality.

The present work seeks to improve the efficiency of photovoltaic grid-connected systems by developing efficient control algorithms. Indeed, two novel MPPT techniques that use the direct control structure are introduced. These techniques are based on the artificial bee colony optimization algorithm, a relatively new member of swarm intelligence algorithms, and are dedicated to the control of one-dimensional and multi-dimensional PV systems. The developed algorithms, do not only allow overcoming the common drawback of the conventional MPPT algorithms, but give simple and robust schemes to achieve MPPT. Furthermore, an improved and efficient version of the well-known deadbeat control algorithm suitable for DSP-based platform implementation is proposed. In this version the control problem is considered for inverters with L and LCL output filters. The developed algorithm allows overcoming the phase shift problem and improving the output current shape quality. Hence, the THD and the PF are significantly improved.

The performances of the proposed algorithms were evaluated using a co-simulation methodology by combining MATLAB/Simulink and Psim software. The obtained results show the effectiveness of these algorithms. Furthermore, experimental verification tests of the two proposed MPPT techniques were also conducted. The obtained experimental results were in good qualitative agreement with the simulations results.

Keywords: Grid connected PV system; Maximum power point tracker; artificial bee colony algorithm; Deadbeat controller; Predictive control; DSP implementation.

RESUME

Les systèmes photovoltaïques gagnent de plus en plus de visibilité, au moment que la demande de puissance mondiale est en augmentation dramatique. La disponibilité inconditionnelle et le respect de l'environnement de ces systèmes sont leurs atouts majeurs. Néanmoins, leur efficacité et la difficulté de leur commande constituent leurs principaux inconvénients. En outre, lorsque les systèmes PV sont connectés aux réseaux de distribution électrique, les compagnies responsables de la production et la distribution d'électricité imposent des normes strictes sur la qualité de la puissance injectée, tels que la valeur de la distorsion harmonique totale (THD) du courant injecté et le facteur de puissance (PF).

Afin de contribuer au développement des systèmes photovoltaïques connectés au réseau plus performants, deux principaux axes sont explorées par les chercheurs. Dans le premier, plusieurs chercheurs ont abordé la question des rendements faibles et des pertes de puissance dans les installations photovoltaïques. Tous les travaux menés dans cette direction ont approuvé l'utilisation d'un optimiseur de puissance, connu sous le nom de suiveur de point de puissance maximale, afin d'améliorer l'efficacité globale des systèmes photovoltaïques. Tandis que dans la seconde axe, tous les efforts de recherche sont orientés vers le développement des stratégies de commande robuste, qui garantissent l'injection d'une puissance qui répondent aux exigences imposées.

Dans cette thèse, l'objectif est de proposer des algorithmes, plus robustes et efficaces, pour la commande des systèmes photovoltaïques connectés au réseau qui permettent d'améliorer leur efficacité et la qualité de la puissance injecté. Pour cela, trois nouveaux algorithmes sont développés:

Premièrement, pour améliorer l'efficacité de ces systèmes, deux nouvelles techniques de suivi de point de puissance maximale, utilisant la structure de commande directe et dédiés à la commande des systèmes PV unidimensionnelles et multidimensionnelles, sont introduits. Les algorithmes développés, basés sur un mécanisme de commande simple et robuste, permettent de surmonter l'inconvénient commun des algorithmes de poursuite de point de puissance maximale classiques.

Deuxièmement, pour améliorer la qualité de la puissance injectée dans le réseau, une version améliorée et efficace de la commande Deadbeat adaptée à l'implémentation sur une plate-forme DSP est également proposée. Dans cette version, le problème de commande est considéré en utilisant deux filtres de sortie différents (L et LCL). L'algorithme développé conduit à surmonter le problème de décalage de phase inhérent à la commande Deadbeat classique et permet d'améliorer la valeur du THD et celle du facteur de puissance.

Pour évaluer les performances des algorithmes proposés, une méthodologie de co-simulation combinant les deux logiciels MATLAB/Simulink et Psim est utilisée. Les résultats de simulation ont montré l'efficacité des algorithmes proposés. En outre, la vérification expérimentale des deux techniques d'MPPT proposées est également menée. Les résultats expérimentaux obtenus ont été en bon accord qualitatif avec les résultats des simulations.

Mots clés: Système photovoltaïque connecté au réseau; Suiveur de point de puissance maximale; Algorithme d'optimisation par colonie d'abeilles; Contrôleur Deadbeat; contrôle prédictif; Implémentation sur DSP.

ملخص

تكتسب النظم الكهروضوئية المزيد والمزيد من الاعتبار، في حين أن الطلب على الطاقة في العالم آخذ في الازدياد. التوفر الغير مشروط لمصدر الطاقة وصداقتها للبيئة هي من المزايا الرئيسية لهذه الأنظمة. ومع ذلك، فإن كفاءتها المنخفضة وصعوبة السيطرة و التحكم بها هي من العوائق الرئيسية. وعلاوة على ذلك، عند توصيل النظم الكهروضوئية بشبكات توزيع الطاقة، فإن مشغلي هاته الأخيرة يفرضون معايير صارمة والعديد من المتطلبات، مثل القيود المفروضة على التشوه التوافقي الكلي (THD) ومعامل القدرة (PF) للتيار المحقون.

لتحسين سلوك النظم الكهروضوئية المتصلة بالشبكة، هناك محورين أساسيين يتم استكشافهما من قبل الباحثين. في المحور الأول، تناول العديد من الباحثين قضية الكفاءة المنخفضة وخسائر الطاقة المرافقة لهته الأنظمة و قد اتفق الجميع على استخدام محسن القوة المعروفة باسم متتبع نقطة الاستطاعة العظمى (MPPT) لتحسين الكفاءة العامة لهته النظم. بينما في المحور الثاني، قد تم تكريس جهود بحثية كبيرة لتطوير استراتيجيات تحكم متينة، والتي تضمن جودة الطاقة المفروضة من قبل مشغلي شبكات توزيع الطاقة الكهربائية.

يسعى العمل المتناول في هاته الاطروحة إلى تحسين كفاءة النظم الكهروضوئية المتصلة بالشبكة، وذلك من خلال تطوير خوارزميات تحكم ذات كفاءة عالية. حيث تم إدخال تقنيتين جديدتين لتتبع نقطة الاستطاعة العظمى واللتين تستخدمان بنية تحكم مباشرة للسيطرة على المولدات الكهروضوئية ذات بعد واحد أو متعدد الأبعاد على التوالي، و هما يستندان على خوارزمية مستعمرة النحل الاصطناعية، والتي تعتبر عضوا جديدا نسبيا من خوارزميات ذكاء السرب. حيث أن الخوارزميات المقدمة، لا تسمح فقط بالتغلب على العائق المشترك لخوارزميات تتبع نقطة الاستطاعة العظمى التقليدية، ولكن هي أيضا ذات مخططات بسيطة. وعلاوة على ذلك، تم اقتراح نسخة محسنة وفعالة من الخوارزمية المعروفة DEADBEAT مناسبة لتنفيذ السيطرة على العاكس بواسطة معالج الإشارة الرقمي (DSP). بحيث تم اعتبار هذا المشكل على نوعين من المرشحات (L و LCL). الخوارزمية المقدمة تحسن بشكل ملحوظ كلا من التشوه التوافقي الكلي ومعامل القدرة للتيار المحقون في الشبكة.

تم تقييم أداء الخوارزميات المقترحة باستخدام منهجية محاكاة عن طريق الجمع بين برنامج MATLAB /SIMULINK وبرنامج PSIM. وقد أظهرت النتائج التي تم الحصول عليها فعالية هته الخوارزميات. بالإضافة إلى ذلك، تم أيضا التحقق التجريبي من التقنيتين المقترحتين لتتبع نقطة الاستطاعة العظمى. وقد جاءت النتائج التجريبية التي تم الحصول عليها في اتفاق نوعي جيد مع نتائج المحاكاة.

كلمات مفتاحية : النظم الكهروضوئية المتصلة بشبكة توزيع الكهرباء، تتبع نقطة الإستطاعة العظمى خوارزمية مستعمرة النحل الاصطناعية، خوارزمية DEADBEAT، السيطرة التنبؤية، معالج الإشارة الرقمي.

CONTENTS

CHAPTER 2

MAXIMUM POWER POINT TRACKING

CHAPTER 3

GRID-CONNECTED INVERTER CONTROL

CHAPTER 4

COMPLETE SIMULATION OF SINGLE PHASE GRID CONNECTED PV SYSTEM

CHAPTER 5

EXPERIMENTAL VERIFICATION OF THE DEVELOPED TECHNIQUES

APPENDICES

LIST OF ILLUSTRATIONS, GRAPHICS AND TABLES

ILLUSTRATIONS AND GRAPHICS

TABLES

INTRODUCTION

Energy is fundamental to sustain the development of nations. Particularly, fossil fuel energy has been the most component used worldwide. However, the expansion of energy-consuming activities in the developed and the emerging countries can lead to two major concerns: the depletion of the most easily accessible energy resources (mainly the oil) and the problem of global warming caused by the rapidly increasing emissions of greenhouse gases such as carbon dioxide and methane. This global nature of energy challenges requires that renewable energy resources should be appropriately managed and used [1].

Renewable energy is commonly defined as the energy that comes from resources which are naturally replenished on a human timescale such as sunlight, wind and geothermal heat. Contrary to conventional energies, renewable energies have minimal, if any, negative impacts on the environment, with no waste products of greenhouse gases.

The sun is the main source of all alternative energies on the earth surface. Wind energy, bioenergy, ocean energy, and hydro energy are derived from the sun. However, the term solar energy refers to the energy that is harvested directly from the sun [2]. Among all of the alternative energy resources, Solar energy has become the most attractive source of renewable energy due to its abundance, versatility, and ease of implementation with minimal environmental impact in terms of land usage [3].

Generation of electricity from the sun can be achieved directly using PhotoVoltaic (PV) cells or through solar concentration to rise steam and drive conventional turbines. Over the last few years considerable progress has been made in the reduction of the cost of PV generated electricity. A photovoltaic system generates electricity by the direct conversion of the sun energy into electricity. This simple principle involves sophisticated technology that is used to build efficient devices, namely solar cells, which are the key components of a PV system and require semiconductor processing techniques in order to be manufactured at low cost and high efficiency [4].

According to the application, photovoltaic generation systems can be divided into the off-grid photovoltaic systems and the grid connected photovoltaic systems. The off-grid photovoltaic inverter systems are used in independent photovoltaic power generation system, applied in the countryside, island, and remote areas of the power supply, communications and urban lighting. While, the grid-connected photovoltaic systems are used in parallel with the traditional utility grid. They range from small residential and commercial rooftop systems to large utility-scale solar power stations.

In grid-connected photovoltaic systems, if the PV system is not supplying sufficient power to local loads (e.g. at night, when there is no solar energy available), the electricity from the grid is used. While, when the power supplied by the PV system is greater than the power consumed by local loads, the excess power can be exported to the utility grid. Unlike off-grid systems, grid-connected systems rarely include an integrated battery solution, as they are still very expensive. Therefore a grid connected system is cheaper, simple to install and flexible.

However, feeding the photovoltaic energy to the utility grid is not evident. It poses some problems in controlling the energy transfer and connecting the two systems together by using static converters, where a judicious control of power conditioning unit components is indispensable for proper functioning. A control unit of such system is mainly composed of two controllers:

The first controller is charged to achieve maximum power point tracking for better efficiency, which tracks the voltage (or current) at where the maximum power of the Photovoltaic Generator (PVG) is obtained. Weather conditions variation (irradiance and temperature) and partial shading of PV generator affect nonlinearly the current-voltage (*I-V)* output characteristics [5], resulting a permanent change in locus of the maximum power point, which makes its tracking very hard. In such situations, conventional MPPT techniques can easily be trapped at local maxima, and so missing the Global Maximum Power Point (GMPP). Therefore, a significant output power can be lost and the overall system yield could be significantly reduced. To overcome this problem, several researchers have proposed global search MPPT techniques, which can extract maximum power from photovoltaic systems under varying atmospheric and partial shading

conditions (PSC). Seeing the effectiveness of soft computing algorithms in resolving complex optimization problems, several soft computing algorithms-based MPPT have been developed and emerged as powerful techniques. Regarding the convergence rate, the convergence speed and the implementation simplicity, swarm intelligence-based MPPT techniques, outperform MPPT techniques that are based on other soft computing algorithms [6].

The second controller ensures that the power injected into the utility grid meets the requirements imposed by standards. Because, it is necessary to have low levels of Total Harmonic Distortion (THD) at the inverter output and a very good Power Factor (PF), close to unity, it is imperative to design high-performance controllers for the inverter. Despite many advanced control techniques that have been developed to improve the THD and to obtain a faster response for the injected current, the deadbeat control technique remains an attractive way for controlling power converters [7].

The main objective of this thesis is to develop efficient control algorithms that allow improving the efficiency and the power quality of grid connected PV systems. Indeed, to enhance the efficiency of these systems, two maximum power point tracking techniques based on Artificial Bee Colony algorithm are introduced. In fact, the good performance of ABC algorithm has been established in different fields. To deal with the power quality problem, an improved and efficient version of the well-known deadbeat control algorithm, suitable for DSP-based platform implementation, is developed.

The content of this thesis is organized as follows:

The first chapter provides an overview of the different components of a single-phase grid connected PV system and gives a review of the recent achievements and the current research activities in this field. The second chapter discusses the developed MPPT approaches. The third chapter presents the proposed inverter controller based on the deadbeat control approach. The fourth chapter gives the simulation results of the overall grid connected PV system controlled using the developed algorithms. The last chapter provides the experimental verification tests of the two developed MPPT approaches. Finally, some conclusions and perspectives of the present work are given.

CHAPTER 1

SINGLE-PHASE GRID CONNECTED PHOTOVOLTAIC SYSTEMS: STATE OF THE ART

1.1. Introduction:

The building blocks of a grid-connected photovoltaic system are shown in figure (1.1). The system is mainly composed of a matrix of PV array, which converts the sunlight to DC power, and a power conditioning unit that converts the DC power to AC power. The generated AC power is injected into the grid and/or utilized by local loads. In some cases, storage devices are used to improve the availability of the power generated by the PV system.

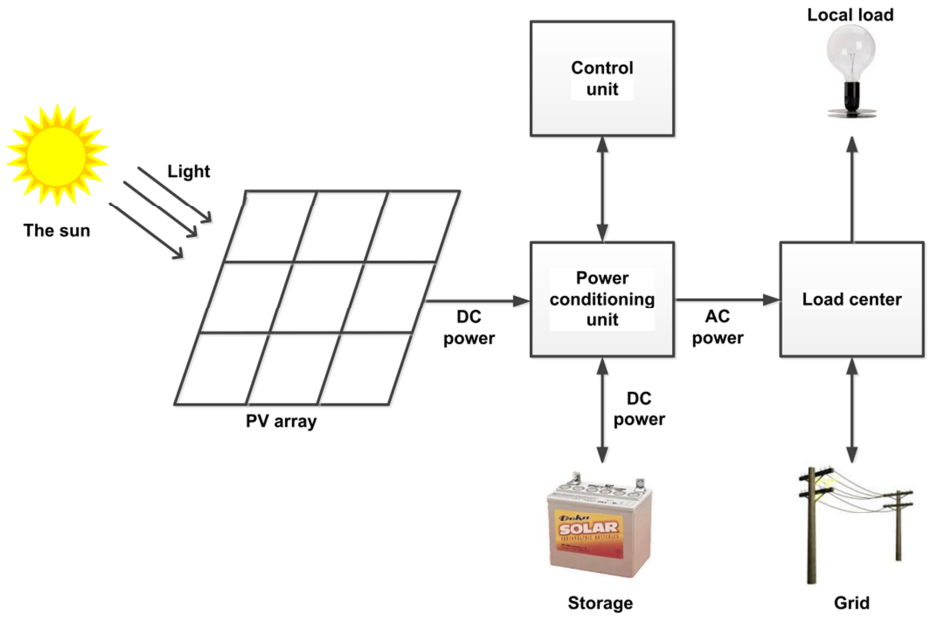

Figure 1.1: Main components of grid-connected photovoltaic systems.

In this chapter, we provide an overview of the different components of a single-phase grid connected PV system, starting from photovoltaic effect to AC power injected into the grid. A review of the recent achievements and current research activities in the field are also provided.

1.2. Photovoltaic array:

1.2.1. Photovoltaic effect:

The photoelectric effect was first noted by the French physicist, Edmund Becquerel, in 1839, who found that certain materials would produce small amounts of electric current when exposed to light. In 1905, Albert Einstein described the nature of light and the photoelectric effect on which photovoltaic technology is based. The first photovoltaic module was built by Bell Laboratories in 1954. It was billed as a solar battery and was mostly just a curiosity as it was too expensive and with a relatively low efficiency of around 4.5% [8]. In the 1960s, the space industry began to make the first serious use of this technology to provide power aboard space crafts, and during the energy crisis in the 1970s, photovoltaic technology gained recognition as a source of power for non-space applications.

By definition, the photovoltaic effect is the direct conversion of light into electricity at the atomic level. Some materials exhibit a property known as the photoelectric effect that causes them to absorb photons of light and release electrons. When light shines on a PV cell, it may be reflected, absorbed, or pass right through. But only the absorbed light generates electricity.

The energy of the absorbed light is transferred to electrons in the atoms of the PV cell. With their new found energy, these electrons escape from their normal positions in the atoms of the semiconductor PV material and become part of the electrical flow, or current, in an electrical circuit. To induce the built-in electric field within a PV cell, two layers of somewhat differing semiconductor materials are placed in contact with one another. One layer is an n-type semiconductor with an abundance of electrons, which have a negative electrical charge. The other layer is a p-type semiconductor with an abundance of holes, which have a positive electrical charge. Sandwiching these together creates a p/n junction at their interface, thereby creating an electric field (see figure (1.2)).

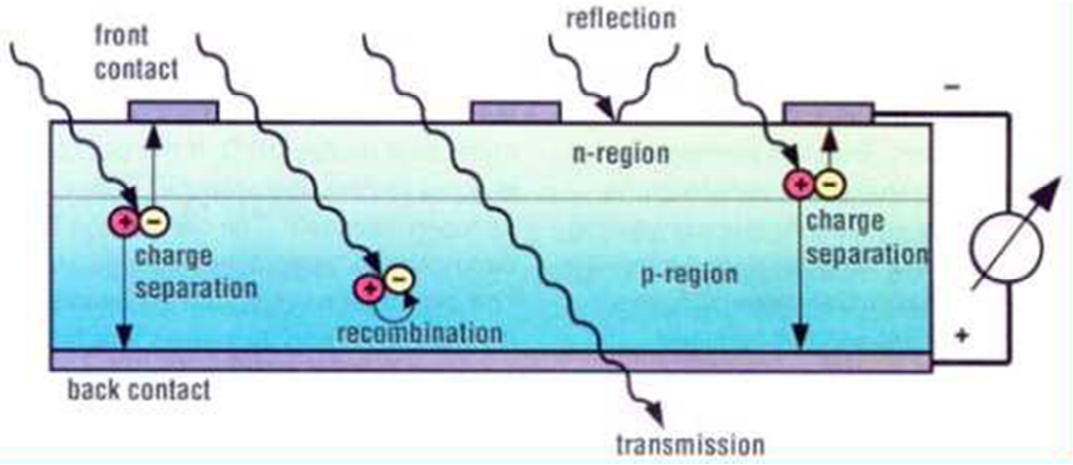

Figure 1.2: Photovoltaic effect principle.

1.2.2. PV technologies:

Many different solar cells are now available, yet more are under development. The range of solar cells spans different materials and structures in the quest to extract maximum power from the device while keeping the cost to a minimum. Devices with efficiencies exceeding 30% have been demonstrated in the laboratory, however, the efficiency of commercial devices, is still less than half this value.

There are two main PV technologies, Crystalline Silicon (c-Si) technology and thin-film technology [9, 10]:

Crystalline silicon photovoltaic cells, known as the first generation technology are currently the most common solar cells in use (about 90% of the world market share in 2013 [11]), mainly because c-Si is stable and it operates at a good efficiency [12, 13]. Despite gaining more favour, c-Si based photovoltaic cells are relatively expensive because of difficulties in the industrial preparation of the high-grade silicon. As the second generation PV cells technology, thin-film PV cells use very thin layers of semiconducting materials, so they can be manufactured in large quantity at low cost, but with low efficiency.

However, both technologies have advantages and disadvantages. It is important to take a variety of factors into account, when making a choice. The comparative table below can serve as a basis for a quick comparison:

Table 1.1: Comparison of photovoltaic technologies.

	Crystalline	**Thin-film**
Material	Mono-crystalline silicon Poly-crystalline silicon	Amorphous silicon Cadmium telluride
Efficiency	13% - 19%	4% - 12%
Price/W	Higher	Lower
Area	Standard	Up to 50% more compared to crystalline
Number of modules in a system	Less	More

Moreover, third generation PV technology try to improve the electrical performance of the second generation while maintaining low production costs [12].

1.2.3. Photovoltaic generator:

A typical PV cell produces a voltage of approximately 0.5 V and a current that depends on the intensity of the sunlight and the area of the cell. To increase the output power, PV cells are connected in series (to increase the output voltage) and in parallel (to increase the output current) [14]. Many cells are packaged together to form a PV module. In turn, these modules can be wired together in a series–parallel combination to form an array that best meets the needs of the application, as shown in figure (1.3).

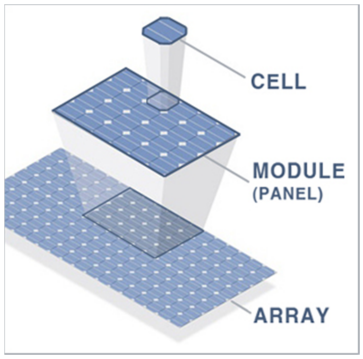

Figure 1.3: Photovoltaic array architecture.

1.2.4. PV cell and module modelling:

The equivalent circuit for the simplest solar cell (Ideal solar cell) model consists of diode and current source connected in parallel, as shown in figure (1.4-a). Where, the current source is directly proportional to the solar irradiation.

On the basis of this circuit diagram, the output current is given by the following expression [15]:

$$I = I_{PH} - I_d = I_{PH} - I_o\left[\exp\left(\frac{V}{nV_t}\right) - 1\right] \tag{1.1}$$

where:

I_{PH} is the photocurrent (A);

I_o is the reverse saturation current (A);

V is the output cell voltage(V);

n is the diode ideality factor.

V_t is the thermal voltage, given by (1.2).

$$V_t = \frac{kT}{q} \tag{1.2}$$

k is the Boltzmann constant $1.38\times10^{-23} J/K$.

q is the charge of electron, $1.6\times10^{-19} C$.

T is the solar cell temperature (K).

The photocurrent I_{PH} of a solar cell depends on many material characteristics. However, it can be approximated as linear-dependent on irradiance and temperature with sufficient accuracy as follow [16]:

$$I_{PH} = \frac{G}{G_{ref}}\left[I_{sc,ref} + \mu_{I_{sc}}(T - T_{ref})\right] \tag{1.3}$$

where:

$I_{sc,ref}$ is solar cell short-circuit current at standard test conditions (STC): $G_{ref} = 1000\,\mathrm{W/m^2}, T_{ref} = 25°C, Air-Mass = 1.5$

$\mu_{I_{sc}}$ is the solar cell short-circuit temperature coefficient, normally provided by the manufacturer (AK^{-1}).

G is the actual irradiance intensity (W/m^2);

G_{ref} is the reference irradiance intensity, 1000W/m^2 ;

The well-known diode saturation current estimation equation is given by [5]:

$$I_o = I_{o,ref}\left(\frac{T_{ref}}{T}\right)^3 \exp\left[\frac{qE_g}{nk}(1/T_{ref} - 1/T)\right] \tag{1.4}$$

where, the nominal saturation current $I_{o,ref}$ at STC is given by:

$$I_{o,ref} = I_{sc,ref} / \left[\exp(V_{oc,ref} / nV_t) - 1\right] \tag{1.5}$$

$V_{oc,ref}$ is solar cell open-circuit voltage at reference condition;

E_g is band-gap energy in the solar cell, (1.12-1.15eV).

The practical PV cell has a series resistance R_s and a parallel resistance R_{sh}. R_s basically depends on the contact resistance of the metal base with the p semiconductor layer, the resistances of the p and the n bodies, the contact resistance of the n layer with the top metal grid, and the resistance of the grid. The R_{sh} resistance is mainly due to the leakage current of the p–n junction and depends on the fabrication method of the PV cell [17].

Thus, a more accurate model is accomplished by adding the series and the shunt resistors to the ideal model, as shown in figure (1.4-b). The current-voltage characteristic equation of a solar cell is then given by:

$$I = I_{PH} - I_o\left[\exp\left(\frac{V + IR_s}{AV_t}\right) - 1\right] - \frac{V + IR_s}{R_{sh}} \tag{1.6}$$

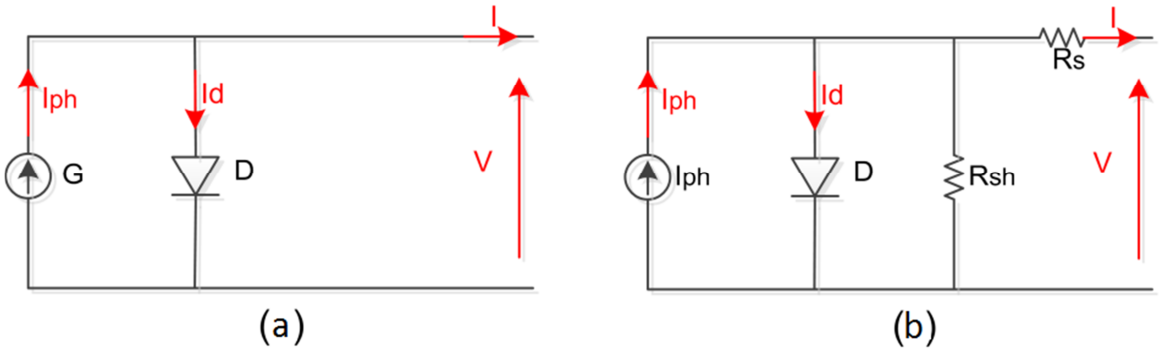

Figure 1.4: two equivalent circuits for single diode model of solar cell.

To achieve the desired voltage and current levels, N_s cells are connected in series and N_p cells are connected in parallel respectively, thus forming a PV module. There for the PV module parameters are scaled according to N_s and N_p as given bellow [18]:

$$I_{ph_{Total}} = N_p \times I_{ph} \tag{1.7}$$

$$I_{o_{Total}} = N_p \times I_o \tag{1.8}$$

$$n_{Total} = N_s \times n \tag{1.9}$$

$$R_{s_{Total}} = \frac{N_s}{N_p} \times R_s \tag{1.10}$$

$$R_{sh_{Total}} = \frac{N_s}{N_p} \times R_{sh} \tag{1.11}$$

The overall PV module model can then be represented by the following figure (figure (1.5)).

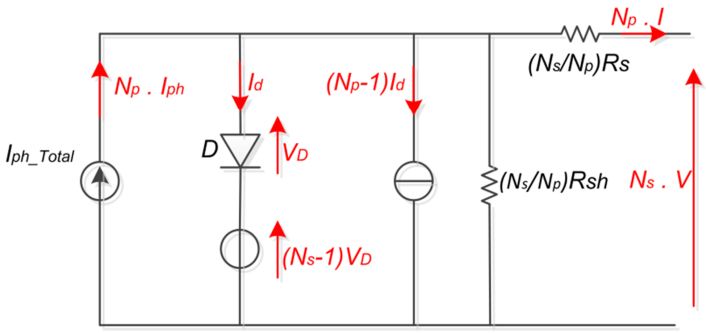

Figure 1.5: PV module circuit model.

Current-voltage characteristic equation of equivalent circuit for the PV module arranged in N_p parallel and N_s series cells is given by [19]:

$$I^M = N_p I_{PH} - N_p I_o \left[\exp\left(\frac{V^M / N_s + I^M R_s / N_p}{n V_t} \right) - 1 \right] - \frac{(N_p / N_s) V^M + I^M R_s}{R_{sh}} \tag{1.12}$$

To estimate the operating cell temperature of PV modules, several models have been developed. Nominal operation cell temperature (NOCT) model is the most commonly used.

In NOCT model, it is simply assumed that, within a short time period (normally less than 1 h), the intensity of the incoming solar irradiance and other parameters affecting the PV modules behaviour are constant. If the variation of rates of overall heat losses to the environment of the PV module is small, then it can be assumed that the rate of heat transfer from the PV module to the environment is steady and the temperatures at each point of the PV module is constant over the short time period [20].

To obtain an NOCT value, an experiment must be conducted under specified conditions and the variations of the environmental conditions must be within the specific ranges. For the crystalline silicon PV module, the testing procedure of NOCT is specified by IEC no. 61215 [21]. NOCT is defined as the mean solar cell junction temperature reached by open circuit cells, under the following standard reference environment (SRE) conditions [21]: solar irradiance on the cell surface is 800 W/m^2, ambient temperature is 20 °C, and wind speed is 1 m/s.

Therefore, the module cell temperature at other environmental conditions can be easily retrieved as given below [20]:

$$T = T_{ambient} + \left(\frac{NOCT - 20}{800} \right) G \tag{1.13}$$

Generally, the NOCT value is an inherent property of each individual module, that can be found in module datasheet [22].

1.2.5. Irradiance and cell temperature effect:

As mentioned previously in section (1.2.4), the *I-V* characteristics of a photovoltaic module strongly depend on irradiance and temperature (equation(1.3)). This becomes very apparent when evaluating equation (1.12) for selected values of temperature and irradiance. Figure (1.6) shows that the output current *I* is mainly influenced by the change in irradiance *G*, whereas the open-circuit voltage V_{oc} remains approximately unchanged. In contrast, for a changing

temperature one can see that the voltage varies widely while the short-circuit current remains unchanged (Figure (1.7)).

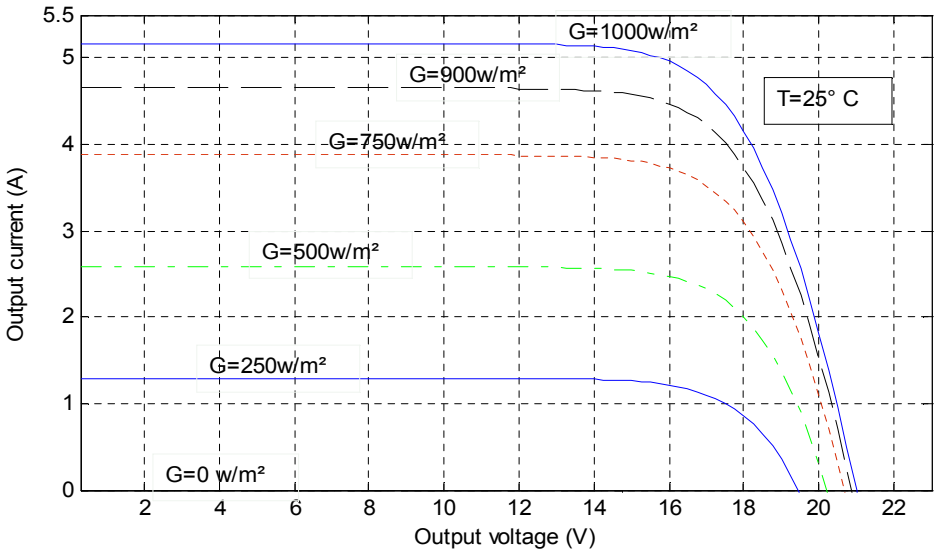

Figure 1.6: *I-V* characteristics of the module for various values of irradiance *G* and fixed temperature.

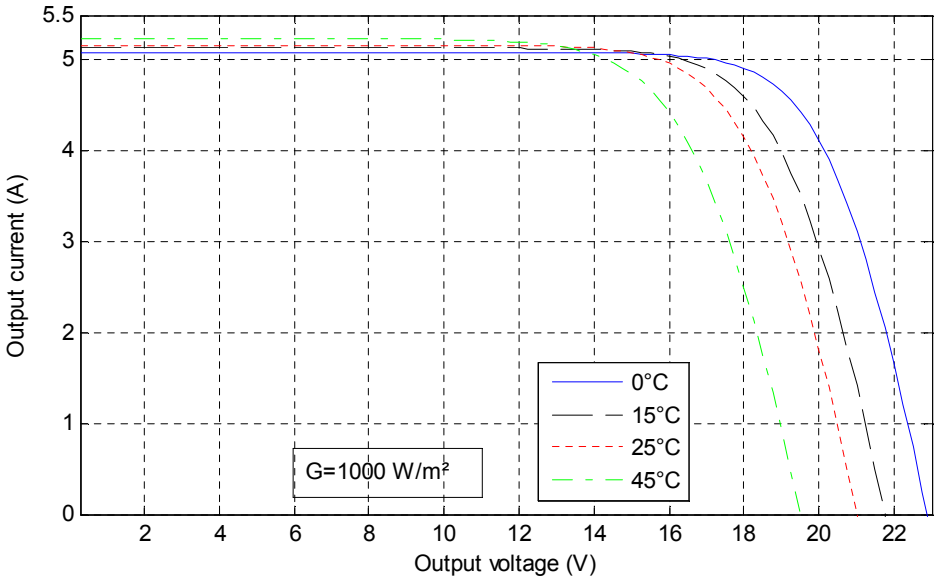

Figure 1.7: *I-V* characteristics of the module for various values of temperature *T* and fixed irradiance.

The corresponding power-voltage (*P-V)* characteristics for variable irradiance and temperature are shown in figures (1.8 and 1.9) respectively. Which show clearly the dependence of the output power of the PV module on both irradiance and temperature. Figure (1.8) shows the output power reduction with the

decreasing of the irradiance, whereas in figure (1.9) the output power reduction is due to the increase of cells temperature.

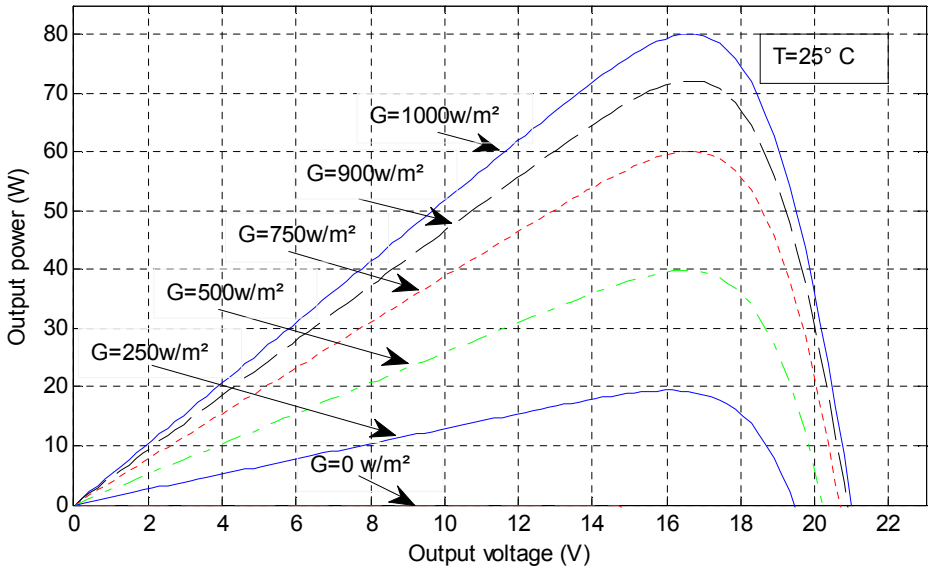

Figure 1.8: *P-V* characteristics of the module for various values of irradiance *G* and fixed temperature.

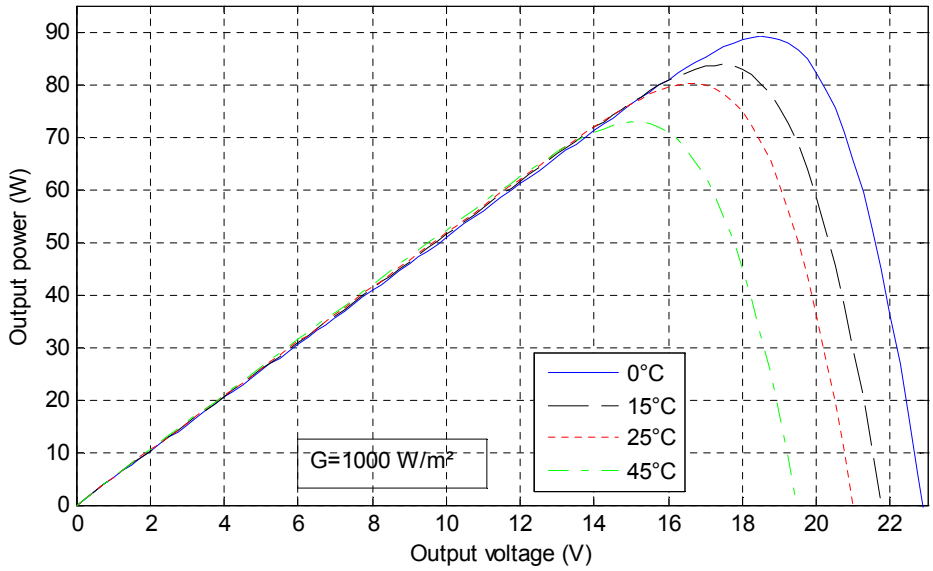

Figure 1.9: *P-V* characteristics of the module for various values of temperature *T* and fixed irradiance.

1.2.6. Maximum power point:

When a load is connected to a photovoltaic generator, the operating point (current and voltage), is obtained by the intersection of the *I–V* characteristics curve of the PVG and the *I–V* characteristics of the load, as shown in figure (1.10). The slope of this curve is *1/R* and the operating point will depend on the value of *R*. For maximum efficiency purpose, the desired operating point should be located at the Maximum Power Point (MPP) (figure (1.11)). The corresponding values for voltage and current are denoted by V_{mpp} and I_{mpp}, respectively. The importance of keeping the operating voltage as close as possible to V_{mpp} is illustrated in figure (1.11). For example, if the operating voltage differs from V_{mpp} by about 10% as indicated by *V1* for the module operating at STC, it will result in an output power reduction of almost 25 %.

Actually, weather conditions variation (irradiance and temperature) and partial shading of PV generator will affect nonlinearly the *I-V* output characteristics. As a consequence, the locus of the maximum power point will permanently change, which makes its tracking very hard.

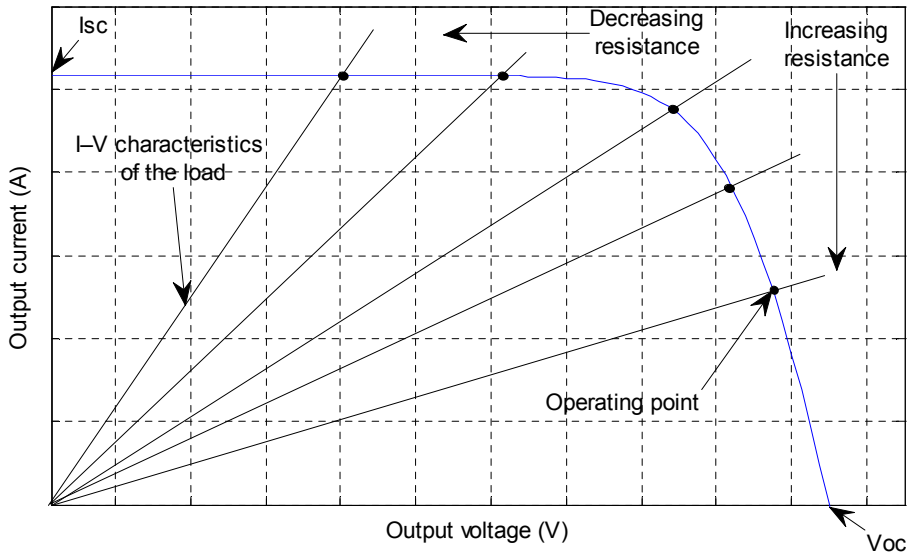

Figure 1.10: Effect of resistive load on PVG operating point.

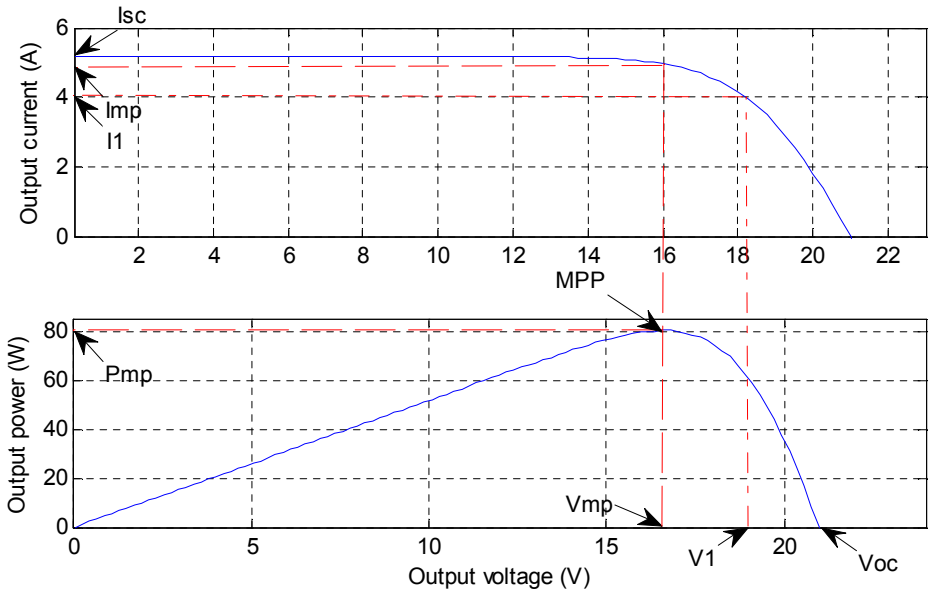

Figure 1.11: Maximum Power Point and the corresponding voltage V_{mpp} and current I_{mpp} for the module operating at STC.

1.2.6.1. Effect of weather conditions on maximum power point:

The instantaneous change of weather conditions (temperature and irradiance) will cause unexpected location of the maximum power point, as shown in figure (1.12).

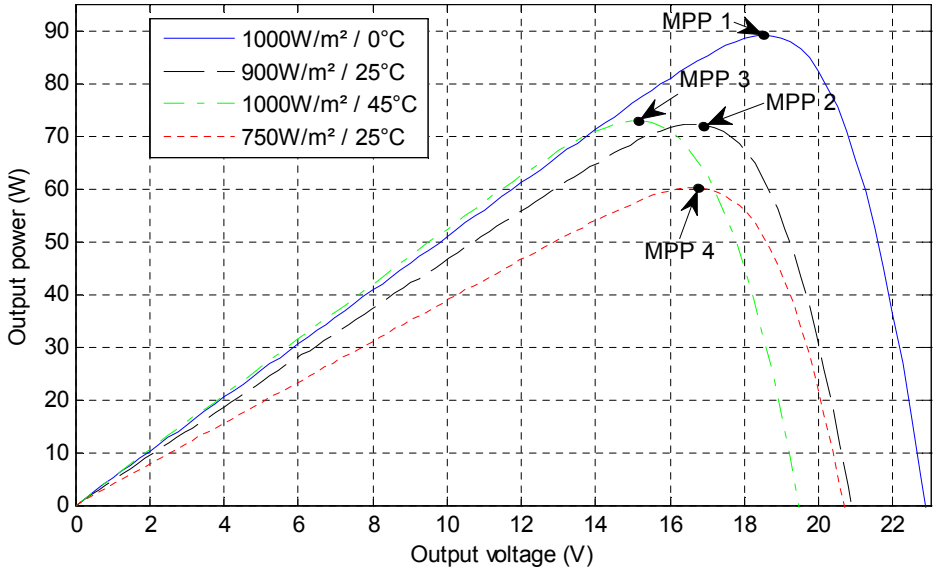

Figure 1.12: Maximum power points of module for instantaneous weather conditions change.

1.2.6.2. Effect of partial shadow on maximum power point:

Ideally, PV systems should be built using identical PV modules and are supposed to operate under uniform irradiance and temperature. However, the occurrence of partial shading cannot easily be avoided because of clouds and obstacles such as trees and buildings (A typical partial shading example is shown in figure (1.13)).

Partial shading not only leads to hot spots in PV modules [9, 10, 23], but is also considered as one of the main causes for reduced energy yields in many PV applications [5, 24].

Figure 1.13: PV array under partial shadow caused by a tree [25].

A. The hot spot problem:

If one of PV cells/modules serially connected have much lower photo-current I_{ph} than others due to partial shading, dust or degradation, it operates as a load for other cells/modules and become reversed biased. This cell/module will then dissipate energy rather than generate it, hence leading to a cell temperature rise. If the temperature is too high, the cell/module can be damaged and affect the whole PV module/array, which is known as the hot spot problem. The most common method to avoid this hot spot problem is to put a bypass diode across a determined group of series connected cells [25], as shown in figure (1.14-a). Under uniform insolation, the bypass diodes are reverse biased and have no impact. When the PV cells are shaded the bypass diodes are forward biased and

the current passes through the diode instead of the PV cells as shown in figure (1.14-b).

The number of bypass diodes per module is a tradeoff between avoiding the hot spots formation and the costs for extra components. For today crystalline silicon PV modules, the optimized number of cells in series per bypass diode is commonly 18 [24].

Hot-spots can also be created when PV modules with different open circuit voltages are connected in parallel, e.g., when one of the PV string in parallel is shaded. In this situation, the PV string with lower open circuit voltage may behave as a load and consume power generated by others. This PV string can be damaged if the temperature is too high. To avoid this problem, blocking diodes are sometimes connected in series with PV string as shown in figure (1.14-a).

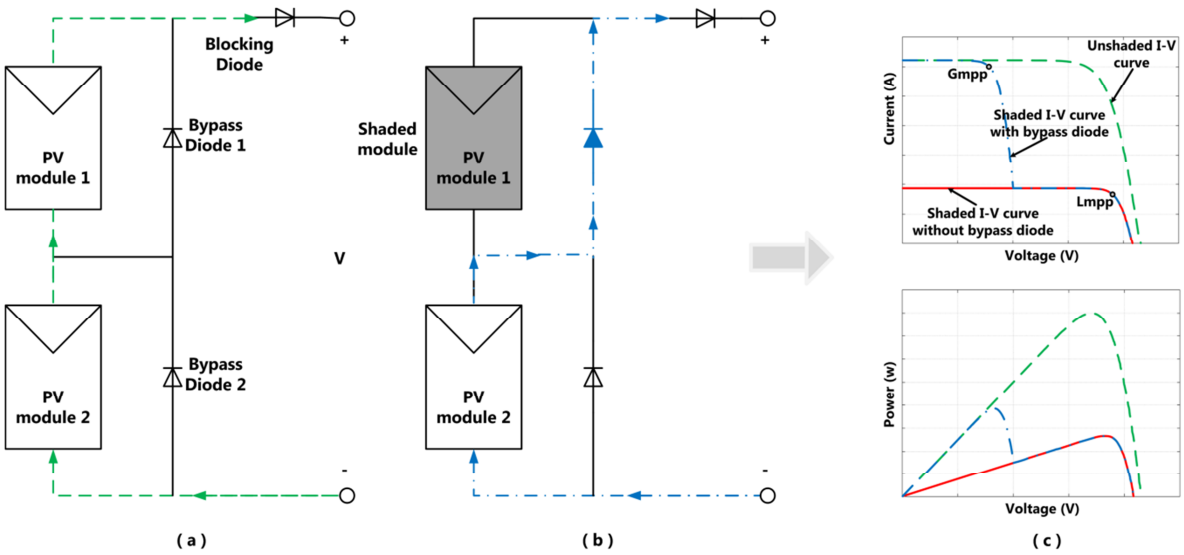

Figure 1.14: Operation of PV array: (a) under uniform irradiation, (b) under PSC, (c) the resulting *I-V* and *P-V* curves for (a) and (b).

B. Output power losses due to partial shading:

As described in the previous section (1.2.6.2.A), bypass diodes are usually used in PV modules to prevent hot-spot damage. However, the bypass diode transforms the *P-V* curves into more complicated shape characterized by multiple peaks as it is shown in figure (1.14-c). Consequently, substantial power reduction

can occur, because of the elimination of the entire shaded cell group by the corresponding bypass diode.

Many research studies have addressed power lowering due to partial shade and some of them have quantified this lowering to be up to 70% [25-27].

1.3. Power conditioning unit:

1.3.1. Power conditioning unit configurations:

In grid connected PV systems, there are two power conditioning unit configurations with respect to the number of power converter stages [28-30]:

- Single-stage converter.
- Dual-stage converter.

For single-stage converter (figure 1.15-a), the maximum power point tracking and the control loops (current and voltage control loops) are all handled by the inverter. For dual-stage converter (figure 1.15-b), the maximum power point tracking is handled by an additional DC-DC converter interfaced between the PV generator and the inverter, while the current and voltage control loops are handled by the inverter stage [30].

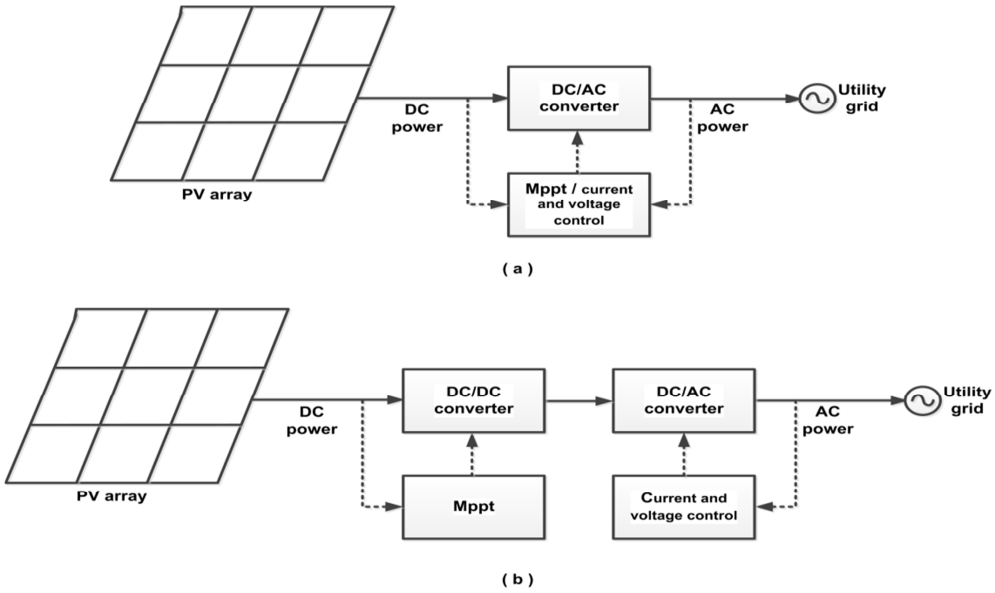

Figure 1.15: Different configurations of Power conditioning unit: (a) single-stage concerter, (b) dual-stage converter.

1.3.2. DC-AC converter (Inverter):

The inverter is a fundamental part of the grid connected PV system, and can be made in different topologies. The most commonly used topology is the full bridge (two level) inverter as shown in figure (1.16). More advanced multilevel inverters (three levels or more) are also used in grid connected PV systems. Some of these topologies are described in [31], such as, series H-bridge multilevel inverter, diode clamped multilevel inverter, flying capacitor structure, etc…. These latter have many advantages such as improved power quality and electromagnetic compatibility (EMC), lower switching losses, and higher voltage capability can be achieved. However, their main disadvantages are the required larger number of switching semiconductors and the small voltage steps which must be supplied on the DC side either by a capacitor bank or multiple PV modules configured to create these voltage steps. Thus, multilevel inverters are suitable for larger PV systems.

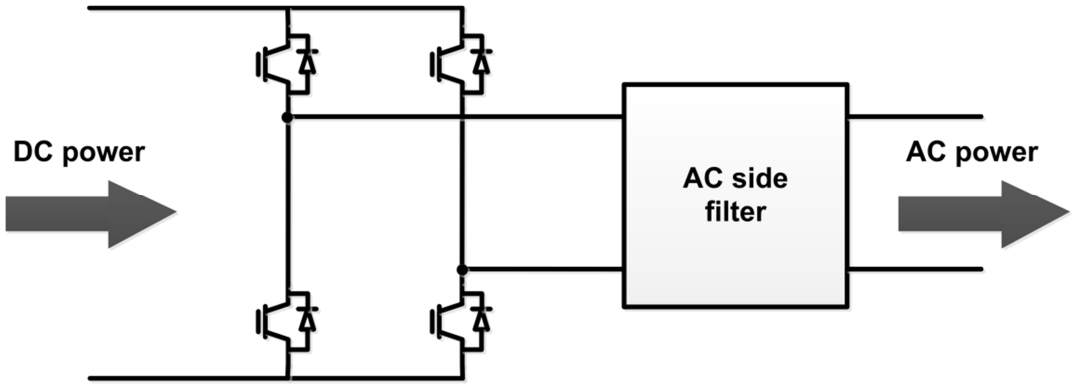

Figure 1.16: Full bridge DC-AC converter.

1.3.3. Inverter categories:

As can be seen in figure (1.17), grid-connected inverters can be classified in two categories:

- Current Source Inverter (CSI).
- Voltage Source Inverter (VSI).

The standard VSI or CSI inverters are the trivial choices to provide single stage DC-AC conversion. Figure (1.17-a), illustrates the standard voltage source inverter in which a DC-link capacitor is connected in parallel with PVG. While, figure (1.17-

b) presents the standard current source inverter in which the inverter is fed from a large DC-link inductor [32].

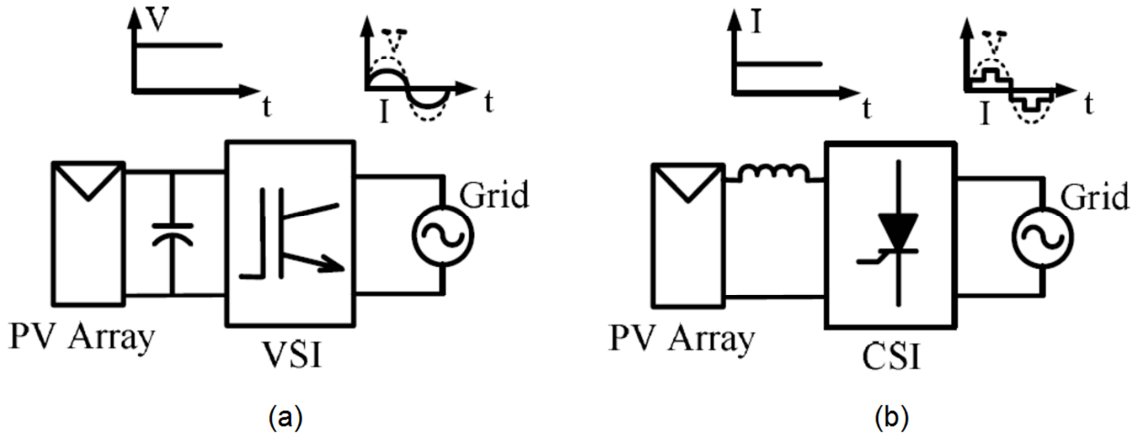

Figure 1.17: Different categories of grid-connected PV systems: (a) voltage source inverter, and (b) current source inverter.

The voltage-source inverter is widely used for grid connected PV systems. However, when employed as a power conditioning unit, VSI normally requires another power electronic converter stage to step up/down the voltage needed at the input of the DC/AC converter. The current-source inverter offers advantages over VSI in terms of short-circuit protection capability and direct output current controllability [33]. However, Poor power factor and harmonics generated by the CSI prevent its use in grid connected systems [34]. In particular, in this thesis voltage-source inverter is addressed.

1.3.4. DC-Link in VSI category:

In order to ensure a power flow from PV side to grid side, the DC bus voltage (U_d) must be higher than the peak value of the grid voltage (V_{grid_rms}) [35]. This DC voltage is estimated using equation (1.14).

$$U_d \geq \sqrt{2} * V_{grid\_rms} + 10\% * V_{grid\_rms} \quad (1.14)$$

A margin of 10% is considered to compensate the voltage drop across the output filter and the switches.

Commonly, a large capacitor is used as DC link, This component is of the upmost importance as it serves three very important functions. The first function is to minimize the voltage ripple across the PV terminals and which results in a ripple

of the output power [36]. Secondly, the capacitor acts as a sink and source every half cycle to help create a balance of power on the DC bus [37]. Lastly, the capacitor is the source for reactive power generation if the control system has the reactive power control functionality [37].

The DC link capacitor C_{DC} is sized according to the equation(1.15). For more details regarding equation (1.15), please refer to Appendix D.

$$C_{DC} = \frac{P_{pv}}{2 * \omega * U_d * \Delta U_d} \tag{1.15}$$

where P_{pv} is the net nominal power from the PVG and ω is the grid pulsation.

To keep the DC bus voltage at its desired value (U_d), a control algorithm must be implemented, more details on DC bus voltage regulation is given in section (I.5.2.1).

1.3.5. DC-DC converters:

The aim of DC-DC switch mode converter is to convert unregulated DC input to regulated or controlled DC output at a desired voltage level. While in PV systems the DC-DC converter is actually controlling the input voltage whatever the output voltage is. With maximum power point tracking algorithms (which will be explained in section 1.5.1) the converter adjusts operation point of the PVG in order to trap it near its optimal operating point. There are several different kinds of DC-DC converters in use in grid-connected PV system, but most of them are based on two basic converter topologies:

- Buck converter (step-down).
- Boost converter (step-up).

The buck converter is often referred to as a step-down converter. Such converter produces a lower output DC voltage than the input voltage. In contrast, the boost converter produces an output DC voltage higher than the input voltage. Buck and boost converters are schematically represented in figure (1.18-a) and (1.18-b) respectively.

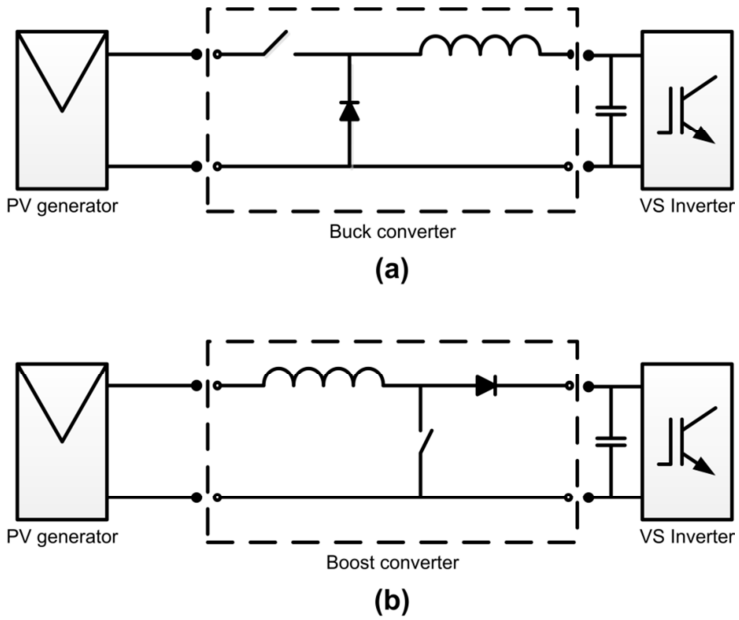

Figure 1.18: DC-DC converters: (a) Buck converter, and (b) Boost converter.

In steady state conditions DC-DC converters can operate differently, depending on the starting point of the current. When the instantaneous inductance current stays at a non-zero value, the converter is operating in the so-called Continuous Conduction Mode (CCM). When the instantaneous inductance current goes to zero before the end of every cycle, the converter is operating in the Discontinuous Conduction Mode (DCM). The condition where the current starts and ends at zero every cycle with continuous conduction mode is referred to as the boundary conduction mode (BCM). More detailed study on buck and boost converters can be found in [38, 39] and the mathematical model of the boost converter is given in appendix C.

In grid-connected PV systems, the input voltage might be higher or lower than the AC voltage. This makes both buck and boost operation necessary, depending on the input voltage. Both converter topologies are also applicable for MPPT. However, in real systems, the boost converter is the more commonly utilized. In small system where the desired DC link voltage cannot be achieved, the boost topology is generally used [40].

1.3.6. AC side filter topologies:

In order to supply the grid with a nearly sinusoidal line current, the inverter is connected to the grid line via a filter. The main objective of the filter is to reduce harmonic content caused by switching semiconductor devices on the injected

current [41]. According to [42], parameters like efficiency, weight and volume have to be considered when choosing the optimal filter topology. Regarding efficiency, filter topologies with reduced losses are required. Although those are relatively small when compared to losses in the inverter, weight and volume of filters are the most important parameters considered in the design.

There are three types of filters used in grid-connected PV systems; L-filter, L-C filter and L-C-L filter as shown in figure (1.19). These different topologies are analysed in [42-45]. Their advantages and disadvantages are pointed out based on the most important features for designing effective filters. Harmonic attenuation, system dynamics and design complexity of these types of filters are among the performance features discussed in the literature.

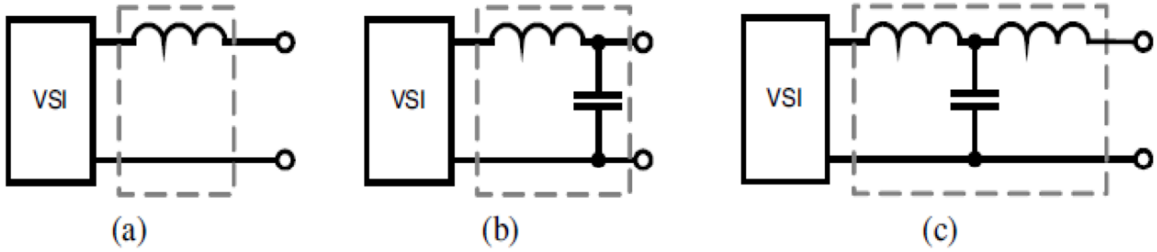

Figure 1.19: Filter Topologies (a) L-Filter (b) L-C Filter (d) L-C-L Filter

A first order filter (Figure 1.19-a) consisting of one inductor is the most commonly used filter in low-power applications to cancel high frequency ripples of current [7]. It is easy to make, and has no resonance problems as higher order filters may have. The major drawback of this filter is the size of the inductor needed to achieve a reasonable attenuation of the current harmonics [46].

Higher order filters consisting of combinations of inductors and capacitors (second order LC filter and third order LCL filter), can give a better attenuation of low-order harmonics, with a bit complicated design procedure than the first order. In grid connected systems the LC filter is seldom used, since the resonance frequency of the filter will vary with the impedance value of the grid. Instead by using a correctly designed LCL filter, this problem is avoided, because the resonance frequency is highly depending on the filter components. In addition, LCL filter will give better attenuation than LC filter, given the same size [47].

The dynamic control of the inverter is more difficult when using LCL filter compared to using a simple L filter. With the LCL filter two more poles and two

more zeroes are introduced compared to the simple L filter. So care must therefore be taken when designing the controller, and the additional poles and zeroes can make the system unstable if not proper damping is introduced [46].

1.4. Grid-Connected PV Standards:

Before designing grid connected converters *for* photovoltaic plants, an overview on rules and regulations that must be followed should be investigated. These rules will however not be the same all over the world. Depending on the grid type there are different considerations to be taken in each country, and therefore there will always be some adaptation to the requirements from the local utilities. The requirements from the local utilities are usually based on a national standards or international standards which deal with the interconnection of distributed resources. These standards are often very similar, but they might have some variations in the degree of limitations and in the used definitions [46]. By looking at the standard from two of the major international standardization organization listed below, an overlook of the most important requirements and limitations can be found.

- International Electrotechnical Commission (IEC).
- Institute of Electrical and Electronics Engineers (IEEE)

Below is a list of the most used standards of interest from IEC and IEEE [48] [49] [50]:

- IEEE Std 1547-2003: Standard for Interconnecting Distributed Resources with Electric Power Systems.
- IEC 61727 Second Edition 2004-12: Photovoltaic systems - Characteristics of the utility interface.
- IEEE STD 929-2000: Recommended Practice for Utility Interface of Photovoltaic Systems

Below is a list of requirements which should be followed when designing PV grid-connected converters, based on the international standard of International Electrotechnical Commission (IEC 61727). This latter, is dedicated for systems with a rate power lower than 10 kW.

1.4.1. Grounding:

Standards require that the PV modules shall be system grounded and monitored for ground faults, to ensure the safety of the public regarding leakage current due to module parasitic capacitance and to prevent undesired effects like cell aging and efficiency reduction [51], especially when the maximum output voltage of the PV modules reaches a certain level, e.g., 50 V [52].

This grounding sometimes involves connecting the negative terminal of the PV array(s) to ground. However, in transformerless systems this might become a problem, especially in single-phase systems with neutral to line connection, where the inverter is already grounded on the grid side [53]. To avoid this problem new transformerless topologies of inverter for high-input-voltage are developed [51, 53].

1.4.2. DC-injection:

DC current injection in the utility grid can saturate the distribution transformers, leading to overheating and trips [54]. For PV inverters with galvanic isolation, this problem does not occur, but transformerless PV inverter topologies shall not inject a DC current higher than >0.5% of the rated injected current under any operating condition. For further information on DC- injection see IEC 61727 §4.4 and IEE 929 §5.2.

1.4.3. Distortion/Harmonics:

It is desirable to have low levels of injected current harmonic distortion, in order to decrease the potential adverse effects on connected equipments. In the standards this is regulated through limiting the allowed current distortion. These limits are summarized in table 1.2. For further information on the harmonic limits see IEC 61727 §4.6 and IEEE 929 §4.4.

Table 1.2: Harmonic current limits.

Harmonic order	Distortion limits
THD	5%
3rd through 9th	4%
11th through 15th	2%
17th through 21st	1.5%
23rd through 33rd	0.6%
above 33rd	0.3%

1.4.4. Power factor:

Commonly, the control function of the inverter is dedicated to regulate the power factor nearly unit (only active power), although in some applications additional control of reactive power can be added. Table 1.3 gives power factor limits according to the standards IEC 61727 §4.7 and IEEE 929 §4.5.

Table 1.3: Power factor limits.

percentage of rated output	Power factor
>10%	>0.85(lagging)
>50%	>0.9(lagging)

1.5. Control unit:

In this thesis the grid connected PV system shown in figure (1.20), is considered. The power conditioning unit used to interface the PV generator and the utility grid consists of a two-stage converter, where a judicious control of power conditioning unit components is indispensable for proper functioning.

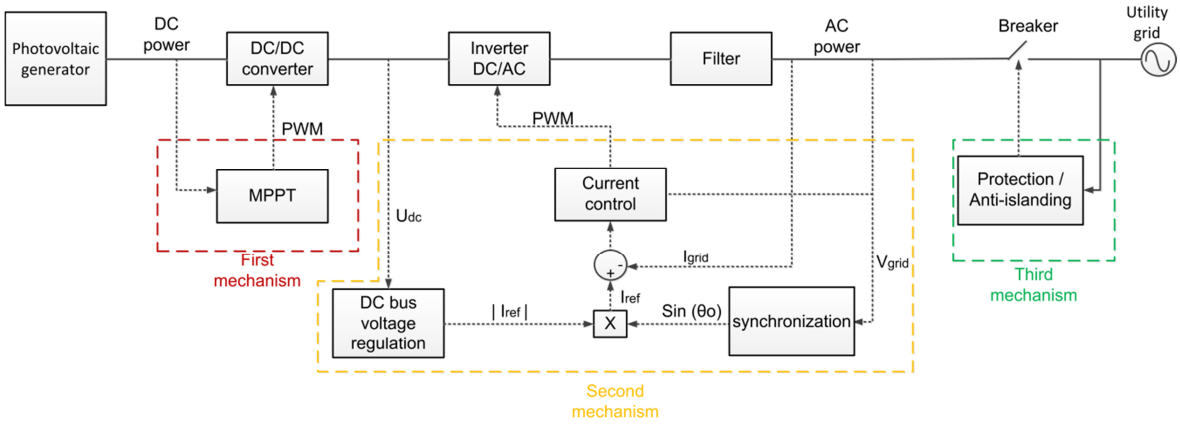

Figure 1.20: Considered grid connected PV system.

The control unit of such system is mainly composed of three control mechanisms. The first one is charged to control the first stage, to achieve maximum power point tracking for more efficiency. The second mechanism is charged to control the second stage, by ensuring that the power injected into the utility grid meets the requirements imposed by the standards (See section 1.4). This latter mechanism is composed of three controllers; DC bus regulation in order to ensure a power flow from PV side to grid side, a synchronization technique that guarantees an injected current synchronized with the grid voltage and an inverter controller. The third mechanism protects system components as well as users.

Hereafter, a review of the recent achievements and current research activities for each mechanism is addressed.

1.5.1. First stage control (DC-DC converter):

To utilize the maximum power produced by the PVG at all times, the control system has to be equipped with a Maximum Power Point Tracker (MPPT) (See figure (1.21)). This latter is a device which tracks the voltage (or current) at where the maximum power is obtained. It is usually implemented by controlling a DC-DC converter, but in single stage converter systems the MPPT is included in the DC-AC inverter control.

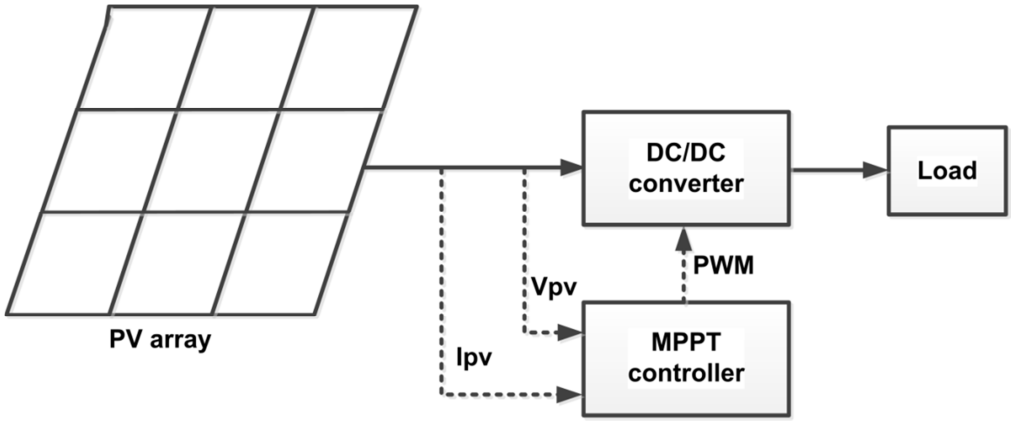

Figure 1.21: Maximum power point tracking circuit diagram.

There are many MPPT techniques that can be found in literature. They can range from conventional techniques to recent developed techniques which share

the same aim of maximizing the PV output power regardless of uniform irradiance or partial shading (see Section 1.2.6 for more details). These MPPT techniques can be categorized based on their characteristics.

1.5.1.1. Comparison factors of MPPT techniques:

The MPPT techniques can be evaluated under the following factors, the design complexity, the ability to track the true MPP, and the convergence speed [55].

A. Design complexity :

It is important to choose the most suitable MPPT based on its design complexity. The implementation of the MPPT algorithms may be done on analogue circuits or digital circuits. Where, digital circuits based MPPT algorithms are less complicated and require simple computer programming.

B. Ability to track the true MPP :

Partial shading condition would lead to the formation of multiple peaks on the *P–V* characteristic, which directly affects the tracking efficiency of algorithms. Thus, developed MPPT techniques should be able to track the true MPP for the extreme environmental conditions.

C. Convergence speed :

A MPPT algorithm should be able to converge to the required operating voltage and current at an acceptable speed, regardless of a gradual or drastic change of environmental conditions.

1.5.1.2. Maximum power point tracking techniques:

The first MPPT techniques, date from the 1970s, are used in aerospace applications, in companies and research centres such as Honeywell Inc and NASA [56-58]. Up until now, various MPPT techniques have been developed.

In this thesis, MPPT techniques reported in figure (1.22) are briefly described. These techniques are systematically categorized into two main groups. The first group includes conventional methods, which are applicable only to track the MPP in photovoltaic systems under uniform irradiance conditions. While, the second group includes global search MPPT techniques, which can extract maximum power from photovoltaic systems under PSC.

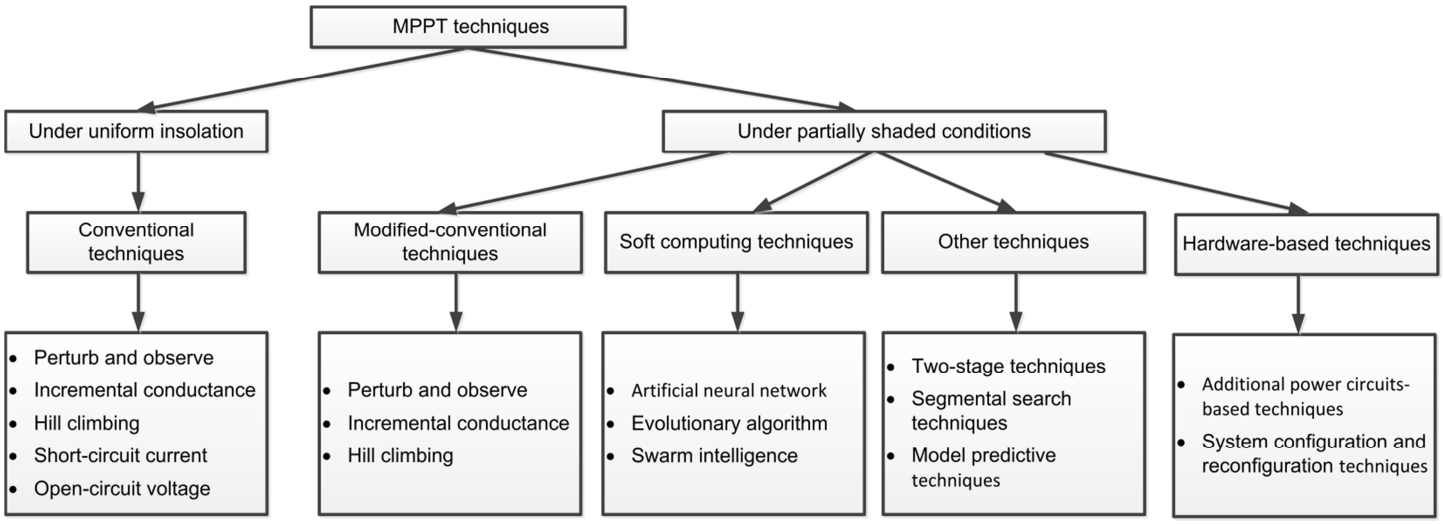

Figure 1.22: Classification of MPPT techniques.

D. Conventional techniques :

Conventional MPPT techniques have proven the ability to track the maximum power point under uniform solar irradiance. The most popular one among these techniques, is the conventional perturb and observe (P&O) technique [59]. This algorithm uses simple feedback arrangement and little measured parameters. In this approach, the module voltage is periodically perturbed and the corresponding output power is compared with that at the previous cycle to determine the next perturbation direction [60]. The second one is the conventional Incremental Conductance (INC) technique, which was developed by K. H. Hussein et al [61]. They used the derivative of conductance to determine the maximum power point. The INC technique is based on the fact that the slope of P-V curve is zero at MPP [62]. This algorithm performs better than P&O algorithm in rapidly varying environment. The hill climbing (HC) technique [63], is basically the same as the P&O. The HC algorithm focuses on the perturbation of the duty-cycle of the power converter to find the MPP. The HC algorithm provides an advantage in its simplicity of operation compared to the P&O technique, but it suffers from the same drawbacks. Fractional Open-circuit voltage [64] and Fractional short-circuit current [65] techniques are the simplest MPPT techniques, based on a linear proportional approximation, to the open-circuit voltage (V_{OC}) and the short-circuit current (I_{CC}) of the PVG. However, these techniques interrupt the system operation

when scanning the entire control range to obtain the V_{OC} and I_{CC}, which yields power losses.

E. Modified-conventional techniques :

As discussed in previous subsection, conventional MPPT techniques are effective under uniform solar irradiance. However, under partially shaded conditions, these MPPTs can fail to track real MPP, because multiple local maxima can be exhibited on the power-voltage characteristic curve. In order to improve their performance, some researchers have proposed some modified conventional techniques, such as, the Modified Perturb and Observe [66], the Modified Incremental Conductance [67], and the Modified Hill Climbing [68]. However, these methods have some drawbacks in terms of complexity and poor convergence rate [67].

F. Soft computing techniques:

Recently, soft computing methods such as Artificial Neural Networks (ANN), evolutionary computation (EC) and swarm intelligence (SI) algorithms have emerged as powerful optimization algorithms for solving complex problems and providing optimal solutions. Parallel, dynamic, decentralized, asynchronous and self-organizing behaviour of the soft computing algorithms are best suited for optimization applications [69, 70]. The effectiveness of soft computing methods in handling nonlinear problems, such that encountered in PV array behaviour, and their implementation simplicity make them very attractive to solve the MPPT problem of PV systems, especially in the case of partial shading and module mismatches [6, 71]. Artificial Neural Networks, are one of soft computing methods that was used in MPPT techniques. Typically, they were used to estimate the MPP with respect to the randomly changing weather conditions [72], and to improve the P&O and IC algorithms [73]. It is known that, using ANN with larger number of hidden nodes leads to more accurate results, but at the expense of longer computational time and complex hardware implementation. Evolutionary computation techniques, such as Genetic Algorithm (GA) [74] and Differential Evolution (DE) [75], have been also proposed to deal with the MPPT problem. However, EC techniques might present a poor convergence rate and slow convergence time [76]. Swarm Intelligence techniques have a good convergence

rate and fast convergence compared to EC techniques [77], though might have more parameters to be determined, which make them inflexible and complex [78]. Particle Swarm Optimization (PSO) and Ant Colony Optimization (ACO) are the most swarm intelligence techniques used in the development of MPPT schemes [79, 80].

G. Other techniques :

Many other Global Maximum Power Point Tracker (GMPPT) techniques that were not categorized into the two previous subsections exist. Such as: - Two-stage techniques [66, 81], which consist to use non-accurate methods in the first stage to determine the approximate GMPP location (i.e., an interval), followed by traditional MPPT methods to determine the precise GMPP location. - Segmental search techniques [82], are based on mathematical theories, finding the GMPP by gradually reducing the search range. - Model Predictive Control (MPC) techniques [83], which can be used to forecast future events and implement controls based on those forecasts; therefore, MPC involves optimizing based on the control quantity required in the current situation.

H. Hardware-based techniques :

In addition to using algorithm-based methods to address the multiple peaks curves caused by PSCs, many researchers have proposed using hardware methods to solve this problem. These methods can be classified as follows: The first class dedicated to small PV systems, which is topology based and need extra additional power circuits to perform global MPPT [84-86]. While, second class is dedicated to large PV systems, which is based on system configuration and reconfiguration: in this class, specific configurations of PV system are proposed such as series-parallel (SP), bridge-linked (BL), and total-crossed-tied (TCT) to produce more power [87-89]. Other works propose to adjust immediately the configuration (reconfiguration) of PV arrays according to the shading pattern to compensate the power losses caused by PSC [84]. Furthermore, the distributed architecture of PV systems is also proposed as a solution [90], in which each power circuit has its own designated controller (multidimensional topology), even if PV modules in the system experience various levels of shading, the distributed architecture can continue to track the GMPP of the entire system.

1.5.2. Second stage control:

The second stage control mechanism must combine three control loops to complete its task. These control loops are, the DC-bus voltage control, inverter switching control and the grid synchronization control. Hereafter, these controllers are briefly reviewed.

1.5.2.1. DC-bus voltage regulation:

Maintaining a constant DC link voltage is necessary to guarantee an excellent operation of PV grid-connected inverters (figure (1.23)). To this end, the DC bus voltage is regulated by adjusting the injected AC line current amplitude. The increase of the injected AC line current amplitude will cause the decrease of the DC bus voltage and vice versa.

Many DC bus voltage regulation strategies can be found in the literature. Constant current adjustment (CCA) and proportional current adjustment (PCA) are the simplest ones [91]. The first one is based on a hysteresis voltage band controller. Inside the hysteresis band, then the reference current will be kept unchanged. If the measured DC bus voltage, V_{dc}, is lower than the low limit of the hysteresis band, then the amplitude of the reference current should be decreased by a constant current command adjustment. On the other hand, if V_{dc} is higher than the high limit of the hysteresis band, then the amplitude of the reference current should be increased by a constant current adjustment. The PCA method is similar to the CCA method except that the adjusting coefficient is proportional to the quantity of the voltage difference between the actual and the desired DC bus voltage. However, despite their simplicity, these strategies have a poor steady-state, slow dynamic response and the choice of adjusting coefficients is very difficult [91].

In order to avoid these problems, PI controller is widely used. The resulting error signal between the actual and the desired DC bus voltage is applied to the PI controller. The output PI controller serves as a reference current for switching control loop of the inverter (See figure (1.23)). Some other control strategies such as adaptive filtering technique [92] and nonlinear PID controller [93] give better performances then PI controller, but are complicated from point of view of design and practical application.

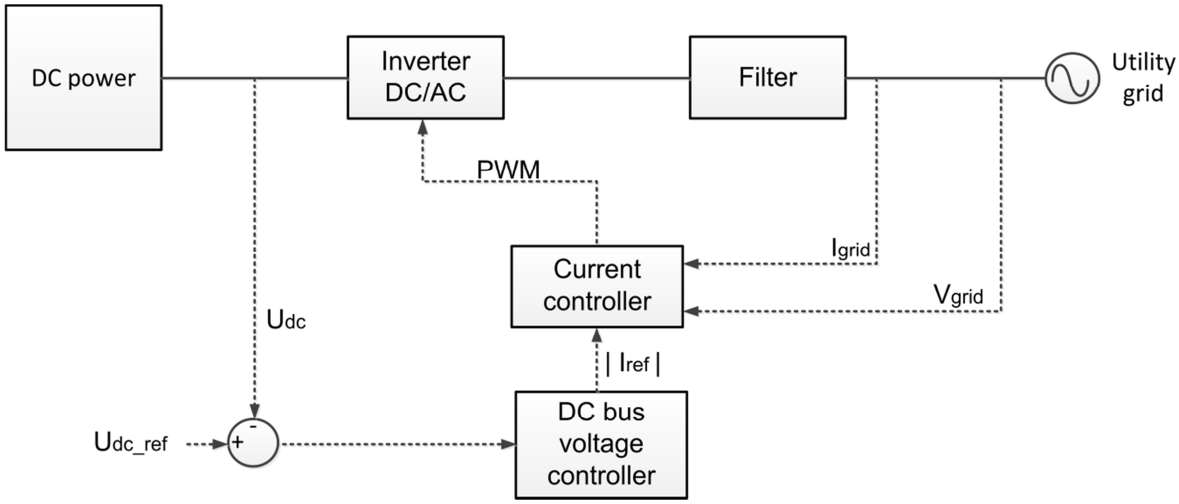

Figure 1.23: DC bus voltage regulation strategy.

1.5.2.2. DC-AC converter control:

In order to control the DC-AC converter, there are two major control strategies, namely: Current Controlled Inverter (CCI) and Voltage Controlled Inverter (VCI). In grid connected system, a current controlled inverter has the advantage of being less susceptible to voltage phase shifts and to distortion in the grid voltage, and has the ability to reduce the THD of the injected current to a minimum. Whereas voltage controlled inverter can result in overloading of the inverter due to small phase errors, and large harmonic currents may occur if the grid voltage is distorted [46]. Thus, in grid connected system, current controlled inverter is the most robust control strategy. Therefore only Current Controlled VSI (CC-VSI) will be considered in this thesis.

Various CC-based control methods have been proposed in grid-connected PV systems. Although these control strategies can achieve the same goals, their performances are quite different. In this section, only the most commonly used methods reported in figure (1.24) are briefly described.

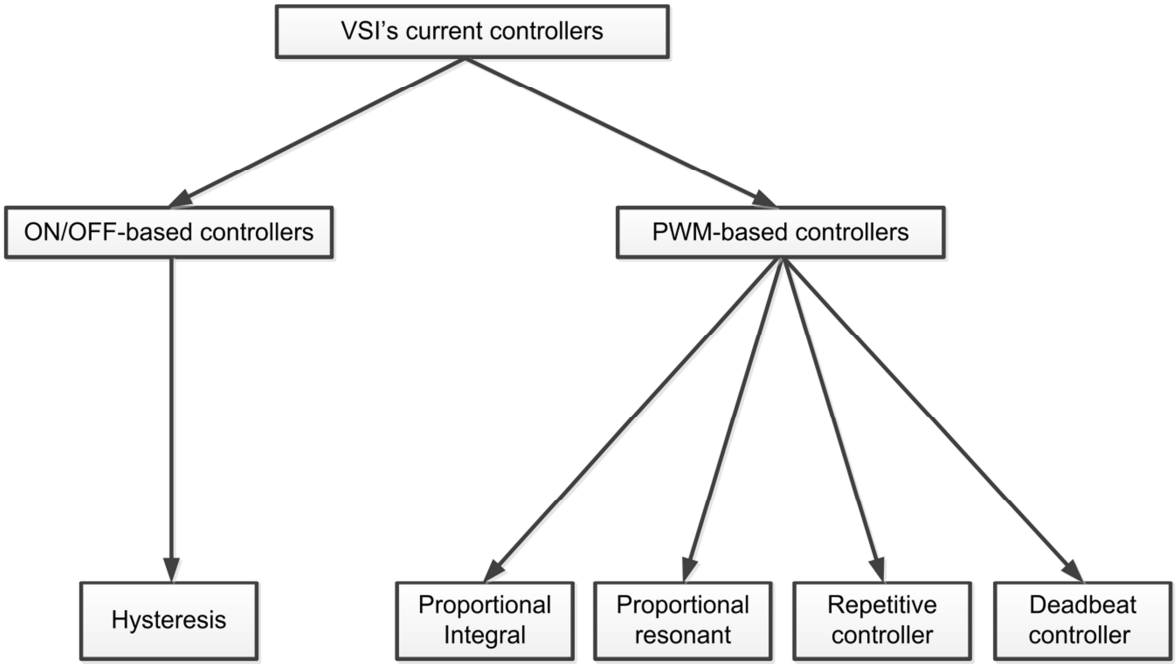

Figure 1.24: Classification of current control VSI methods.

A. Hysteresis controller:

In the hysteresis controller, actual line and reference current are used to derive the signal switching of the inverter. Lower and upper hysteresis band limits are directly related to the minimum and the maximum allowed pre-set error. When the reference current is changed, the line current has to stay within these limits. The range of the error signal directly controls the amount of ripples in the output current from the inverter which is called the hysteresis band. Hysteresis controllers present many advantages like simplicity, fast dynamic response, and robustness. However, the drawback of this type of controller is an uneven and random switching frequency pattern, which makes the filtering of output waveform quite complex and expensive. Moreover, it results in additional stresses on the switching devices [94]. Although there are a number of active researches to improve the hysteresis current control technique [95], but applying variable frequency noises into the utility grid is not recommended because it can trigger unpredictable resonances in the grid utility [94].

B. Proportional-integral controller:

Proportional-integral (PI) controllers [96] were used as a former grid connected current controller. Their gain is determined via (1.16):

$$G_{PI}(s) = K_P + \frac{K_I}{s} \tag{1.16}$$

where K_P and K_I are the proportional and the integral gain respectively.

However, this controller exhibits two well-known drawbacks: the inability to track a sinusoidal reference without steadystate error and a poor disturbance rejection capability [97]. This is due to the poor performance of the integral action when the disturbance is a periodic signal.

B. Proportional resonant controller :

The ideal proportional resonant controllers (PR) [98] present a high gain around the natural resonant frequency ω, which is given by (1.17).

$$G_{PI}(s) = K_P + \frac{K_I s}{s^2 + \omega^2} \tag{1.17}$$

where ω, K_P and K_I represent the resonance frequency, proportional and the integral gain respectively.

These controllers rather than PI controllers can cancel the steady state error between the reference and the injected current by achieving a very high gain around the resonance frequency [98]. However, PR controllers as PI controllers are unable to give a large loop gain at the multiple harmonic frequencies to provide a good compensation for a wide band of harmonics [99].

D. Repetitive Controller :

Repetitive controllers (RC) are also introduced as an alternative to improve the grid-connected system output current. RC controllers perform superior error cancelation for periodic signals by presenting a large magnitude of the loop gain at the fundamental frequency and its integral multiples. However, repetitive controller suffers from some drawbacks, such as: slow dynamic and a large memory requirement [100, 101]. Sliding mode controller [102], odd-harmonic repetitive controller [101] and dual-mode repetitive controller [103], are part of RC controllers.

E. Deadbeat Controller :

The deadbeat controller belongs to the family of predictive controllers [104]. They are based on a common principle: foreseeing the evolution of the controlled quantity (the injected current) and on the basis of this prediction the average voltage is calculated and produced by the converter (by using pulse width modulator) [105]. The controller is developed on the basis of the model of the filter and of the grid, which is used to predict the system dynamic behaviour. The advantages of predictive dead-beat control are fast dynamic response and accurate reference tracking. However, this controller is a model-based regulator, so it is sensitive to parameter variations, and has a time delays, since it regulates the current when it achieves its reference at the end of the next switching period.

1.5.2.3. Synchronisation:

Grid synchronization of single-phase grid-connected PV inverter lies in the accurate detection of the attributes of the grid voltage in order to tune an internal oscillator of power converter controllers to the oscillatory dynamics imposed by the grid. This synchronization is important to:

- Deliver power at a power factor within pre-determined limits (See section 1.4.4), or within limits given by the utility if there is a need for reactive power compensation.
- Reduce the harmonic current content, by applying a “clean” reference current.
- Minimize the grid connection transients.

Usually, the main attributes of interest for interfacing photovoltaic energy to the grid are the amplitude and the phase-angle of the fundamental frequency component of the grid voltage [54].

Grid synchronization techniques can be classified into two main groups, namely: the frequency-domain and the time-domain synchronisation methods:

- Frequency-domain methods: are usually based on some discrete implementation of the Fourier analysis [106], and Wavelet Transform (WT) [107]. The use of frequency domain entails significant operating advantages; e.g. linear differential equations with constant coefficients in the time domain can be solved by using ordinary algebraic equations in the frequency domain and complicated convolution integrals can be

transformed into simple multiplications [54], which allows to design simples techniques.

- Time-domain methods: are based on some kind of adaptive loop that enables an internal oscillator to track the component of interest of the input signal (grid voltage) by using a feedback loop. The most extended synchronization method in engineering applications is the phase-locked loop (PLL) [108]. The latter provides continuous information about the phase-angle and amplitude of the grid voltage, which allows current controllers and modulators to be implemented [54]. Improved structures of PLL are also introduced, by using some kind of quadrature signal generator (QSG) [109], and adaptive mechanism [110].

1.5.3. Protection mechanism:

Under certain undesirable circumstances (depending on the grid voltage level and the frequency range), the PV grid-connected system should be designed to disconnect from the network via its on-board protection mechanism to prevent any damage, as shown in figure (1.25). To this end, the system must open the breaker in response to any unusual grid condition in a certain amount of time.

The maximum allowable response time for a grid-connected inverter to stop energizing in the case of voltage level change, are listed in Table 1.4 [111], where V_{nom} is the RMS nominal voltage of the grid at the point of common coupling (PCC):

Table 1.4: Maximum trip time for grid-connected systems.

Voltage	**Maximum time to stop energizing**
$V_{grid} < 50\% V_{nom}$	0.1s
$50\% V_{nom} \leq V_{grid} < 85\% V_{nom}$	2.0s
$85\% V_{nom} \leq V_{grid} < 110\% V_{nom}$	Continuous operation
$110\% V_{nom} \leq V_{grid} < 135\% V_{nom}$	2.0s
$135\% V_{nom} \leq V_{grid}$	0.05s

The default limits normal operating frequency are set according to IEC 61727 §5.2.2, which states that when the utility frequency is outside of the rated frequency (± 1 Hz), the system shall cease to energize the utility within 0,2s.

It is noted, however, if the utility returns to normal operating range of Voltage/frequency within the allowed time, the converter does not have to cease energizing the utility grid [49].

Furthermore, in the event of loss of grid utility supply, the system should also disconnect from the grid, otherwise it could continue to provide energy to the network, this situation is known as "islanding" and can cause many problems, such as:

- Safety concerns: if an island occurs, grid utility maintenance staff may be faced with unexpected live wires.
- End-user equipment damage: customer equipment could theoretically be damaged if operating parameters differ greatly from the norm. In this case, the utility is liable for the damage.
- Grid equipment damage: reclosing the circuit onto an active island may cause problems with the grid utility equipment.
- Inverter confusion: reclosing onto an active island may cause confusion among the inverters.

According to IEC 61727 standard, a utility distribution system is islanded when it is out of the normal operation specifications for voltage and/or frequency. When this situation occurs, the PV system must cease to energize the utility grid within 2s of loss of the grid utility.

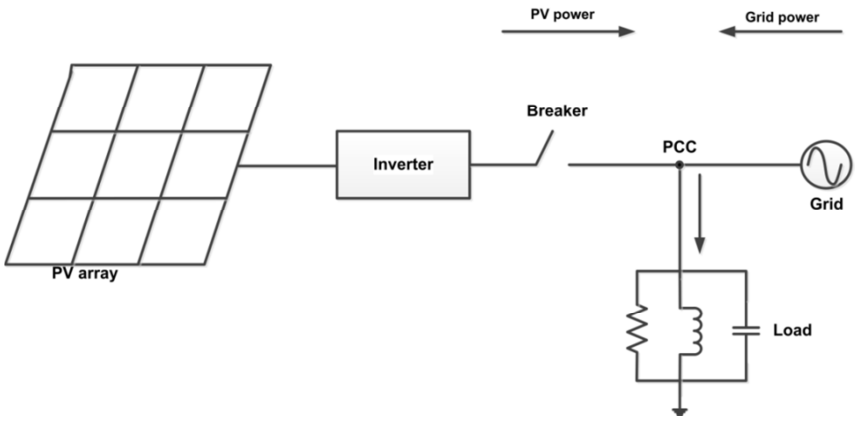

Figure 1.25: PV grid connected system with protection mechanism.

1.5.3.1. Islanding detection methods:

The reliability of islanding detection methods can be represented by the non-detection zone (NDZ), defined in the power mismatch between the power produced by the PV system and the power produced by the utility (active power mismatch versus reactive power mismatch) at the point of common coupling (PCC), in which the islanding is not detectable. For further details, refer to reference [112].

Islanding detection methods may be divided into three categories: passive methods, active methods, and remote methods [113-115].

- Passive islanding detection techniques are based on monitoring the grid parameters that typically change during islanding (typically amplitude, frequency, phase or harmonic of the voltage). Their advantages are easy implementation, no degradation of the PV inverter power quality, and not cost effective. Their primary drawbacks are a relatively large NDZ and their ineffectiveness in multi-inverter systems [116, 117]. The most commonly used passive islanding detection techniques are [115]:
    - Over/under voltage and over/under frequency (OV/UV & OF/UF).
    - Phase jump detection (PJD).
    - Voltage harmonic monitoring and current harmonic monitoring.
    - Rate of change of power output (ROCOP).
    - Rate of change of frequency (ROCOF).

- Active techniques inject a small disturbance at the PV inverter output for islanding detection. With active methods, the NDZ can be significantly reduced. However, their main drawbacks are the possibility of deteriorating the output power quality which might destabilize the PV inverter. In addition, To the need (usually) for additional controllers leading to an increased complexity [116]. The most popular active islanding detection techniques are:
    - Impedance measurement (IM).
    - Sliding mode frequency shift (SMS) or active phase shift (APS).
    - Sandia frequency shift (SFS) or active frequency drift with positive feedback.

- Remote islanding detection techniques are based on the communication between the utility and the inverter [117]. This technique does not have NDZ and does not degrade the power quality in multi-inverter systems. It is effective but cost effective to implement (especially in small systems) and has a complicated communication techniques. The common communication-based techniques are:

- Power line carrier communication (PLCC).
- Signal produced by disconnect (SPD).
- Supervisory control and data acquisition (SCADA).

1.5.3.2. Reconnection:

When the inverter has ceased to energize the utility grid, the inverter should not reconnect before the frequency and voltage have been maintained within the specified limits for at least 5 min. After that 5 minutes, the inverter should automatically reconnect to the utility.

1.6. Grid connected photovoltaic system configurations:

In general, four types of grid-connected PV system configurations are identified [28, 30]:

- Central plant inverter.
- Multiple string DC-DC converter with single output inverter.
- Multiple string inverter.
- Module integrated inverter.

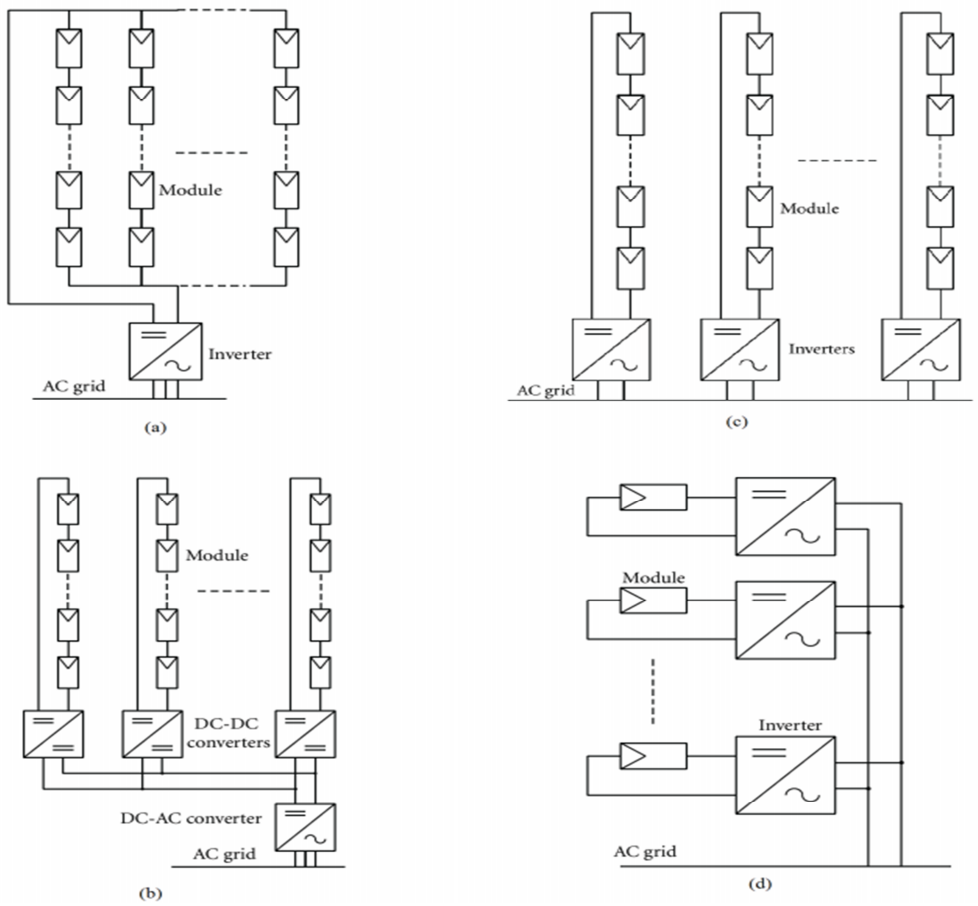

Figure 1.26: System configurations: (a) central plant inverter, (b) multiple string DC-DC converter, (c) multiple string inverter, and (d) module integrated inverter.

The central plant inverter configuration is shown in figure (1.26-a). It consists of a large inverter which is interfaced between the PV modules and the utility grid to convert the output DC to AC power. In this system, the PV modules are serially connected to form a string and several such strings are connected in parallel to form a single DC bus. The strings produce sufficiently high voltage, and the parallel connections increase the output current level.

In multiple string DC/DC converter, as shown in figure (1.26-b), each string have an additional DC-DC converter linked to a common DC bus, and then feeding a central inverter.

Figure (1.26-c) illustrates the multiple string inverter configuration, which includes one inverter for each string. The outputs of these inverters are fed directly into the utility grid. This arrangement is not badly affected by the shading of the string. It is also not seriously affected by inverter failure.

In the module integrated inverter system (figure 1.26-d), each module (typically 50–300W) will have a small inverter. It is expected that high volume of small inverters will bring down the cost.

1.7. Storage devices:

In grid-connected photovoltaic systems, it is not so common to use energy storage devices. This is due to the fact that the grid can be utilized as an "unlimited" energy source or sink, thus additional energy storage is unnecessary [40]. Nevertheless, in some applications temporary storage of the produced energy might be needed for several reasons. In such case, some extra capacity might be useful to stabilize the grid during short periods of high power consumption and to supply critical or sensitive loads during abnormal grid conditions or blackout.

1.8. Conclusion:

A state of the art of single-phase grid connected photovoltaic systems has been given and discussed. The grid connected PV system shown in figure (1.20) was chosen to be considered in this thesis. In this system, the power conditioning unit used to interface the PV generator and utility grid consists of two-stage full-bridge voltage source inverter, with both L-filter and LCL-filter. In order to obtain the desired DC link voltage under any operating conditions, the step-up (boost) DC-DC converter is used. The inverter operates in the current controlled mode to ensure a high power-factor and low harmonic distortion in the injected current.

For the control unit, the swarm intelligence-based MPPT and the deadbeat method are used in the first and the second power stage respectively.

Finally, the DC bus regulation is ensured using a PI controller, the grid synchronisation is achieved using QSG based PLL technique and (OV/UV & OF/UF) method is used for anti-islanding detection.

CHAPTER 2

MAXIMUM POWER POINT TRACKING

2.1. Introduction:

As was mentioned in the first chapter, the overall efficiency of the grid connected photovoltaic systems, depends primarily on the used control strategy for tracking the maximum power point in order to extract all or almost all the power collected by the PV generator.

In this context, this chapter discusses two developed MPPT approaches, which use the direct control structure, dedicated to the control of one-dimensional and multidimensional PV systems, respectively. These approaches are based on a relatively new member of swarm intelligence algorithms, which is the artificial bee colony algorithm. The two developed MPPT approaches are tested on PV systems which connect directly the PVGs to a resistive load, to permit a thorough inspection, while grid connected tests are conducted in chapter 4.

2.2. Direct control structure:

Figure (2.1) shows the block diagram of a conventional structure of MPPT scheme. Typically, it consists of two independent control loops [27, 118]. The first one is the voltage control loop that works by comparing the sensed PV voltage with a reference signal obtained from the MPPT block. The output of this loop is used as a reference for the second loop (the current control loop). The latter tries to bring the tracking error to zero at the MPP [27]. Since PI controllers are easy to design and have a low cost, they are widely used in these loops. However, PI controllers based approaches present two main drawbacks: slow transient response and possible undesirable oscillations around the MPP. Specifically, the PI controller requires enough time to reach steady state operation increasing the time interval between two successive reference outputs from MPPT controller and therefore deteriorates the dynamic behaviour [119]. Moreover, the inherent nonlinearities in the PV power source may cause a severely degradation on the performance of the PI controller due to improper tuning of its gain parameters which even lead to instability and a loss of energy from the PVG.

Alternatively, the MPPT controller can be operated without of control loops as mentioned above. This control type is known as the direct MPPT control scheme [120]. Its general block diagram is shown in figure (2.1). Both PI control loops are eliminated and the duty cycle is directly computed by the algorithm. The general advantages of the direct control structure can be briefly stated as below:

- A simple tracking structure.
- Significant reduction of the computation time.
- No tuning for the PI controller gains.

In short, it replaces sophisticated MPPT control with a more simplified structure while maintaining optimal results.

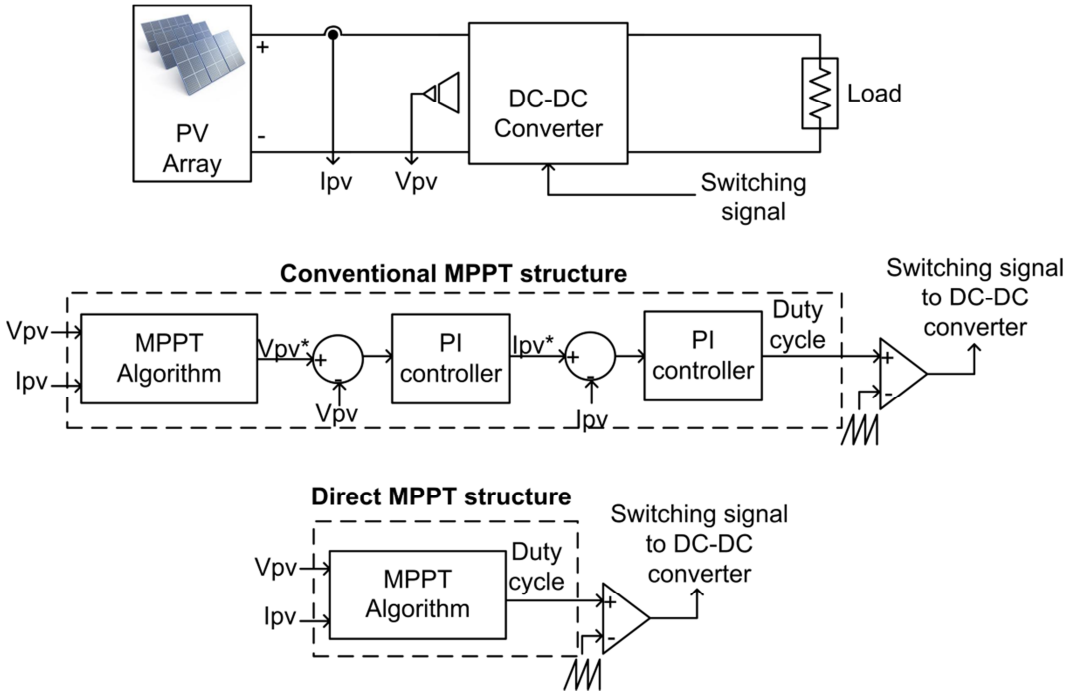

Figure 2.1: Conventional and direct control structures.

2.3. Multidimensional PV System topology:

The power loss due to the partial shading conditions can be minimized if the PV system is divided into a number of smaller subsystems (see section 1.5. 1. 2. A), where each one is controlled with its own converter. This mode, known as multidimensional PV system is shown by figure (2.2-a). However, if the number of subsystems is too high, it requires a relatively high number of voltage and current sensors. In order to reduce the cost as well as to solve the problems with

controlling scheme, the number of sensors should be reduced. Towards this end, a new configuration shown in figure (2.2-b) is proposed; where a single pair of voltage and current sensors is sufficient to implement the MPPT scheme. Therefore, this configuration performs a good compromise between the increase of the output power of the PV system and the reduction of the number of sensors needed at the same time. The latter configuration is preferred when applying swarm intelligence algorithms such as particle swarm optimization, Differential Evolutionary and Ant Colony Optimization by taking advantage of their capability to solve multidimensional problems.

Many researchers have used the multidimensional configuration to prove the effectiveness of their proposed MPPT methods. For example,Miyatake, Veerachary, Toriumi, Fujii and Ko [121] have evaluated the PSO-based MPPT, Keyrouz and Georges [122] have proposed the combination of Bayesian Fusion and PSO and Jiang, Maskell and Patra [123] have evaluated the ACO-based MPPT. In this chapter, the multidimensional PV System is used to evaluate the developed ABC-based MPPT techniques.

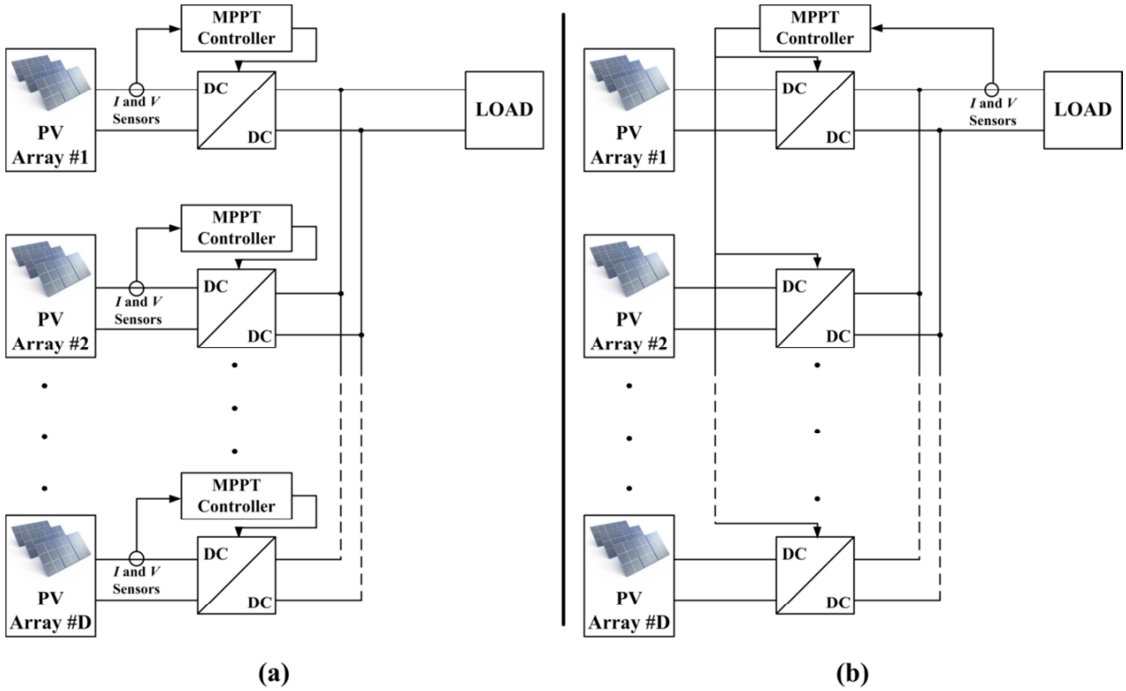

Figure 2.2: Multidimensional PV system (a) Controlled by multiple controllers; (b) Controlled by a single controller.

2.4. MPPT techniques used in comparison tests:

As discussed in section (1.5.1.2), MPPT techniques can be categorized in two groups: the first group includes conventional techniques, which are applicable only to track the MPP in photovoltaic systems under uniform irradiance conditions. While, the second group includes global search MPPT techniques, which can extract maximum power from photovoltaic systems under varying atmospheric and partial shading conditions. Within this second group, soft computing algorithms-based MPPT have emerged as powerful power optimization techniques, in view of their effectiveness. While, on basis of the convergence rate, the convergence speed and the implementation simplicity, swarm intelligence-based MPPT techniques, outperform other soft computing algorithms based techniques [6].

In order to perform comparison tests for the developed techniques with other MPPT techniques, we had to choose the most popular algorithms. For such needs P&O from conventional techniques and PSO from swarm intelligence-based MPPT techniques are chosen and their detailed codes are given here after.

2.4.1. Perturb and observation technique (*P&O)*:

The P&O algorithms are widely used in control of MPPT thanks to their simple structure and reduced number of necessary measured parameters [6]. Three techniques have been proposed in the literature for implementing the P&O algorithm: reference voltage perturbation [124], reference current perturbation [125], and direct duty cycle perturbation [126].

Direct duty cycle perturbation is the simplest method because it has not need an auxiliary controller (usually a PI controller) to regulate the output voltage or current of the PV generator. As the name implies, the concept behind the direct duty cycle perturbation method is based on observation of PVG output power and its perturbation by changing the duty cycle (d) of the DC-DC converter. The algorithm increments or decrements continuously the duty cycle based on the previous value of power until it reaches the MPP [127]. When $dP/dDC>0$ and the duty cycle is perturbed in a specific direction, it's known that perturbation moves the operating point of PVG to the MPP, the P&O method will then continue to perturb the duty cycle in the same direction. When $dP/dDC<0$, the perturbation moves the operating point of PVG away from the MPP, then the P&O method

reverses the direction of the perturbation. Figure (2.3) shows a block diagram for the direct duty cycle perturbation technique.

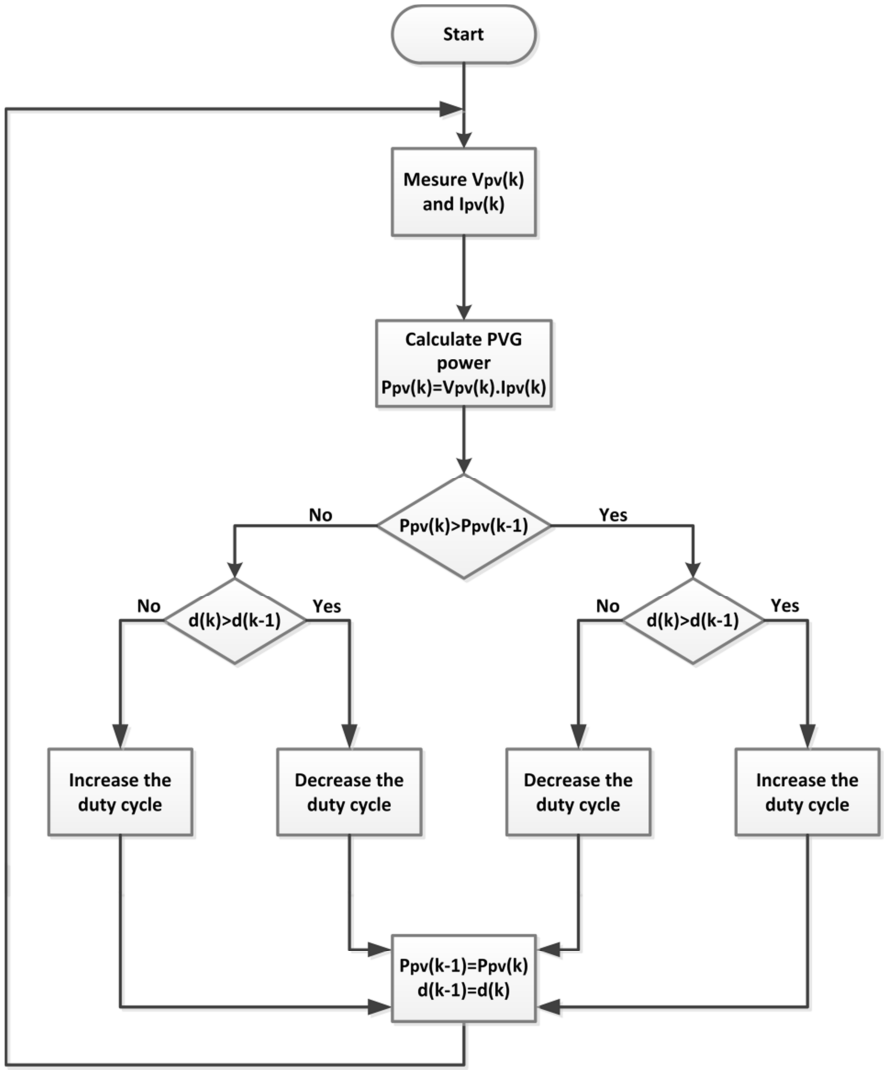

Figure 2.3: Flow chart of perturb and observe MPPT algorithm.

2.4.2. Particle swarm optimization (*PSO*):

Particle swarm optimization (PSO) is a swarm intelligence based optimization technique developed by Dr. Eberhart and Dr. Kennedy in 1995. It was inspired from the behaviour of organisms such as a flock of birds and a shoal of fish. PSO is an optimization method that iteratively tries to improve a candidate solution (known as particle) with regard to a given measure of quality. These particles move around in the search-space according to simple mathematical formulae, exploiting their position and velocity. Each particle is influenced by its own best

position and the best known positions in the search-space, guided by the neighborhoods best position. The general idea of particles movement in PSO is illustrated in figure (2.4).

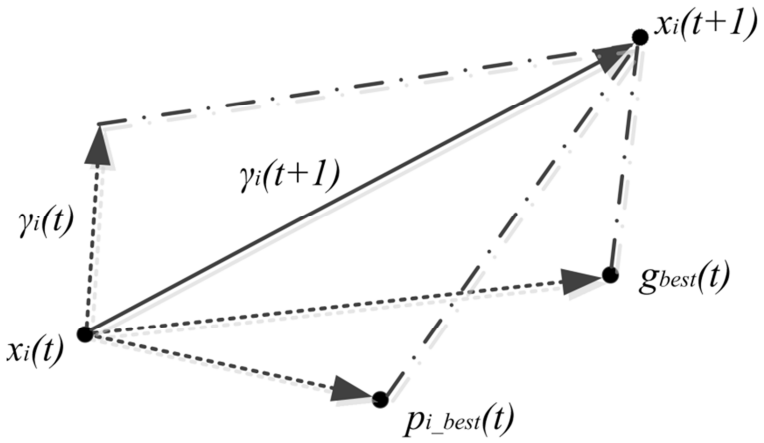

Figure 2.4: Particles movement in PSO.

The individual particles position is defined by:

$$x_i^j(t+1) = x_i^j(t) + \gamma_i(t+1) \tag{2.1}$$

Where: $x_i(t)$ is the i_{th} particle at time t, p_{i_best} is the personal best position of i_{th} particle at time t, $g_{best}(t)$ is the global best position of the swarm at time t and γ_i represent the velocity component and is calculated by:

$$\gamma_i(t+1) = \omega\gamma_i(t) + C_1 rand(0,1)(p_{i\_best}(t) - x_i(t)) + C_2 rand(0,1)(g_{best}(t) - x_i(t)) \tag{2.2}$$

The parameter ω is called the inertia weight and controls the magnitude of the old velocity v in the calculation of the new velocity, whereas C_1 and C_2 determine the significance of p_{i_best} and g_{best}, respectively.

Since partially shaded *P–V* curve exhibits multiple peaks, PSO method is envisaged to be very effective to track the global MPP under this condition. Thus, several research works have proposed PSO-based MPPT algorithms [79, 80, 128-130].

To apply the PSO algorithm in MPPT problem to find the global MPP, parameters of the PSO algorithm need to be specified. These parameters include the inertia weight, acceleration coefficients, swarm size and maximum iterations. Then, a solution vector of duty cycles initialized and the algorithm transmits duty

cycles to the power converter. These duty cycles (represented by x in (2.1)) serve as the initial particles in the first iteration. All particles are heading towards their local best position *Pbest*. Among these particles, one of them is the global best g_{best} which gives the best fitness value. After calculating the velocity, which serves as a perturbation to the duty cycle, a new position of the duty cycle is found. Through successive iteration all particles move towards global best position. The detailed pseudo-code of PSO algorithm is given below.

Detailed pseudo-code of the PSO algorithm:

Begin
1: Setting values of the control parameters of PSO algorithm:
inertia weight ω; acceleration coefficients C_1 and C_2;
swarm size *N*; and maximum iterations number max_generation.
Initialization
2: Set the generation number *cycle = 0*;
Initialize a population of *N* particles;
Initialize velocities γ_i of the particles:
Repeat
3: Calculate p_{i_best} and g_{best}
4: Evaluate the fitness of particles
5: For each particles {
Calculate its new velocity by using (2.2)
Update its position by using (2.1)
}
6: Increase the generation count: *cycle = cycle + 1*
Until
7: The stopping criterion is satisfied

2.5. Developed ABC-based MPPT approaches:

Recently, swarm intelligence-based MPPT techniques are envisaged to be very effective to deal with the MPPT problem. These new MPPT methods offer significant benefits as: fast convergence speed, reduction in computational effort, and a compact solution for multivariable problems. However, they may suffer from some problems such as:

- Algorithm convergence dependence to initial position of agents which gives a poor convergence rate in some situation (PSO).
- Several algorithm parameters to be determined, which makes these algorithms inflexible and complex (PSO, ACO).

ABC is a relatively new member of swarm intelligence techniques. It was proposed by Karaboga in 2005 [77], based on foraging behaviour, learning, memorizing and information sharing characteristics of honeybees. Several research papers have already evaluated the performances of ABC algorithm against different approaches like PSO, ACO and several other optimization techniques [131-134]. Their finding states that the main advantages of the ABC algorithm are its simplicity [135], light computing complexity, high solutions accuracy [131, 136, 137], convergence independent of the initial conditions [138] and its ability to deal with local minima [77]. At present, the ABC algorithm has been successfully applied in distinct fields of science such as electrical engineering: in power flow optimization and optimal sizing of photovoltaic systems [139, 140], control engineering: in enhancement of control algorithms [141], image processing: in block matching techniques [142], mechanical engineering: in optimization of design approaches [143] and many others.

In this section, a novel ABC-based MPPT with direct control method for PV systems working under PSC is discussed. With this MPPT control scheme, the duty cycle is adjusted directly by the algorithm without the need of using a linear controller (see section 2.2). The proposed MPPT scheme advances the state-of-the art through the following contributions:

- Excellent tracking capability with a good accuracy.
- No requirement of knowledge about the characteristics of the PVG.
- The use of just two control parameters, allowing great flexibility and simplicity.

2.5.1. Fundamentals of ABC optimisation algorithm:

The artificial bee colony algorithm is a swarm based algorithm that was introduced for solving multidimensional and multimodal optimisation problems. The algorithm is specifically based on the model proposed by Tereshko and Loengarov [144-146] for the foraging behaviour of honeybee colonies.

In the ABC algorithm, the artificial bees are classified into three groups: employed bees, onlooker bees and scouts. A bee that is currently searching for food or exploiting a food source is called an employed bee. A bee waiting in the

hive for making decision to choose a food source is named as an onlooker. Employed bees whose food sources cannot be improved through a predetermined number of trials become scouts and their food sources are abandoned. The number of food sources is equal to the number of employed bees and also equal to the number of onlooker bees. Analogously, in the optimization context, the position of a food source represents a candidate solution of the optimization problem and the nectar amount of a food source corresponds to the quality (fitness) of the associated solution.

At the initialisation phase, the ABC generates a randomly distributed initial population of SN solutions. Each solution is produced within its limits according to the equation below:

$$x_i^j = x_{\min}^j + rand[0,1](x_{\max}^j - x_{\min}^j) \quad i = 1,2,...,SN \quad j = 1,2,...,D \tag{2.3}$$

where $x_{\min}^j$ and $x_{\max}^j$ represent the minimum and the maximum of the parameter *j* and D is the number of optimization parameters.

After initialization, the population of the solutions is subject to repeated cycles $C = 1,2,...,MCN$, of the search processes of the employed bees, the onlooker bees and the scout bees.

For each cycle, every employed bee produces new solution v_{ij} according to equation (2.4) and then evaluates its fitness fit_i.

$$v_{ij} = x_{ij} + \phi_{ij}(x_{ij} - x_{kj}) \tag{2.4}$$

where $k \in \{1,2,...,SN\}$ and $j \in \{1,2,...,D\}$ are randomly chosen indexes. Although *k* has to be different from *i*. ϕ_{ij} is a random number between [-1, 1].

After the information is shared by the employed bees, each onlooker finds new solution v_{ij} within the neighbourhood of x_i by using equation (2.4), based on the probability P_i defined as:

$$P_i = \frac{fit_i}{\sum_{n=1}^{SN} fit_n} \tag{2.5}$$

where fit_i is the fitness value of the solution x_i.

The value of each generated candidate solution v_{ij} that is not within the boundary of the allowed search space is updated so that it will be within this space.

The fitness of each new produced candidate solution v_{ij} is compared with that of its old one. If the new solution has an equal or better fitness than the old solution, it replaces the old one in the memory. Otherwise, the old one is retained in the memory. In other words, a greedy selection mechanism is employed in the selection operation between the old and the candidate one.

At the end of each search cycle, if the fitness of a solution cannot be improved and the predetermined number of trials, which is called ‘‘*limit*”, is exhausted, then the solution will be abandoned by scout bee and a new solution is randomly searched. The new solution x_i will be generated using equation (2.3).

It is clear, from the above explanation, that there are three control parameters in the basic ABC: the number of candidate solutions which is equal to the number of employed and onlooker bees *SN*, the value of “*limit*” and the maximum cycle number *MCN*.

The detailed pseudo-code of the ABC algorithm is given below:

Detailed pseudo-code of the ABC algorithm:

Begin

1: Setting values of the control parameters of ABC algorithm:
the number of employed and onlooker bees *SN*; the value of *limit*;
the maximum cycle number *MCN*.

Initialization

2: Set the generation number *cycle = 0*;
Generate the initial solutions $x_i, i = 1,2,...,SN$ using equation (2.3)

3: Evaluate the fitness (fit_i) of the population

Repeat

4: For each employed bee {
Produce new solution v_i using equation (2.4)
Calculate the value fit_i
Apply the greedy selection process }

5: Calculate the probability values P_i for the solutions x_i by equation (2.5)

6: For each onlooker bee {
Select a solution x_i depending on p_i
Produce new solution v_i by using equation (2.4)
Calculate the value fit_i
Apply the greedy selection process }

7: If there is an abandoned solution for the scout Then replace it with a new solution which will be randomly produced using equation (2.3)

8: Memorize the best solution achieved so far

9: cycle = cycle + 1

Until

10: The stopping criterion is satisfied

2.5.2. Application of ABC to the MPPT problem:

The ABC-based optimization described in section (2.5.1) is now applied with a slight change made in the scout bees phase, to realize the MPPT algorithm for Photovoltaic Generation System (PGS) operating under PSC with direct control technique.

To realize the direct control ABC-based MPPT, each candidate solution is defined as the duty cycle value *d* of the *DC-DC* converter, so the optimization problem has one parameter to be optimized ($D = 1$). Thus, equations (2.3) and (2.4) become:

$$d_i = d_{\min} + rand[0,1](d_{\max} - d_{\min}) \tag{2.6}$$

$$new\_d_i = d_i + \phi_i(d_i - d_k) \tag{2.7}$$

The fitness of each solution (duty cycle) is chosen as the generated power Ppv of the PGS. Then equation (2.5) becomes:

$$P_i = \frac{Ppv_i}{\sum_{n=1}^{SN} Ppv_i} \tag{2.8}$$

To evaluate the duty cycles, the digital controller successively outputs the PWM signal according to the value of d_i, and then the PV voltage Vpv_i and current Ipv_i can be measured and the corresponding power (Ppv_i) of each duty cycle d_i can be calculated. It should be noted that in order to acquire correct samples, the time interval between two successive duty cycle evaluations (*Ts*) has to be greater than the power converter settling time.

In the original ABC algorithm, at the end of each search cycle the abandoned solution that has not improved its fitness over a predetermined number of cycles (*limit*) is replaced by a new randomly chosen solution. If this strategy is used in the MPPT algorithm, the stopping criterion stops the search process before the *limit* cycle be reached, because the power *Ppv* remains unchanged (premature convergence). Thus, a very important phase that gives ability to the algorithm to escape from local minima is eliminated. In this work a different strategy for the scout bees' phase is proposed to avoid that problem, which consists in replacing the duty cycle giving less power at the end of each search cycle, by another randomly chosen value.

The application procedure of the proposed method can be divided in four phases:

- *Initialisation phase:*

Set the algorithm parameters by including the number of candidate solutions SN, the maximum cycle number MCN and the control period *Ts*. Then, a randomly distributed initial SN duty cycles are generated using equation (2.6) and evaluated.

$$d_i \quad (i = 1, 2, ..., SN)$$

- *Employed bees phase:*

The employed bees duty cycles are updated using (2.7) and then evaluated. Then, the greedy selection process is applied and the probability value P_i for each duty cycle d_i using equation (2.8) is calculated.

- *Onlooker bees phase:*

The roulette wheel selection *is used to* recruit the onlooker bees for local searching around the chosen duty cycle value which is depending on the calculated probability P_i. The new duty cycles are evaluated and then the greedy selection process is applied.

- *Scout bees phase:*

Equation (2.7) is used to replace the duty cycle giving less power with the new randomly chosen duty cycle. The fitness of the generated duty cycle is then evaluated.

At the end of each search cycle, the algorithm memorizes the best solution achieved so far and repeats the procedure from the employed bees phase until the Maximum Cycle Number (*MCN*) is reached or until the power value remains unchanged within a specified number of cycles.

Usually, the real working environment of the PV system is always changing due to the varying weather conditions, and as a result, the global MPP is always changing. This requires the MPPT algorithm to have the ability to search for a global MPP for the new weather condition. For this purpose, the search process has to restart with a total re-initialization whenever the weather conditions are changed. Here, we use the following strategy to detect these changes:

$$\frac{|Ppv_{new} - Ppv_{last}|}{Ppv_{last}} \geq \Delta Ppv(\%) \tag{2.9}$$

The search process of a new MPP will be executed again whenever the inequality, given above, is satisfied. This ensures that the MPPT algorithm can always find the global MPP under various working environmental conditions.

The flowchart of the proposed ABC-based MPPT algorithm of PV systems is shown in figure (2.5).

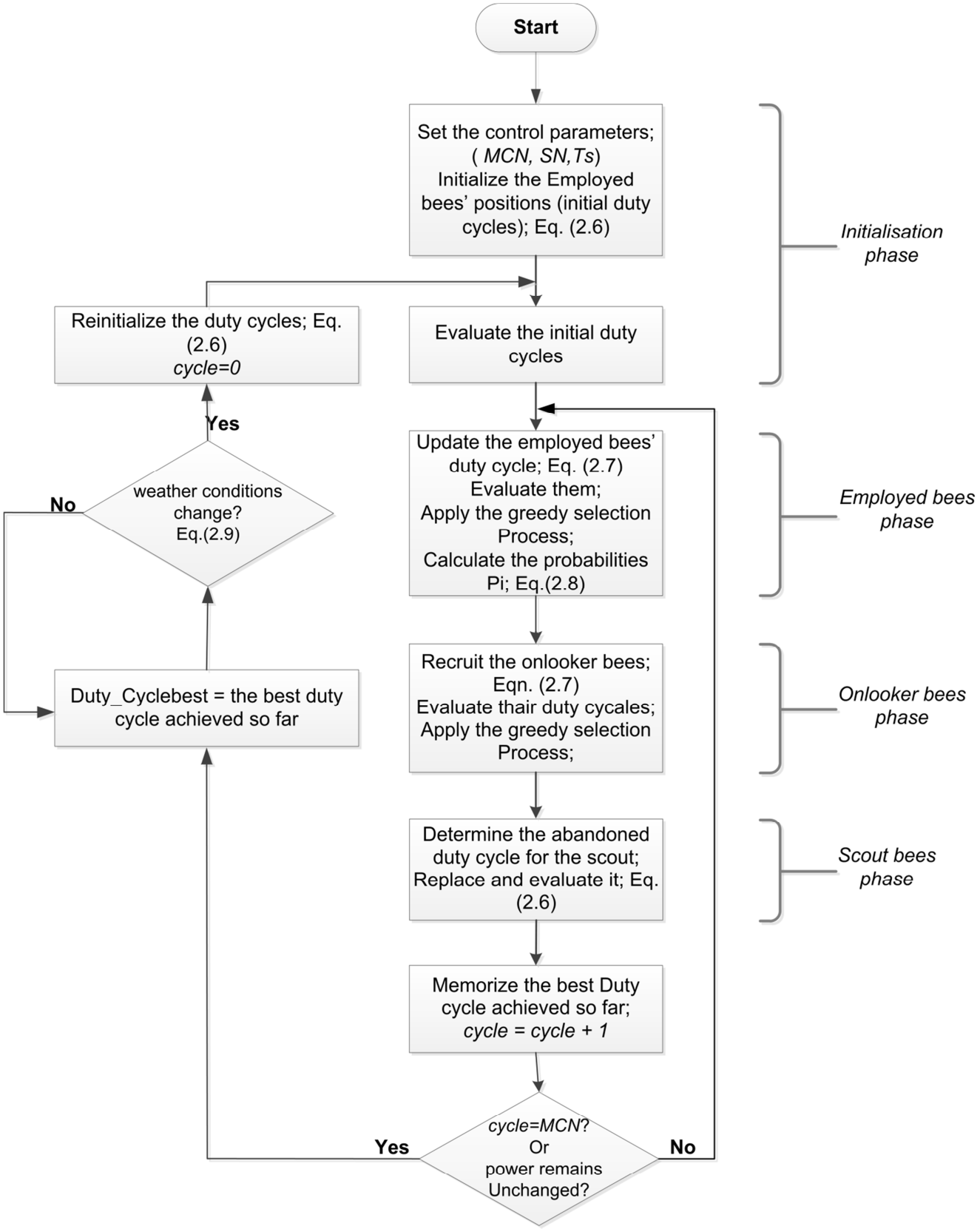

Figure 2.5: Flowchart of the proposed ABC-based MPPT with direct control technique for PV system.

2.5.3. ABC-based MPPT for multiple photovoltaic arrays:

The novel ABC-based MPPT described in section (2.5.1) is now adapted to control a multidimensional (modular) configuration of PV arrays, where the duty cycles of DC-DC converters are regarded as the control variables to maximize the power output (load power), each candidate solution is defined as a vector of duty cycle values d_i^j of DC-DC converters, so equations (2.3) and (2.4) become:

$$d_i^j = d_{\min}^j + rand[0,1](d_{\max}^j - d_{\min}^j) \quad i = 1,2,...,SN \quad j = 1,2,...,D \tag{2.10}$$

$$new\_d_{ij} = d_{ij} + \phi_{ij}(d_{ij} - d_{kj}) \tag{2.11}$$

where $d_{\min}^j$ and $d_{\max}^j$ represent the minimum and the maximum limit of the duty cycle search range of the converter *j* and D is the number of PV subsystems.

The fitness of each solution (duty cycles vector) is chosen as the load power $Pload$. Then Equation (2.5) becomes:

$$P_i = \frac{Pload_i}{\sum_{n=1}^{SN} Pload_i} \tag{2.12}$$

2.6. Simulation results:

In this simulation study, a co-simulation methodology combining Matlab/Simulink and Psim environments has been adopted to assess the feasibility and the effectiveness of the proposed MPPT algorithms. The PV arrays and the boost converter were implemented in Psim environment while the MPPT algorithms were implemented in Matlab/Simulink environment. Comparisons of the proposed algorithm against P&O and PSO-based MPPT, under dynamic weather conditions, were also performed.

The parameters of the used PV modules are listed in Table 2.1.

Table 2.1: Parameters of the used PV modules (BP SX 80).

Parameter	Value
maximum power	80W
open circuit voltage	21 V
maximum power voltage	16.8 V
short circuit current	5.17 A
maximum power current	4.75 A
temperature coefficient	-0.080 V/°C
configuration	2s1P (2 bypass diodes)

The step-up (boost) DC-DC converters chosen for interfacing between the PVG and the resistive load have been designed and rated in appendix D. The rated values found are presented in the table below:

Table 2.2: DC-DC converters component' values and operating conditions.

Component/Parameter	Value
Input capacitor	220 uF
Boost inductor	2 mH
Output capacitor	220 uF
Switching frequency	20 kHz
Maximum input voltage	51.1 V
Maximum input current	5.17 A
Maximum output voltage	126.5 V
Maximum output current	1.26 A

The control period should be set as low as possible without causing instability in the system, which can be done by considering the dynamic step response of the system. The system must be allowed to reach a new steady state condition before the next perturbation (or be within a certain limit of the new steady state condition). The mathematical background for optimizing the control period of MPPT algorithms is presented in [147]. In this simulation study the control period has been chosen equal to 0.05s ($Ts = 0.05s$).

2.6.1. ABC-based MPPT for a single photovoltaic array:

The 160-W system, given in figure (2.6), is implemented and used to evaluate the performance of the proposed MPPT algorithm.

This system consists of two PV module connected in series, a boost converter and a digital controller in which the MPPT algorithms under test are implemented. Figure (2.7) shows the implemented Simulink model, and figure (2.8) shows the Psim circuit of the boost converter and the PV array, where two bypass diodes protecting eighteen cells in each module are considered.

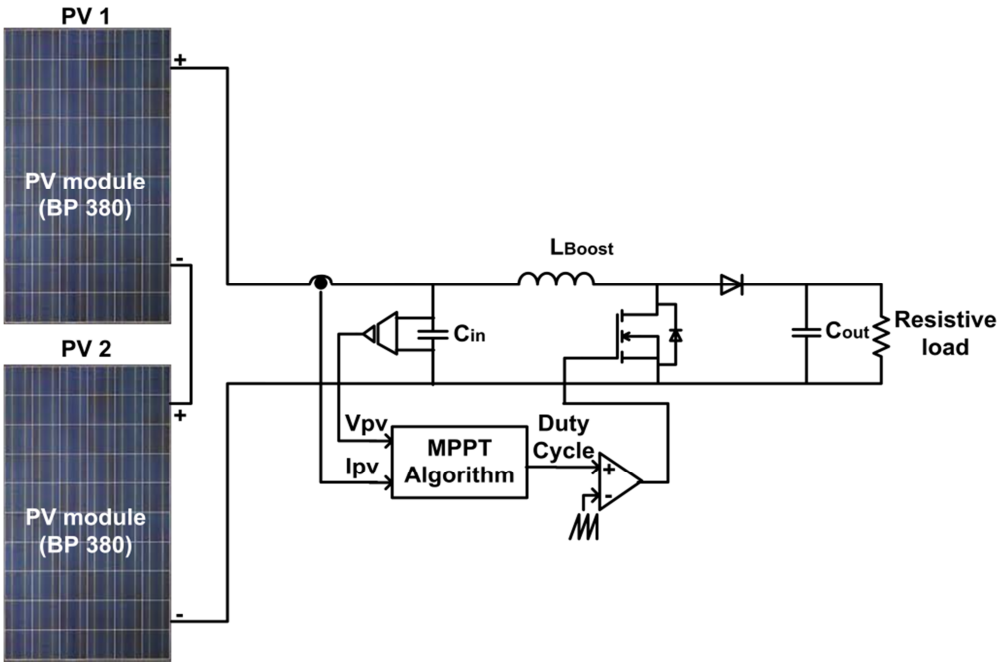

Figure 2.6: System block diagram.

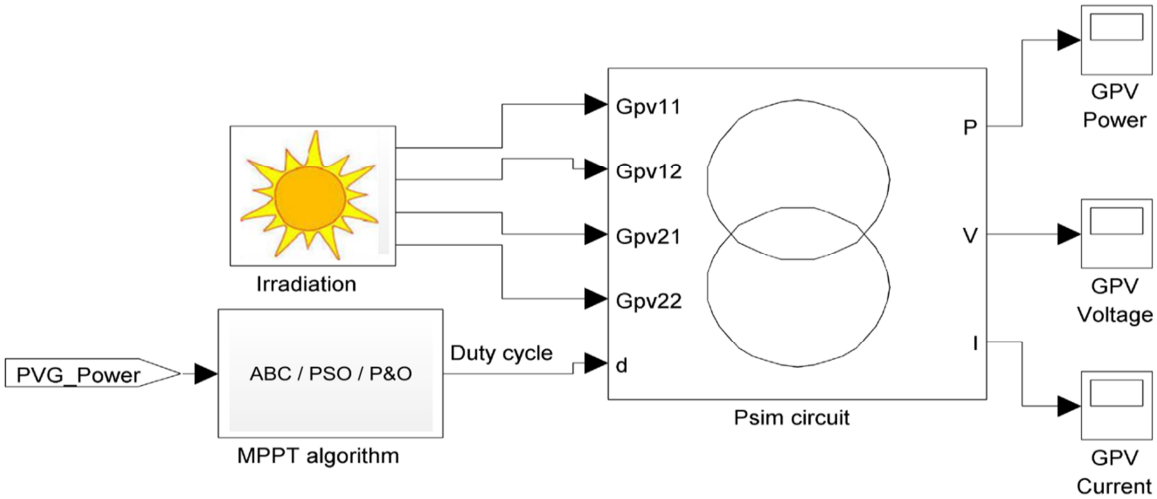

Figure 2.7: Implemented simulink model.

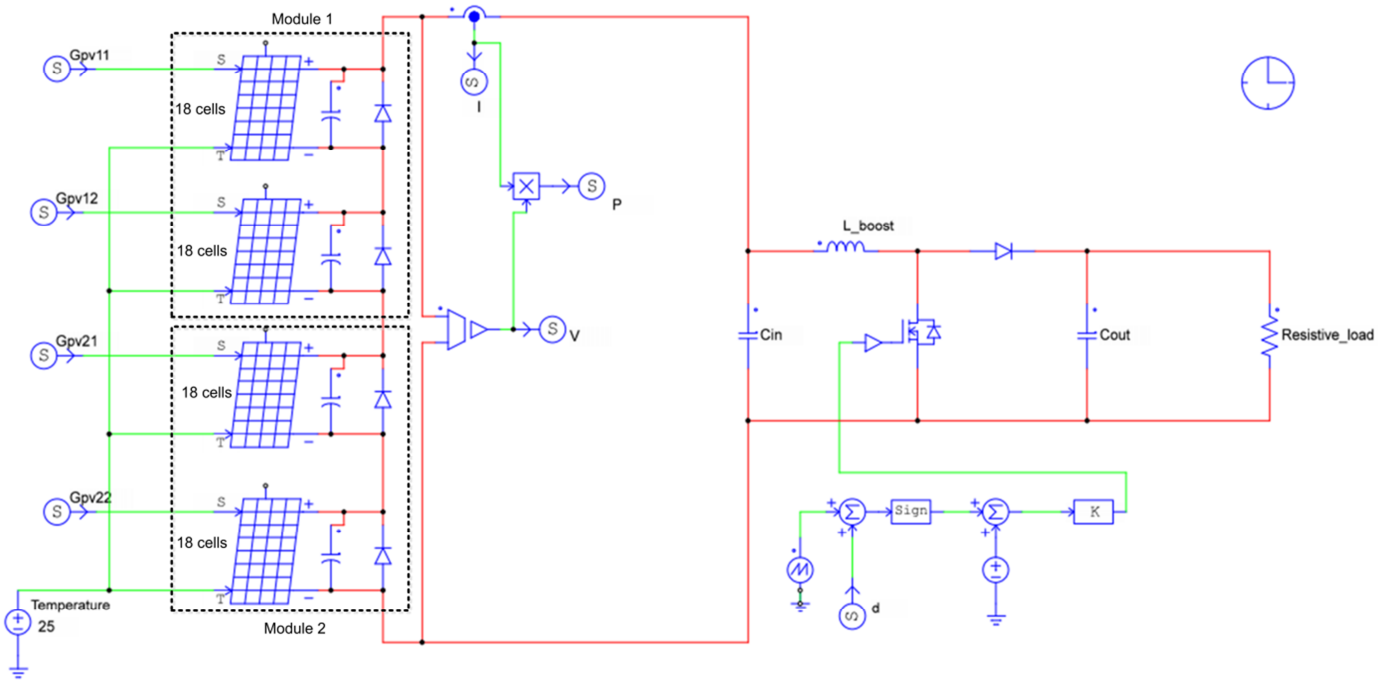

Figure 2.8: Psim circuit of the PV array and the boost converter.

2.6.1.1. Parameterization of the ABC algorithm:

In the proposed MPPT algorithm, the number of candidate solutions (SN) influences the convergence speed and the tracking performance of the algorithm. More bees makes it easier to find the global MPP with a good accuracy, but more time will be required. Less bees gives a fast convergence, but the convergence rate could be unsatisfactory. Therefore, a trade-off between fast convergence speed and the convergence rate should be achieved when choosing the number of candidate solutions SN. Figure (2.9) shows the relationship between the number of candidate solutions (SN) and the convergence rate for all cases investigated in the simulations. The relationship between the number of candidate solutions (SN) and the average convergence time is shown in figure (2.10). Since our objective for the MPPT algorithm is to get fast convergence with a high convergence rate, SN has been chosen equal to 3. The maximum cycle number is set to 30 cycles; the largest number reached in these tests is 15 cycles.

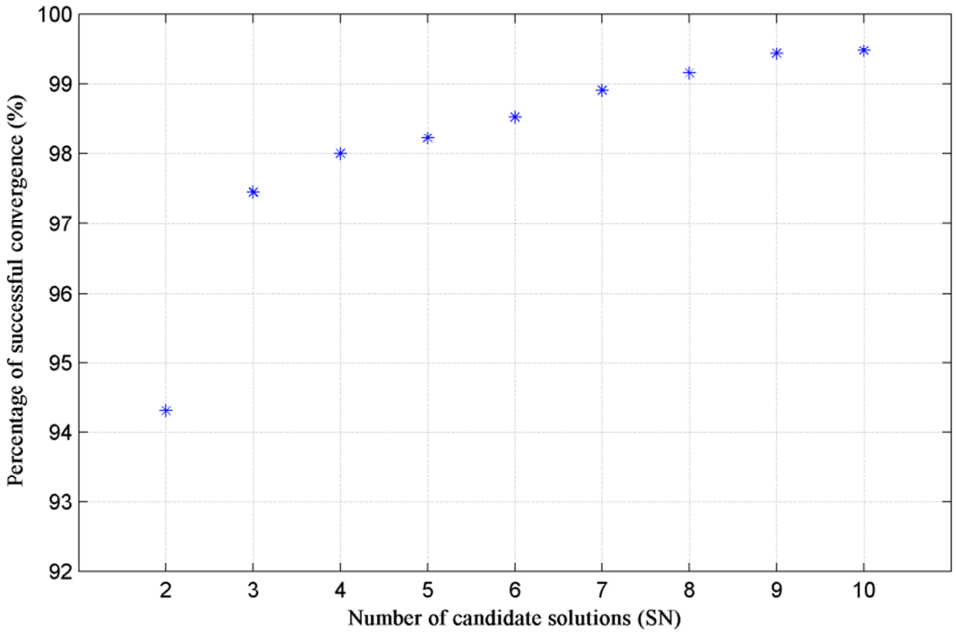

Figure 2.9: Relationship between the number of candidate solutions (SN) and convergence rate.

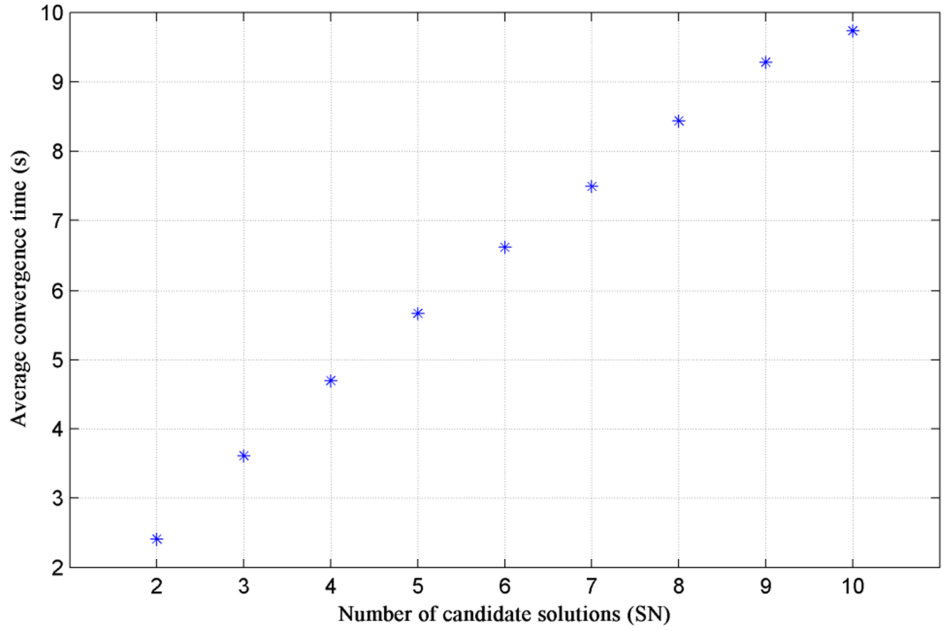

Figure 2.10: Relationship between the number of candidate solutions (SN) and the average convergence time.

According to these obtained results, the parameters values of the implemented ABC-based MPPT algorithm are: *SN*=3 bees and *MCN* = 30 cycles.

2.6.1.2. Power tracking with various shading patterns:

A simulation study was carried out to validate the ability of the proposed ABC-based MPPT to track the global MPP under steady and transient shading patterns. Since it is very difficult to test all the non-uniform irradiance conditions, only some shading patterns are considered in the study. The four used shading patterns (SPs) are listed in Table 2.3. For SP1, the irradiance on all the PV sub-modules is uniform; as a result, only one peak appears in the *P-V* characteristic curve. For SP2 there are two peaks, while for SP3 and SP4 there are three peaks.

Table 2.3: Considered shading patterns.

Pattern N°.	**Shading pattern [Gpv11, Gpv12, Gpv21, Gpv22] (W/m^2)**
SP1	[1000, 1000, 1000, 1000]
SP2	[1000, 500, 1000, 1000]
SP3	[1000, 700, 100, 1000]
SP4	[1000, 500, 100, 1000]

Table 2.4: Performance of the proposed ABC-based MPPT under various shading patterns.

Pattern N°	**Ideal output power (W)**	**Output power obtained (W)**
SP1	159.652	159.380
SP2	117.896	116.568
SP3	88.948	88.377
SP4	74.140	73.976

For each of the above four cases, the ABC-based MPPT algorithm is executed 1000 times. The ideal power values and the average values of the extracted power are shown in table 2.4. It is shown that the proposed ABC-based MPPT is able to successfully track the global MPP. In fact, the extracted power is very close to the ideal power in all cases. The distribution of the average values of the extracted power from the PV modules, over the shading patterns, is shown in figure (2.11). The results obtained indicate that the effectiveness of the proposed method is not affected by the initial conditions of the search process. The ability to find the global MPP for the new weather conditions is very important. In order to illustrate the tracking ability of the proposed ABC-based MPPT algorithm under transient irradiance conditions, we have considered three cases – Case 1: SP

changes from SP1 to SP2; Case 2: SP changes from SP1 to SP3, and Case 3: SP changes from SP1 to SP4. The power, the voltage, the current transient characteristics and the corresponding duty cycle for Cases: 1, 2 and 3 are shown in figures (2.12-2.14), respectively. The weather conditions change detection value ($\Delta Ppv(\%)$) is set to 2 %. It can be seen that when the shading pattern changes from a uniform condition to a partially shaded condition at 8 s, the proposed MPPT algorithm can find the global MPP for the new shading pattern.

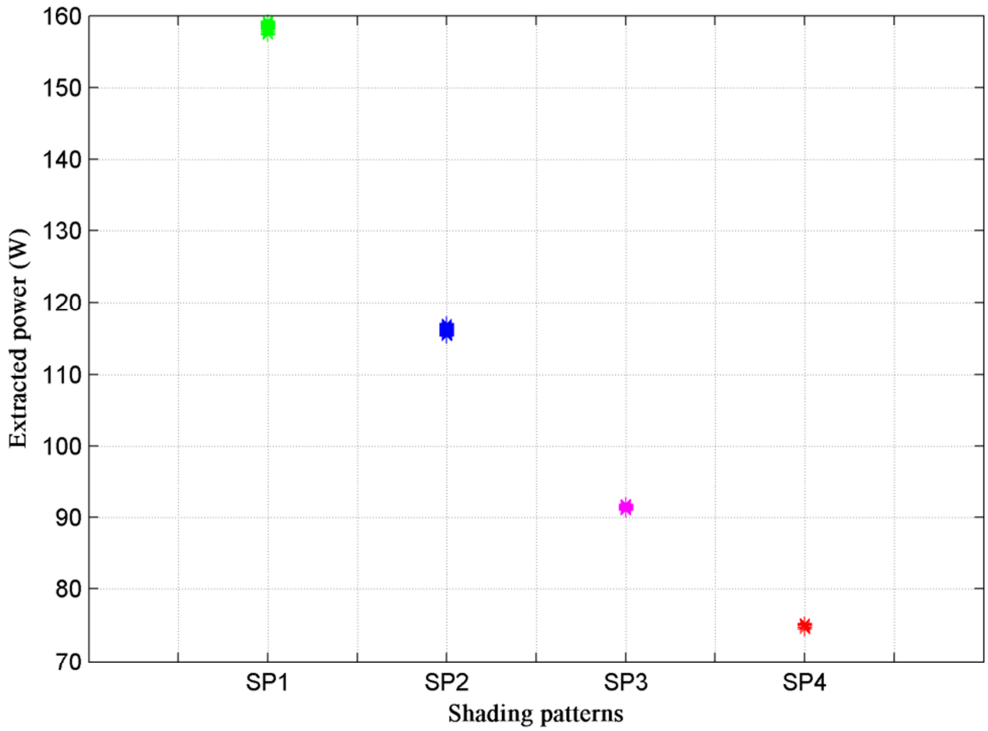

Figure 2.11: Power extracted by the ABC-based MPPT algorithm for the four different shading patterns.

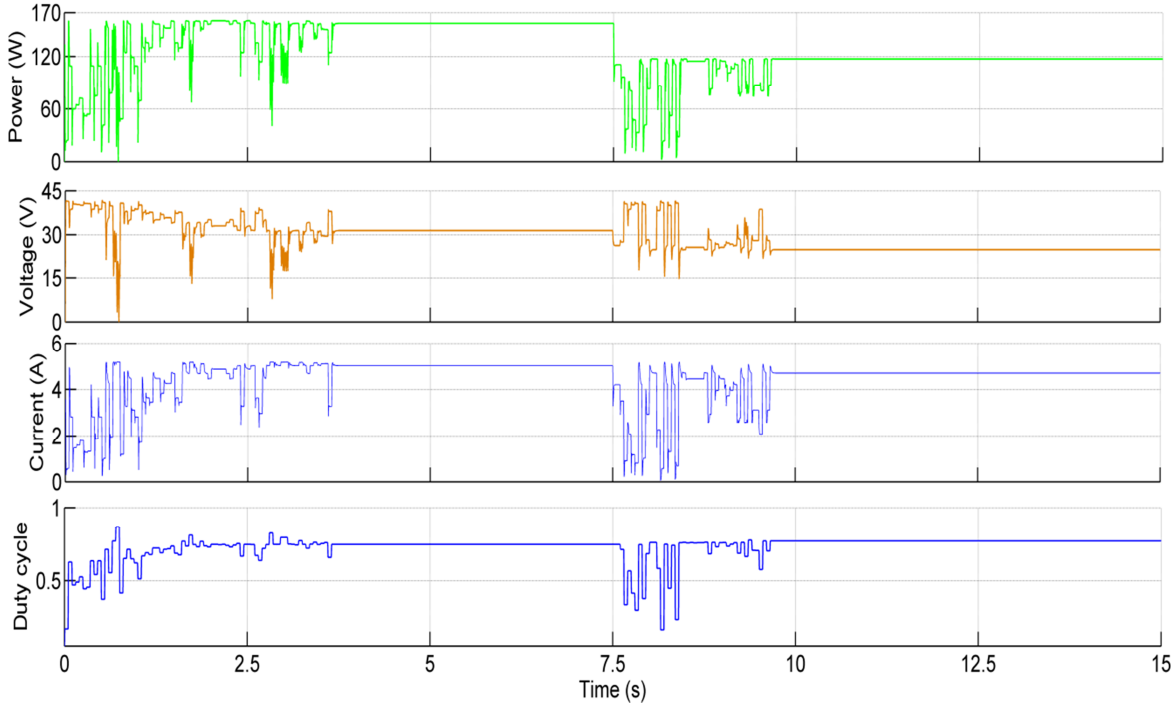

Figure 2.12: Shading pattern SP1 to shading pattern SP2.

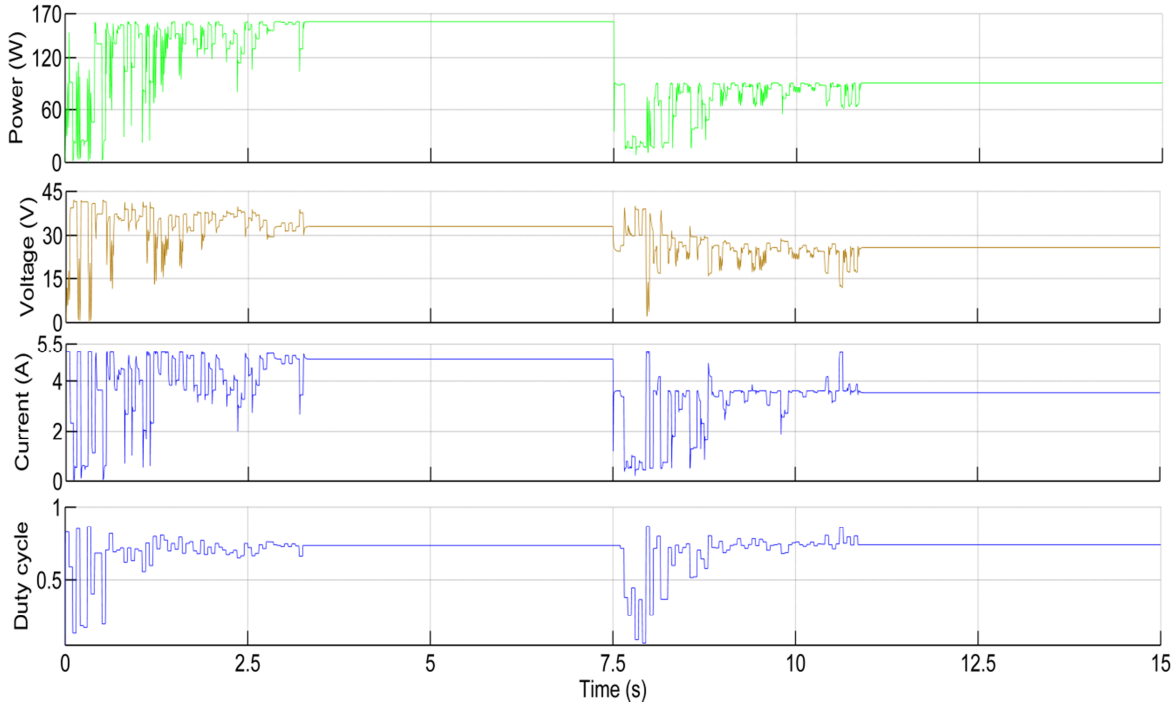

Figure 2.13: Shading pattern SP1 to shading pattern SP3.

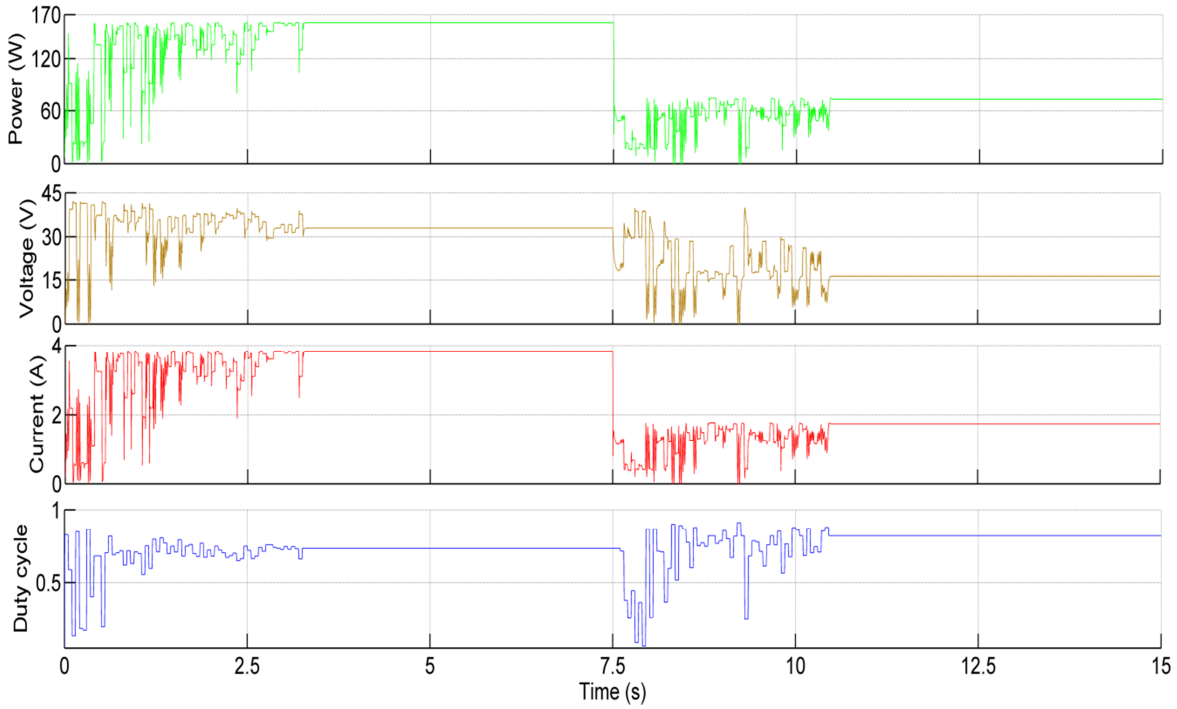

Figure 2.14: Shading pattern SP1 to shading pattern SP4.

2.6.1.3. Comparison of the proposed MPPT with PSO based approach:

This comparative study is performed with the PSO based-MPPT approach proposed in [130]. The parameter settings of the implemented PSO-based MPPT algorithm are listed in table 2.5. The detection parameter value of the weather conditions change ($\Delta Ppv(\%)$) is set to 2 % for both algorithms.

First, the comparison is carried out on the basis of three statistical indicators, given in table 2.6. Thus, both algorithms are executed 1000 times for each shading pattern given in Table 2.4. It can be noticed that the ABC based-MPPT algorithm gives better performance, in term of number of successful convergence, when the PV array working under PSC. However a slight difference with respect to the accuracy and the average convergence value is reported where the ABC based-MPPT algorithm has a slow convergence speed toward the GMPPT compared to the PSO based-MPPT algorithm.

Table 2.5: PSO Algorithm parameters used in the study.

Parameter	Symbol	Value
number of particles	*N*	6
maximum cycle number	max_generation	30
inertia weight	w	0.4
cognitive coefficient	c1	1.2
social coefficient	c2	1.6

Table 2.6: Comparison between the ABC and the PSO based MPPT algorithms under different shading patterns.

Pattern N°/ Algorithm		Number of successful convergence (%)	Accuracy (%)	Average convergence cycle
SP1	ABC	99.80	99.83	9.39
	PSO	99.20	99.66	7.95
SP2	ABC	97.70	98.87	9.57
	PSO	90.20	99.06	8.41
SP3	ABC	96.70	99.36	10.32
	PSO	87.10	98.22	9.22
SP4	ABC	95.60	99.78	10.27
	PSO	78.40	98.56	9.17

The second comparison study is based on the real daily power production of the PV array subject to non-uniform daily irradiation. For this purpose, the simulation was carried out using real weather profiles of a typical Algerian sky. Figure (2.15) gives the chosen temperature and four irradiance daily profiles in order to be applied to each PV sub-module.

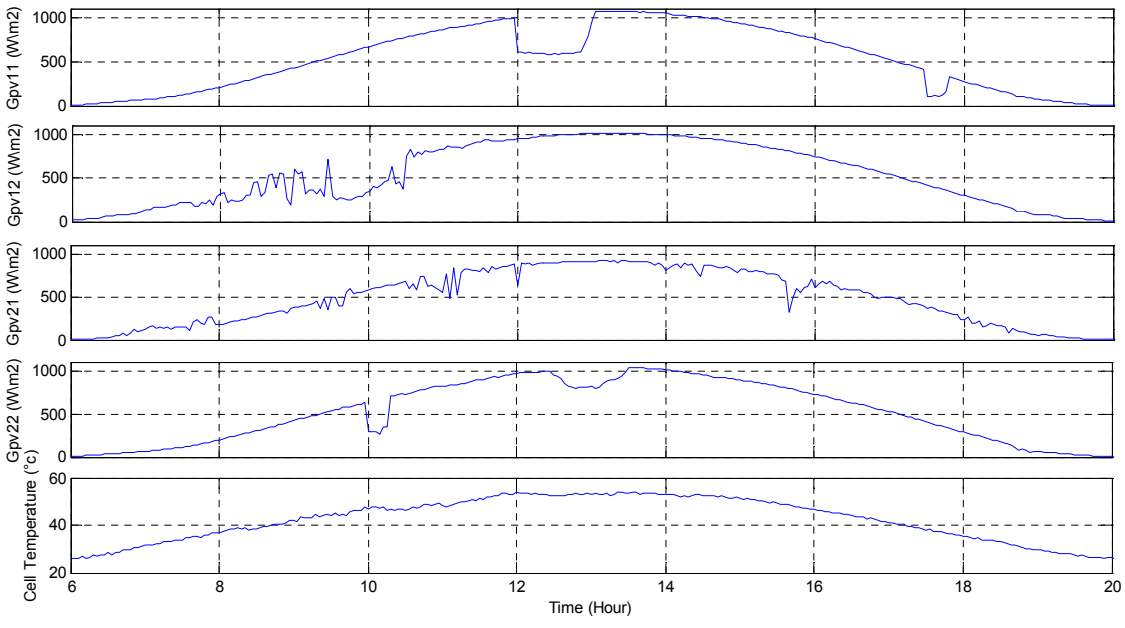

Figure 2.15: Fourteen hour typical Algerian daily profiles of irradiance and temperature (6.00 am–8.00 pm).

Figure (2.16) reports the simulation results for the extracted power using ABC, PSO and P&O-based MPPT controllers when irradiance and temperature profiles shown in figure (2.15) are used. The data were recorded with a sampling period of 3 minutes. It can be clearly seen that for the whole profile of 24 h, MPP tracking performed by the proposed method is extremely accurate compared with both PSO-based method and P&O algorithm. The proposed method yields an average power of 2.28% more than the PSO-based method; This is due to the partial shading condition periods which can trap the PSO-based optimization algorithm in local minima. The *P&O* power tracking method show lower generated energy compared with that of the stochastic search techniques (ABC, PSO). This is mainly due to the inherent inability of the algorithm to identify the global optimum point when the power curve exhibits multiple local MPPs. This is more clearly highlighted in the bar-graph of figure (2.17), in which the hourly array yield (Y_A) is reported. The latter is defined as the hourly power output of the PV array divided by the peak power of the installed PV array, given by:

$$Y_A = \frac{\sum_{n=1}^{n} P_{PVarray} / n}{P_{PVarray\_\text{peak}}} \tag{2.13}$$

where *n* is the samples number and $P_{PVarray\_\text{peak}}$ is the peak power of the installed PV array.

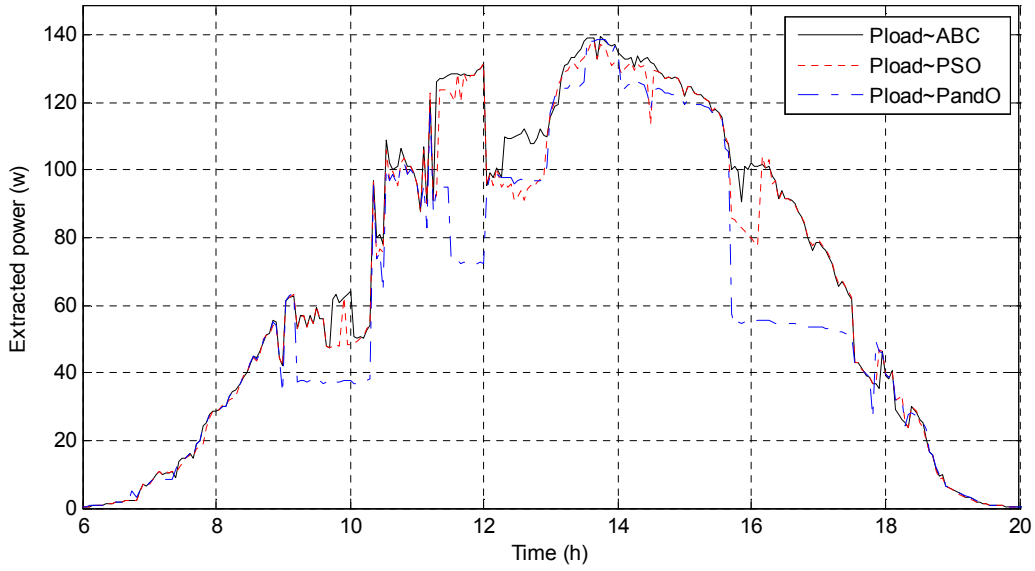

Figure 2.16: Simulation results for the 14 h (6.00 am–8.00 pm) Algerian profiles (extracted powers).

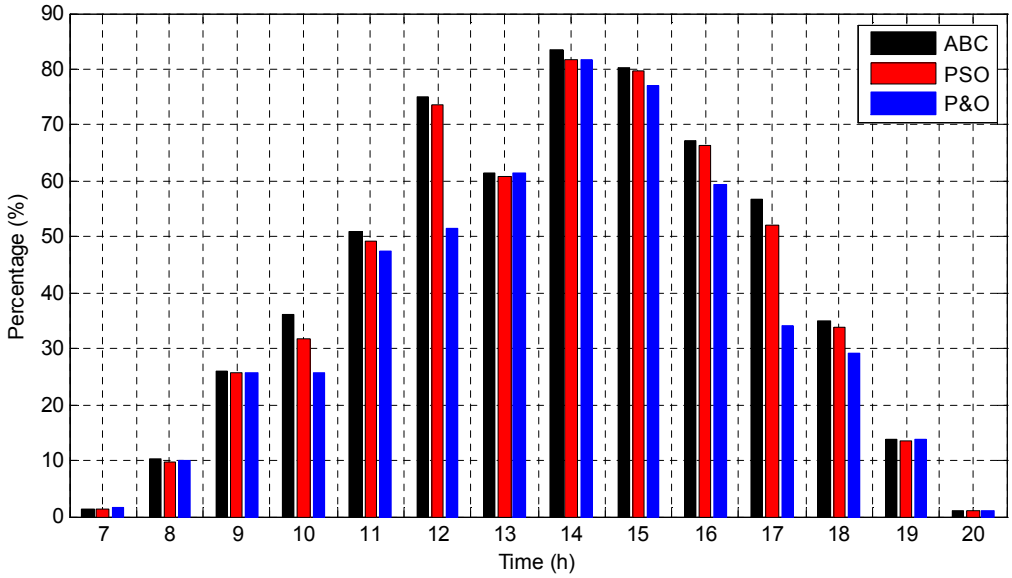

Figure 2.17: Hourly array yield.

2.6.2. ABC-based MPPT for multiple photovoltaic arrays:

The 320-W system, given in figure (2.18), is implemented and used to evaluate the performance of the proposed MPPT algorithm for multiple photovoltaic arrays.

This system consists of two strings of two PV modules connected in series, tow DC-DC converters one for each string and a digital controller in which the MPPT algorithms under test are implemented. Figure (2.19) shows the implemented

Simulink model, and figure (2.20) shows the Psim circuit of the boost converter and the PV generator, where two bypass diodes protecting eighteen cells in each module are considered.

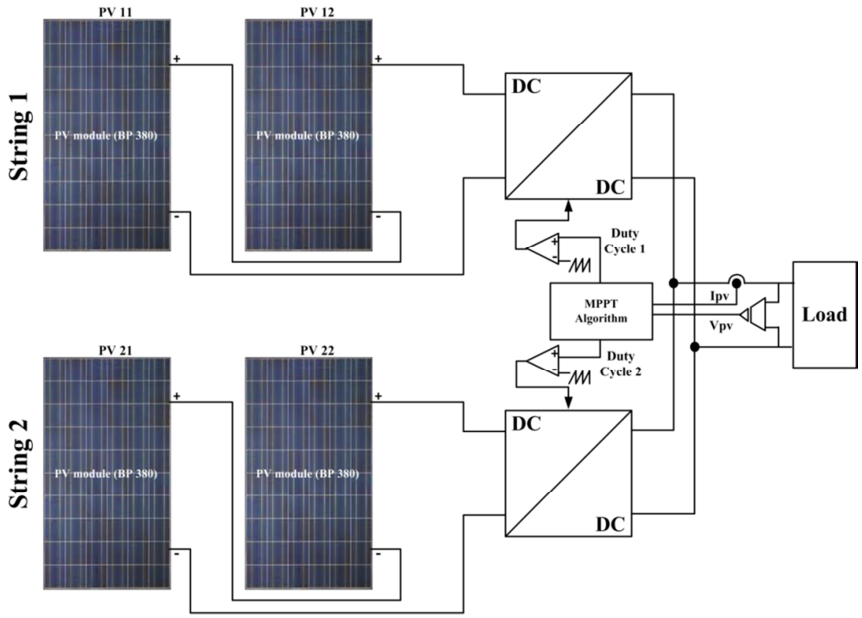

Figure 2.18: System block diagram.

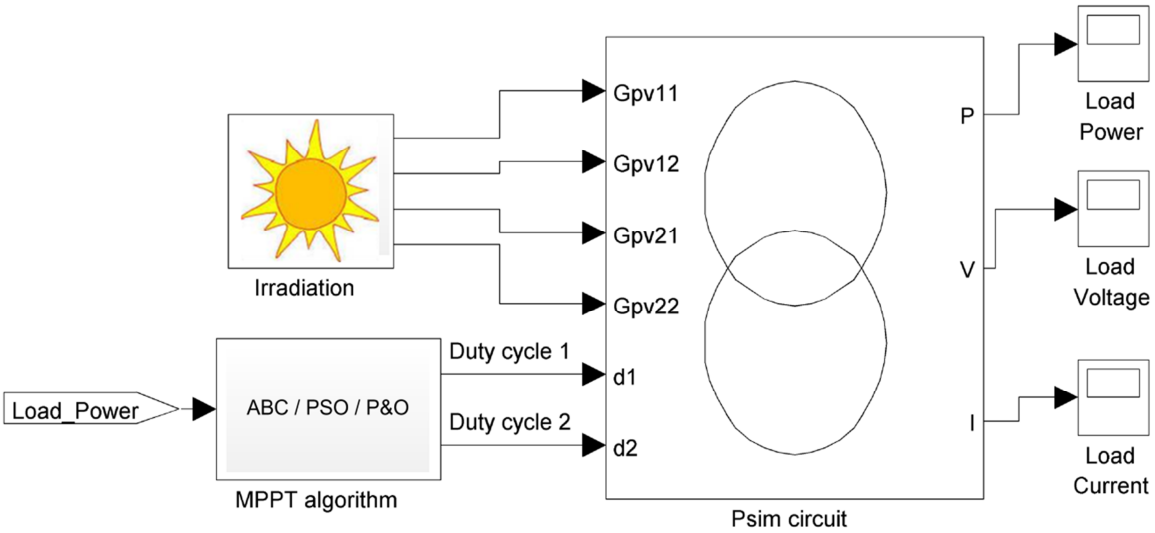

Figure 2.19: Simulink model of the proposed MPPT algorithm.

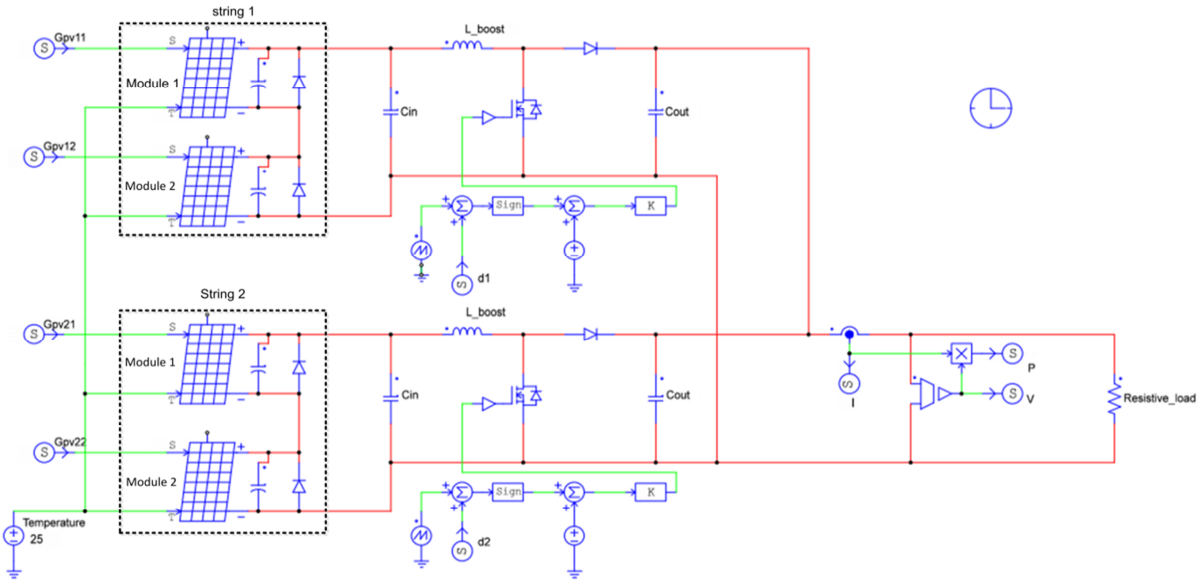

Figure 2.20: Psim circuit of PV arrays and boost converters.

2.6.2.1. Parameterization of the ABC algorithm:

Figure (2.21) shows the relationship between the number of candidate solutions (SN) and the convergence rate for all cases investigated in the simulations. The relationship between the number of candidate solutions (SN) and the average convergence time, when *Ts* is chosen equal to 0.05s, is shown in figure (2.22).

Following the same procedure outlined in section (2.6.1.1), SN has been chosen equal to 4. The maximum cycle number is set to 30 cycles.

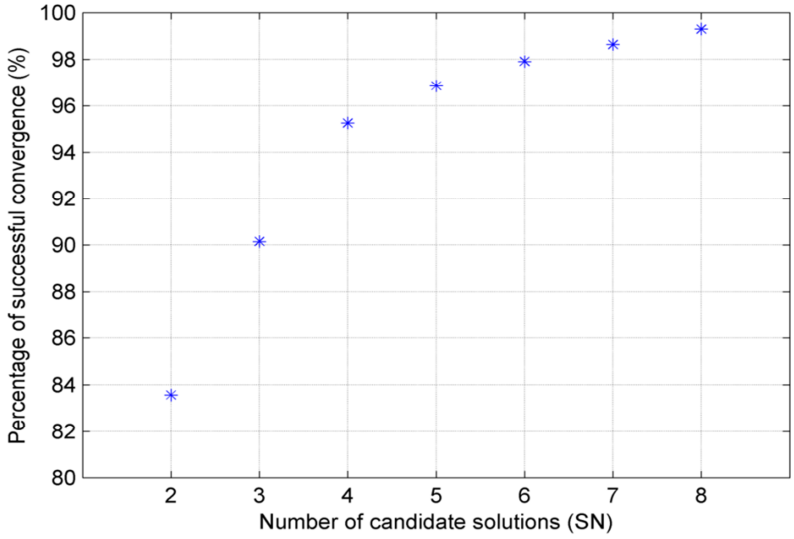

Figure 2.21: Relationship between the number of candidate solutions (SN) and the convergence rate.

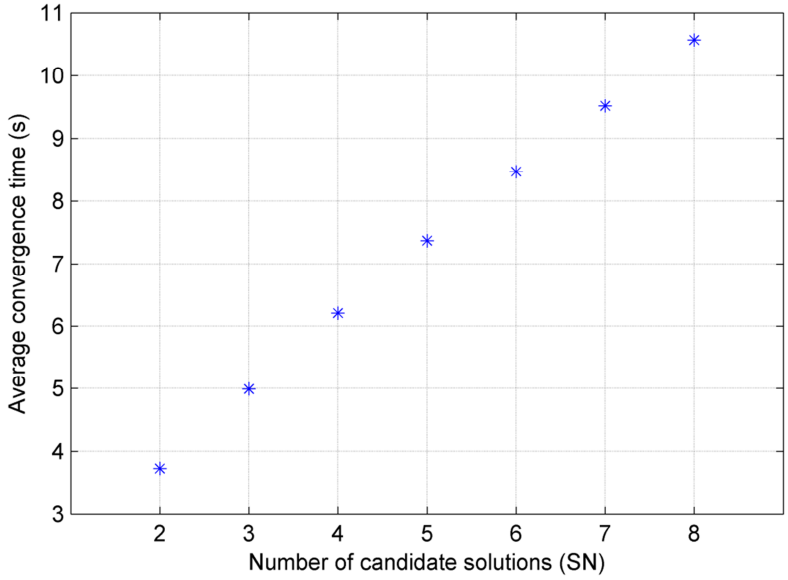

Figure 2.22: Relationship between the number of candidate solutions (SN) and the average convergence time.

2.6.2.2. Power tracking with various shading patterns:

A simulation study was carried out to validate the ability of the proposed ABC-based MPPT algorithm to track the global MPP under steady and transient shading patterns. The three used shading patterns (SPs) are listed in table 2.7 and showed in figure (2.23).

Table 2.7: Considered shading patterns.

Pattern N°	**Shading pattern [Gpv11, Gpv12, Gpv21, Gpv22] (W/m^2)**
SP1	[1000, 1000, 1000, 1000]
SP2	[1000, 1000, 1000, 250]
SP3	[250, 1000, 1000, 100]

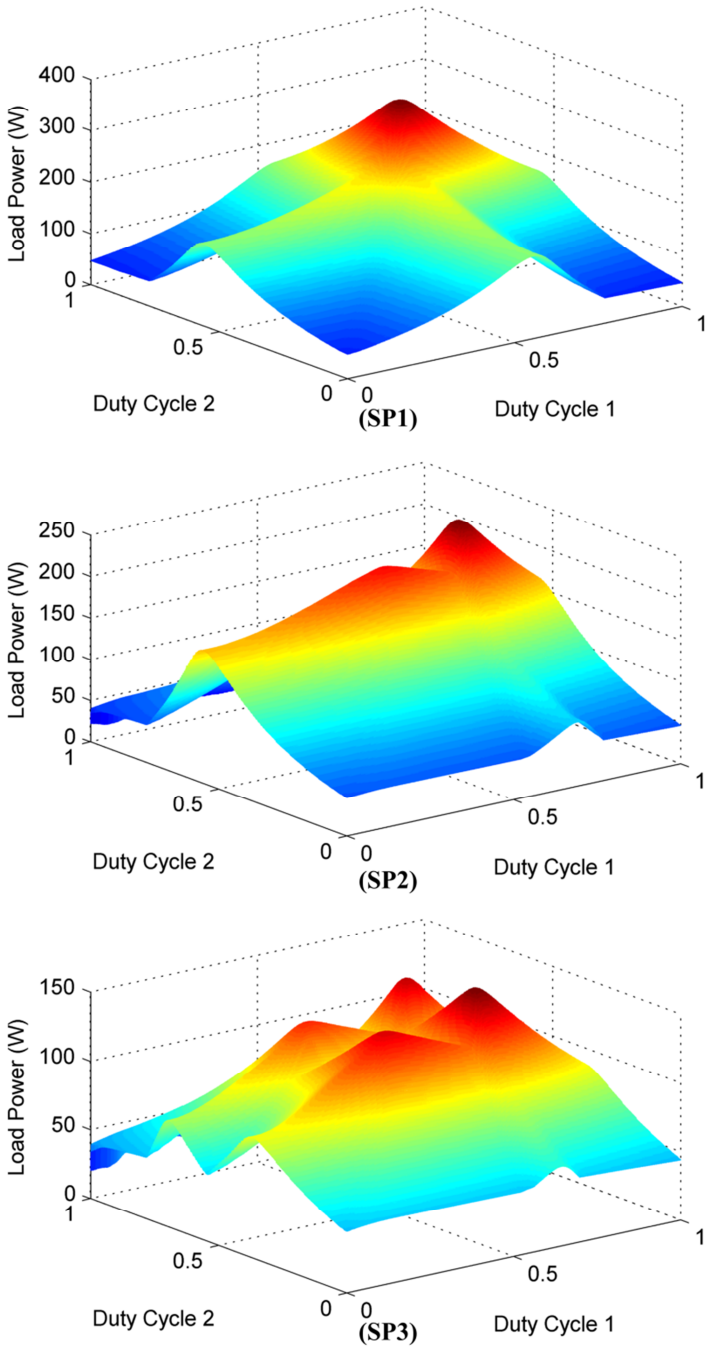

Figure 2.23: Load power versus Duty cycles.

For each of the above three cases, the ABC-based MPPT algorithm is executed 1000 times. The ideal power values and the average values of the extracted power are shown in Table 2.8. It is shown that the proposed ABC-based MPPT is able to successfully track the global MPP of the multiple photovoltaic arrays. In fact, the extracted power is very close to the ideal power in all cases.

Table 2.8: Performance of the proposed ABC-based MPPT under various shading patterns.

Pattern N°.	Ideal output power (W)	Output power obtained (W)
SP1	321.03	319.08
SP2	237.53	235.47
SP3	145.43	144.45

The ability to find the global MPP for the new weather conditions is very important. In order to illustrate the tracking ability of the proposed ABC-based MPPT algorithm under transient irradiance conditions, we have considered two cases:

– Case 1: SP changes from SP1 to SP2.

- Case 2: SP changes from SP1 to SP3.

The power, the voltage and the current transient characteristics and the corresponding duty cycles for cases 1 and 2 are shown in figures (2.24) and (2.25), respectively. The weather conditions change detection value ($\Delta Ppv(\%)$) is set to a value of 2 %. It can be seen that when the shading pattern changes from a uniform condition to a partially shaded condition at 10 s, the proposed MPPT algorithm can find the global MPP for the new shading pattern.

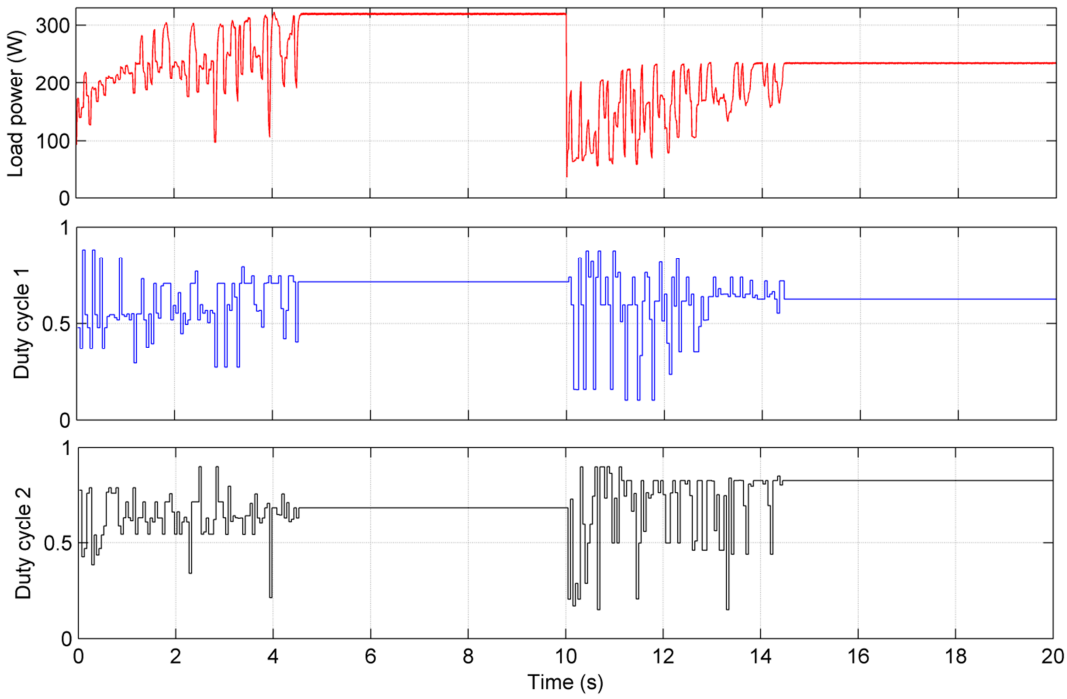

Figure 2.24: Shading pattern SP1 to shading pattern SP2.

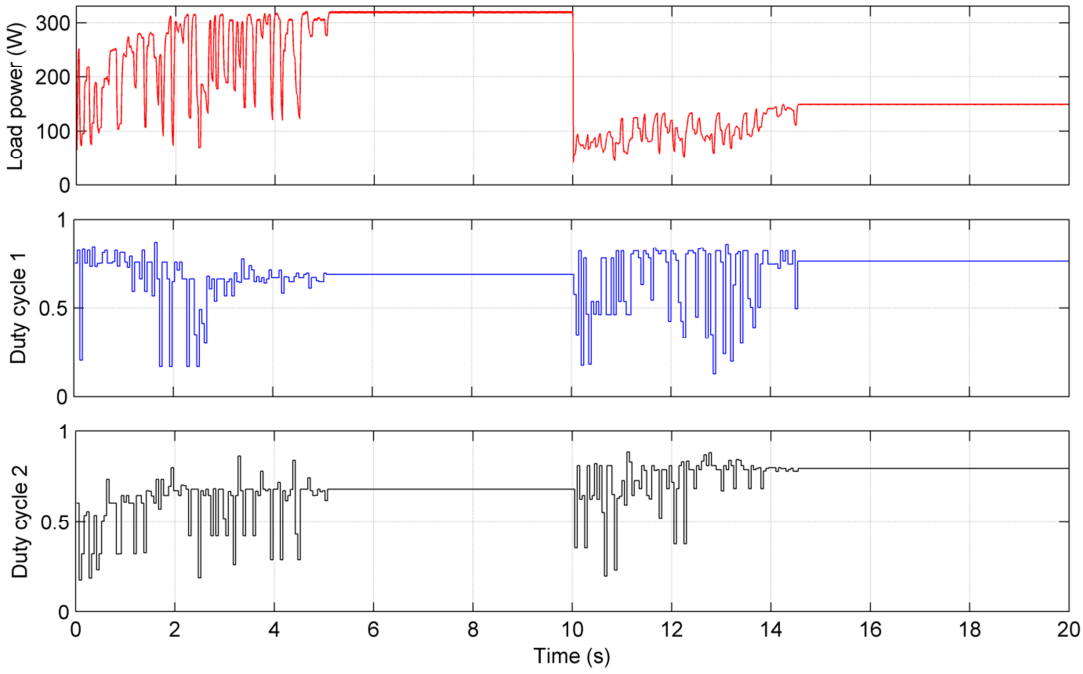

Figure 2.25: Shading pattern SP1 to shading pattern SP3.

2.6.2.3. Comparison of the proposed MPPT with PSO based approach:

The purpose of this study is to compare the new ABC-based MPPT algorithm with PSO-based MPPT algorithm proposed in [121]. The parameter settings of the implemented PSO-based MPPT algorithm are listed in table 2.9. This comparison is carried out using three criteria and executing both MPPT algorithms 1000 times for each one of the shading patterns given in table 2.10. From table 2.10, it can be seen that the ABC algorithm is a good choice, in terms of the number of successful convergence, for the MPPT purpose under PSC. There is a slight difference in the accuracy and the average convergence cycle values obtained by these two methods.

Table 2.9: PSO Algorithm parameters used in the study.

Parameter	Symbol	Value
number of particles	*N*	8
maximum cycle number	max_generation	30
inertia weight	w	0.4
cognitive coefficient	c1	1.2
social coefficient	c2	1.6

Table 2.10: Comparison between the ABC and the PSO based MPPT algorithms under different shading patterns(Successful convergence).

Pattern N°	Algorithm	Successful convergence test (%)	Average extracted Power (w) (Successful convergence)	Accuracy	Average convergence cycle
PS1	ABC	100	319.08	99.39	13.94
	PSO	100	320.57	99.86	11.48
PS2	ABC	95.3	235.47	99.13	13.87
	PSO	77.1	237.08	99.85	11.03
PS3	ABC	90.5	144.45	99.32	12.24
	PSO	64.6	145.16	99.82	10.26

To show further the effectiveness of the proposed method, in real environmental condition, a simulation study is conducted using real weather profiles of a typical Algerian sky. Figure (2.26) gives the chosen temperature and four irradiance daily profiles in order to be applied to each PV module.

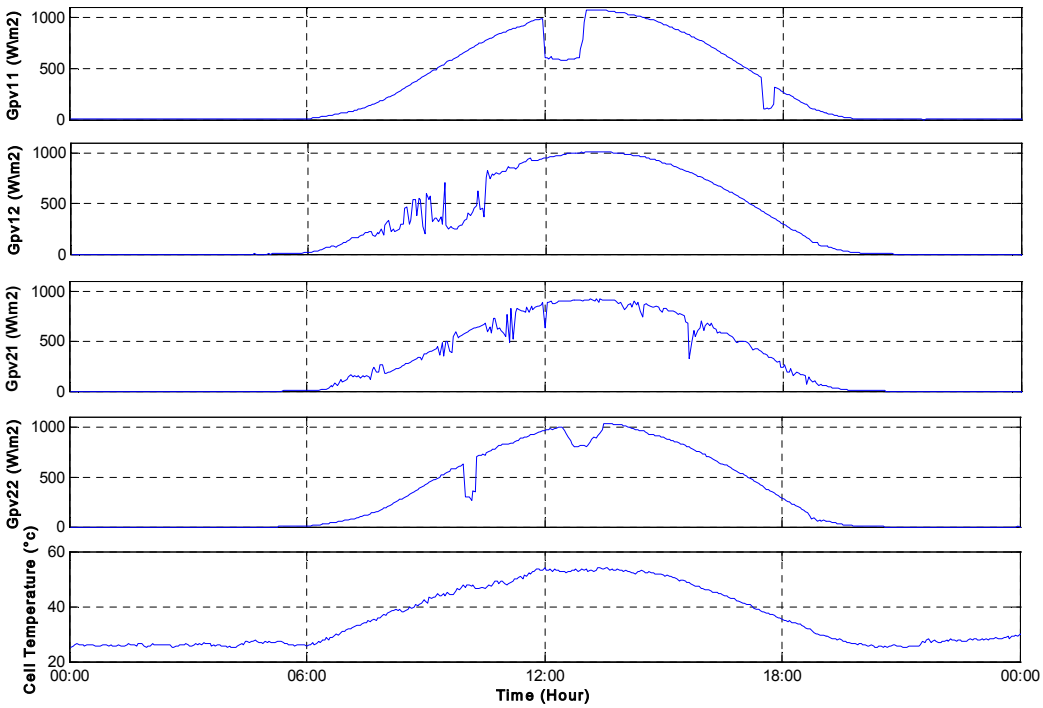

Figure 2.26: Typical Algerian daily profiles of irradiance and temperature.

Figure (2.27) shows the simulation results for the extracted and the mean power using the ABC and PSO methods when the real irradiance and temperature profiles shown in figure (2.26) are used. The data are recorded with a sampling period of 3 minutes. It can be clearly seen that for the whole profile of 24 h, MPP tracking performed by the proposed method is extremely accurate compared with both PSO-based method and P&O algorithm. The proposed method yields an average power of 3.58% more than the PSO-based method; This is due to the partial shading condition periods which can trap the PSO-based optimization algorithm in local minima. The *P&O* power tracking method shows lower generated energy compared with that of the stochastic search techniques (ABC, PSO). This is mainly due to the inherent inability of the algorithm to identify the global optimum point when the power curve exhibits multiple local MPPs. This is more clearly highlighted in the bar-graph of figure (2.28), in which it is reported the hourly array yield (Y_A).

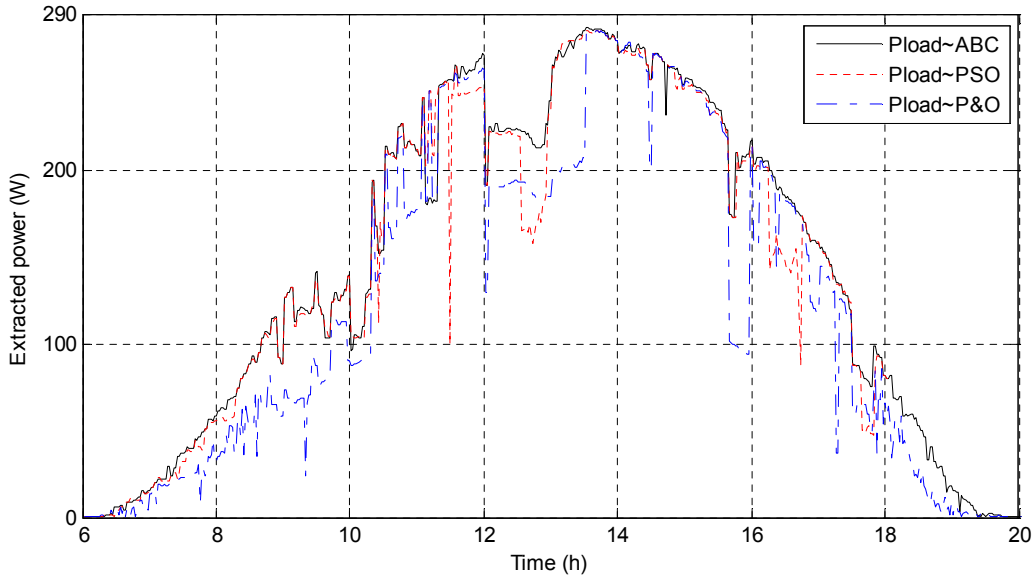

Figure 2.27: Simulation results for the 24 h (00:00 – 00:00) Algerian profiles.

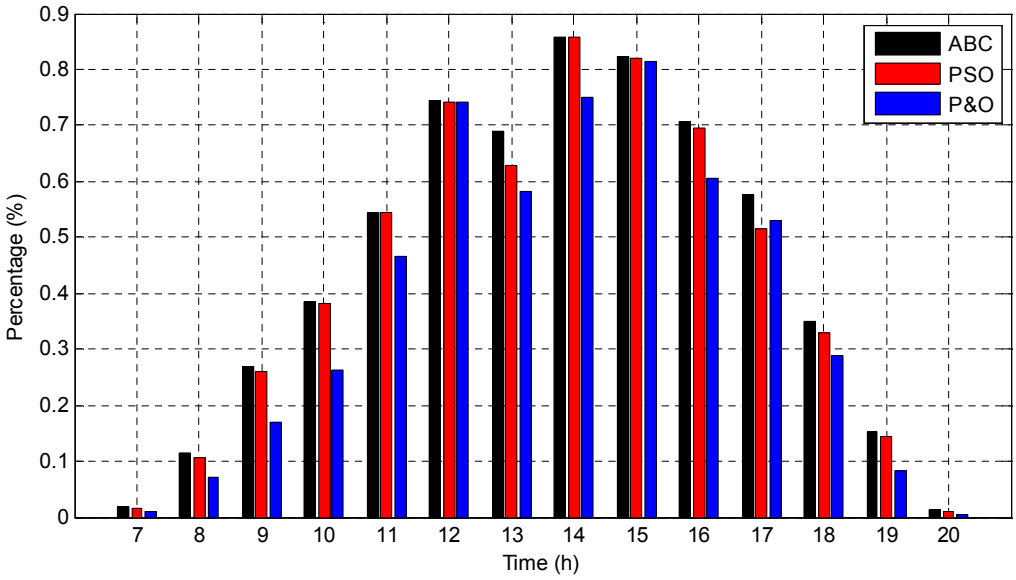

Figure 2.28: Hourly array yield.

2.7. Conclusion:

This chapter presents a fairly exhaustive study covering our developed techniques based on a relatively new member of stochastic algorithms, the Artificial Bee Colony algorithm.

In a first part, we discussed a consistent analysis of the direct control structure and the multidimensional PV system topology used in our developed techniques. MPPT techniques used in comparison tests were also discussed in detail.

In the second part, the feasibility and the effectiveness of the proposed algorithm were investigated by considering various shading patterns on a PV system and also by using real monitored irradiance and temperature profiles. The simulation results have shown that, compared to conventional MPPT techniques – P&O , the proposed ABC-based MPPT algorithm provides better performance to find the global MPP under various shading conditions. As a result, it ensures to extract more power from the PV generator. Compared to the recent popularly used techniques – PSO-based MPPT, it provides better tracking performance in finding the global MPP. In addition, it shows some advantages over the PSO-based MPPT. For instance, the proposed control algorithm requires only two control parameters and its convergence is not dependent on the initial conditions. This algorithm provides another optional tool to maximize the injected power in grid connected PV systems.

CHAPTER 3

GRID-CONNECTED INVERTER CONTROL

3.1. Introduction:

As was mentioned in the first chapter, in grid-connected photovoltaic systems, it is necessary to have low levels of total harmonic distortion at the inverter output and a very good power factor, close to unity, so it is imperative to design a high performance controller for the inverter. To this end, many advanced control techniques have been developed.

Due to its good performance and simplicity, deadbeat control appears as an attractive way for the control of grid-connected inverter. However, conventional deadbeat controllers suffer from the presence of two delays; the first is inherent to the deadbeat control algorithm and causes a steady-state error, and the second arises when the algorithm is implemented in a DSP-based platform and has more serious consequences. It affects the system stability and leads to the appearance of ripples and phase shift in the output current.

In this chapter, an improved and an efficient version of the well-known deadbeat control algorithm suitable for DSP-based platform implementation is proposed to avoid both aforementioned delays. The control problem is considered for an inverter with an output L-filter and an output LCL-filter.

3.2. System Description:

The basic scheme of the grid-connected DC/AC pulse-width modulated (PWM) converter used in this study is shown in figure (3.1) [148], which is a current-controlled voltage source converter. Two type of output filter are considered (L-filter and LCL-filter). The low-pass inductance filter (figure 3.2-a) is commonly used in low-power applications to cancel high frequency ripples of current; while the LCL-filter (Figure 3.2-b) is used for low-frequency switching and high-power applications [149].

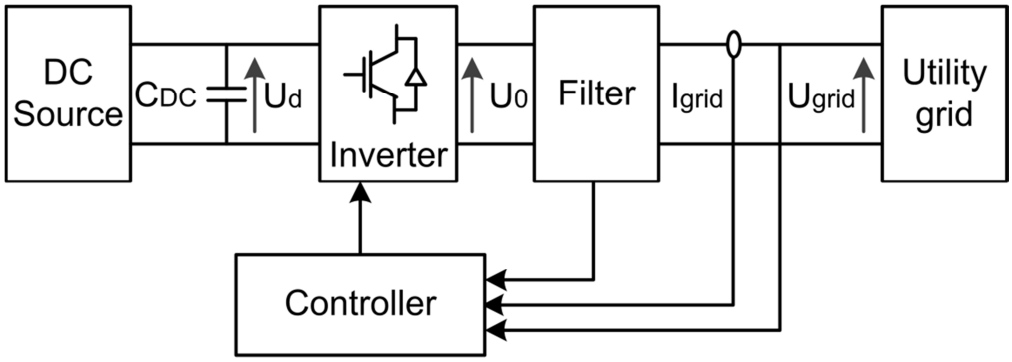

Figure 3.1: Grid-connected system.

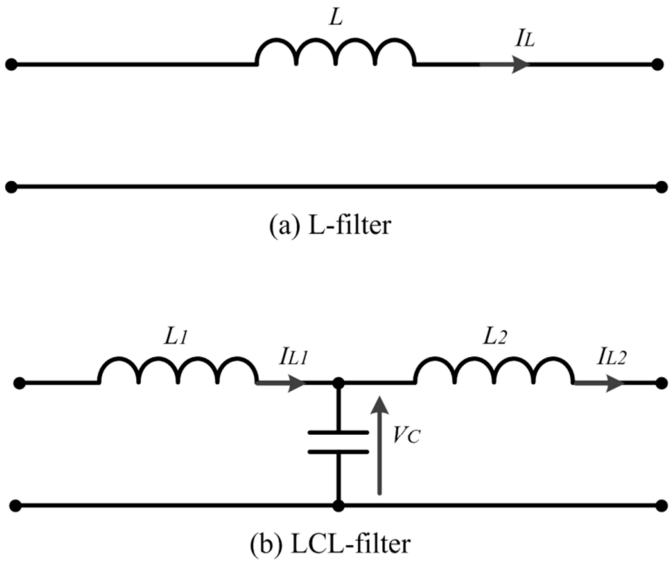

Figure 3.2: Considered filters: (a) L-filter and, (b) LCL-filter.

3.3. Deadbeat Control Algorithm "Classical Approach":

Predictive control appears as an attractive control of power converters due to its fast dynamic response [150]. Several control algorithms have been presented under the name of predictive control, as presented in [151]. The most well-known scheme is deadbeat control. At present, it has been successfully applied in the control of inverters [152-159], rectifiers [160], active filters [161], uninterruptible power supplies (UPSs) [162, 163], etc.

Hereafter, the derivation procedures of the traditional deadbeat control approach applied to the grid-connected inverter are presented for both output filters (L-filter and LCL-filter).

3.3.1. Inductive filter case:

According to figures (3.1 and 3.2-a), the output current is related to the output voltage of the inverter and the utility grid voltage by the following equation:

$$L\frac{dI_L(t)}{dt} = U_0(t) - U_{grid}(t) \tag{3.1}$$

where L is the filter inductance, $I_L(t)$ is the current in inductance L (the injected current), $U_{grid}(t)$ is the grid voltage, and $U_0(t)$ is the inverter output voltage.

The discrete form of equation (3.1) is given by the following expression:

$$I_L(k+1) = I_L(k) + \frac{T}{L}U_0(k) - \frac{T}{L}U_{grid}(k) \tag{3.2}$$

where T is the sampling period.

The pulse width of the DC voltage at the output terminals of the H-bridge denoted by $\Delta T(k)$ is assumed to be centered at each switching cycle, as shown in figure (3.3).

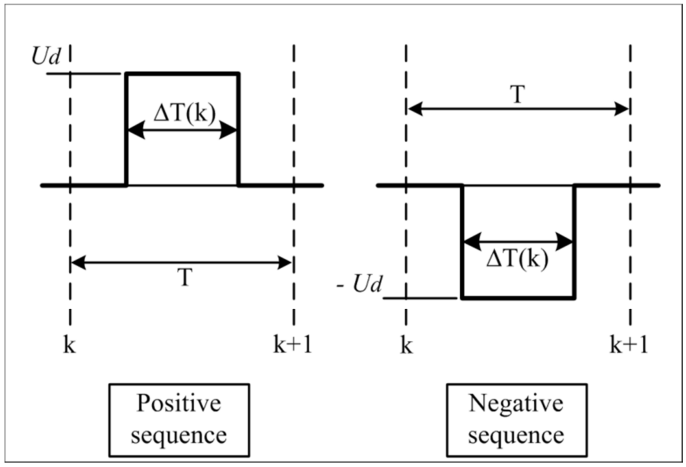

Figure 3.3: Pulse-width pattern.

When $U_0(t)$ is replaced by $U_d * \Delta T(k)$, Equation (3.2) can be rewritten as follows:

$$I_L(k+1) = I_L(k) + \frac{T}{L}\Delta T(k)U_d - \frac{T}{L}U_{grid}(k) \tag{3.3}$$

In the traditional deadbeat control, at each control period k, the current $I_L(k+1)$ is replaced with the reference current $I_L^*(k)$, then duty cycle $\Delta T(k)$, which allows bringing the injected current I_L to its reference I_L^*, is given by:

$$\Delta T(k) = \frac{\frac{L}{T}(I_L^*(k) - I_L(k) + U_{grid}(k))}{Ud} \tag{3.4}$$

3.3.2. LCL-filter case:

Although the LCL-filter has higher filtering capability than the simple L-filter, it does not allow a direct control of injected current. In this topology, a nearly sine wave current to be injected into the utility grid is obtained by controlling the capacitor voltage. So according to the circuit of figure (3.2-b), the output current is given by:

$$\frac{dI_{L2}(t)}{dt} = \frac{V_C(t) - U_{grid}(t)}{L_2} \tag{3.5}$$

where L_2 is the interconnection inductance, $I_{L2}(t)$ is the current in inductance L_2 (the injected current), and $V_C(t)$ is the capacitor voltage.

The discrete form of equation (3.5) is written as:

$$I_{L2}(k+1) = I_{L2}(k) + \frac{TV_C(k)}{L_2} - \frac{TU_{grid}(k)}{L_2} \tag{3.6}$$

As mentioned above, the current $I_{L2}(k+1)$ in equation (3.6) is replaced by the reference current $I_{L2}^*(k)$. The capacitor voltage reference $V_C^*(k)$ needed to let the injected current $I_{L2}(k)$ be equal to its reference current $I_{L2}^*(k)$ is then given by:

$$V_C^*(k) = \frac{L_2}{T}(I_{L2}^*(k) - I_{L2}(k) + U_{grid}(k)) \tag{3.7}$$

To apply the deadbeat control algorithm allowing the calculation of $V_C^*(k)$, the discrete-time state equations of the power plant (figures 3.1 and 3.2-b) are described below:

$$\frac{dX(t)}{dt} = AX(t) + BU(t) \tag{3.8}$$

Where

$$A=\begin{bmatrix} 0 & \frac{-1}{L_1} & 0 \\ \frac{1}{C} & 0 & \frac{-1}{C} \\ 0 & \frac{1}{L_2} & 0 \end{bmatrix};\quad X(t)=\begin{bmatrix} I_{L1}(t) \\ V_c(t) \\ I_{L2}(t) \end{bmatrix};$$

$$B=\begin{bmatrix} \frac{1}{L_1} & 0 \\ 0 & 0 \\ 0 & \frac{-1}{L_2} \end{bmatrix};\quad u(t)=\begin{bmatrix} U_0(t) \\ U_{grid}(t) \end{bmatrix};$$

The discrete form of this representation can be obtained using the following equation:

$$X(k+1)=\varphi X(k)+\gamma u(k) \tag{3.9}$$

where

$$\varphi=\exp(AT)=1+AT+\frac{A^2T^2}{2!}+\ldots+\frac{A^nT^n}{n!}+\ldots;$$

$$\gamma=\left[IT+\frac{A\,T^2}{2!}+\ldots+\frac{A^{n-1}T^n}{n!}\right]*B;$$

$$X(t)=\begin{bmatrix} I_{L1}(t) \\ V_c(t) \\ I_{L2}(t) \end{bmatrix};\quad u(t)=\begin{bmatrix} U_0(t) \\ U_{grid}(t) \end{bmatrix};$$

For $n=3$, it can be written from equation (3.9):

$$V_C(k+1)=\varphi_{21}I_{L1}(k)+\varphi_{22}V_C(k)+\varphi_{23}I_{L2}(k)+\gamma_{21}U_0(k)+\gamma_{22}U_{grid}(k) \tag{3.10}$$

When $\varphi_{21},\varphi_{22},\varphi_{23}$ and γ_{21},γ_{22} are the second line elements of the matrix φ and γ, respectively.

In equation(3.10), replacing $V_C(k+1)$ by $V_C^*(k)$ and $U_0(t)$ by $U_d*\Delta T(k)$, the required pulse width $\Delta T(k)$ is obtained as follows:

$$\Delta T(k) = \frac{V_C^*(k) - \varphi_{21} I_{L1}(k) - \varphi_{22} V_C(k) - \varphi_{23} I_{L2}(k) - \gamma_{22} U_{grid}(k)}{\gamma_{21} U_d} \quad (3.11)$$

Equation (3.11) denotes the implicit manner of controlling the injected current by direct control of the capacitor voltage $V_C(k)$ using a deadbeat controller.

3.4. Drawbacks of the Traditional Deadbeat Control Algorithm:

In the traditional deadbeat control algorithm, besides the delay introduced by the control law used to compute the duty cycle, another delay is introduced when implementing this algorithm in a DSP-based platform. These delays affect the system stability and give rise to current ripples and phase shift between the injected current and the grid voltage [152, 153, 155, 164, 165].

3.4.1. Phase Delay Caused by Control Algorithm:

As is illustrated in figure (3.4), the first delay of one control period is created by the control algorithm itself and is due to the fact that the current $I_L(k+1)$ is replaced by the reference current $I_L^*(k)$ (L-filter case), and the current $I_{L2}(k+1)$ and the capacitor voltage $V_C(k+1)$ are replaced by $I_{L2}^*(k)$ and $V_C^*(k)$, respectively (LCL-filter case). Thus, the injected current $I(k)$ is phase shifted by one control period to its reference $I^*(k)$.

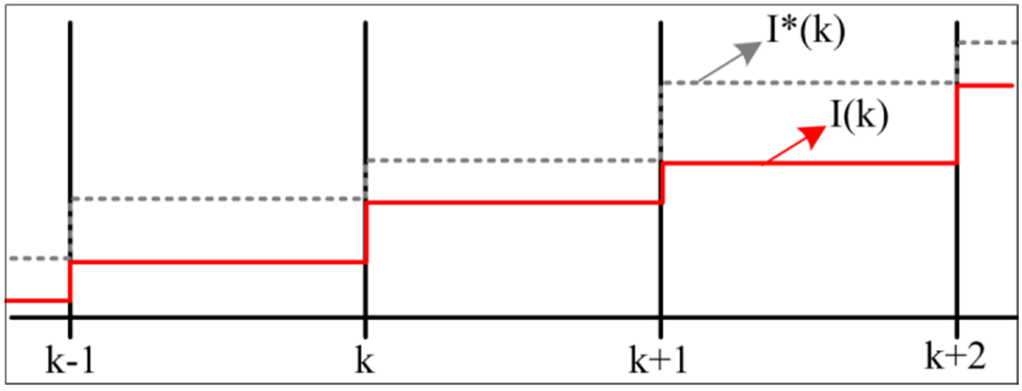

Figure 3.4: Time delay of traditional deadbeat algorithm.

3.4.2. Phase Delay Caused by DSP Implementation:

The second delay is due to the internal architecture of DSP. Indeed, when using a DSP, the PWM signal is generated by comparing the values of two specific registers. The content of the register containing the duty cycle value should not be

modified during the current control period. Since the pulse width is limited by the time that the sampling and the computing operations take, the obtained duty cycle cannot be applied at the current control period. To overcome this difficulty, the duty cycle computed value is written to the shadow register of the DSP during the current control period, and it is automatically written to the comparison register at the beginning of the next control period [156]. Hence, the duty cycle value computed at the current control period will not be effective until the next control period, as shown in figure (3.5). This leads to a shift of one control period, and then much higher ripples will appear in the injected current.

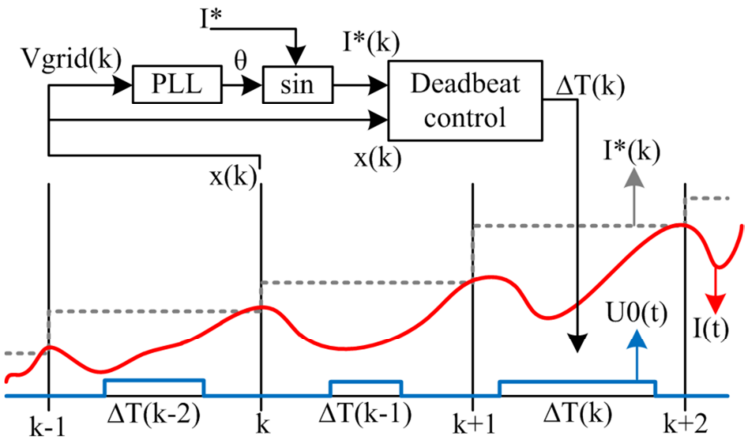

Figure 3.5: Time delay due to DSP implementation.

Much research has proposed several solutions to deal with the aforementioned delays: using state observers, delay compensators, or prediction algorithms. In [154, 155], the authors introduced state observers to estimate the future samples of the required variables for computing the pulse width of the next control cycle. The resulting algorithm becomes more complicated, and its performance depends on the accuracy of the used observers. To decrease the control delay of the deadbeat control algorithm, Zeng et al in [159], presented a new solution that uses a dual-timer sampling scheme to properly arrange the sampling timing. This method requires a high-speed analog-to-digital converter (ADC) and an optimized code of the control algorithm. A control algorithm that allows computing the switching duty cycle of photovoltaic grid-connected inverter in advance was proposed by Yang et al. [156]. It combines the deadbeat technique and the based Taylor formula prediction algorithm. In this algorithm, several equations with long regressors are used to predict each state variable that can significantly increase

the computation time and the required memory space. A method that can overcome the shortcoming of complicated dynamic phase angle compensation in a three-level grid-connected inverter was proposed in [158]. This approach, based on a dual-timer sampling scheme, uses a prediction method to estimate the future values of the required variables and requires a high-speed ADC. Other versions of deadbeat control that use neural networks and fuzzy logic as sinusoidal predictors have also been developed [165, 166]. Such prediction models are complex and require an excessive computation.

3.5. Proposed method for deadbeat controller improvement:

As showed in the previous section, the conventional deadbeat controller suffers from the presence of two delays. In this section, the based prediction algorithm that allows overcoming this drawback is given.

To eliminate the delay caused by the control law used to compute the duty cycle, the one-control-period-ahead predicted values of $I^*(k)$ (i.e. $I^*(k+1)$) are used as reference rather than the actual values of $I^*(k)$. Hence, the delay due to the deadbeat control algorithm will be cancelled, and the injected current $I(k)$ will be equal the actual reference $I^*(k)$, as shown in figure (3.6).

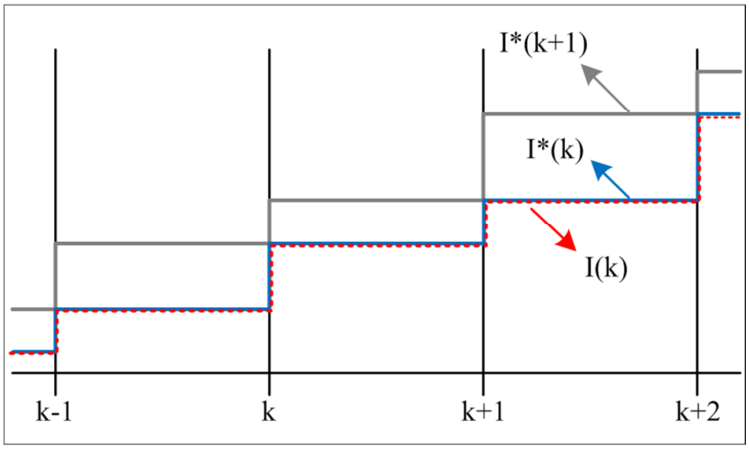

Figure 3.6: Time Correction of inherent deadbeat controller delay.

On the other hand, to eliminate the delay created when implementing the algorithm in a DSP board, computing of the duty cycle ΔT of the $(k+1)^{th}$ control period must be anticipated within the k^{th} control period. Hence, the state variables values at the $(k+1)^{th}$ sampling instant, upon which the duty cycle depends, must

be predicted during the k^{th} control period. Regarding the statement concerning the cancelation of the delay due to the deadbeat algorithm, the injected current must follow the two-control-period-ahead shifted reference current $I^{*}(k+2)$.

As shown in figure (3.7), the main difference between the conventional and improved approaches resides on the added prediction block. This allows computing the duty cycle $\Delta T(k+1)$ at the k^{th} control period by using an appropriate reference current and applying it in its $(k+1)^{th}$ control period.

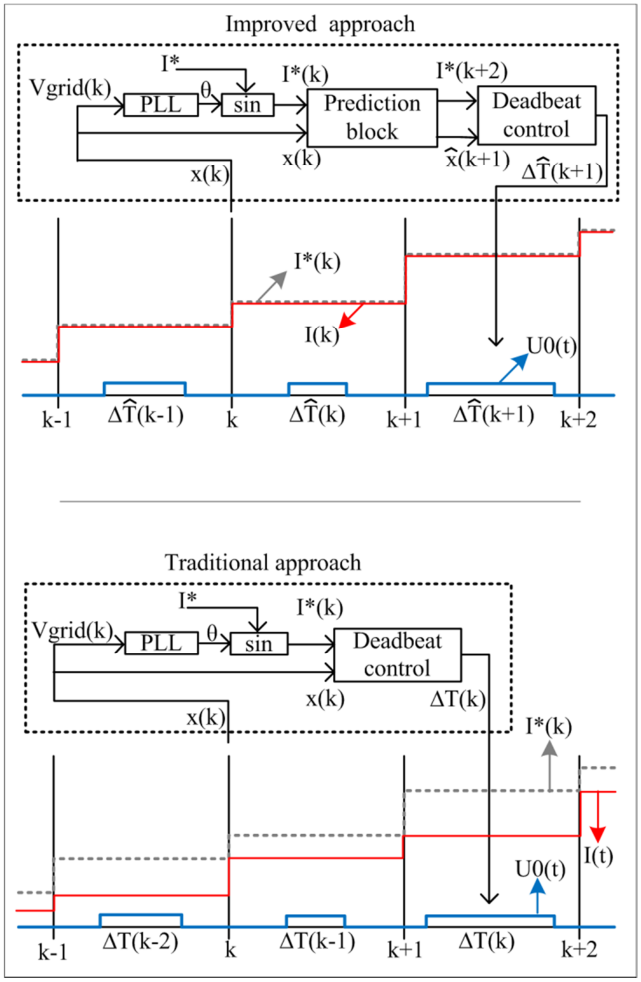

Figure 3.7: Main difference between conventional and improved approaches.

Unlike the already-proposed deadbeat control techniques that use complex and time-consuming prediction models [155-159, 165, 166], the strong point of the proposed approach is the simplicity of its prediction model, which is linear and its coefficients are estimated off-line. These features are made possible by exploiting

prior knowledge of the shapes of the state variables. In fact, these variables can be classified into three categories.

- The reference variables are pure sinusoidal signals, which are real, centred, and stationary. So, they are predictable signals with a second-order recurrence relationship given in equation (3.12) [167]:

$$\hat{x}(k+1) = a_0 x(k) + a_1 x(k-1) \tag{3.12}$$

where a_0 and a_1 are the parameters to be estimated.

- The values of the controlled state variables at the $(k+1)^{th}$ sampling time are estimated by using their reference values and the resulting error of the previous estimation. Thus, it is assumed that the value of the state variable at the $(k+1)^{th}$ sampling instant will be equal to its reference value in the same instant ($\hat{x}(k+1) = x^*(k+1)$), and then the prediction error in the previous sampling instant k is compensated to avoid error accumulation. This is given by the following equations:

$$\begin{aligned} \hat{x}(k+1) &= x^*(k+1) - e(k) \\ e(k) &= x^*(k) - x(k) \end{aligned} \tag{3.13}$$

- The measured state variables have a disturbed sinusoidal shape, such as the grid voltage. Nevertheless, the values of their next samples can be well considered as a linear combination of their previous values. Since, in a grid-connected system, the sampling frequency is usually high enough, the state variables can be considered as changing linearly. Consequently, a linear extrapolation from previous values can be used [165, 168]. Hence, the prediction model given by equation (3.12) is a good choice to estimate the future values of these state variables.

Based on these points, a prediction model that uses a single equation to predict the values of all the state variables needed in computing the duty cycle value that allows avoiding the aforementioned time delays is developed. The variables to be predicted are gathered, according to their category, in table 3.1.

Table 3.1: Variables categories.

Filters	Reference variables	Controlled state variables	Measured state variables
L	$I_L*(k+1)$ $I_L*(k+2)$	$I_L(k+1)$	$U_{grid}(k+1)$
LCL	$I_{L2}*(k+1)$ $I_{L2}*(k+2)$	$I_{L2}(k+1)$ $V_c(k+1)$	$U_{grid}(k+1)$ $I_{L1}(k+1)$

The estimation procedure of the prediction model coefficients given in equation (3.12) using the recursive least-square (RLS) algorithm is illustrated in figure (3.8).

The Recursive least squares is an adaptive filter which recursively finds the coefficients that minimize a weighted linear least squares cost function relating to the input signals.

Since all the state variable shapes are sine wave, the results of parameters estimation will be the same as that seen in figure (3.9), where:

$$x(k) = \sin(2*\pi*50*k) \tag{3.14}$$

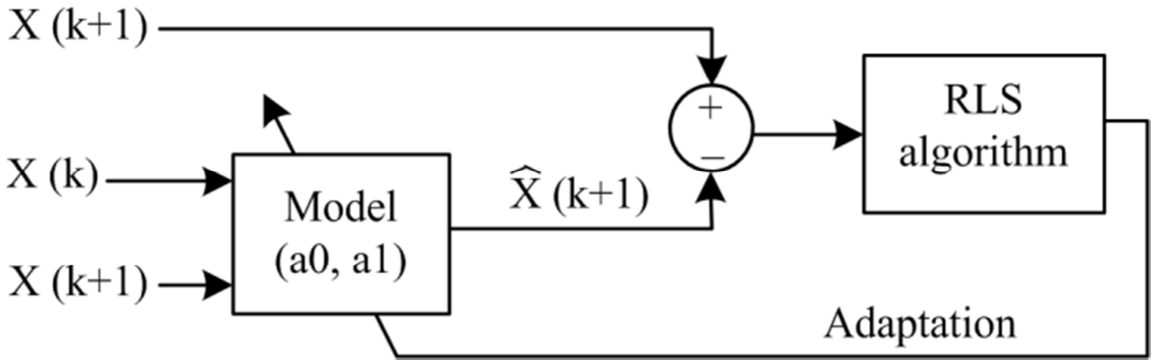

Figure 3.8: Procedure for parameters estimation.

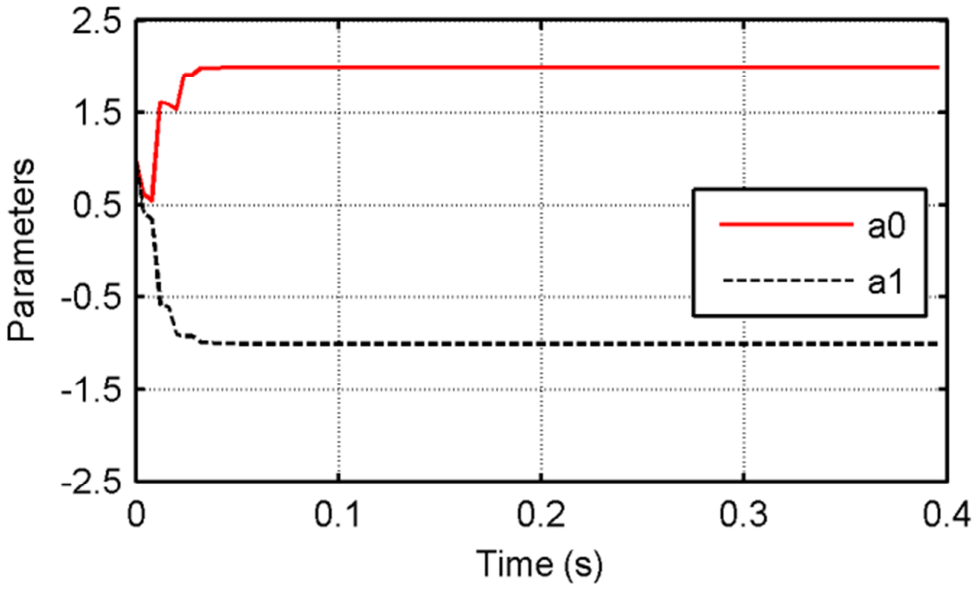

Figure 3.9: Parameters evolution.

Simulation results of a pure and disturbed sine waves prediction have shown the good accuracy of the chosen model (figures 3.10 and 3.11).

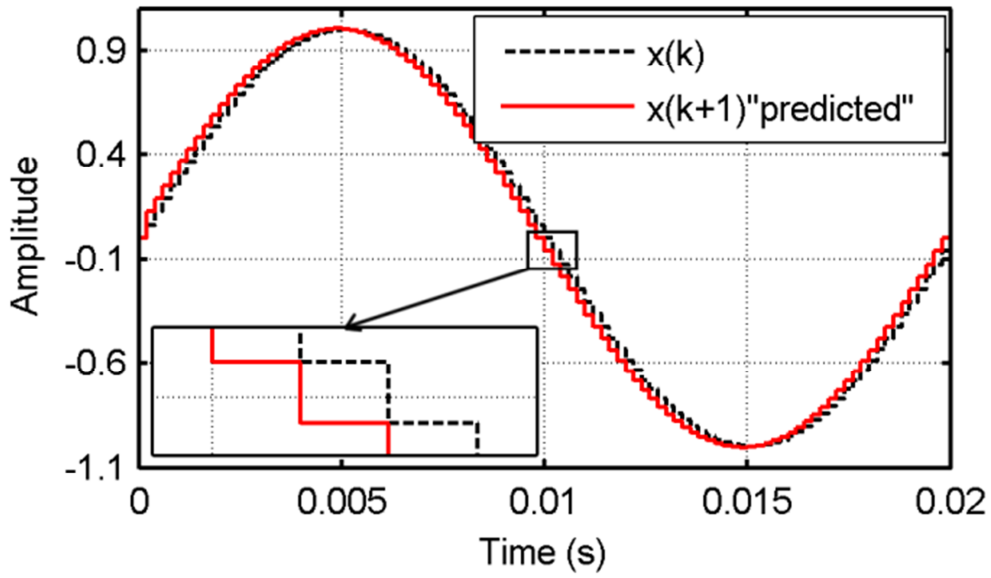

Figure 3.10: Prediction of a purely sinusoidal signal.

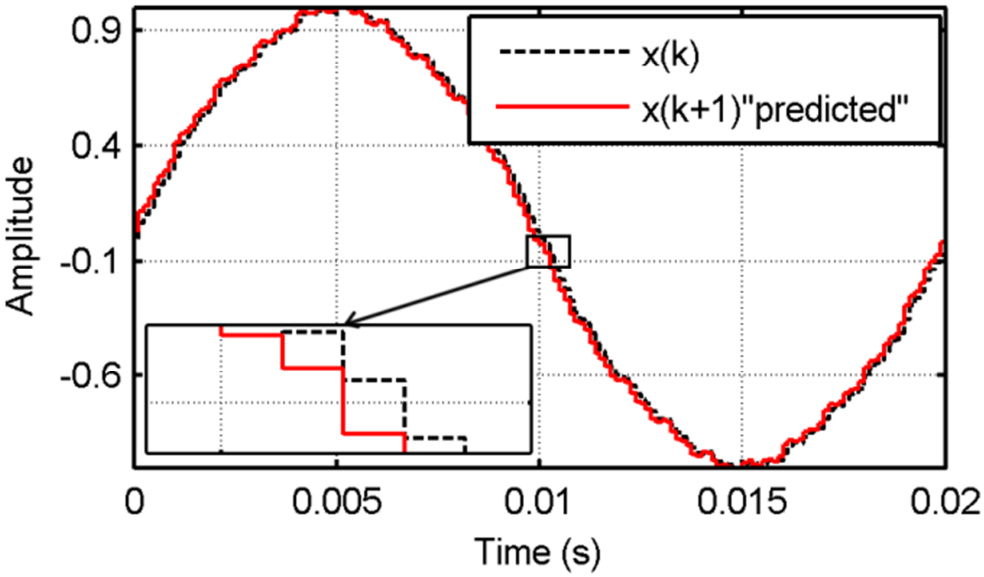

Figure 3.11: Prediction of a distorted sinusoidal signal ($\mathrm{THD}_{50} = 8.55\%$).

The developed algorithm of the improved deadbeat control has been tested on the two output filters of the grid connected inverter—the L-filter and the LCL-filter.

3.5.1. Inductive filter case:

Applying the methodology explained in Section (3.5) on the deadbeat controller when using an inductive filter, equation (3.4), which gives the expected pulse width, becomes:

$$\Delta T(k+1) = \frac{\frac{L}{T}\left(\hat{I}_L^{*}(k+2) - \hat{I}_L(k+1)\right) + \hat{U}_{grid}(k+1)}{Ud} \tag{3.15}$$

where the prediction of measured, controlled, and reference state variables are given below:

$$\hat{U}_{grid}(k+1) = a_0 U_{grid}(k) + a_1 U_{grid}(k-1) \tag{3.16}$$

$$\begin{aligned} \hat{I}_L(k+1) &= \hat{I}_L^{*}(k+1) + e(k) \\ e(k) &= I_L(k) - I_L^{*}(k) \end{aligned} \tag{3.17}$$

$$\hat{I}_L^{*}(k+1) = a_0 I_L^{*}(k) + a_1 I_L^{*}(k-1) \tag{3.18}$$

$$\hat{I}_L^{*}(k+2) = a_0 \hat{I}_L^{*}(k+1) + a_1 I_L^{*}(k) \tag{3.19}$$

The Simulink model of the proposed controller is given in figure (3.12). In this model, the DSP behaviour is simulated by adding a delay block of one control period.

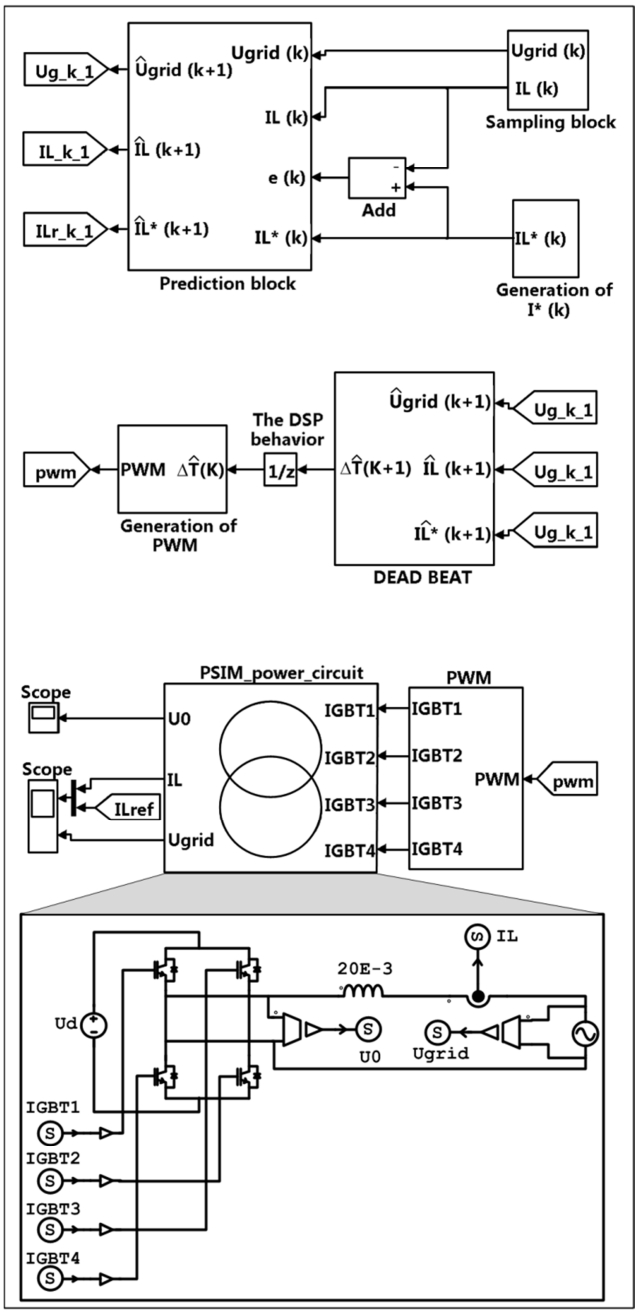

Figure 3.12: Simulink model of the proposed controller (inductive filter case).

3.5.2. LCL-filter case:

When the aforementioned methodology is applied on the deadbeat controller in the LCL-filter case, equation (3.11) becomes:

$$\Delta T(k+1)=\frac{\hat{V}_C^{\,*}(k+1)-\varphi_{21}\hat{I}_{L1}(k+1)-\varphi_{22}\hat{V}_c(k+1)-\varphi_{23}\hat{I}_{L2}(k+1)-\gamma_{22}\hat{U}_{grid}(k+1)}{\gamma_{21}U_d} \quad (3.20)$$

where the prediction of measured, controlled, and reference state variables are given below:

$$\begin{aligned}\hat{I}_{L2}(k+1)&=\hat{I}_{L2}^{\,*}(k+1)+e_{I_{L2}}(k)\\ e_{I_{L2}}(k)&=I_{L2}(k)-I_{L2}^{\,*}(k)\end{aligned} \quad (3.21)$$

$$\hat{I}_{L2}^{\,*}(k+1)=a_0 I_{L2}^{\,*}(k)+a_1 I_{L2}^{\,*}(k-1) \quad (3.22)$$

$$\begin{aligned}\hat{V}_C(k+1)&=\hat{V}_C^{\,*}(k+1)+e_{Vc}(k)\\ e_{Vc}(k)&=V_C(k)-V_C^{\,*}(k)\end{aligned} \quad (3.23)$$

$\hat{V}_C^{\,*}(k+1)$ is obtained by replacing equations ((3.16), (3.21), and (3.22)) in equation (3.7):

$$\hat{V}_C^{\,*}(k+1)=\frac{L_2}{T}\{\hat{I}_{L2}^{\,*}(k+1)-\hat{I}_{L2}(k+1)+\hat{U}_{grid}(k+1)\} \quad (3.24)$$

Since, to compensate the controller delay, the two-step-ahead shifted prediction $I_{L2}^{\,*}(k+2)$ is used instead of $\hat{I}_{L2}^{\,*}(k+1)$, equation (3.24) becomes:

$$\hat{V}_C^{\,*}(k+1)=\frac{L_2}{T}\{\hat{I}_{L2}^{\,*}(k+2)-\hat{I}_{L2}(k+1)+\hat{U}_{grid}(k+1)\} \quad (3.25)$$

where

$$\hat{I}_{L2}^{\,*}(k+2)=a_0\hat{I}_{L2}^{\,*}(k+1)+a_1 I_{L2}^{\,*}(k) \quad (3.26)$$

Finally, the current $\hat{I}_{L1}(k+1)$ can be computed as follows:

$$\hat{I}_{L1}(k+1)=a_0 I_{L1}(k)+a_1 I_{L1}(k-1) \quad (3.27)$$

The Simulink model of the proposed controller, when using an LCL filter, is given in figure (3.13).

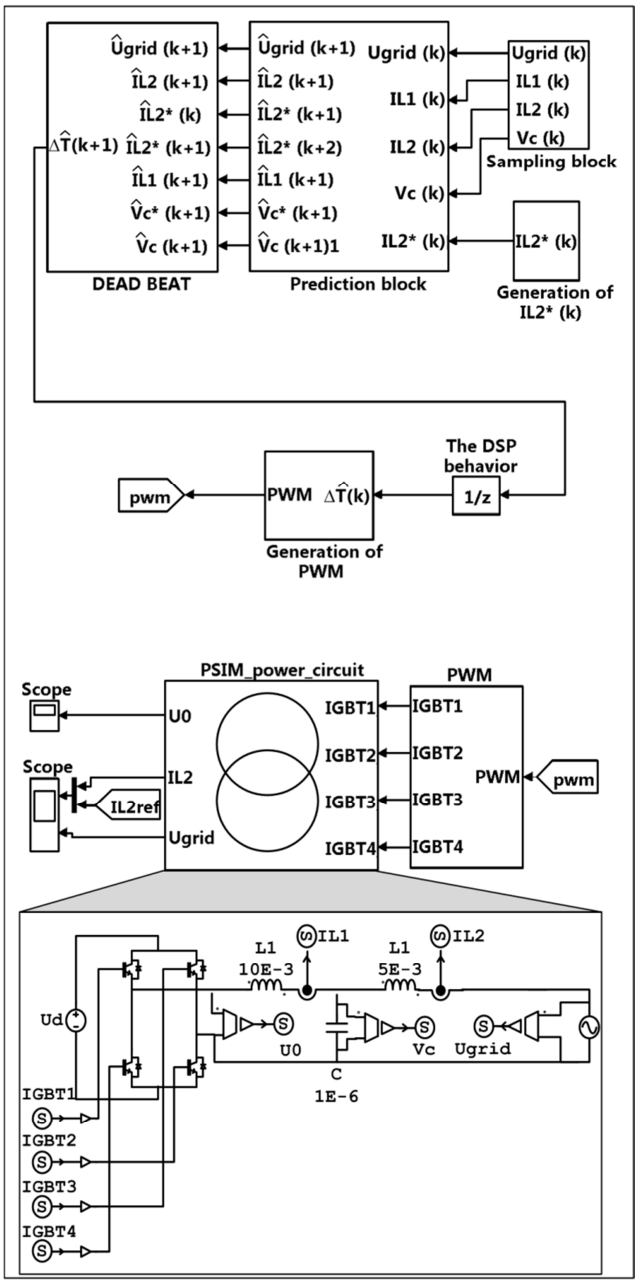

Figure 3.13: Simulink model of the proposed controller (LCL filter case).

3.6. Simulation Results:

The developed controllers are implemented using a co-simulation methodology by combining MATLAB/Simulink and Psim environments. The single-phase inverter and its output filters are implemented in the Psim environment, while the control algorithm is implemented in the MATLAB/Simulink environment.

Inverters and filters used in this simulation have been modelled and rated in appendix E. The values of all parameters used in simulation are given in table 3.2.

Table 3.2: Simulation parameters.

Parameters	**Value**	**Parameters**	**Value**
DC bus (U_d)	400 (V)	a_0	2
Grid voltage (V_{grid} RMS)	220 (V)	a_1	-1
Load rate	2.2 (kW)	L	20 (mH)
Utility frequency	50 (Hz)	L_1	10 (mH)
Sampling frequency	10 (kHz)	C	7 (µF)
Switching frequency	10 (kHz)	L_2	5 (mH)

3.6.1. Inductive filter case:

The simulation results of the conventional and proposed controllers when an inductive filter is used are given in figures (3.14–3.17). As is shown in figure (3.14), there is a phase shift between the grid-connected and reference currents; hence, the PF cannot be equal to 1. This phase shift is compensated, and the current waveform is significantly improved when the proposed controller is used (figure 3.15). A comparison between the results of the two controllers is made in figure (3.16). It appears that the proposed controller is more efficient than the conventional one. The PF and the THD values for the two controllers are given in table 3.3.

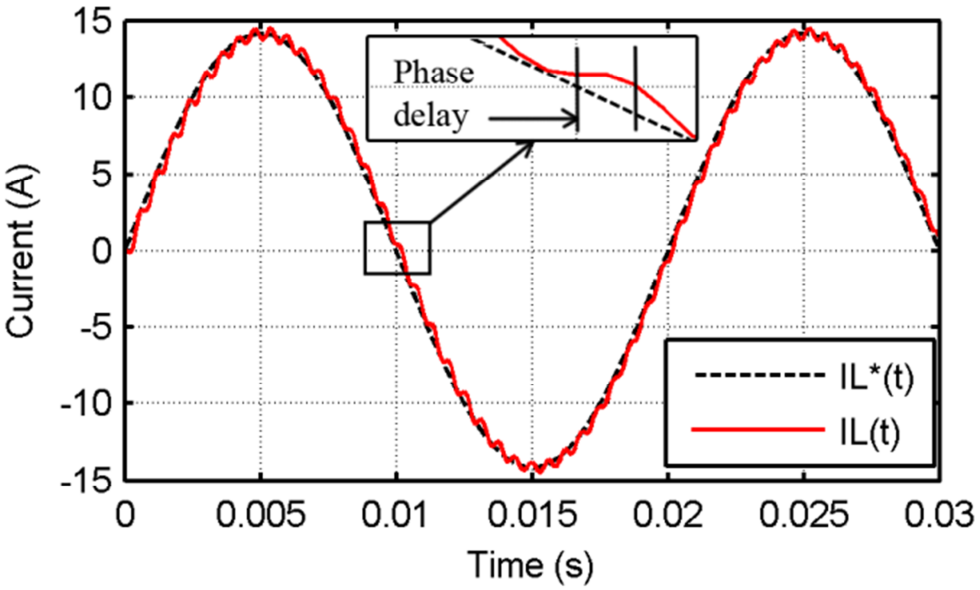

Figure 3.14: Injected and reference currents for conventional deadbeat controller (inductive filter case).

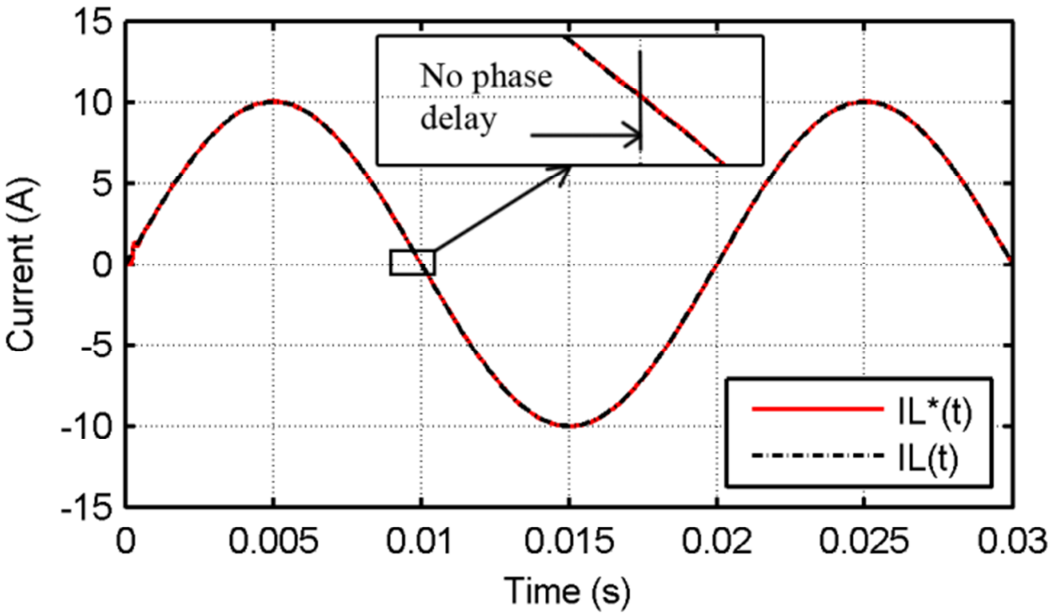

Figure 3.15: Injected and reference currents for proposed controller (inductive filter case).

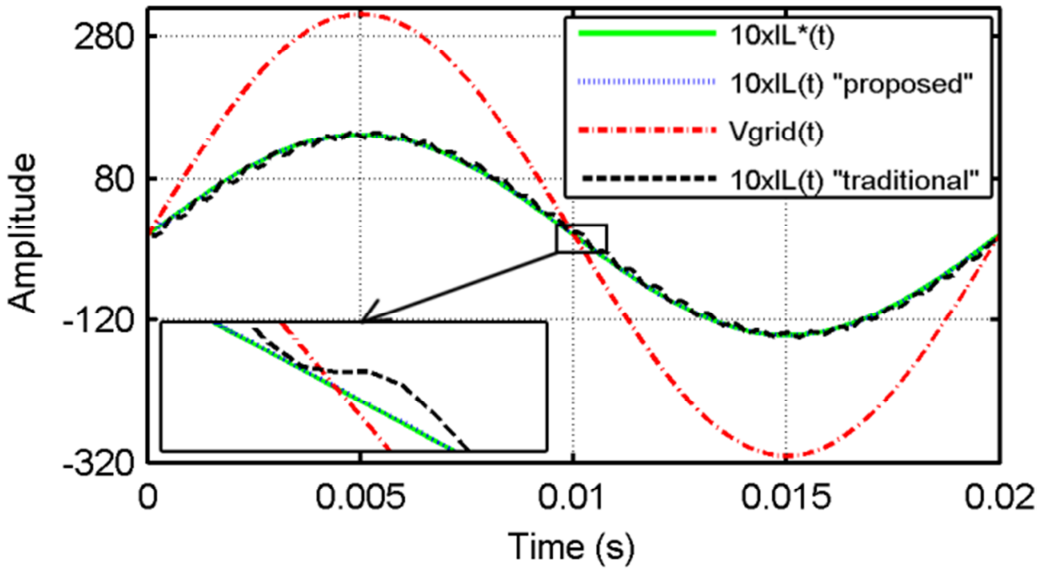

Figure 3.16: Comparison between conventional and proposed approaches (inductive filter case).

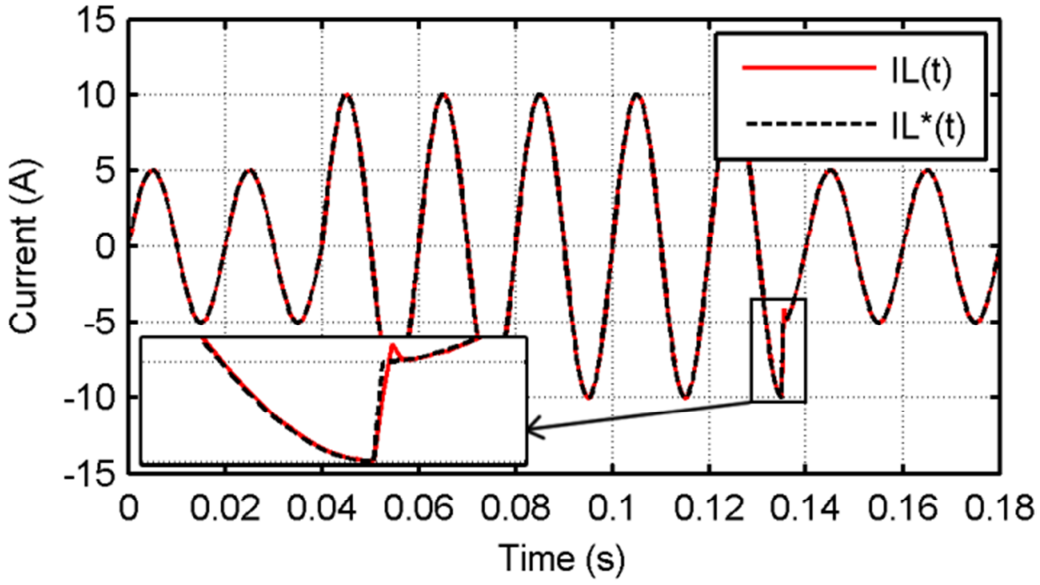

Figure 3.17: Typical dynamic simulation performance (inductive filter case).

Table 3.3: Performance comparison (inductive filter case).

Approaches	**PF (%)**	**THD_{50} (%)**
Traditional	99.9003	2.73
Proposed	99.9914	1.12

3.6.2. LCL-filter case:

Figure (17) shows a typical dynamic simulation performance of the inverter system using the proposed controller. The simulation results of the conventional and proposed controllers when using an LCL-filter are given in figures (3.18–3.21). For the case of the conventional deadbeat controller, figure (3.18) shows that, in addition to the ripples that are present in the injected current waveform, the reference and injected currents are phase shifted. In the case of the improved deadbeat controller, these ripples and the phase shift are eliminated (figure 3.19). A comparison between the results of the two controllers is made in figure (3.20). The proposed controller is more efficient than the conventional one. Table 3.4 gives the PF and the THD values for the two controllers. Figure (3.21) shows a dynamic performance of the inverter system using the improved controller.

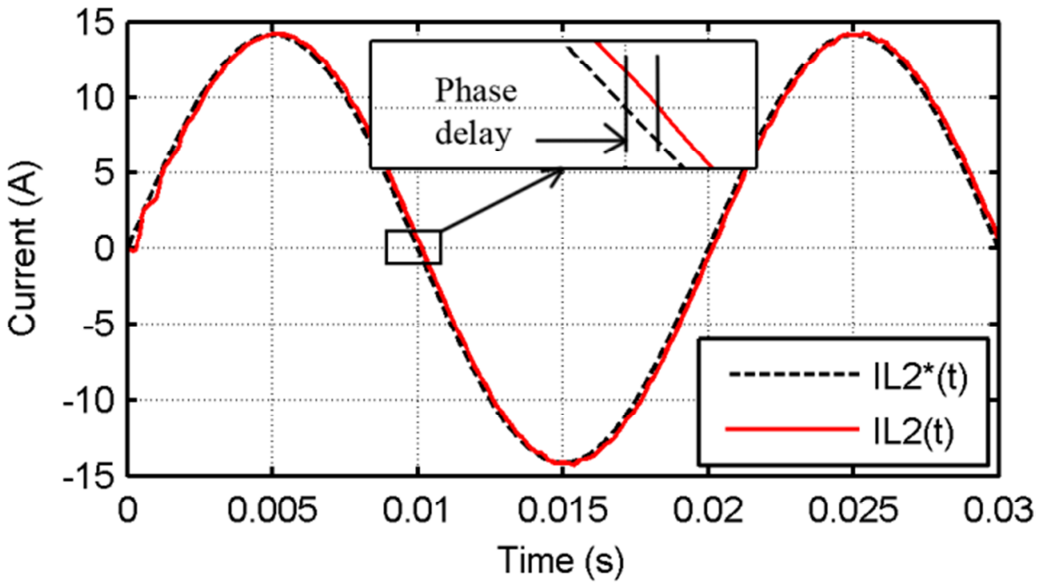

Figure 3.18: Injected and reference currents for conventional deadbeat controller (LCL-filter case).

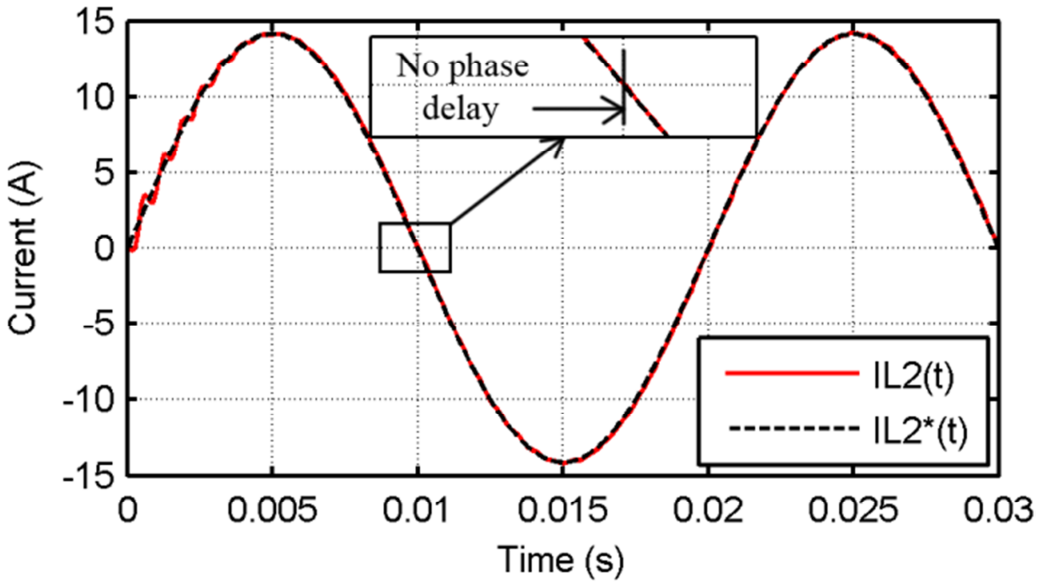

Figure 3.19: Injected and reference currents for proposed controller (LCL-filter case).

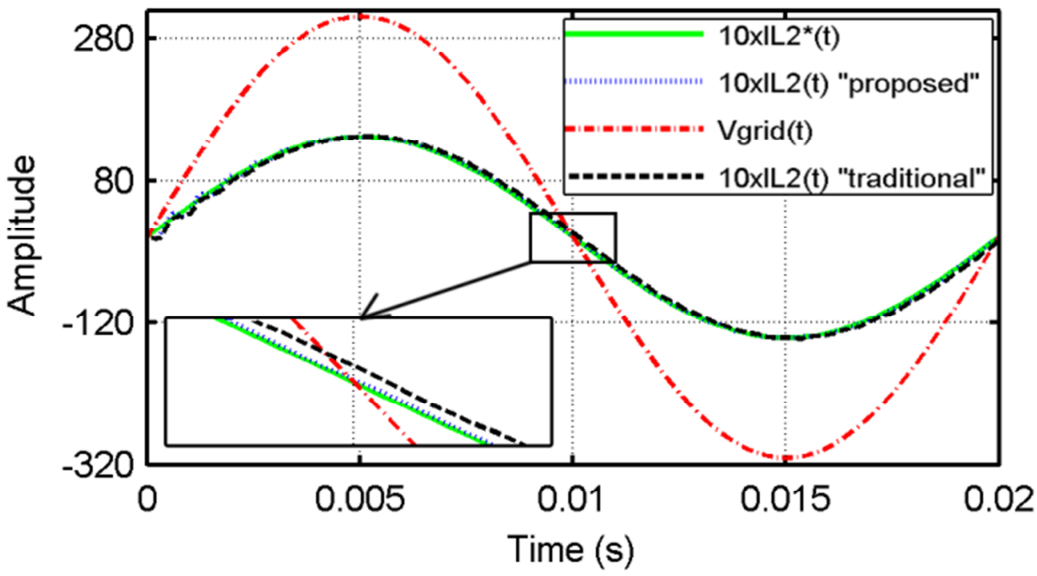

Figure 3.20: Comparison between conventional and proposed approaches (LCL-filter case).

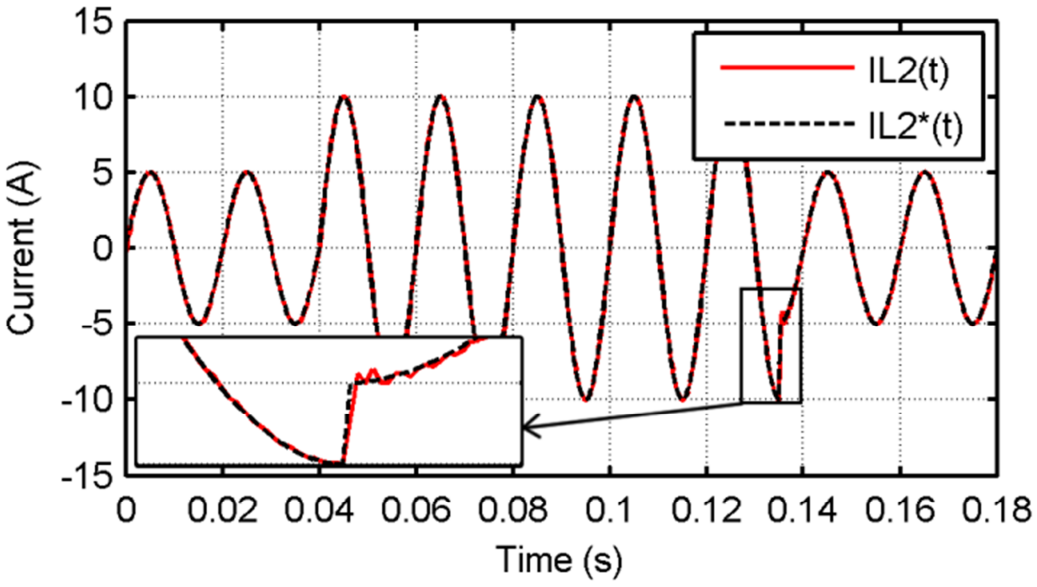

Figure 3.21: Typical dynamic simulation performance (LCL-filter case).

Table 3.4: Performance comparison (LCL-filter case).

Approach	**PF (%)**	**THD_{50} (%)**
Traditional	99.7757	0.64
Proposed	99.9995	0.29

3.7. Conclusion:

In this chapter, simple and efficient version of the deadbeat control algorithm has been introduced. It allows overcoming the main weakness of the conventional deadbeat control algorithm when it is implemented in a DSP board. The proposed algorithm is given and studied for both an output L-filter and an output LCL-filter. These configurations are the most used in grid-connected inverters. In the design procedure of the developed controller, a simple linear prediction model is used to compute the future values of all the state variables required for computing the expected duty cycle. By using such a model, it is possible to compute and apply the expected duty cycle within the same sampling cycle. This fact leads to overcoming the phase shift problem, and hence, the THD and the PF values are improved. The developed algorithm was used to control a grid-connected inverter and the co-simulation results have shown the effectiveness of the developed approach. In particular, a nearly sine wave current with a practically unity PF and low harmonic content was obtained.

CHAPTER 4

SIMULATION OF WHOLE SINGLE PHASE GRID CONNECTED PV SYSTEM

4.1. Introduction:

In the previous chapters we have separately tested the proposed ABC-based MPPT and the prediction-based deadbeat control techniques. To assess their effectiveness in grid connected photovoltaic systems, this chapter gives a complete computer simulation program of the single phase grid connected PV system shown in figure (4.1).

This chapter starts by introducing auxiliary controllers which are of prime interest for the proper functioning of the entire PV system. These controllers are: grid synchronisation, DC bus voltage regulation and protection mechanism.

Thereafter, simulation results of the complete system output variables such as: PV output power, DC bus voltage, inverter current, grid current and load current under different operating conditions are presented.

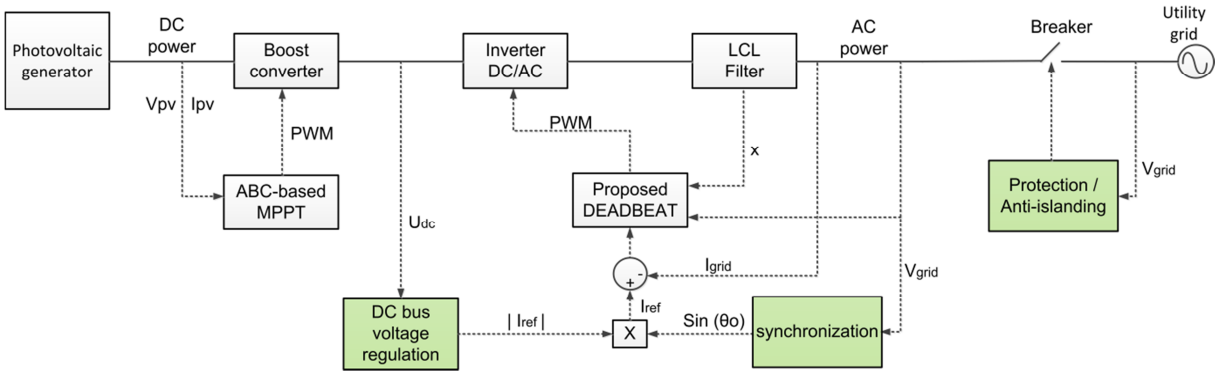

Figure 4.1: Block diagram of a grid connected PV system with a complete control scheme.

4.2. Grid synchronization:

Grid synchronization mechanism is very important in single-phase PV grid-connected systems. Its main objective is to allow inverter synthesized current waveform to be synchronized with the grid voltage waveform in order to ensure a nearly unity power factor. Typical synchronisation mechanism in grid connected PV system is illustrated in figure (4.2).

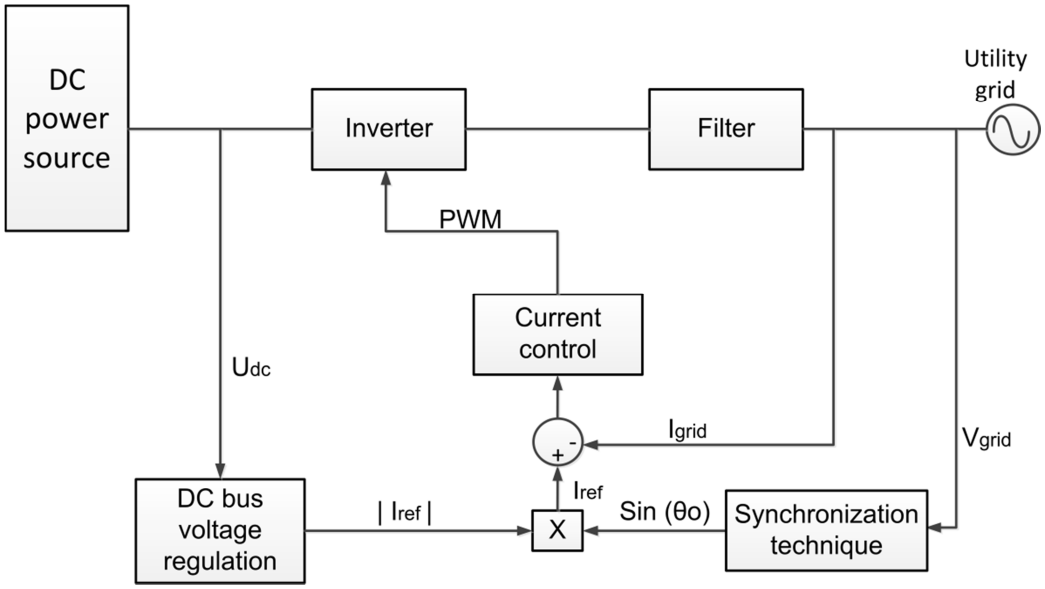

Figure 4.2: Typical synchronisation mechanism.

The existing synchronization methods can be divided into two main categories; frequency-domain and time-domain. Due to their simplicity, robustness, and effectiveness, the PLL-based techniques, from the time-domain category, have gained much more attractiveness in grid connected PV applications [169, 170].

A basic PLL technique is a closed-loop feedback control system, which synchronizes its output signal in frequency, as well as in phase, with the grid voltage fundamental component. It is composed of three basic parts, namely: phase detector (PD), low-pass filter (LF), and voltage-controlled oscillator (VOC), as illustrated in figure (4.3). The difference between phase angle of the input and that of the output signal is measured by the phase detection and passed through the low-pass filter. The LF output signal drives the voltage-controlled oscillator to generate an output signal, which could follow the input signal (grid voltage).

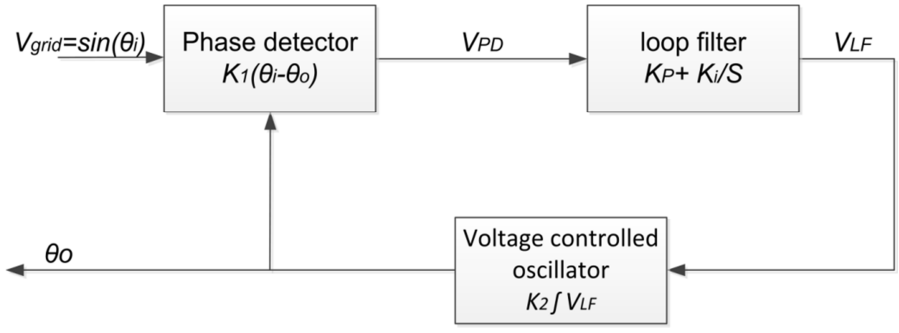

Figure 4.3: Basic structure of a phase locked loop.

If a first order low-pass filter is used as a loop filter, the model of a single phase PLL will typically be a second order system, described by the equation given in (4.1). The details of the PLL modelling can be found in [54].

$$\frac{\theta_o}{\theta_i} = \frac{\frac{K_1 K_2 G_{LF}(s)}{s}}{1 + \frac{K_1 K_2 G_{LF}(s)}{s}} = \frac{K_1 K_2 K_p s + K_1 K_2 K_i}{s^2 + K_1 K_2 K_p s + K_1 K_2 K_i} \tag{4.1}$$

where θ_i, θ_o are the phase of input and the output signals, K_1, K_2 are the gains of PD and VCO respectively, G_{LF} is the LF transfer function and K_p, K_i are its proportional and integral gains.

According to equation (4.1), when $K_1 = K_2 = 1$ the damping ratio ξ and the natural frequency ω_n can be given by:

$$\xi = \frac{K_p}{2\omega_n} \tag{4.2}$$

$$\omega_n = \sqrt{K_i} \tag{4.3}$$

An approximation of the settling time at 5% for second order systems with a damping factor lower than 1, is given by [171, 172]:

$$t_s = \frac{3}{\xi \omega_n} \tag{4.4}$$

Taking the natural frequency expression from equation (4.4) and replacing it in equation (4.2) and equation (4.3), the LF can be tuned as a function of the damping ratio and the settling time as follows:

$$K_p = \frac{6}{t_s} \tag{4.5}$$

$$K_i = \left(\frac{3}{\xi t_s} \right)^2 \tag{4.6}$$

It should be noted that the main difference among various single-phase PLL techniques is the configuration of the phase detector [169]. At present, the most employed PLL topology is the synchronous reference frame (SRF) PLL shown in

figure (4.4), where v_α is the single-phase voltage input, v_β is an internally generated signal that is a 90 degrees shifted version of v_α [173]. The Park transformation block, given by equation (4.7), changes the reference frame, bringing the system voltages from an $\alpha-\beta$ stationary reference frame to a $d-q$ rotating synchronous reference frame.

$$\begin{bmatrix} v_d \\ v_q \end{bmatrix} = \begin{bmatrix} \sin\theta_o & \cos\theta_o \\ \cos\theta_o & -\sin\theta_o \end{bmatrix} \begin{bmatrix} v_\alpha \\ v_\beta \end{bmatrix} \tag{4.7}$$

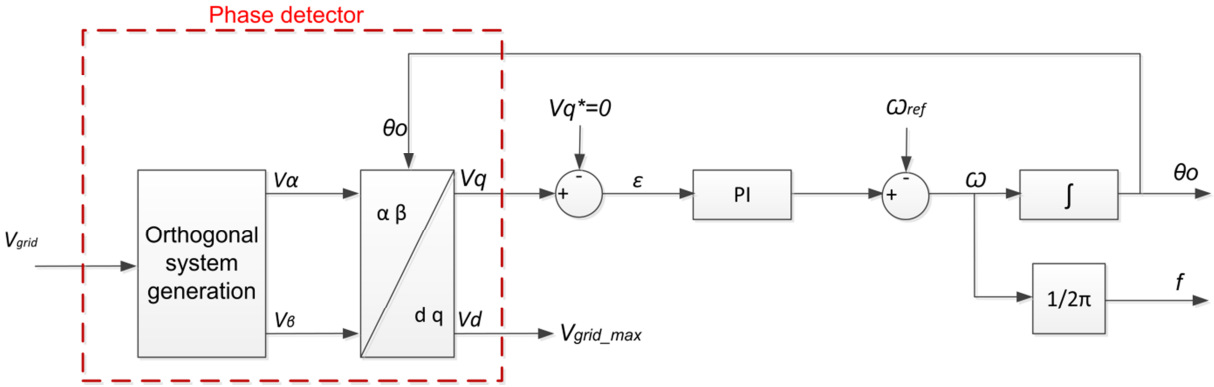

Figure 4.4: Block diagram of the single-phase SRF-PLL.

Assuming a harmonic-free grid voltage, the expression of the *q*-axis component which is feed to the PI controller is:

$$V_q = V_\alpha \cos\theta_o - V_\beta \sin\theta_o \tag{4.8}$$

for

$$\begin{aligned} V_\alpha &= V_{grid} \sin\theta_i \\ V_\beta &= V_{grid} \cos\theta_i \end{aligned} \tag{4.9}$$

The equation (4.8) becomes:

$$V_q = V_{grid} \sin\theta_i \cos\theta_o - V_{grid} \cos\theta_i \sin\theta_o \tag{4.10}$$

leading to:

$$V_q = V_{grid} \sin(\theta_i - \theta_o) \tag{4.11}$$

where, V_q is the phase detector output signal, V_{grid} is the amplitude of the grid voltage, θ_i is the angle of grid voltage and θ_o is the estimated angle.

Using the same procedure for the *d*-axis component V_d, its amplitude is given by:

$$V_d = V_{grid} \cos(\theta_i - \theta_o) \tag{4.12}$$

When θ_o becomes close to θ_i, V_q in equation (4.11) will be equal zero and the PLL will be locked. In this situation, according to equation (4.12), V_d will be equal to the input voltage amplitude.

Concerning quadrature signal generation, many techniques are presented in the literature. The simplest way is that uses a transport delay of T/4 to introduce a phase shift of 90 degrees. In this case, all the harmonics of the input signal are characterized by the same time delay. Other approaches are based on the inverse Park transformation, inverse Hilbert transformation or through the use of a second order generalized integrator (SOGI) [174, 175].

In this thesis, the second order generalized integrator is considered. This choice was motivated by the results of different comparative studies of single phase PLL algorithms for grid synchronization applications [169, 173, 176], which have concluded that SOGI-OSG method could be the best candidate for single-phase applications under both healthy and faulty grid conditions. The general structure of SOGI-OSG structure is depicted in figure (4.5).

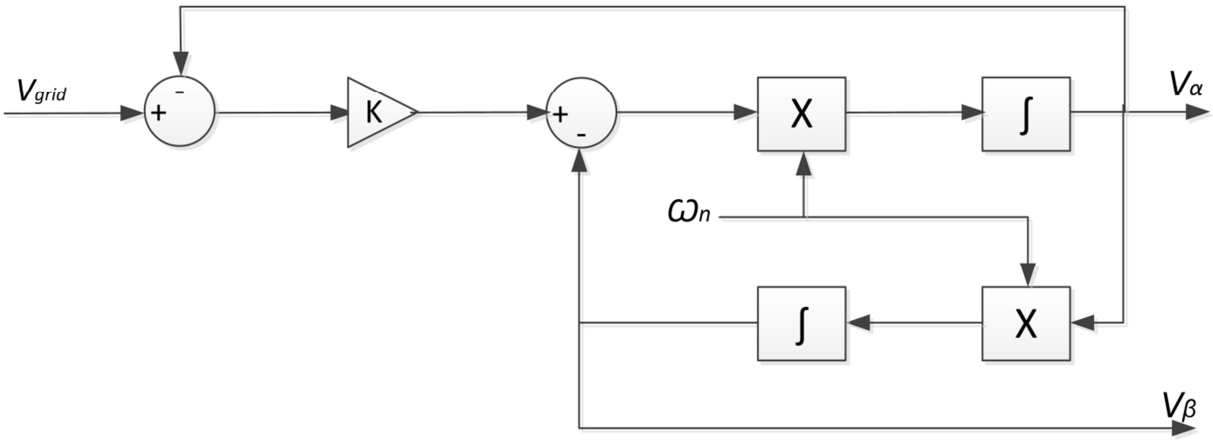

Figure 4.5: OSG-SOGI structure.

The structure of the OSG-SOGI is shown in figure (4.5). The input signal V_{grid} is the voltage signal measured at the PCC. As output signals, two sine waves (v_α and v_β) with a phase shift of $\pi / 2$ are generated. The component v_α has the same phase and amplitude as the fundamental of the input voltage signal V_{grid}.

The SOGI acts like an infinite gain band-pass filter whose transfer function is defined in (4.13) [177]. The closed-loop transfer functions ($H_\alpha(s) = V_\alpha / V_{grid}(s)$ and $H_\beta(s) = V_\beta / V_{grid}(s)$) of the OSG-SOGI, as presented in figure (4.5), are defined in (4.14) and (4.15) respectively.

$$H_{SOGI}(s) = \frac{\omega_n s}{s^2 + \omega_n{}^2} \tag{4.13}$$

$$H_\alpha(s) = \frac{V_\alpha(s)}{V_{grid}(s)} = \frac{K\omega_n s}{s^2 + K\omega_n s + \omega_n{}^2} \tag{4.14}$$

$$H_\beta(s) = \frac{V_\beta(s)}{V_{grid}(s)} = \frac{K\omega_n{}^2}{s^2 + K\omega_n s + \omega_n{}^2} \tag{4.15}$$

where ω_n represents the undamped natural frequency of the SOGI which is equal to the estimated frequency, and *K* is the gain which affects the bandwidth of the OSG-SOG.

4.2.1. Simulation results:

The selected grid synchronisation method is simulated and its performance evaluations are presented hereafter. All the simulation results are related to the bloc diagram presented in figure (4.3). The block "Orthogonal system generation" has been replaced with the structure presented in figure (4.5). Controller parameters of the PLL structure were set as shown in table 4.1, with $\xi = 0.707$ and $t_s = 0.06\,s$:

Table 4.1: PLL controller parameters.

Simulation parameter	Value
Kp	100
K_i	5001
Filtering capability (K)	0.8

To show the effectiveness of the selected PLL scheme several test have been carried out. In the first test the behaviour of the PLL bloc has been performed in case of clean sinewave of grid voltage. The obtained simulation results are shown in figures (4.6), (4.7) and (4.8).

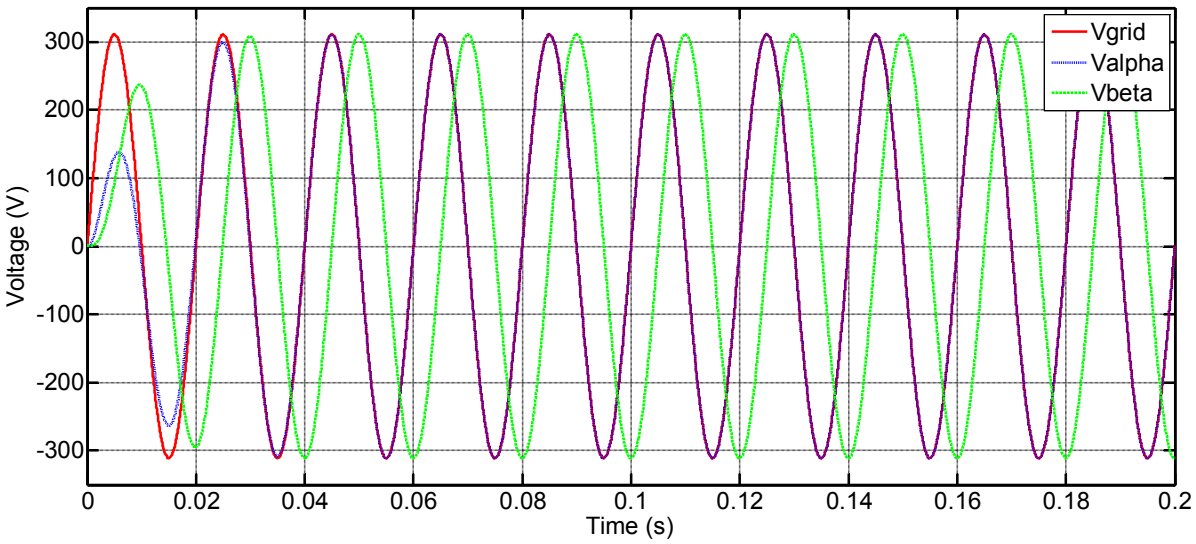

Figure 4.6: Alpha V_α and beta V_β components of a clean sinewave grid voltage.

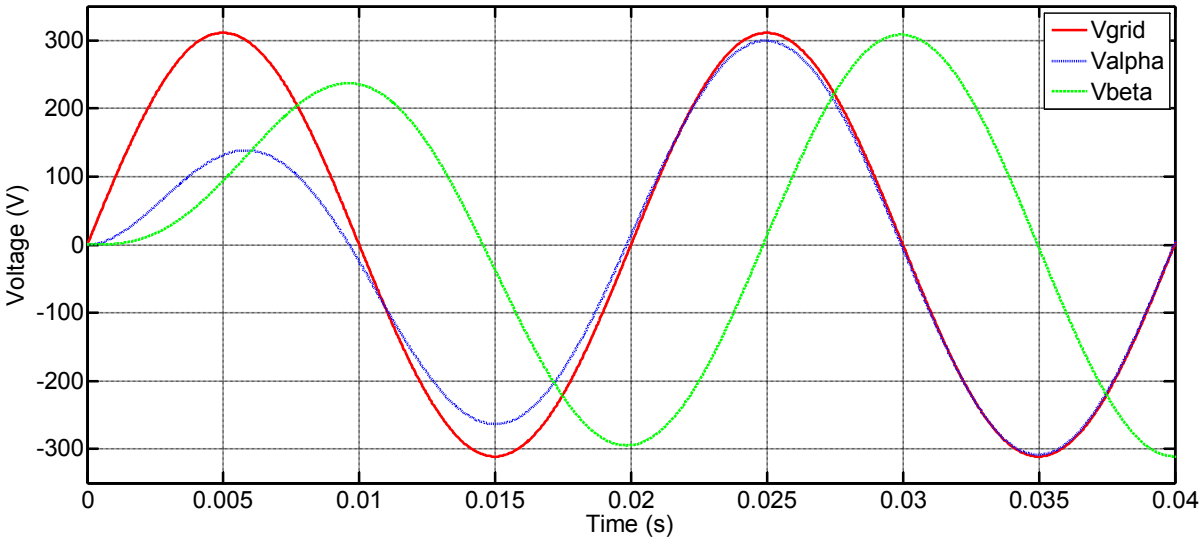

Figure 4.7: Zoom of figure (4.6).

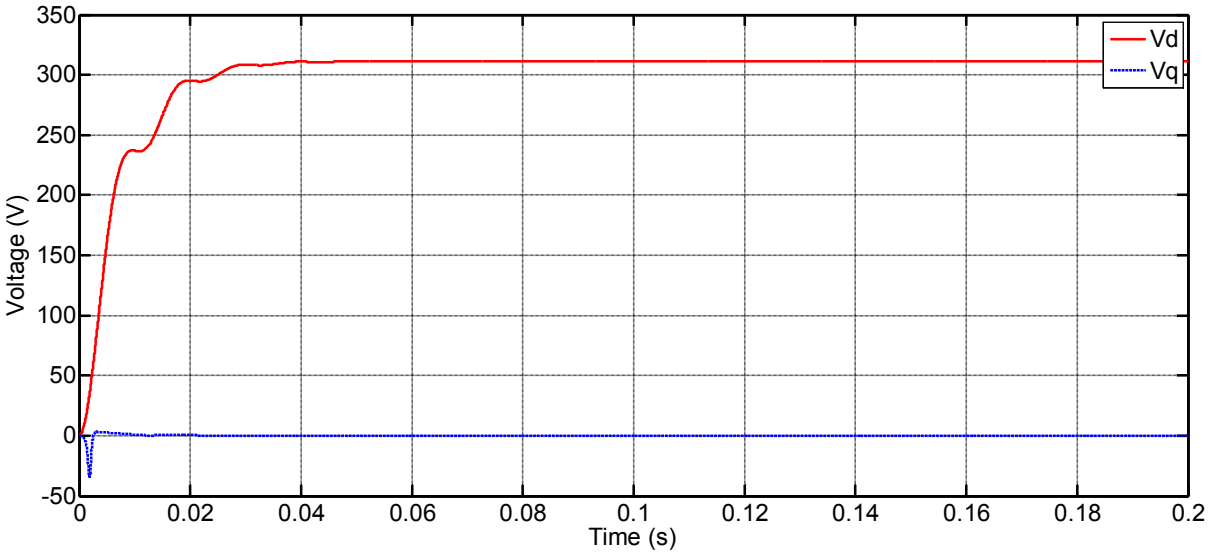

Figure 4.8: Direct V_d and quadrature V_q components of a clean sinewave grid voltage.

In the second test, the performance of the PLL scheme is tested against a distorted grid voltage (*THD=8%*) and under a grid voltage drop of 50%. The simulation results shown in figures (4.6), (4.7) and (4.8) are waveforms showing time evolution of grid voltage and alpha-beta grid voltage components, direct V_d and quadrature V_q components, frequency estimation and phase estimation respectively.

It can be noted that the selected SOGI-PLL scheme has given efficient results; highly immunity against deformed grid voltage and accurate frequency and phase estimation were obtained. It is also recorded that the settling time is in accordance with pre-set value (t_s=*0.06*).

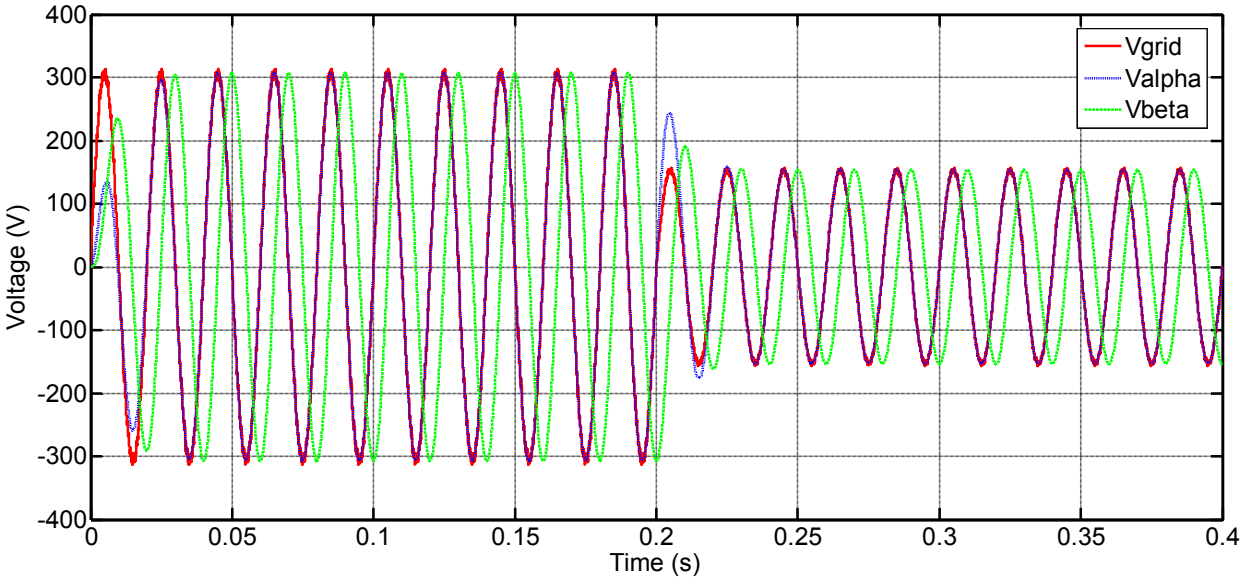

Figure 4.9: Alpha beta components of the grid voltage under voltage sag of 50% and THD 8%.

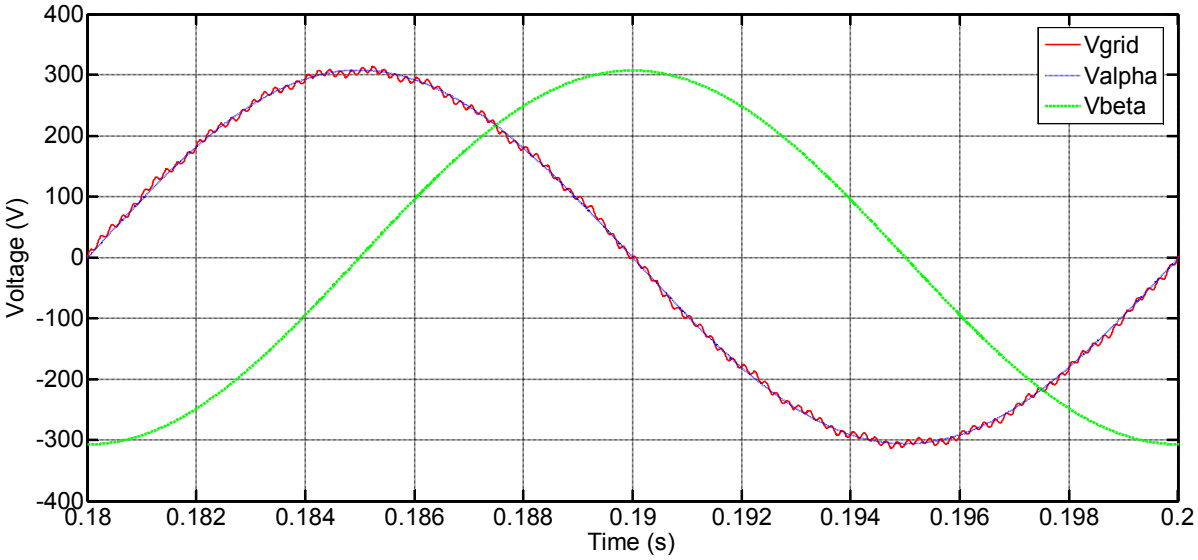

Figure 4.10: Zoom of figure (4.9).

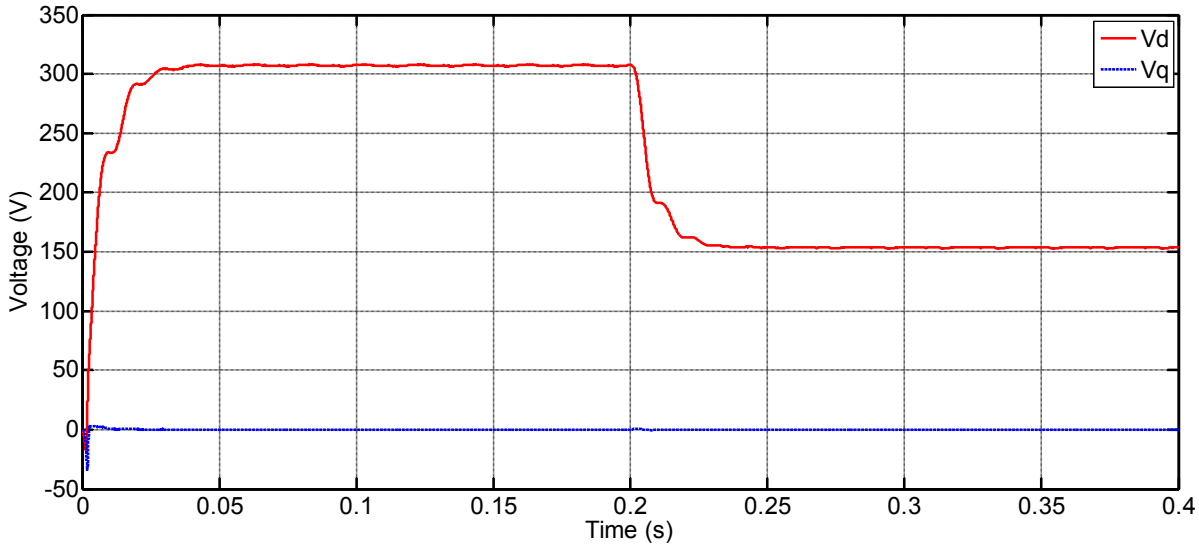

Figure 4.11: Direct V_d and quadrature V_q components of the grid voltage under voltage sag of 50% and THD 8%.

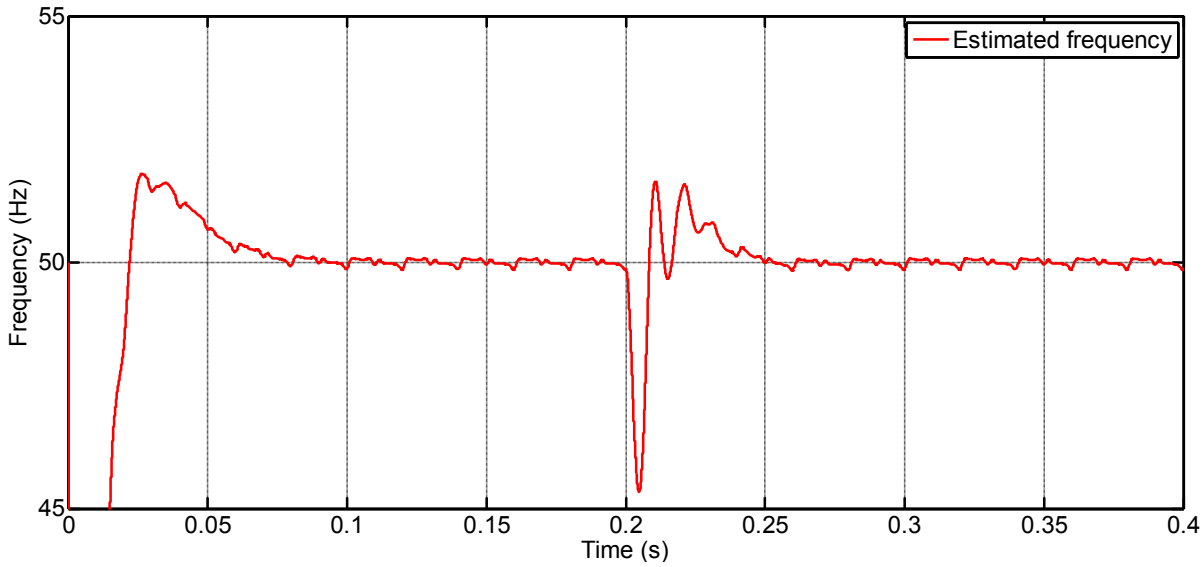

Figure 4.12: frequency estimation of the grid voltage under voltage sag of 50% and THD 8%.

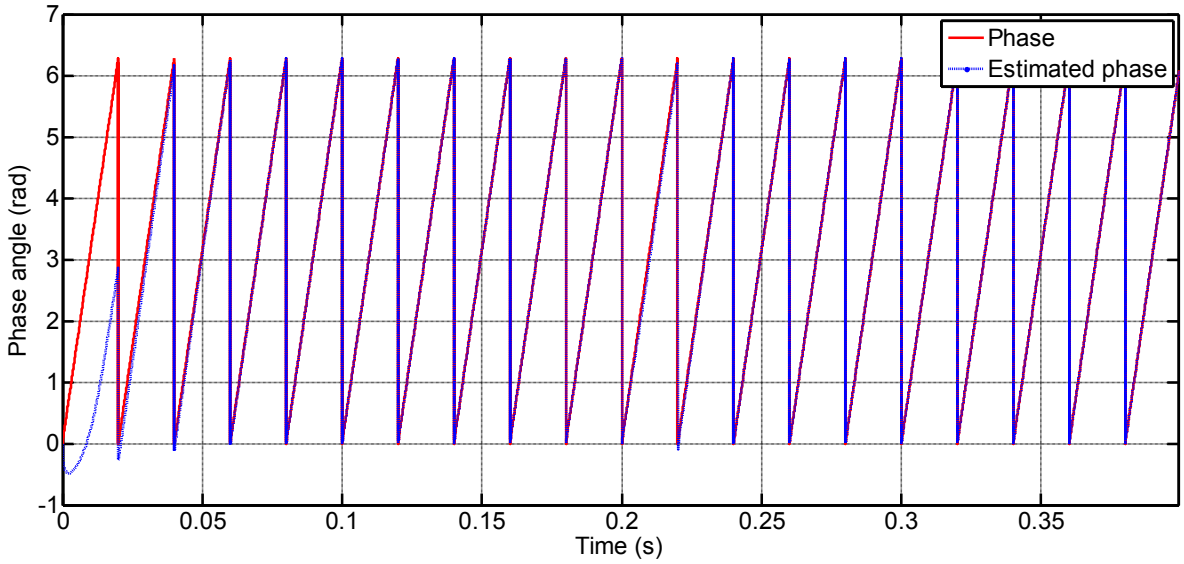

Figure 4.13: Phase estimation for the grid voltage under voltage sag of 50% and THD 8%.

Two other relevant tests, frequency and phase jump that can occur in the utility grid, have been also simulated. The obtained results are given by figures (4.14), (4.15), (4.16) and (4.17). Fast and accurate tracking of both frequency and phase of the grid voltage are achieved. In the frequency jump test, the grid voltage frequency change from 50 Hz to 51 Hz and its distortion level is taken equal to 8%. While in the phase jump test, at 0.3s a step change of 60 degrees occurs in the grid voltage with an amplitude decrease of 25%.

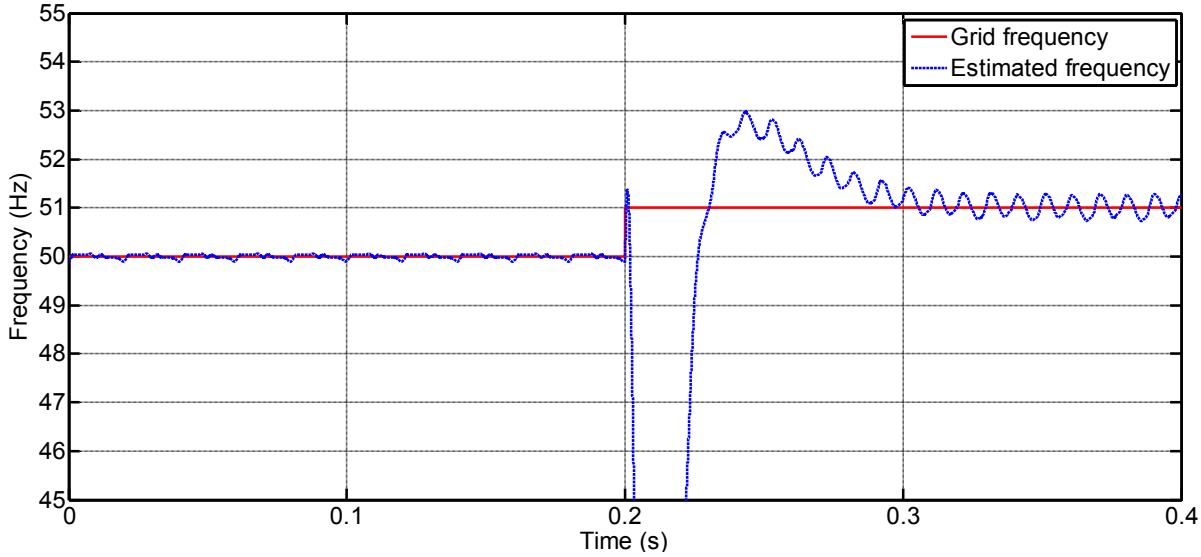

Figure 4.14: Grid frequency estimation when the grid frequency steps from 50 Hz to 51 Hz.

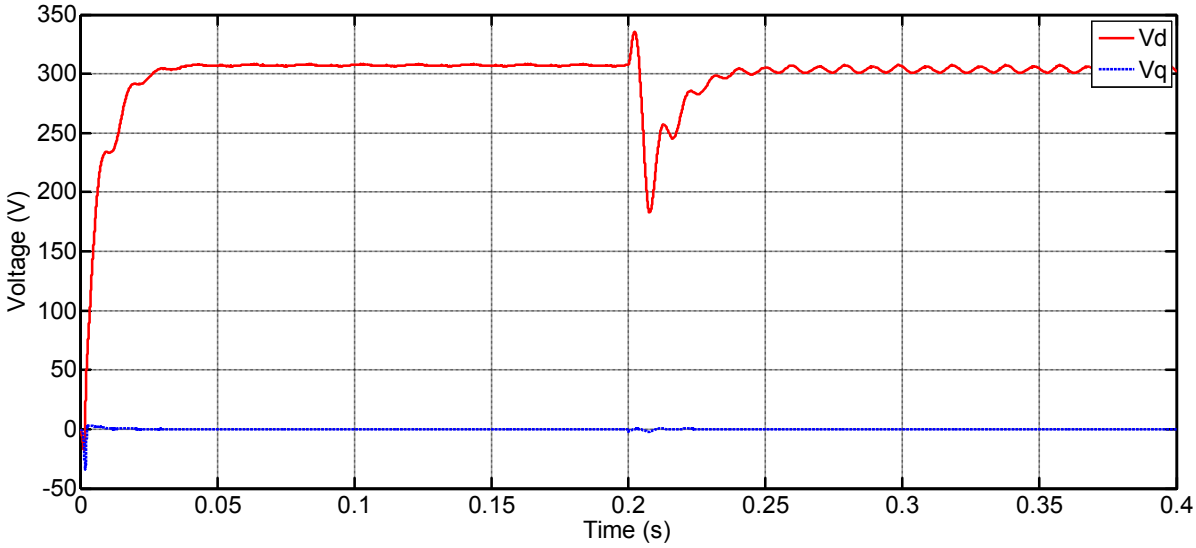

Figure 4.15: Direct V_d and quadrature V_q components of the grid voltage when the grid frequency steps from 50 Hz to 51 Hz.

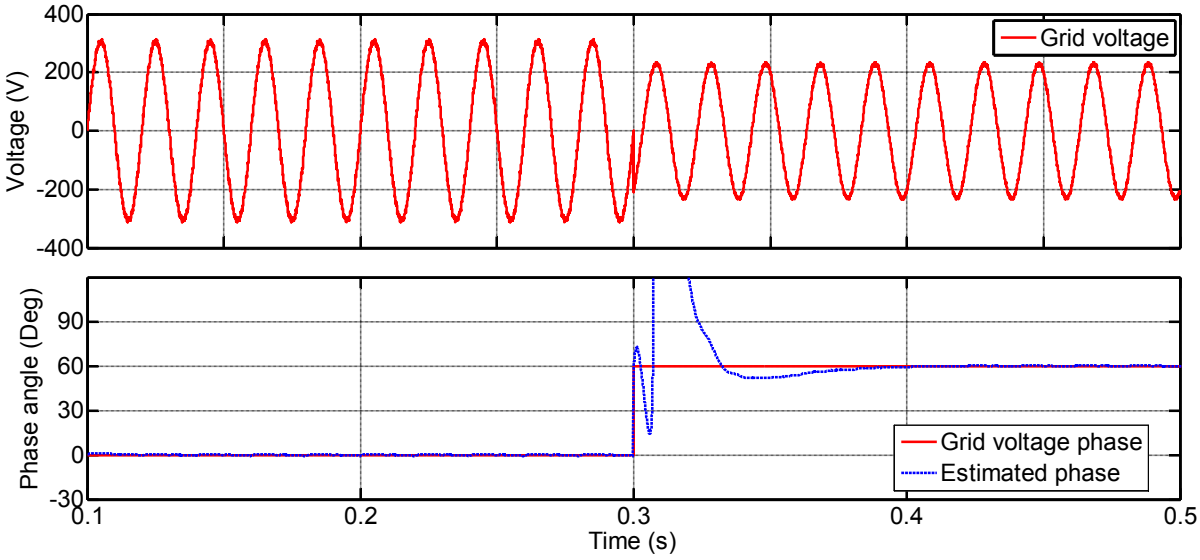

Figure 4.16: Grid phase estimation when the grid phase jumps of 60 degrees.

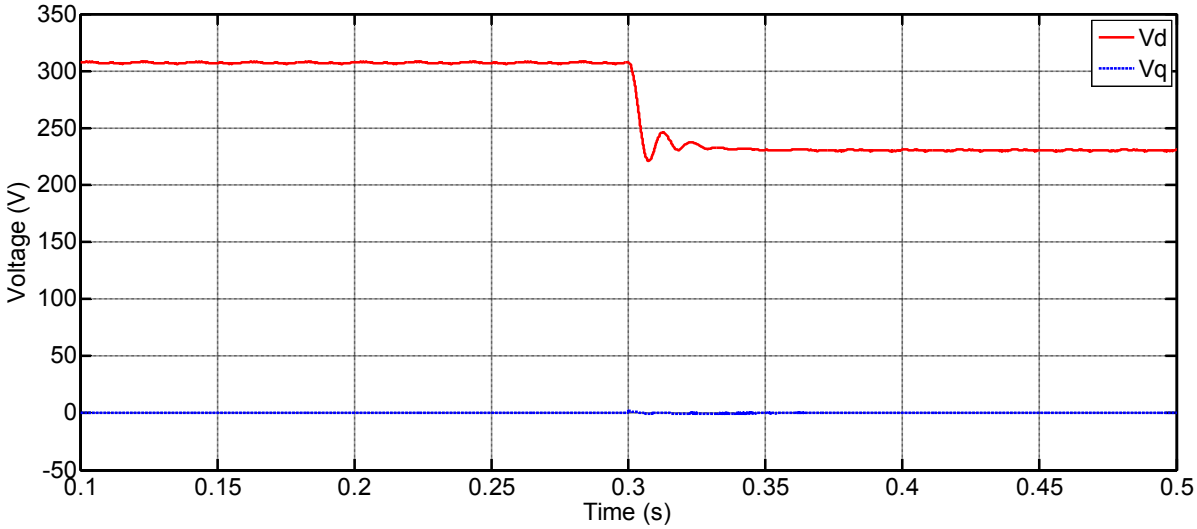

Figure 4.17: Direct V_d and quadrature V_q components of the grid voltage when the grid phase jumps to 60 degrees.

It can be noted that the SOGI-PLL has provided a very good dynamic response in all considered cases.

4.3. DC bus voltage regulation:

The DC bus voltage control is an indispensable task in the control of PV grid connected inverters. To guarantee an excellent operation, a constant DC link voltage must be maintained. The block diagram of the DC bus voltage control loop is shown in figure (4.11).

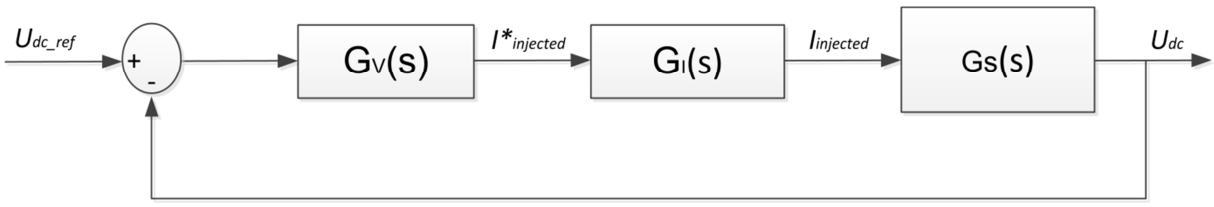

Figure 4.11: Block diagram of the DC bus voltage control loop.

where:

Gv(s), *Gi(s)* and *Gs(s)* are the transfer functions of the DC bus voltage controller, the current controller and the system, respectively.

On the basis of the conservation of energy principle, the transfer function of the system can be derived as follow:

$$P_{DC} = P_{AC} \tag{4.16}$$

$$U_{DC} C_{DC} \frac{dU_{DC}}{dt} = V_{grid} I_{injected} \tag{4.17}$$

$$U_{DC}(s) = \frac{1}{C_{DC} s} \frac{V_{grid} I_{injected}}{U_{DC}} \tag{4.18}$$

The system transfer function from $I_{injected}$ to U_{DC}, *Gs(s)* will be:

$$G_s(s) = \frac{V_{grid}}{C_{DC} U_{DC} s} \tag{4.19}$$

In this thesis, a proportional-Integral controller is chosen as DC bus voltage controller, therefore:

$$G_v(s) = \frac{K_p s + K_i}{s} \tag{4.20}$$

In addition, at high operating switching frequency, the current control must be much faster to ensure that the injected current $I_{injected}$ follows the reference current $I^*_{injected}$. Hence, we can assume that a closed loop current controller transfer function will be equal to unity [178, 179]. Therefore, the block diagram in the previous figure is simplified as shown in figure (4.12).

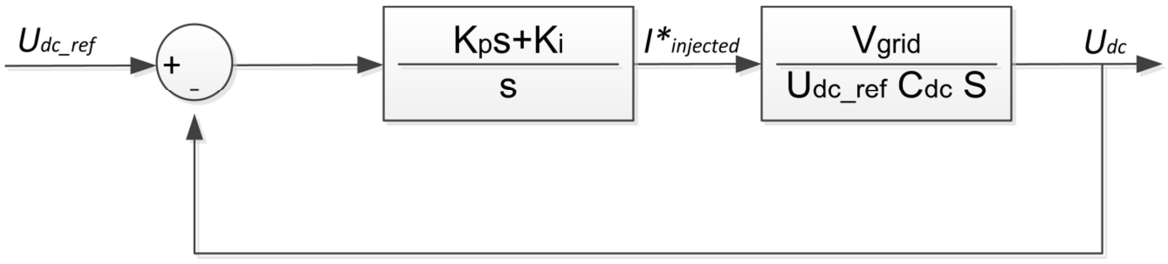

Figure 4.12: Simplified block diagram of the DC bus voltage control loop.

From the simplified block diagram of figure (4.12), the transfer function of the closed loop system can be written:

$$\frac{U_{dc}}{U_{dc\_ref}} = \frac{\frac{KG_v(s)}{s}}{1 + \frac{KG_v(s)}{s}} = \frac{KK_p s + KK_i}{s^2 + KK_p s + KK_i} \tag{4.21}$$

where:

$$K = \frac{V_{grid}}{U_{dc\_ref} C_{dc}} \tag{4.22}$$

$G_v(s)$ is the PI controller transfer function, K_p , K_i are the proportional and integral gains, respectively.

From equation (4.21), the relation between U_{dc} and U_{dc_ref} has a second order transfer function form. Hence, the damping ratio ξ and the natural frequency ω_n can be given by:

$$\omega_n = \sqrt{KK_i} \tag{4.23}$$

$$\xi = \frac{KK_p}{2\omega_n} \tag{4.24}$$

Taking the natural frequency expression from equation (4.4) and replacing it in equation (4.23) and equation (4.24), the PI controller can be tuned as a function of the damping ratio ξ and the settling time t_s as follows:

$$K_p = \frac{6}{Kt_s} \tag{4.25}$$

$$K_i = \left(\frac{3}{\sqrt{K}\xi t_s} \right)^2 \tag{4.26}$$

4.3.1. Simulation results:

To assess the effectiveness of the selected DC bus voltage controller, a 1.92 kWp PV grid connected system is implemented. The grid RMS voltage is specified to 220 V. The DC link voltage reference is estimated using equation (4.27). The voltage value of 400 V at the DC bus is chosen as reference.

$$V_{bus} \geq \sqrt{2} * 220 + 10\% * 220 \tag{4.27}$$

The DC link capacitor C_{DC} is sized according to the equation below:

$$C_{DC} = \frac{P_{pv}}{2 * \omega * U_{DC} * \Delta U} \tag{4.28}$$

For $P_{pv} = 1.92kW$, $\omega = 100\pi$ and $\Delta U = 2\%$, the DC link capacitor value is $C_{DC} = 1.9mF$. Thus $K = 289.47$.

The parameters of the DC bus voltage controller have been set, for $\xi = 0.707$ and $t_s = 0.06$, according to table 4.2.

Table 4.2: Parameters values of the DC bus voltage controller.

Simulation parameter	Value
K_p	0.3454
K_i	17.2701

Figure (4.13) shows the power profile generated by the photovoltaic array, in which the power decreases from 1.92kW to 1 kW at t=0.6s, then returns to 1.92 kW at t=1s. This power jump has been chosen to be large enough in order to verify both the dynamic response and the stability of the DC bus control loop.

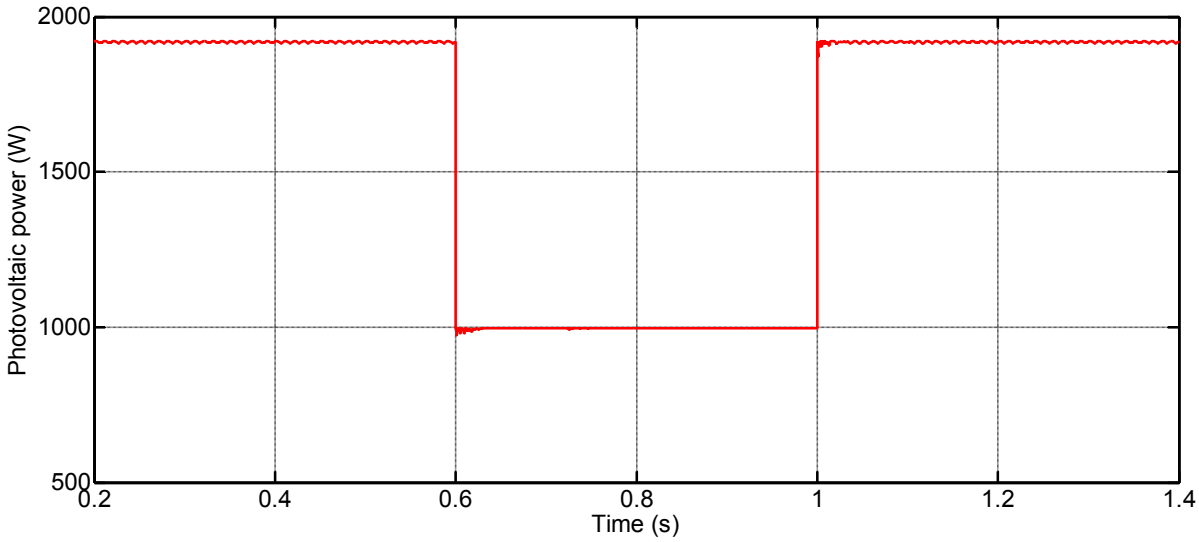

Figure 4.13: Generated photovoltaic power.

Simulation results shown in figure (4.14) give the waveforms of the DC reference current obtained at the output of the PI controller and the regulated DC bus voltage. It can be observed that the DC bus voltage has been significantly regulated and stabilized in 0.06 second. The injected AC current for the same power profile is represented in figure (4.15), where the amplitude shape is in

accordance with the DC reference current. These results show the ability of the PI controller to regulate the DC bus voltage in different operating situations.

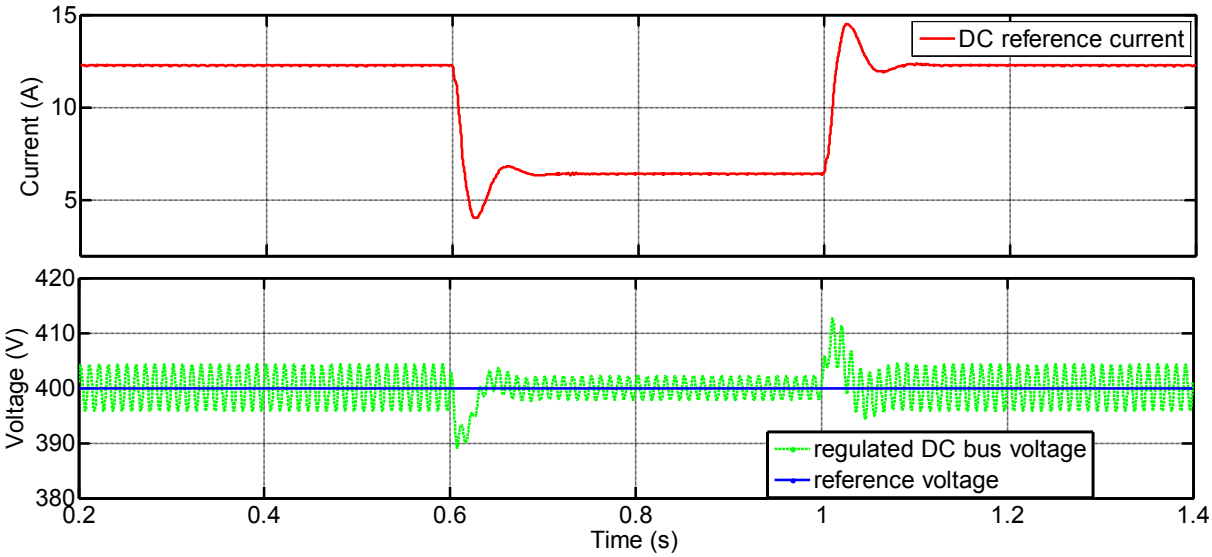

Figure 4.14: Waveforms of the DC reference current obtained by the controller and the regulated DC bus voltage.

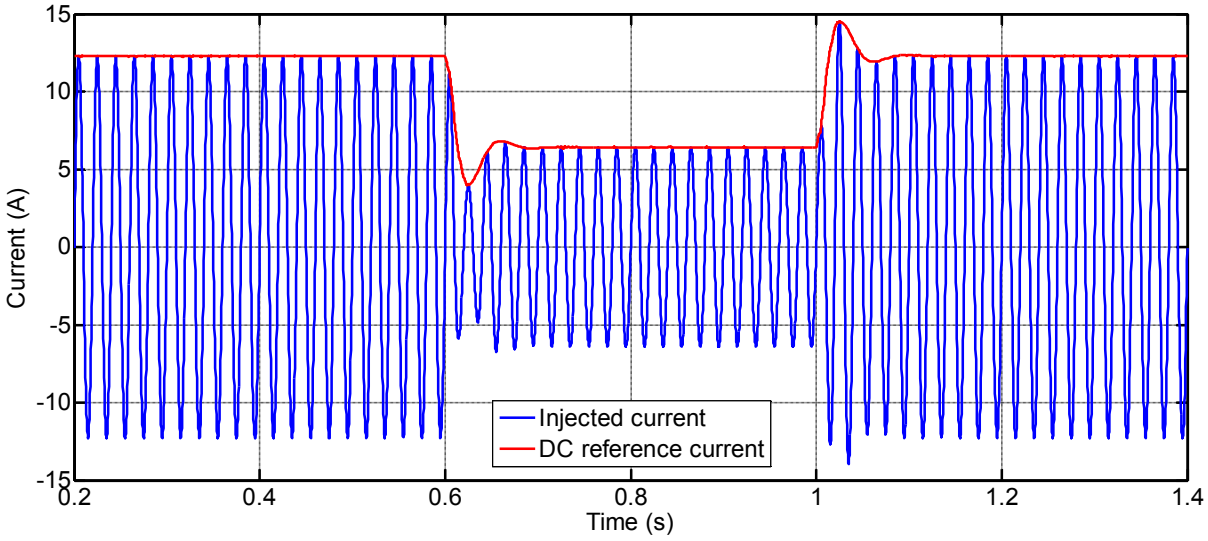

Figure 4.15: Waveforms of the reference current and the injected current.

4.4. Protection mechanism:

The aim of the protection mechanism in grid connected PV systems is to stop energizing the utility grid if its parameters (voltage /frequency) are out of their

normal operating range or in the event of total loss of grid utility supply (see section 1.5.3).

In all grid-connected PV systems, over/under frequency (OUF) and over/under voltage (OUV) protection mechanisms are required. These protection mechanisms cause the PV inverter to stop supplying power to the utility grid if the frequency or amplitude of the voltage at the point of common coupling (PCC) goes outside of prescribed limits (see section 1.5.3). This protection mechanism protects consumers' equipment and also serves as an anti-islanding detection method in the event of total loss of grid utility supply.

Given its simplicity and its dual role, OUV and OUF protection method has been implemented in our system as a protection mechanism. It should be noted that the standard over/under voltage and frequency protective devices alone are generally considered to be insufficient as islanding detection method, given its large non-detection zone (NDZ).

OUV and OUF protection method is a passive islanding detection method. It allows the detection of islanding phenomenon through the measure of voltage and frequency at the PCC, and subsequent comparison with the preset limits for proper operation. If the measured values are outside the established range, the inverter is stopped or disconnected. Figure (4.16) shows a PV grid connected system configuration feeding a local load and powers flow.

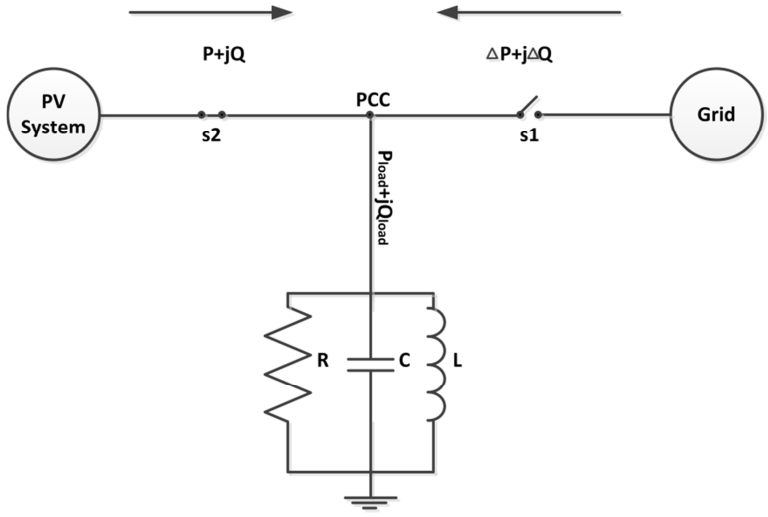

Figure 4.16: PV grid connected system configuration and powers flow.

It is usually assumed that the local load can be modelled as a parallel RLC circuit because, for most islanding detection methods, some types of RLC loads cause the most difficulty in detection [180]. When the utility grid is connected (s1 is closed), the real and reactive powers P + jQ flow from the PV system to PCC node, and Pload + jQload flows from node PCC to the local load. ΔP+jΔQ is the power which flows from utility grid to PCC node. These power equations are given in equation (4.29).

$$\begin{aligned} P_{load} &= P + \Delta P \\ Q_{load} &= Q + \Delta Q \end{aligned} \tag{4.29}$$

Resonant frequency f_0 and quality factor Q_f of the RLC parallel load, are defined as follows [180]:

$$f_0 = \frac{1}{2\pi\sqrt{LC}} \tag{4.30}$$

$$Q_f = R\sqrt{\frac{C}{L}} \tag{4.31}$$

Non-detection zone of active power and reactive power are given bellow [181]:

$$\left(\frac{V_{grid\_rms}}{V_{\max}}\right)^2 - 1 \le \frac{\Delta P}{P} \le \left(\frac{V_{grid\_rms}}{V_{\min}}\right)^2 - 1 \tag{4.32}$$

$$Q_f\left[1-\left(\frac{f_{grid}}{f_{\min}}\right)^2\right] \le \frac{\Delta Q}{P} \le Q_f\left[1-\left(\frac{f_{grid}}{f_{\max}}\right)^2\right] \tag{4.33}$$

Equations (4.34) and (4.35), prove that if the active power and the reactive power mismatches (ΔP and ΔQ) are within the specified range, the operating frequency and voltage will remain inside the nominal range, making islanding detection impossible.

For $V_{grid\_rms} = 220V$ and $f_{grid} = 50Hz$, according to IEC 62727 standard $V_{\max} = 242V$, $V_{\min} = 187V$, $f_{\max} = 51Hz$ and $f_{\min} = 49Hz$. To reasonably cover all distribution line configurations [50], Q_f must be selected equal to 2.5. In this case the non-detection zone is given by:

$$-17.35\% \leq \frac{\Delta P}{P} \leq 38.40\% \tag{4.34}$$

$$-10.30\% \leq \frac{\Delta Q}{P} \leq 9.70\% \tag{4.35}$$

From equations (4.34) and (4.35), NDZ area can be mapped as shown in figure (4.17).

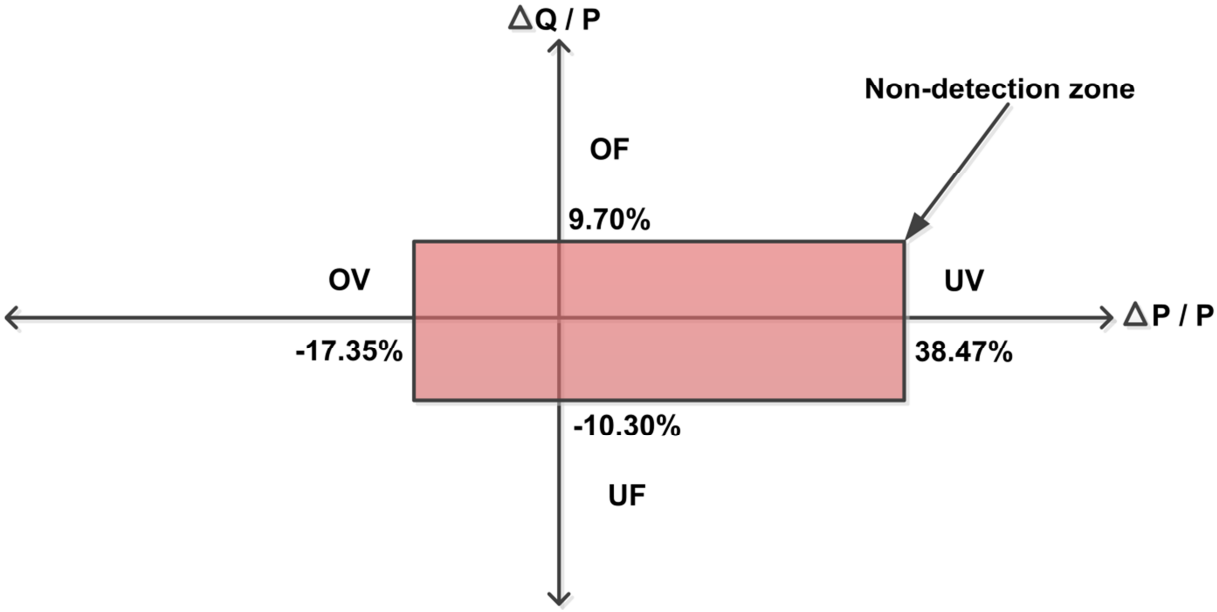

Figure 4.17: NDZ mapping of OUV and OUF protection mechanism.

Furthermore, in PV grid connected system without reactive power control scheme, equations (4.29), (4.34) and (4.35) become:

$$\begin{aligned} P_{load} &= P + \Delta P \\ Q_{load} &= \Delta Q \end{aligned} \tag{4.36}$$

$$-17.35\% \leq \frac{\Delta P}{P} \leq 38.40\% \tag{4.37}$$

$$0 \leq \frac{\Delta Q}{P} \leq 9.70\% \tag{4.38}$$

4.4.1. Simulation results:

To assess the effectiveness of the selected protection mechanism, a 1.92 kW PV grid connected system without reactive power control scheme is implemented. In what follows, several cases, such as: Grid voltage change, Grid frequency

change and islanding condition that require the intervention of the protection mechanism have been considered.

- *Case 1: grid voltage change*

To show the effectiveness of the implemented protection mechanism against a grid voltage change, we have simulated a grid voltage drop from 220 Vrms to 170 Vrms at t = 5s. The minimum threshold voltage is instantly detected. The protection mechanism makes a delay of 2s as required by the standard (IEC 61727) to disconnect the PV generator, as shown in figure (4.19).

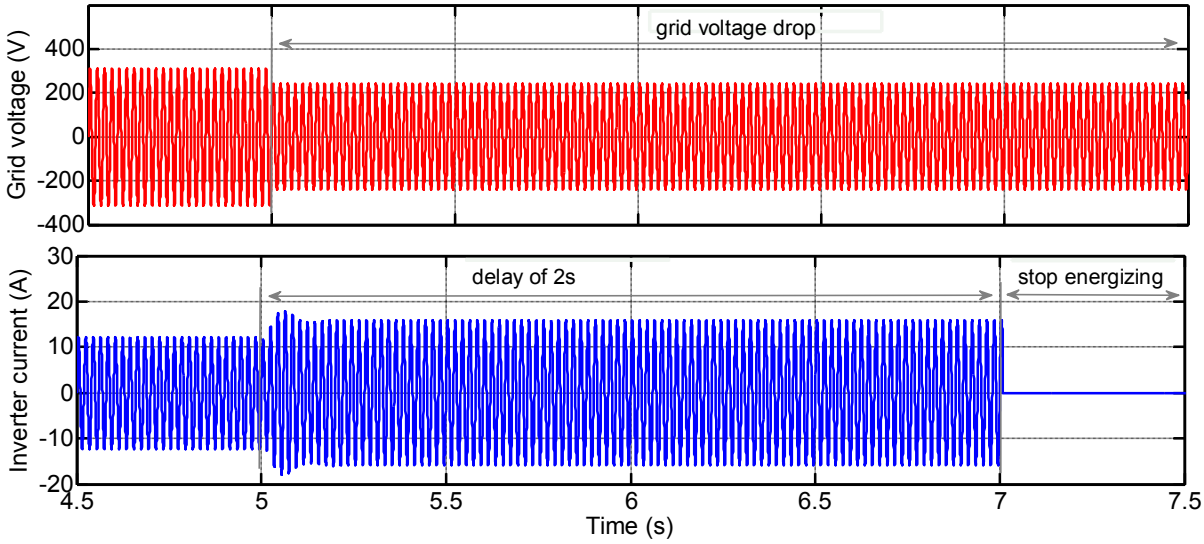

Figure 4.19: Protection mechanism against a grid voltage drop.

- *Case 2: grid frequency change*

The effectiveness of the implemented protection mechanism against a grid frequency change is shown in figure (4.20). The grid frequency increases from 50 Hz to 53 Hz at t = 5s. The maximum threshold frequency is instantly detected, a timer is started, and after 0.2s the protection mechanism isolates the PV generator, as required by the standard (IEC 61727).

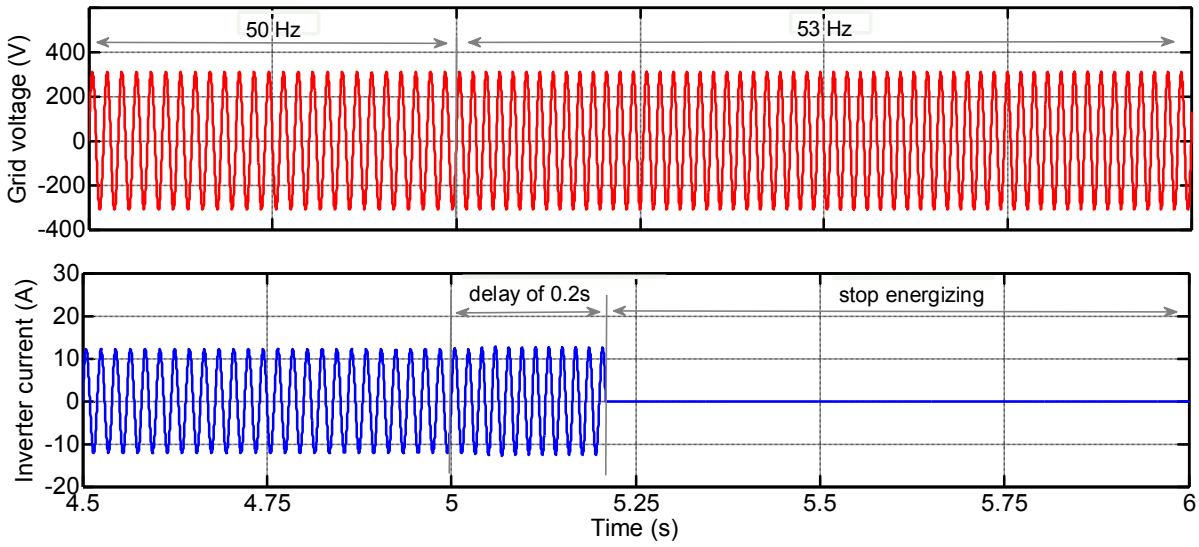

Figure 4.20: Protection mechanism against a grid frequency increase.

- *Case 3: islanding condition*

According to equations (4.37) and (4.38), the NDZ of OUV and OUF protection method for the implemented system is given bellow:

$$-333.12\ W \leq \Delta P \leq 737.28\ W \tag{4.39}$$

$$0\ VAR \leq \Delta Q \leq 186.24\ VAR \tag{4.40}$$

To keep the system outside the NDZ, we have chosen a load for $\Delta P = -633.5\ W$ and $\Delta Q = 633.5\ VAR$, which is presented in figure (4.21-a).

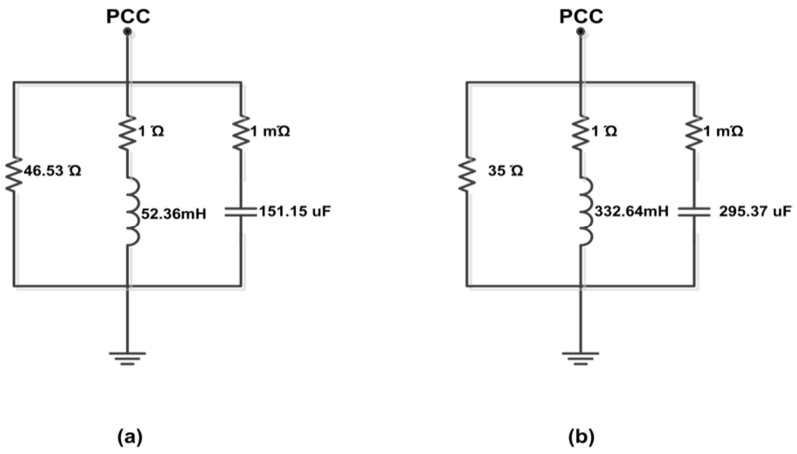

Figure 4.21: local loads.

The loss of the grid has been simulated at t = 5s. The protection mechanism instantly detects the change in voltage and frequency, after 0.2s the protection mechanism isolates the PV generator, as shown in figure (4.22).

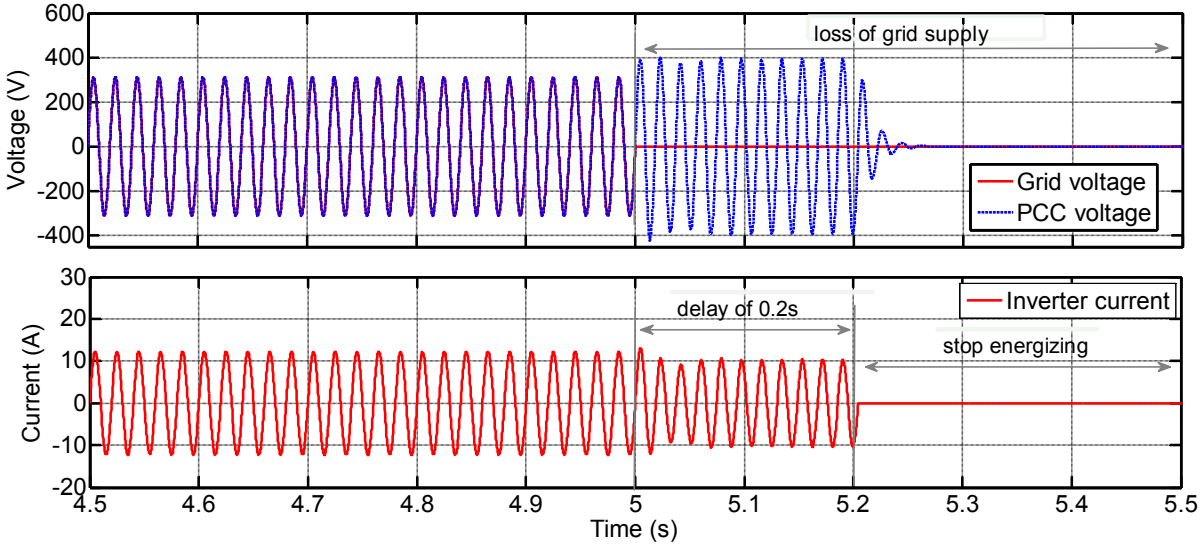

Figure 4.22: System out of the NDZ.

In order to show the failure of the selected anti-islanding detection mechanism, we have chosen a load shown in figure (4.21-b) ($\Delta P = -99\ W$ and $\Delta Q = 98\ VAR$), which brings the system in the NDZ. The simulation results shown in figure (4.23) demonstrate the failure of the detection method, where power generated from the PV system continues to energize the utility grid and no isolation has occurred.

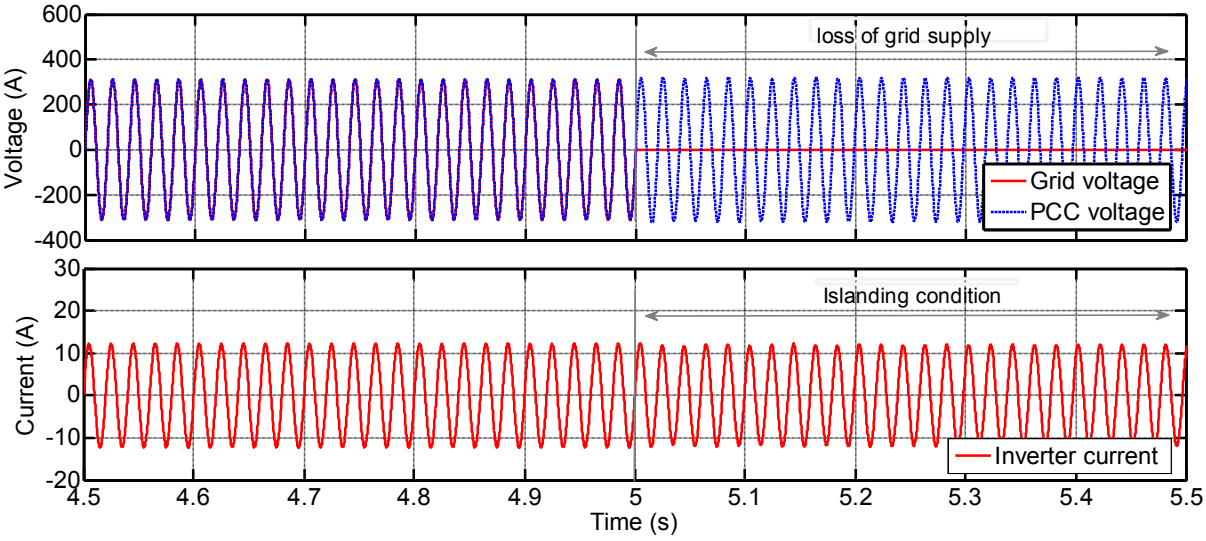

Figure 4.23: System in the NDZ.

4.5. Simulation of the whole system:

In this section, the 1.92 kW PV system, given in figure (4.24) is considered to demonstrate the operation of the different developed control algorithms for each part of the PV grid connected system namely: MPPT, DC bus control, inverter control, synchronization technique and protection mechanism.

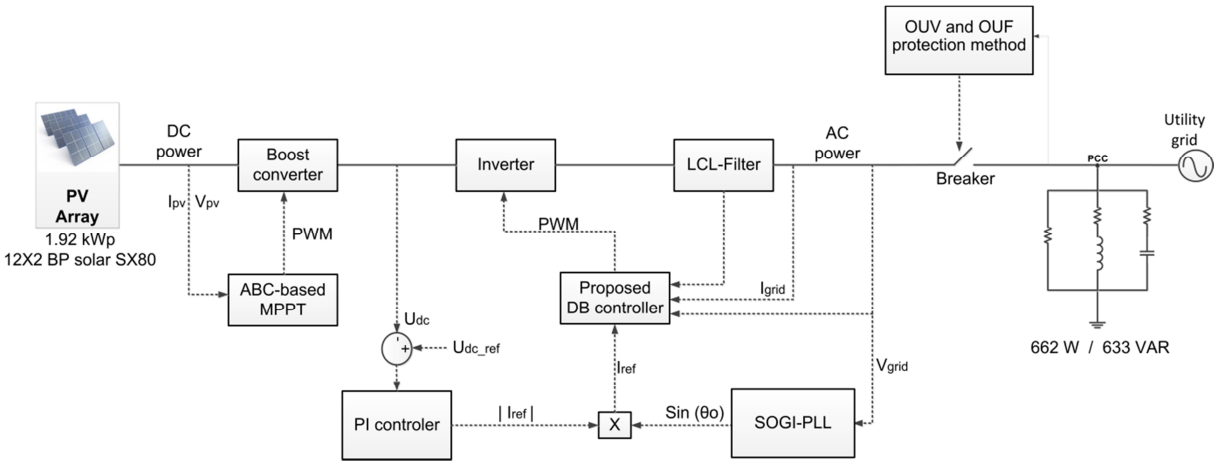

Figure 4.24: Considered grid connected PV system.

The boost converter chosen for interfacing between the PVG and the inverter has been modelled and rated in appendix D, while the inverter output LCL-filter has been modelled and rated in appendix E. The table 4.3 gives the different component values and rated operating conditions.

Table 4.3: Component values and rated operating conditions.

Boost converter		**Inverter/LCL filter**	
Component/Parameter	**Value**	**Component/Parameter**	**Value**
Input capacitor	220 uF	L_1	10 (mH)
Boost inductor	2 mH	C	7 (µF)
DC link capacitor	1.9 mF	L_2	5 (mH)
Switching frequency	50 kHz	Switching frequency	10 (kHz)
Maximum input voltage	306.6 V	Utility frequency	50 (Hz)
Maximum input current	10.34 A	Grid voltage (RMS)	220 (V)
DC bus voltage	400 V	/	/

In this thesis we have adopted a co-simulation strategy, where, the physical system is implemented in Psim environment, while the control algorithms are implemented in Matlab/Simulink environment. Figure (4.25) shows the implemented Simulink model that includes the ABC-based MPPT algorithm, the PI controller for DC bus voltage regulation, the SOGI-PLL as synchronisation method, the developed deadbeat algorithm as a current controller and the OUV and OUF as protection mechanism.

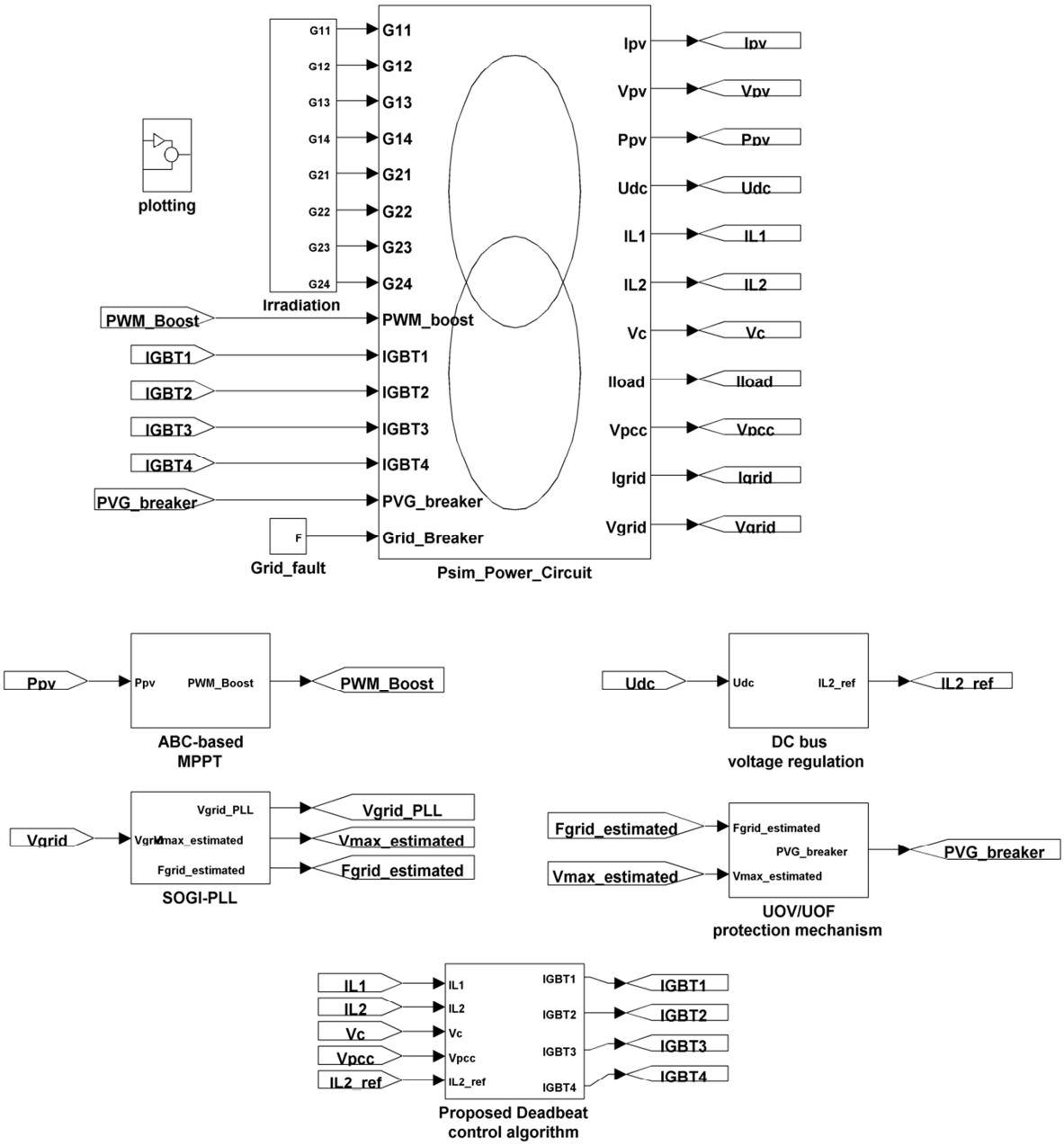

Figure 4.25: Implemented Simulink model.

The Psim schematic model, including the PV generator, the boost converter with the DC link capacitor, the full bridge single phase inverter, the output LCL filter, the local load and the utility grid, is given by figure (4.26).

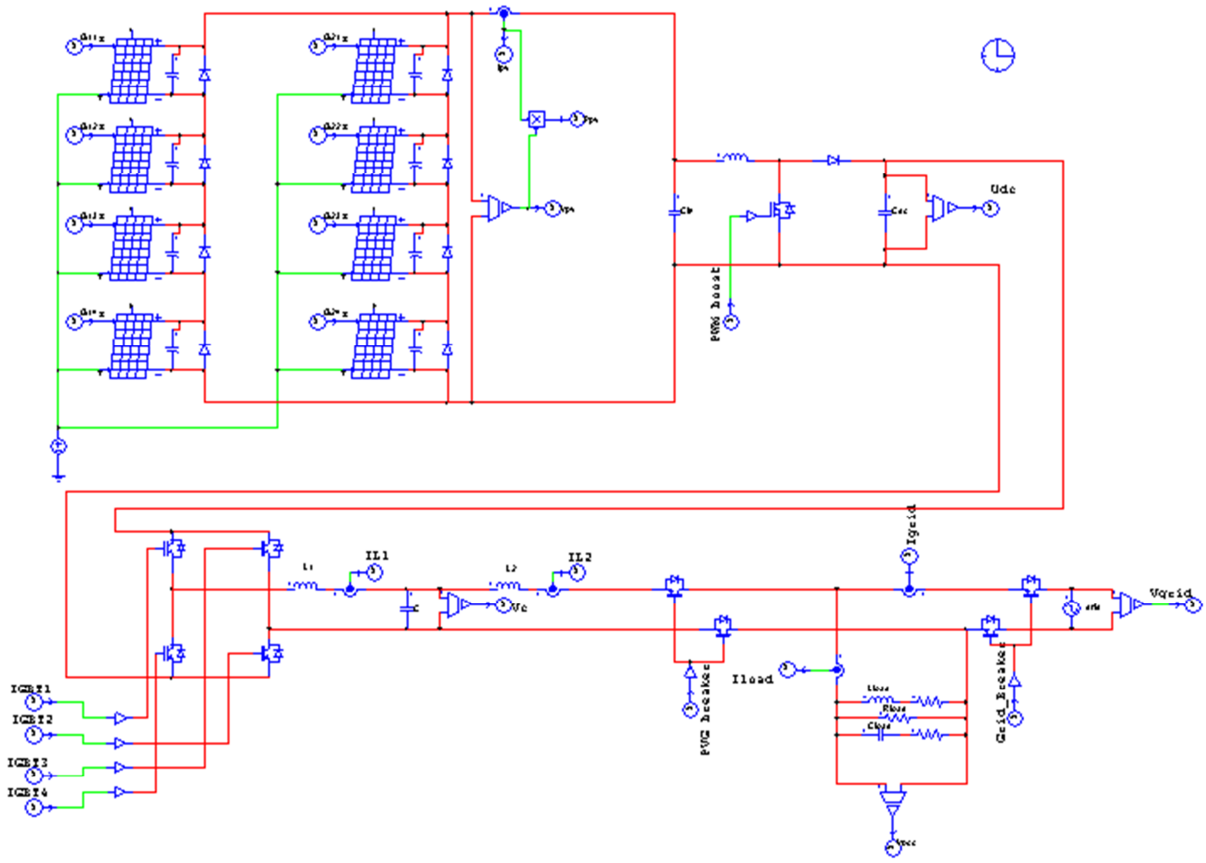

Figure 4.26: Psim schematic model.

Three tests have been carried out:

Test 1: Power flow

In this first test, we want to show the power flow (active and reactive power) flowing between the photovoltaic generator, the grid supply and the load. Given that the implemented inverter produce only active power and the reactive power required by the load is ensured by the grid, four power flow patterns can take place:

- The first case is shown in figure (4.26-a), in which the PV generator produces an active power higher than the active power consumed by the load. In this case, the rest of the power produced is exported to the grid.
- The second case is shown in figure (4.26-b), in which the PV generator produces only active power required by the load, so, in this case, no active power is exchanged between the system and the grid.

The inverter, the load and the grid current waveforms, and the active power contribution at the PCC node of the two first cases are shown in figure (4.27). We note here, that the positive power value reveals that the power is imported from the grid, and the negative one means that the power is exported to the grid.

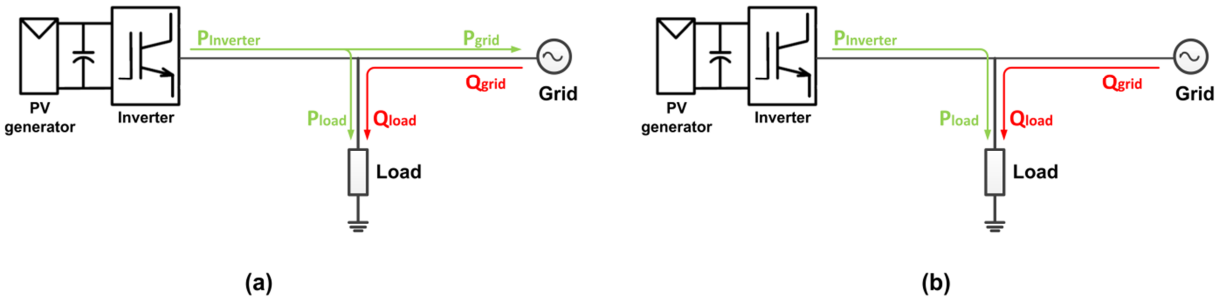

Figure 4.26: Powers flow in case: (a) The PVG exports active power to the load and grid, (b) The PVG produces only the active power required by the load.

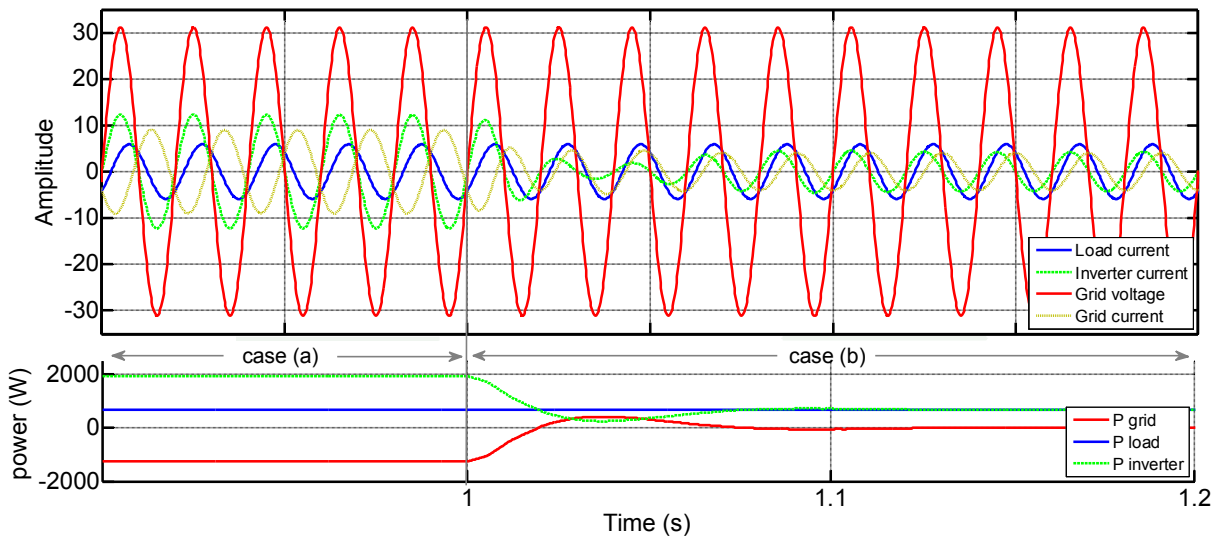

Figure 4.27: Inverter, load, and grid current waveforms and power contributions at PCC node for the case (a) and (b).

- The third case is shown in figure (4.28-c), in which the PV generator produces an active power lower than the active power consumed by the load. In this case, the power deficit is compensated by the grid.
- The latest case is shown in figure (4.28-d), in which the PV generator does not produce any power. In such case the grid supply the totality of the active and reactive power required by the load.

The inverter, the load and the grid current waveforms, and the active power contribution at the PCC node of the two latest cases are shown in figure (4.29).

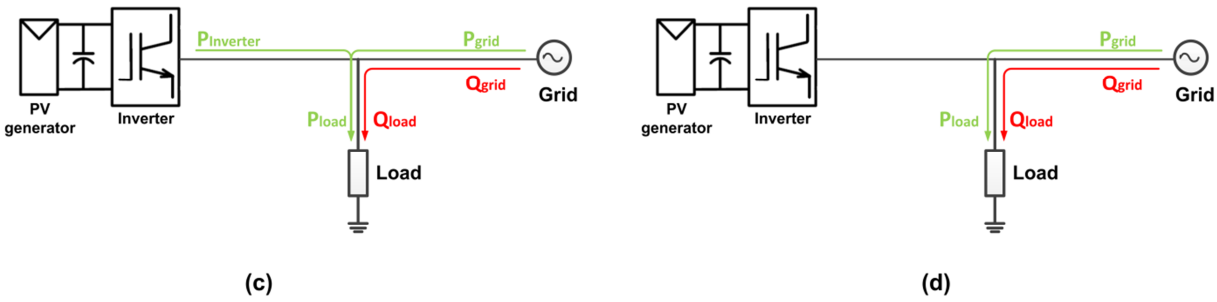

Figure 4.28: Powers flow in case: (a) The PVG produces a portion of the active power required by the load, (b) The PVG does not produce any power.

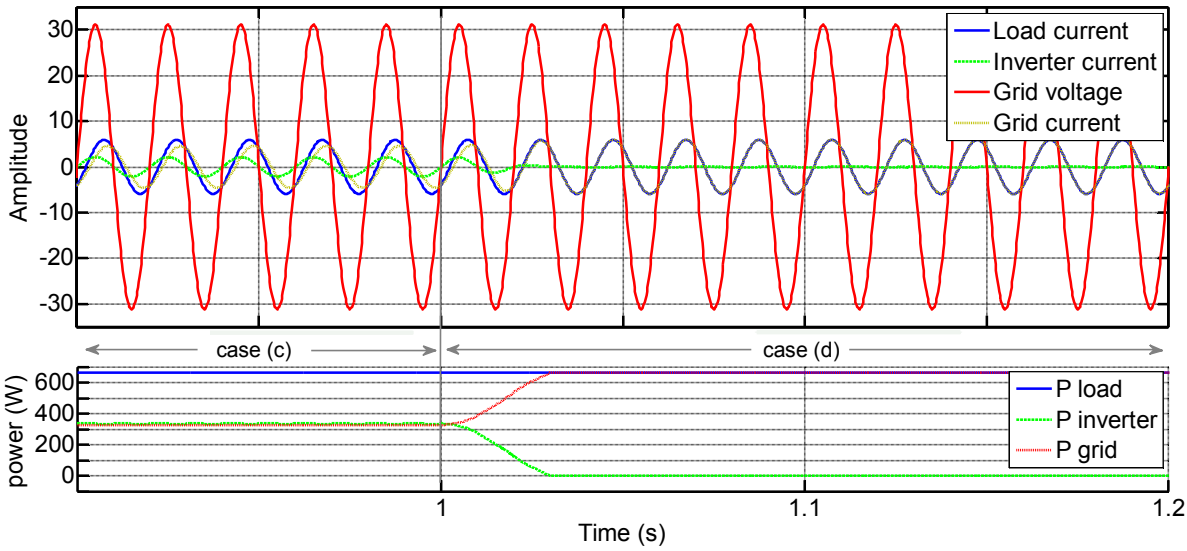

Figure 4.29: Inverter, load and grid current waveforms and power contributions at PCC node for the case (c) and (d).

Test 2: Maximum power point tracking

In the second test, we want to verify the ability of the proposed ABC-based MPPT to track the global MPP in grid connected system. To this end, a simulation study was carried out under uniform irradiation and transient shading patterns. *P-V* characteristics of the PV generator for uniform irradiation and the considered partial shading are shown in figure (4.30) with SP1 and SP2, respectively.

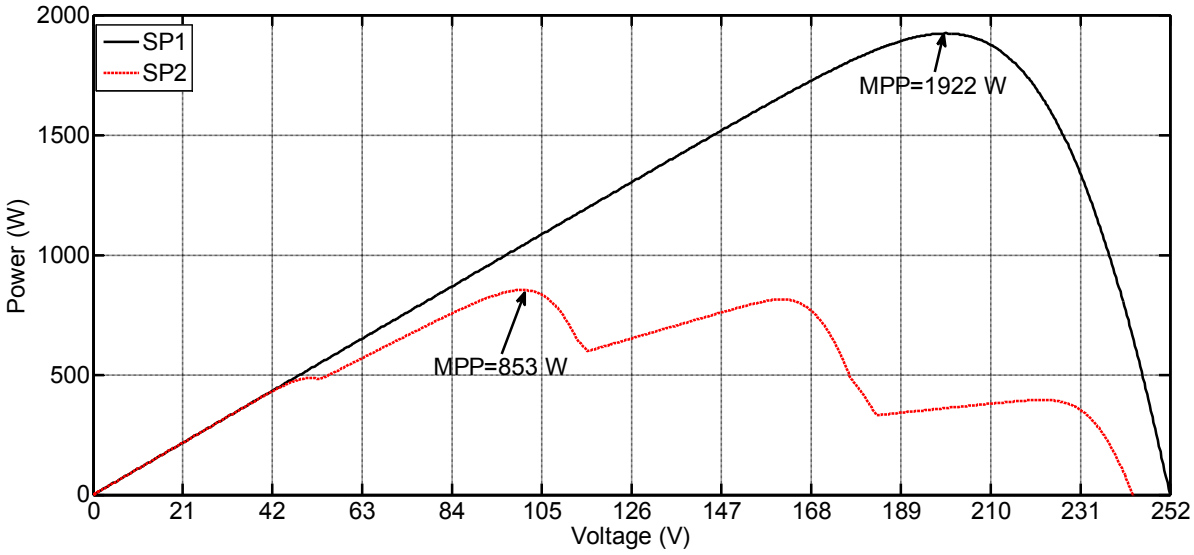

Figure 4.30: Shading patterns.

In this test the photovoltaic generator works under uniform irradiation condition until a partial shade occur at *t=20s*. Time evolution of the PVG power and the duty cycle of the boost converter show the MPP tracking capability. The obtained results (figure (4.31)) clearly show the convergence of the process search guided by the ABC-based MPPT algorithm toward the global maximum power point in both conditions (uniform and shaded patterns). Transit and steady state behaviour of the inverter current are shown in figure (4.32).

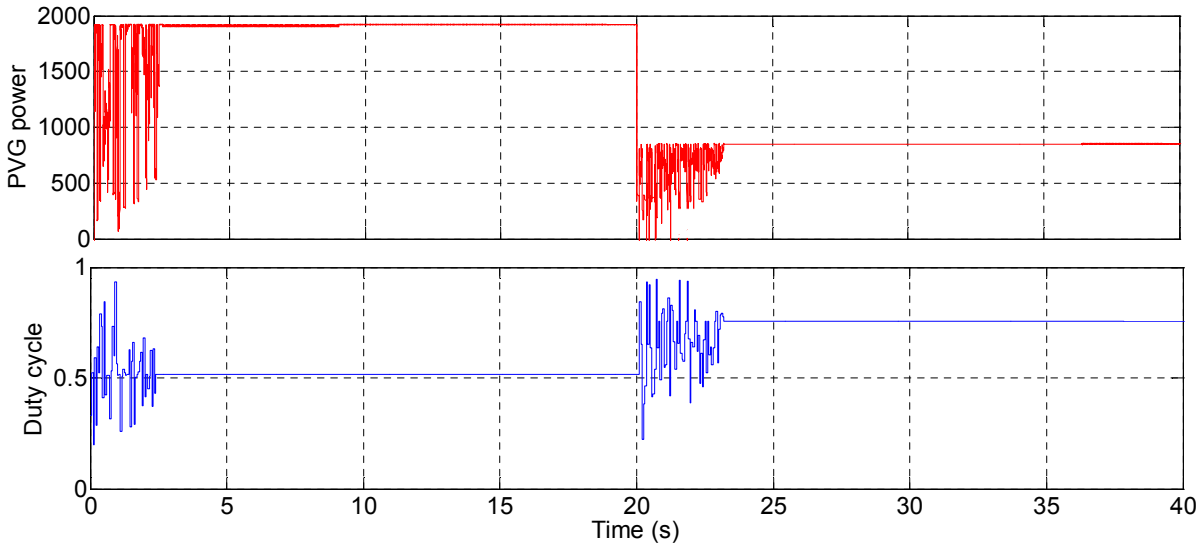

Figure 4.31: Maximum power point tracking.

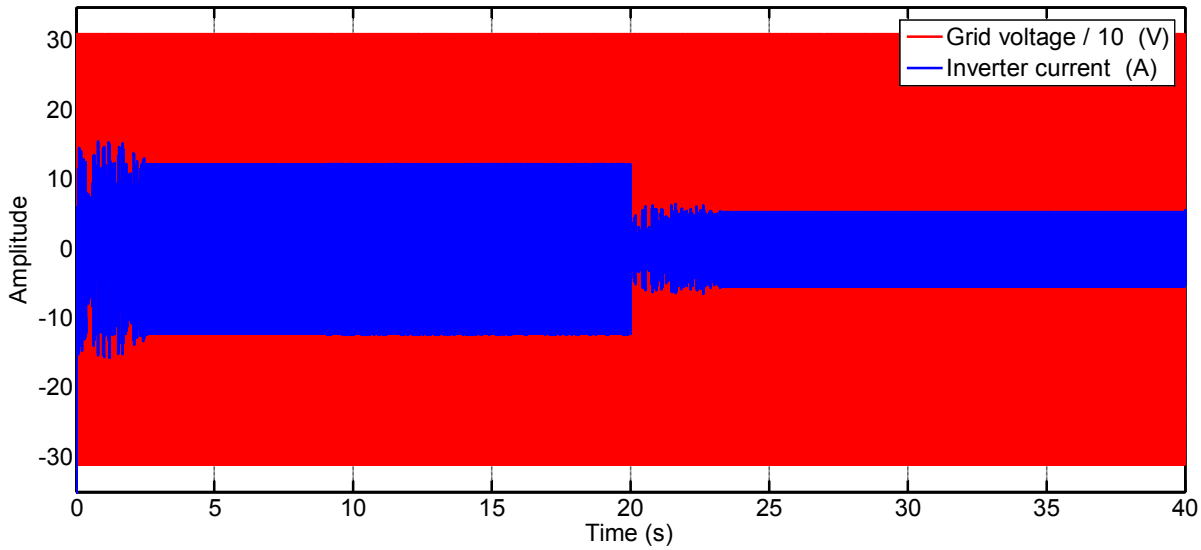

Figure 4.32: Grid voltage and inverter current waveforms.

Actually, the transit operation of the current inverter amplitude does not affect the load current, which continue to receive a clean waveform current as the difference is compensated by the grid. This is clearly shown in figure (4.33) and (4.34).

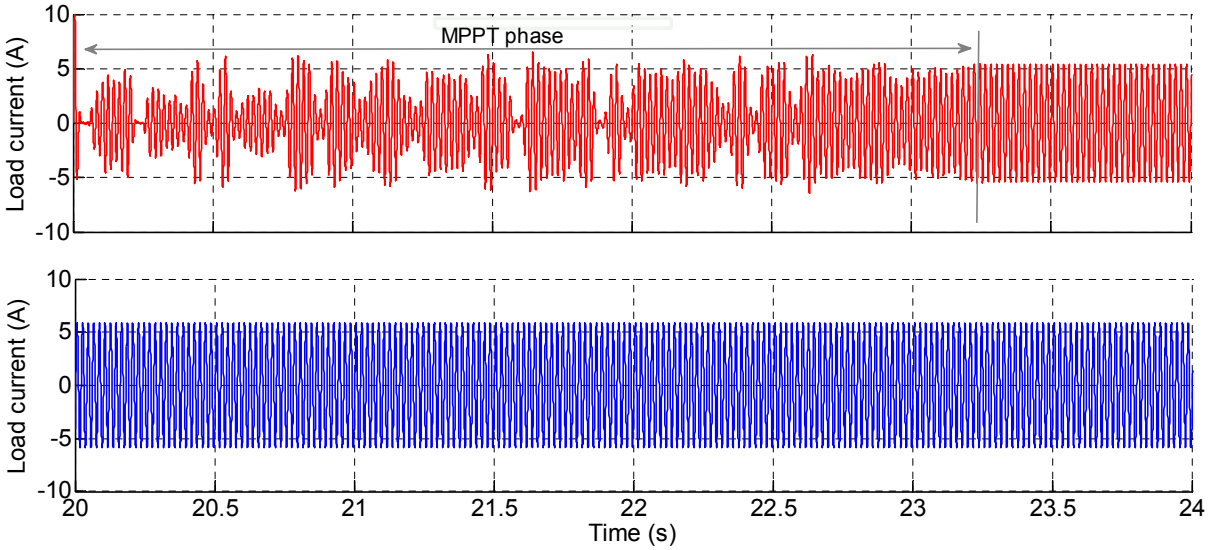

Figure 4.33: Inverter and load current in MPP search phase.

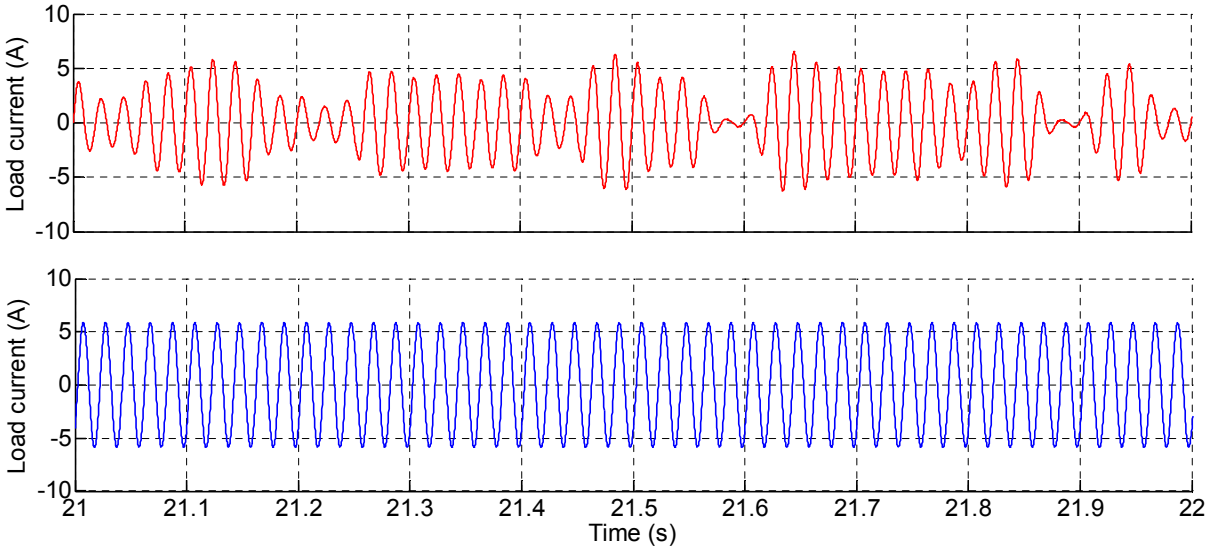

Figure 4.34: Zoom of figure (4.33).

Steady state behaviour of the inverter current shown in figure (4.35), demonstrates the expected control performance of the overall control scheme. It can be observed that the waveform of the injected current is clearly sinusoidal and in phase with the grid voltage.

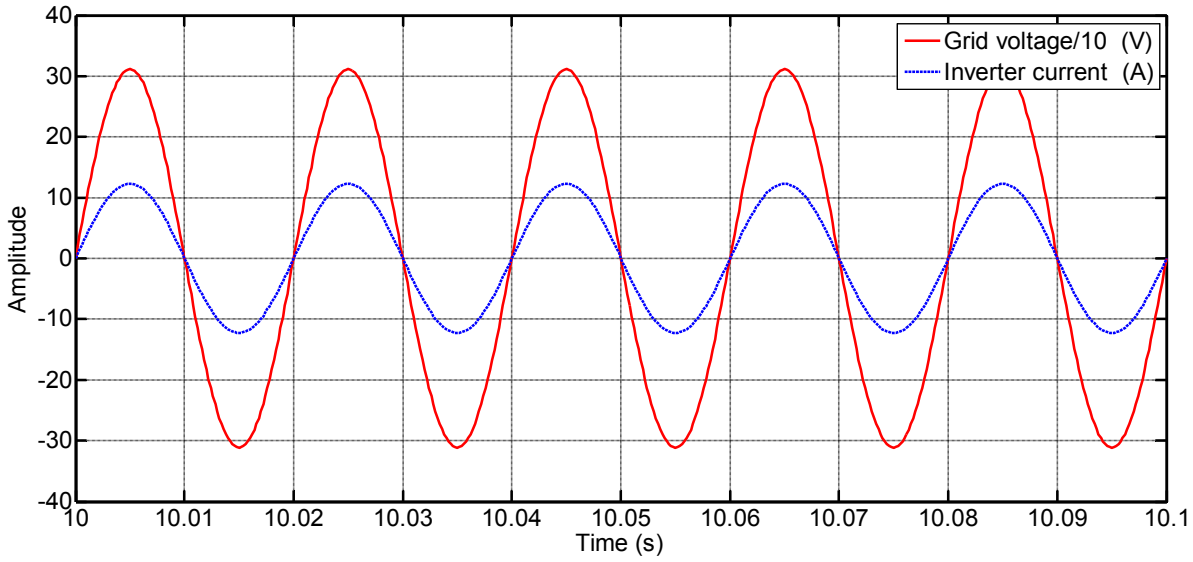

Figure 4.34: Grid voltage and inverter current in normal operating conditions.

Figure (4.35) shows the regulated DC bus voltage. It can be observed that the DC bus voltage is significantly regulated at 400 V even in maximum power point search phases, which shows the robustness of the implemented PI controller.

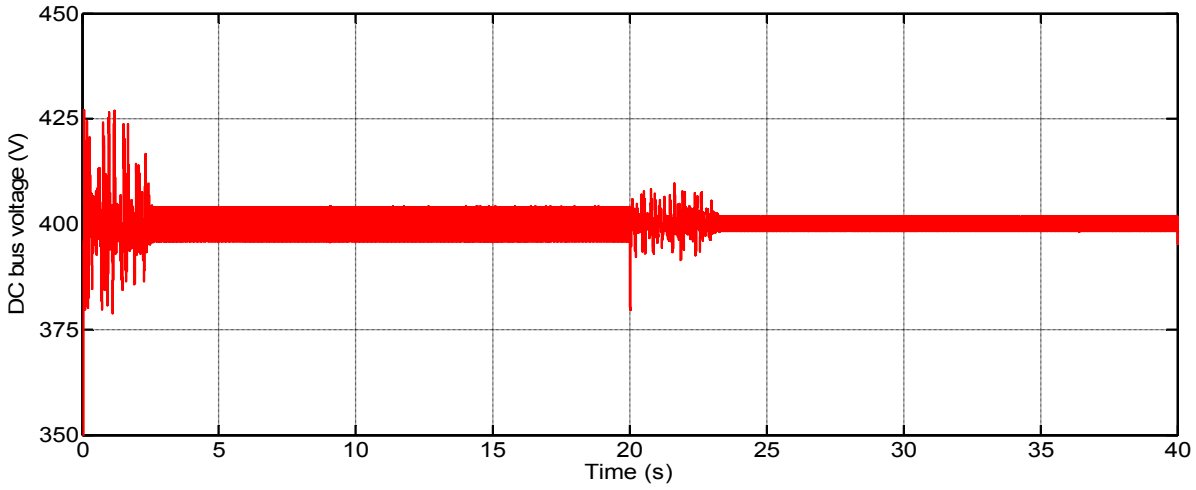

Figure 4.35: DC bus voltage.

Test 3: Protection mechanism

In the latest test, we want to verify the effectiveness of the adopted protection mechanism. To this end, a simulation study, in which the grid utility is lost at *t=40s* and returned at *t = 45s,* was carried out.

Figures (4.36) and (4.37) show the intervention of the protection system when the grid utility is lost at t = 40s. The protection mechanism instantly detects the change in voltage and frequency, then after 0.2s the protection mechanism isolates the PV generator as expected. When the utility grid comeback at t = 45s, the system reconnect the GPV after 5s (noting that the standard requires 5 minutes to reconnect).

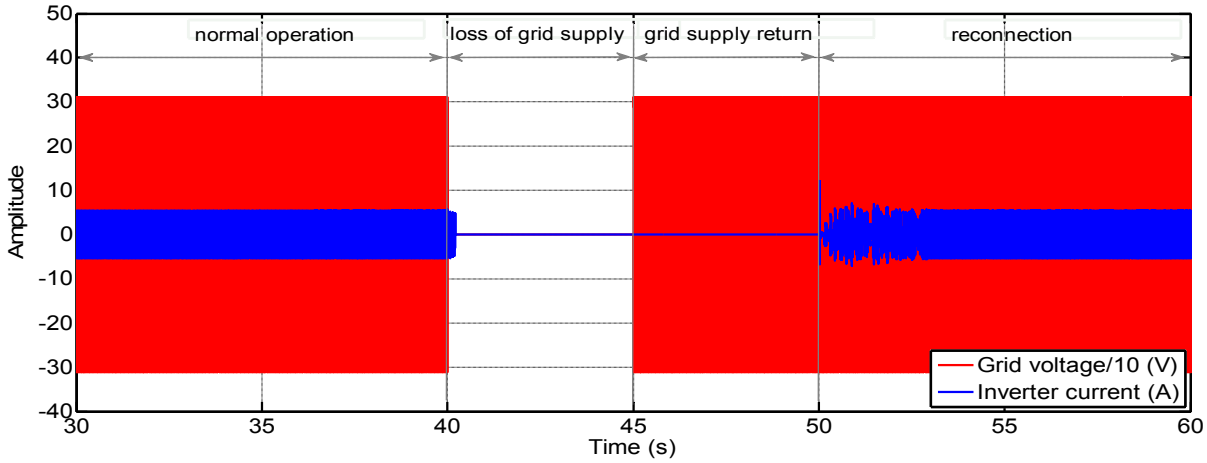

Figure 4.36: Islanding detection.

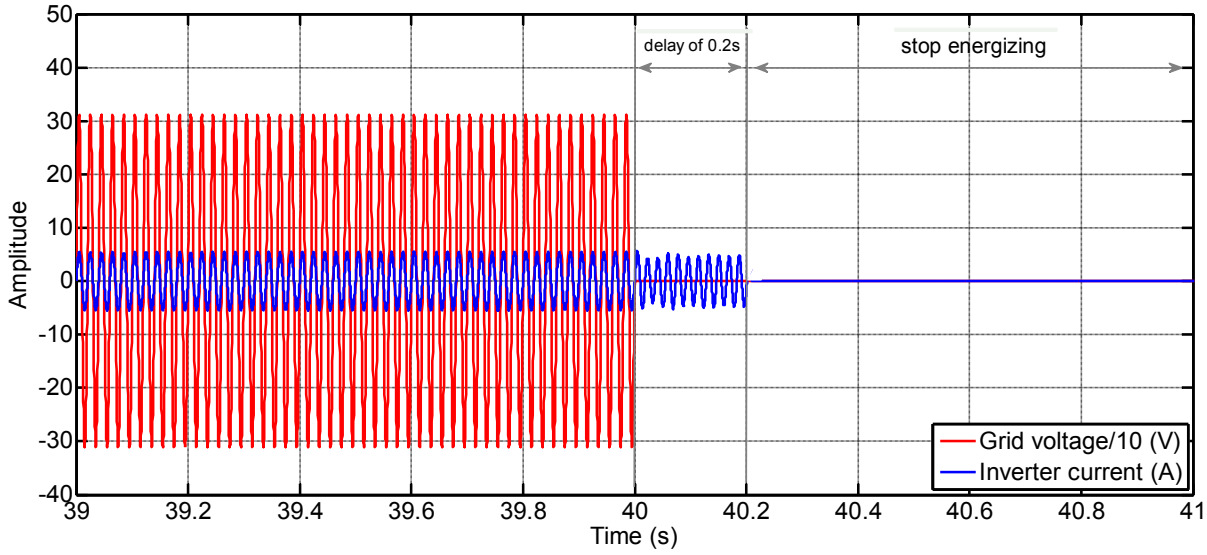

Figure 4.37: Zoom of figure (4.36).

4.6. Conclusion:

To assess the effectiveness of the proposed ABC-based MPPT and the prediction-based deadbeat control techniques in grid connected system, a complete computer simulation of the overall grid connected PV system has been carried out. The grid interconnected photovoltaic system performance was investigated and analysed under variable environmental conditions and grid loss. The obtained results have shown the interaction between the different components of the grid connected PV system and demonstrate the satisfactory performance of the proposed control schemes.

CHAPTER 5

EXPERIMENTAL VERIFICATION OF THE DEVELOPED MPPT TECHNIQUES

5.1. Introduction:

In this chapter, the experimental results of the developed MPPT techniques are given. The test bench composed of PV modules, two parallel mounted Boost converters, current and voltage measurement boards, a resistive load, a DSP board and a personnel computer is used. First, the design details of this test bench are given, and then the results of the proposed ABC-based MPPT techniques, introduced in chapter 2, are presented for different work conditions.

5.2. Test bench:

5.2.1. Test bench configuration:

The block diagram of the used test bench is shown in figure (5.1).

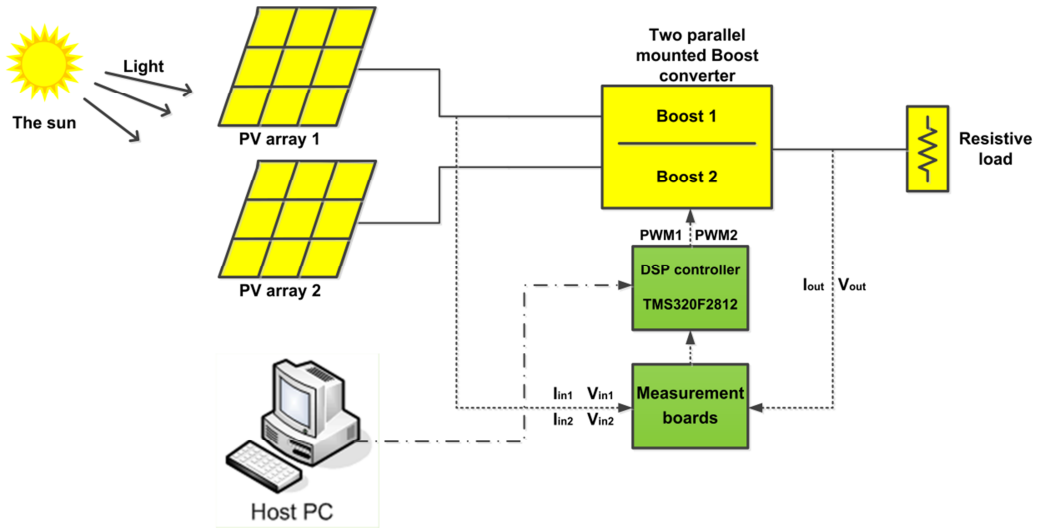

Figure 5.1: Test bench block diagram.

The yellow blocks indicate the part of the test bench where the actual power transfer is happening, from the PV generator, through the converters, to the resistive load. The green blocks indicate the control part (digital part) of the test bench, which allow collecting the required values from the power circuits and generates the PWM signals sent to the converters to control the power transfer.

In fact, the realized test bench involves two photovoltaic systems; each system consists of a PV generator of 160 w and a DC/DC boost converter. The two systems are parallel mounted on a resistive load and controlled by a DSP board. With such configuration, both developed MPPT techniques (ABC-based one-dimensional and multidimensional MPPT techniques) can be tested; this is made possible by omitting one system in case of one-dimensional MPPT technique test.

5.2.2. Test bench components:

5.2.2.1. PV generator:

In the test bench, the PV generator consists of two separate strings of two PV modules (BP SX80) each one. Thus, two PV systems can be formed, by connecting each string to a DC/DC boost converter.

Figure (5.2) shows the real used PV generator with an artificial shade made with sheets.

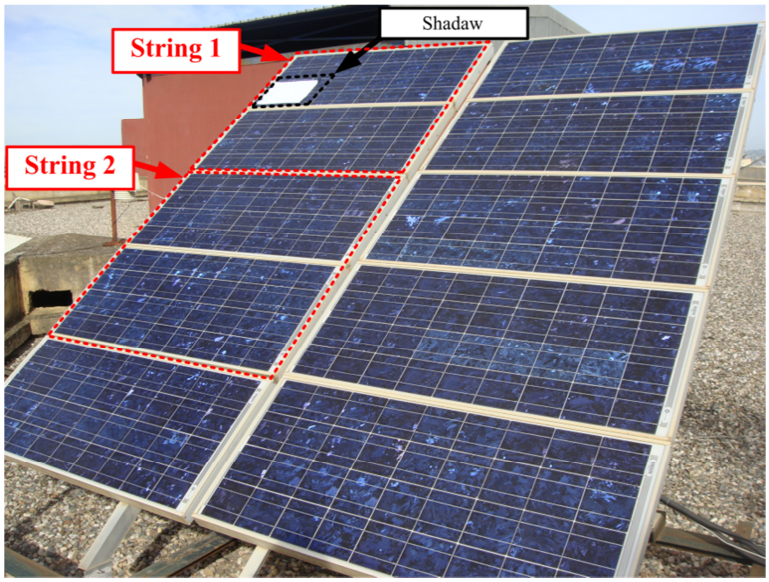

Figure 5.2: Real PV generator with an artificial shade.

5.2.2.2. Boost converters circuit:

The block diagram of the realized Boost converters circuit is shown in figure (5.3), it involves two Boost converters and an optical isolation stage for each converter.

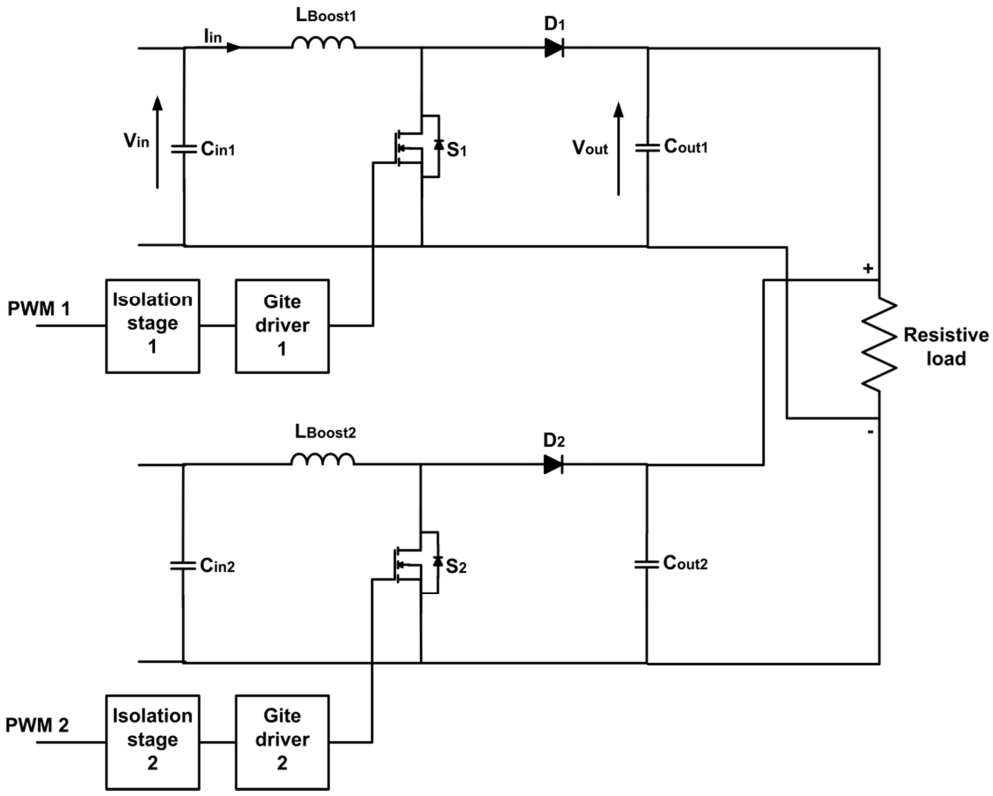

Figure 5.3: Block diagram of the realized Boost converters circuit.

Next to the modelling and the rating procedure of the used Boost converters given in appendix (D) and summarized in table 2.2, the converters components have been chosen as follow:

a) Inductors selection:

As is well known, with less value of inductance there is more current ripple. A large value of inductance will reduce the current ripple and the discontinuous current mode will be surely avoided. However, using a high value of inductor will be associated with high inductor resistance (L_r), large size and high cost.

According to the calculations made in appendix (D), the minimum required inductance value is 1.7 mH. So, the inductor of 2 mH is chosen.

Moreover, the selected inductor must bear the RMS current (I_{Lrms}) flows through it without saturating. The RMS current flows through the inductor is given by [182]:

$$I_{Lrms} = \frac{2}{\sqrt{3}} Iin \tag{5.1}$$

With a maximum input current of ($L_{in\_\max} = 5.17\,A$), the selected inductor must bear an RMS current of ($I_{Lrms} = 6\,A$).

Finally, we have opted for the inductor (**6001163A00**), shown in figure (5.4). It has a low resistance inductor ($L_r = 0.3\ ohm$), inductance value of ($L = 1mH$) and an RMS current up until ($I_{Lrms} = 7\,A$). Due to the component availability, two **6001163A00** inductors were connected in series to give a total required inductor value ($L = 2mH$ with $L_r = 0.6ohm$).

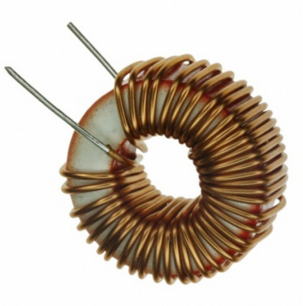

Figure 5.4: Chosen inductors for converters.

b) Switching devises selection:

Choosing the right switch is an important part in power electronic devices, so less power losses is required. IGBT and MOSFET can both be used as the main switch in the boost converter, but if consideration is given to the main characteristics of the switch: maximum current, maximum voltage and maximum frequency. The MOSFET switch is used in the boost converters; it has a moderate cost, low switching losses and does not need complex operations. There is a wide variety of power MOSFET switches. We can choose the most suitable for the system's needs by looking at the rate of the current and the voltage, because:

$$I_{Mosfet\_rms} = \frac{2}{\sqrt{3}} I_{in}$$
$$V_{Mosfet} = V_{out} \qquad (5.2)$$

and also by looking at low losses of the MOSFET switch; the static drain-source on resistance (R_{ds_on}) must be low enough to minimize conduction loss. The used power Mosfet switch, that meets the above-mentioned requirements, is the component IRF640.

However, a pulse-width-modulation controller cannot provide the output current required to drive the gate capacitance of the MOSFET and a gate driver is

required. A gate driver is a power amplifier that accepts a low-power input from a controller and produces a high-current drive input for the gate of a high-power transistor. In this work the commercial MOSFET gate driver (IR2110) is used, with independent high and low side referenced output channels. The output driver features a high pulse current buffer stage designed for minimum driver cross-conduction. Propagation delays are matched to simplify its use in high frequency applications. We note that, only the low side output is being used to drive one boost converter's MOSFET. So, two MOSFET gate driver (IR2110) are used in the Boost converters circuit.

Figure (5.5) shows the circuit diagram for the IR2110 using as a single low-side driver.

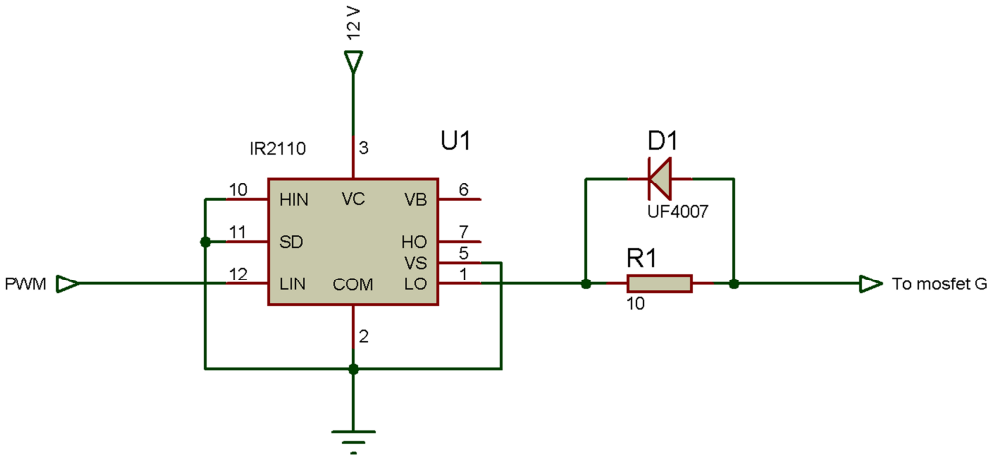

Figure 5.5: Using the IR2110 as a single low-side driver.

c) Diodes selection:

The diode is a semiconductor device that is controlled by its own voltage and current. When a diode is forward biased, it starts to conduct with a small forward voltage (V_F) across it. When the diode is reverse biased it stays in the off state. The diode can also contain a series Resistance-Capacitor Snubber circuit that can be connected in parallel with the diode device, however in this work the Snubber circuit of the diode is neglected to avoid losses. The diode selection is based on the average forward current ($I_{F(AV)}$) and the repetitive peak reverse voltage (V_{RRV}), because [182]:

$$I_{diode\_rms} = \frac{2}{\sqrt{3}} I_{in}$$
$$V_{diode} = V_{out} \quad (5.3)$$

where, the maximum values of input current and output voltage of the boost converter are:

$$I_{in\_\max} = 5.17A$$
$$V_{out\_\max} = 126.5V \quad (5.4)$$

To minimize losses the reverse recovery time (T_{rr}) and forward voltage (V_F) should be as low as possible [183]. Thus, the selected diode is the component STTH3010w (figure (5.6)). It has a large average forward current ($I_{F(AV)} = 30A$), a large repetitive peak reverse voltage ($V_{RRV} = 1000V$), a low forward voltage ($V_F = 0.895V$) and a very good reverse recovery time ($T_{rr} = 32ns$).

Figure 5.6: Chosen diode for converters.

d) Input capacitors selection:

The minimum value for the input capacitors, calculated in the appendix (D), is $C_{in\_\min} = 6.25uF$, and they have to bear a maximum voltage of $V_{in\_\max} = 51.1\ V$. This minimum value is necessary to stabilize the input voltage due to the peak current requirement of switching power supply. The chosen input capacitor (MCLPR400V227M26X40), shown in figure (5.7), has a value of 220μF and a maximum voltage of 400V.

Figure 5.7: Chosen capacitor for converters.

e) Output capacitors selection:

The output filter capacitors are mainly used to meet the output voltage ripple and converter stability requirement. The output capacitors supply the entire load current during the time when the switch is on.

The minimum value for the output capacitors, calculated in the appendix (D), is $C_{out\_\min} = 47.5uF$, and they have to bear a maximum voltage of $V_{out\_\max} = 126.5\ V$. So, we have chosen the same model (MCLPR400V227M26X40) as in the input capacitors.

f) Optical isolation stage design:

Since the DSP is very sensitive to any kind of external disturbances (eg, high voltages or currents caused by instability or error in the system), it is necessary to use an optical isolation stage to isolate the DSP from the high power circuit. The opto-isolator (PC817) and its circuit diagram, shown in figure 5.8, is used.

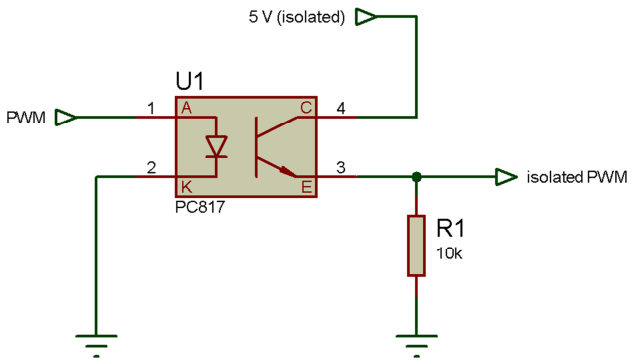

Figure 5.8: PC817 Optoisolator circuit diagram.

On the other hand, the used DSP (TMS320F2812) have PWM outputs of 3.3V referenced to GND. So, they are very sensitive to the noise errors. To solve this

noise problem, differential signals must be used. For this purpose, the used PWM outputs are converted into differential signals by means of an integrated differential line driver circuit (AM26LS31) before going to the opto-isolators.

Thus, the optical isolation stage has two purposes: the first one is the noise rejection and the second one is the galvanic isolation. The circuit diagram of the optical isolation stage is given in figure 5.9.

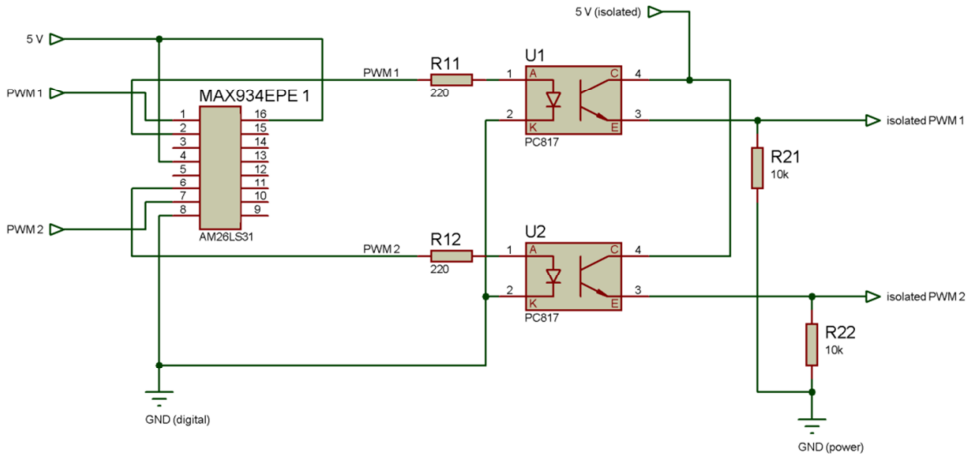

Figure 5.9: Circuit diagram of the optical isolation stage.

The circuit diagram of the complete Boost converters is shown in figure (5.10).

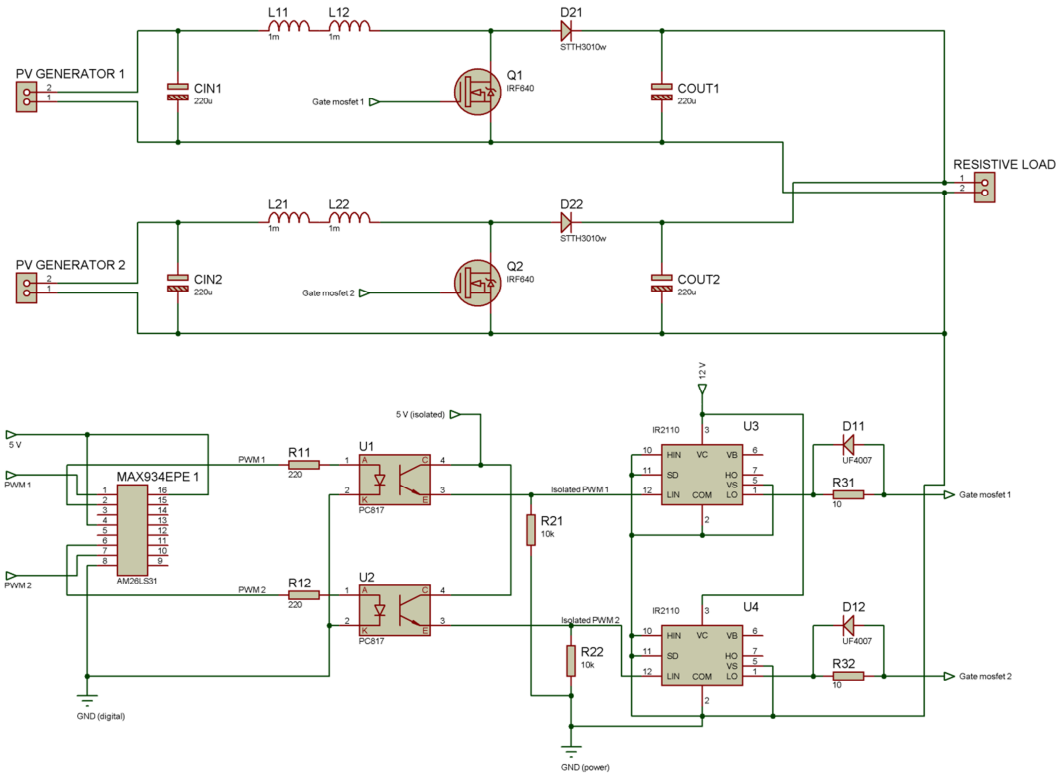

Figure 5.10: Circuit diagram of the complete Boost converters circuit.

5.2.2.3. Current and voltage measurement interface cards:

The measurement interface cards, as the name suggests, are the interface between various current and voltage signals used for control purposes and the DSP. The inputs of the ADC of the DSP controller chosen for this application are limited to 0 to 3 V. Therefore the power signals have to be scaled and conditioned appropriately to generate unipolar signals of magnitude variation between (0 to 3V).

The chosen control schemes require one DC voltage measurement channel and one DC current measurement channel. But, for more flexibility in data collection, boards with several measurement channels: two channels in the voltage measurement interface card and four channels in the current measurement interface card are realized.

a) Voltage measurement interface card:

The different stages involved in the design of each channel of the voltage measurement interface card can be seen in figure (5.11). The purpose of each stage is explained below in detail.

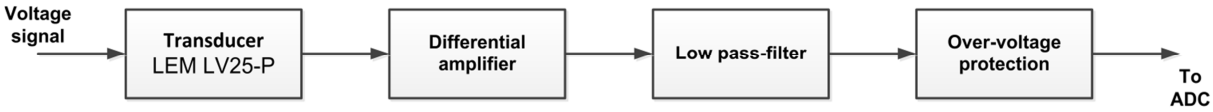

Figure 5.11: Stages of the voltage measurement interface circuit.

- *Transducer*:

The transducer LEM LV25-P shown in figure (5.12) is used. The measurement is based on the hall-effect. Thus, it provides galvanic isolation between the high voltage side and the measurement side.It is connected in parallel and the desired measurement range is set by choosing resistor values on its input (R_1). The resistor should be set so that 10mA is passed into the device at the nominal voltage. The current is then converted with a conversion ratio of 2500:1000, a 10mA current into the terminal corresponds to a 25mA current on the output terminal [184]. Further, the resistor (R_M) should be chosen so that the voltage induced in the secondary circuit does not exceed the maximum 3V, the allowed voltage on the DSP board inputs.

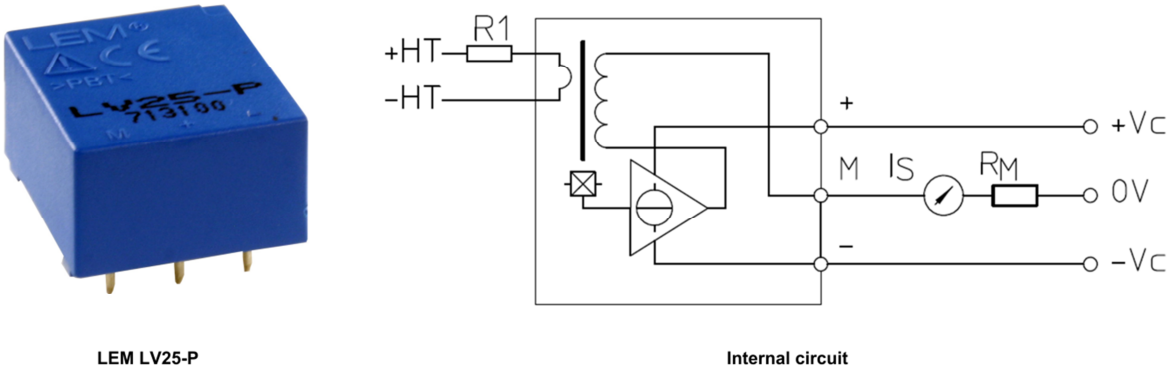

Figure 5.12: Voltage transducer.

- *Differential amplifier:*

The difference of the signals (positive and negative) is amplified at this stage. The Common Mode Rejection (CMR) property of this stage helps to reduce the incoming noise and offers better signal to noise ratio at the output [185]. The circuit diagram of the differential amplifier with a gain of 2 is shown in figure below.

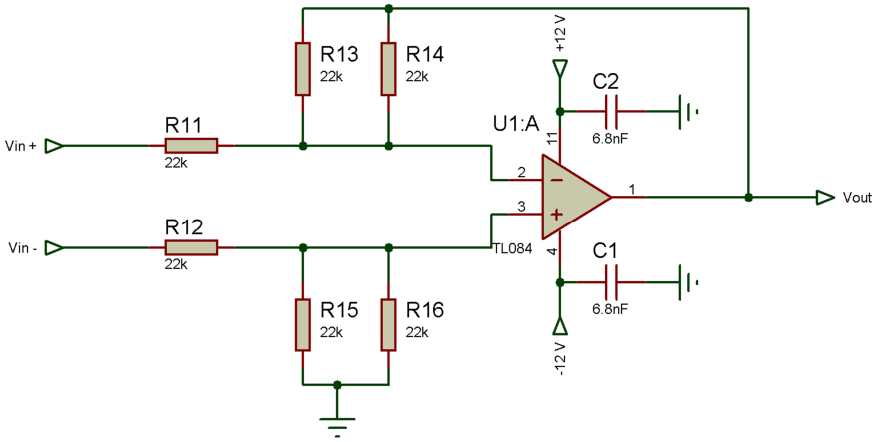

Figure 5.13: Differential amplifier circuit diagram.

- *Low-pass filter:*

The low pass filter stage is applied to remove the high frequency noise coupled to the current and voltage signals. Ideally the cut-off frequency of this filter must be half the sampling frequency of the ADC in order to filter the frequency components, which can cause aliasing effect.

In the present work, a third order Butterworth filter is designed for voltage measurement channels, with a cutoff frequency of 100 kHz. The circuit is built using TL084 operational amplifiers. The last RC stage of the third low pass filter is

placed close to the ADC input point to remove high frequency noise that might have been coupled with the signal.

The circuit diagram of the low-pass filter stage with a gain of 0.5 is shown in figure below.

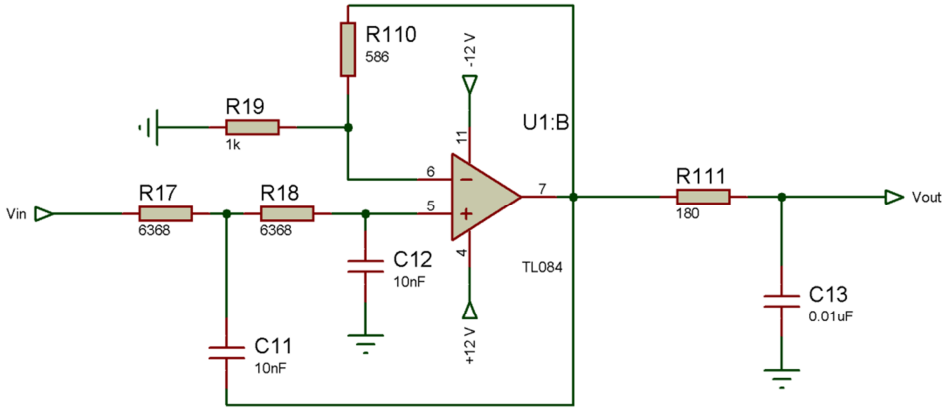

Figure 5.14: Low-pass filter stage circuit diagram.

- *Over-voltage protection:*

The ADC of the DSP is very sensitive to voltage input other than the specified level (0-3 V). For the protection purpose, it is necessary to add a voltage clamping stage at the input of the ADC. A transistor (BC178), a resistor and a zener diode (BAT85) based protection circuit is built as the last stage of each measurement channel, which prevents the voltage at the output of the card from exceeding 3 V. Figure (5.15) shows the circuit diagram of the over-voltage protection stage.

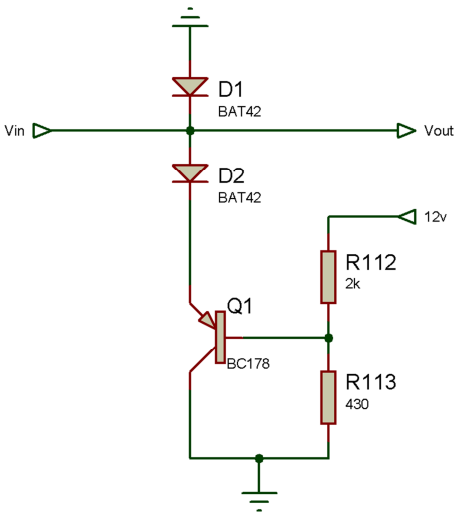

Figure 5.15: Over-voltage protection stage circuit diagram.

The circuit diagram of one voltage measurement channel is shown in Figure (5.16).

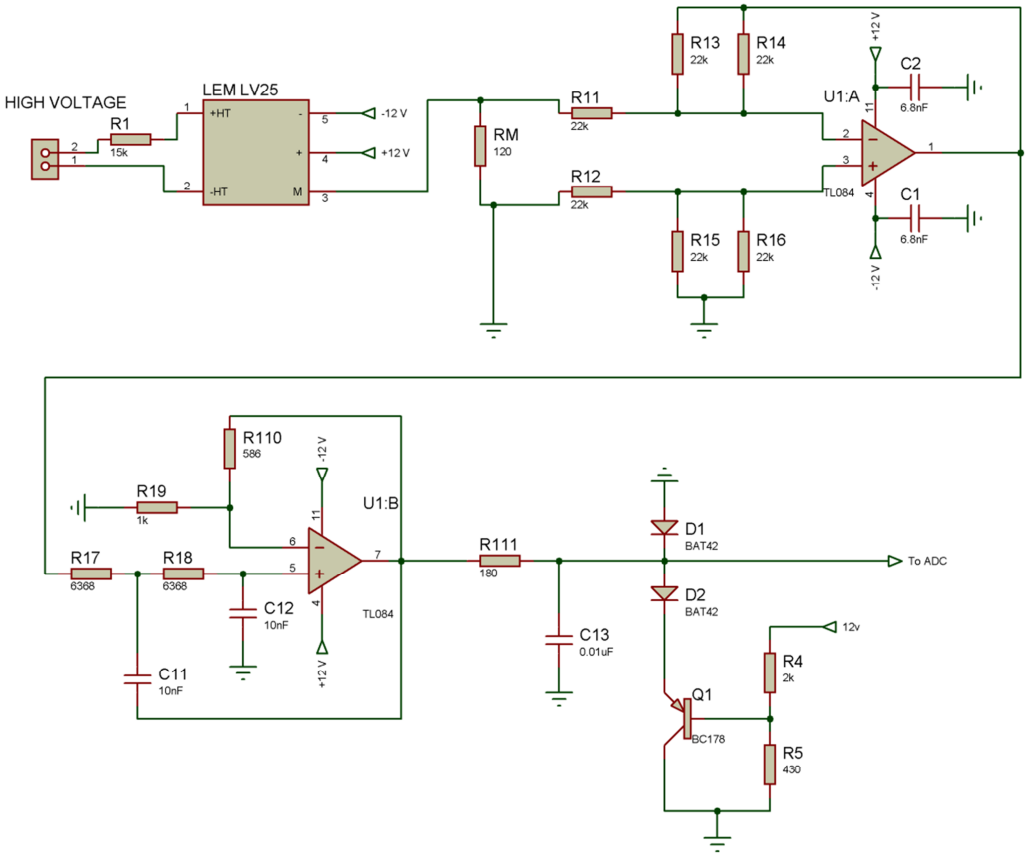

Figure 5.16: Circuit diagram of one voltage measurement channel.

b) Current measurement interface card:

The current measurement interface card involves four channels based on high precision Hall-effect sensors.

The sensor (ACS714) is a hall effect-based linear current sensor which operates between 4.5 - 5.5 V. It has a bidirectional current input which ranges from -5 to 5 A. The sensor will output an analog voltage which is linearly proportional to the input current. When Vcc is 5V, the output voltage is centred at 2.5 V with a sensitivity of 0.185 V/A. When there is a positive current, it will increase the output voltage and vice versa. In addition, the ACS714 contains an internal resistor, a FILTER pin connection to the printed circuit board, and an internal buffer amplifier. With this circuit architecture, a simple RC filter via the addition of a capacitor (CF) from the FILTER pin to ground can be implemented. The buffer amplifier inside of

the ACS714 (located after the internal resistor and FILTER pin connection) eliminates the attenuation caused by the resistive divider effect. Therefore, the ACS714 device is ideal for use in high-accuracy applications that cannot afford the signal attenuation associated with the use of an external RC low-pass filter.

In the realised current measurement board, each current sensor is passed through a voltage divider to convert its maximal output voltage (3.425 V) to a suitable value (3 V). The filter capacitors (C_F) of 100nF are chosen to obtain a maximum noise of 50mA with a maximum rise time of 291µs. Finally, the same Over-voltage protection stage used in the voltage measurement interface board is also used at the enf of each current measurement channel.

The schematic of one current measurement channel is shown in figure 5.17.

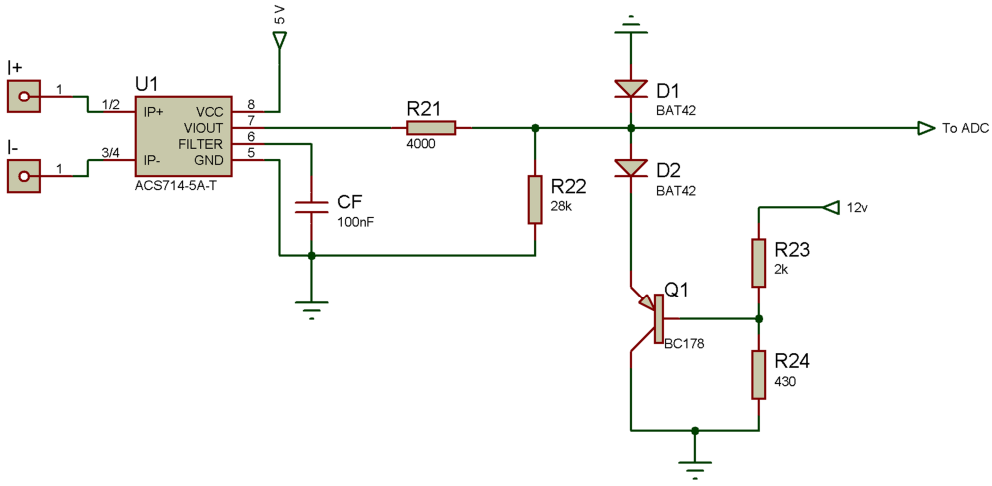

Figure 5.17: Current Measuring channel.

5.2.2.4. Controller:

The DSP board eZdsp TMS320F2812 (figure (5.18)) of Texas Instrument is used to implement and execute the control algorithms. The F2812 DSP is a high performance 32-bit fixed-point DSP. It is a member of the TMS320C28xx DSP generation, which is designed to meet a wide range of applications, such as digital motor control, digital power supply and other embedded control systems. The F2812 DSP is able to generate 16 PWM signals and is equipped with many on-chip peripherals including ADCs, which makes it suitable for control of the PV system.

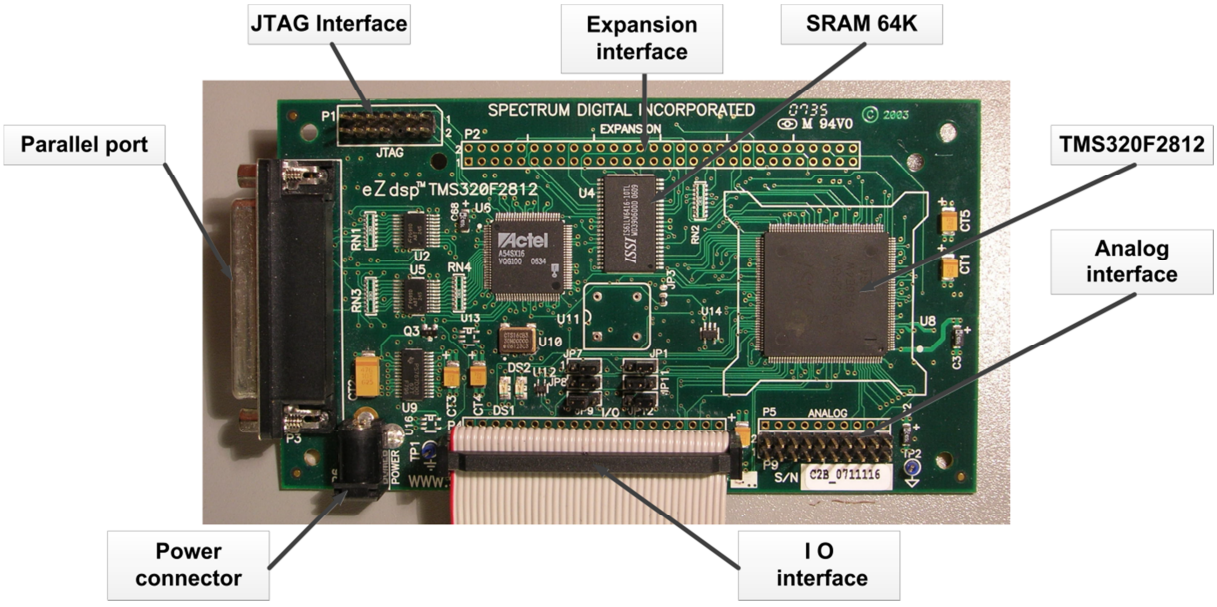

Figure 5.18: DSP board.

5.3. Experimental results:

Both ABC and PSO-based MPPT control programs are developed in a C++ environment and each control algorithm is implemented, using the DSP board, as a timer-interrupt driven routine. A control period of 0.05s is used and the control parameters are set exactly as in the simulation tests.

Figure (5.19) shows the used test bench.

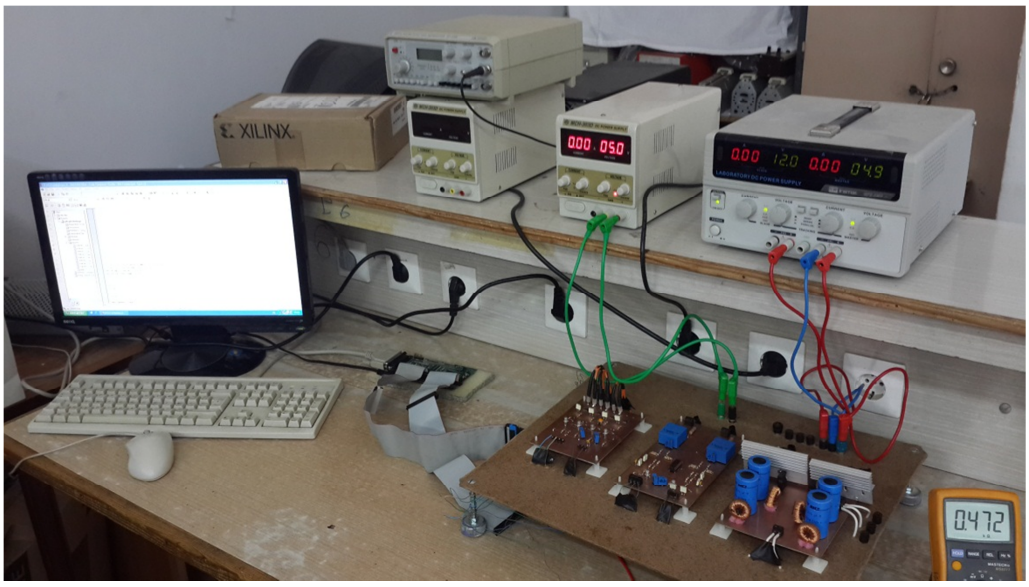

Figure 5.19: Test bench.

5.3.1 ABC-based MPPT for a single photovoltaic array:

To experimentally assess the performance of the proposed ABC-based MPPT a photovoltaic system, that consists of one string of 160 w and is connected to a resistive load via a DC/DC boost converter, is used (the second PV system from the test bench is omitted). The real-time test measurements are performed for the following cases:

a) test of the algorithm tracking capabilities for various shading patterns,

b) comparison between the proposed MPPT and the PSO based approach.

5.3.1.1. Power tracking with various shading patterns:

Two tests are performed to highlight the proposed algorithm ability to track the global maximum power point in both cases static and dynamic.

In the first experiment, the I–V and P–V curves are recorded when the PV array is subject to uniform irradiance conditions. These characteristics are shown in figures (5.20-a) and (5.20-b), respectively. According to these figures, the corresponding voltage and current of the MPP are 23.8 V and 3.66 A. The corresponding dynamic responses of the voltage and the current of the PV array are given in figure (5.21). It can be seen that the generated voltage and current in figure (5.21) are around 23.5 V and 3.6 A, presenting a good agreement with results shown in figures (5.20).This result shows the good operating of the proposed MPPT algorithm under uniform insolation conditions.

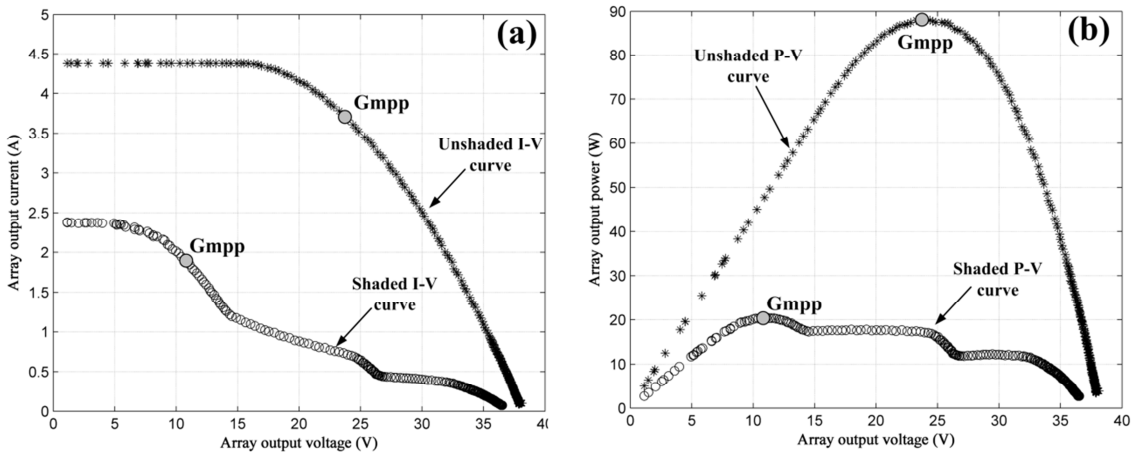

Figure 5.20: I–V and P-V curves of the PV array under uniform insolation and partial shaded conditions.

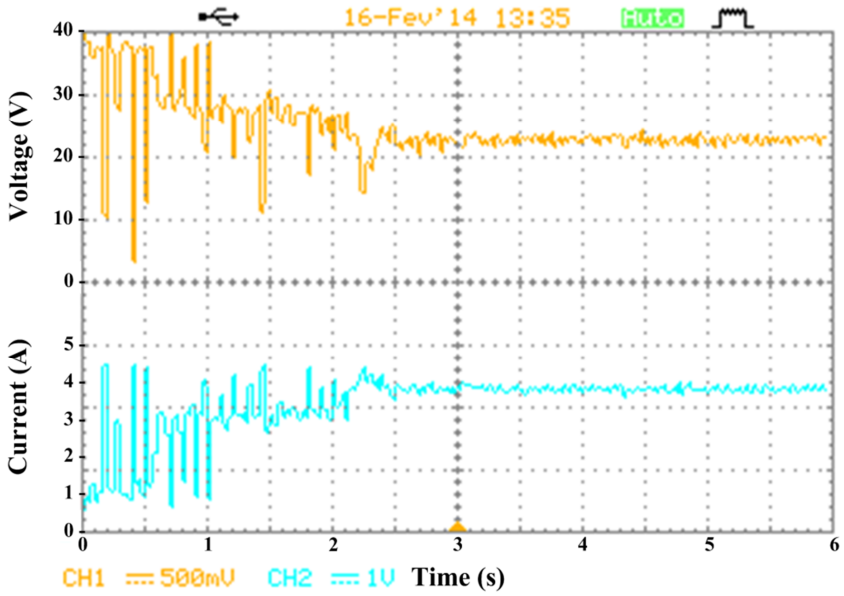

Figure 5.21: Corresponding array voltage, and current waveforms under uniform insolation condition.

In the second experiment, the PV array operates under uniform insolation condition until the instant 6 s when a part of the PV array is intentionally shadowed as shown in figure (5.2). The new recorded *I–V* and *P–V* curves are shown in figure (5.20). The behaviour of the MPPT algorithm before and during the partial shadow is shown in figure (5.22). As it can be seen in this figure, the generated PV power is around 20 W, which is the maximum achievable power according to figure (5.20).

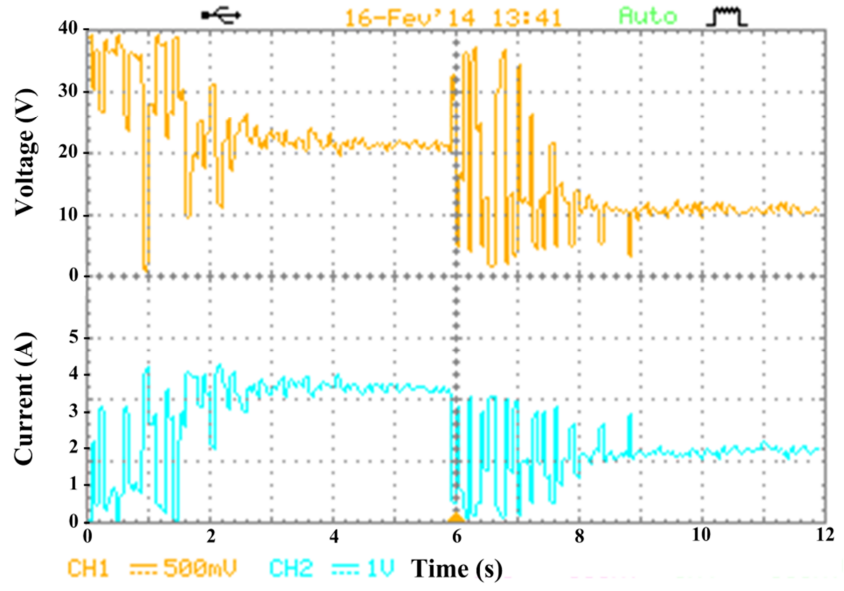

Figure 5.22: Behavior of the new MPPT algorithm before and during the occurence of partial shadow.

5.3.1.2. Comparison with the PSO-based approach:

In this experiment a comparison between the proposed ABC-based MPPT and the PSO-based MPPT is carried out under three shading patterns (SP1: 1 peak; SP2: 2 peaks; SP3: 3 peaks). In this comparison, for each pattern, both MPPT algorithms are executed 200 times. The obtained results, given in Table 5.1, show the better performance of the ABC-based MPPT especially in term of the number of successful convergence.

Table 5.1: Comparison between the ABC and PSO based MPPT algorithms under different shading patterns.

Pattern N°/ Algorithm		**Number of successful convergence (%)**	**Accuracy (%)**	**Average convergence cycle**
SP1	ABC	98.50	99.22	10.1
	PSO	97.50	98.53	8.9
SP2	ABC	96.00	98.52	10.3
	PSO	89.50	98.26	9.1
SP3	ABC	93.50	98.76	10.4
	PSO	76.00	97.83	9.3

5.3.2. ABC-based MPPT for multiple photovoltaic arrays:

The test bench composed of two PV systems of 160w each one that are mounted on parallel on a resistive is used to assess the performance of the proposed ABC-based MPPT algorithm of multiple photovoltaic arrays. The real-time test measurements are also performed for the above-mentioned cases.

Figures (5.23-a:c) show the patterns, with one peak (SP1), two peaks (SP2) and three peaks (SP3), considered in this experimental study. Each shading pattern is obtained by sweeping the duty cycle of the DC converters in the range of 10% to 90% with a step change of 0.8%. The obtained data from this sweeping procedure are collected using the DSP board and plotted in 3D using MatLab software.

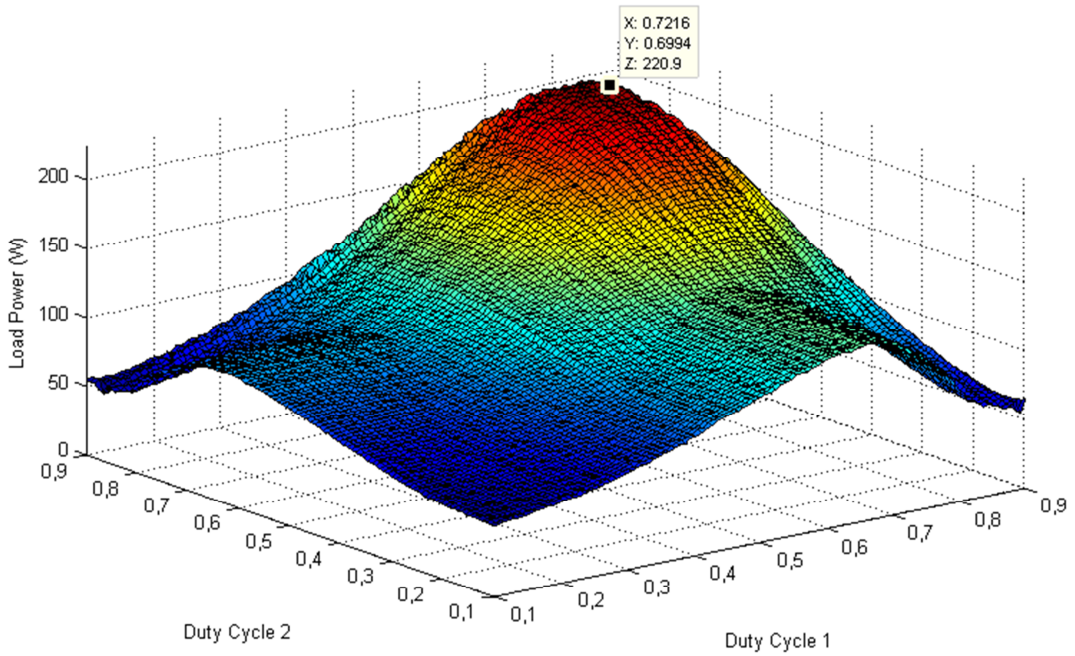
X: 0.7216
Y: 0.6994
Z: 220.9
Load Power (W)
200
150
100
50
0
0,9
0,8
0,7
0,6
0,5
0,4
0,3
0,2
0,1
Duty Cycle 2
0,1
0,2
0,3
0,4
0,5
0,6
0,7
0,8
0,9
Duty Cycle 1

(a)

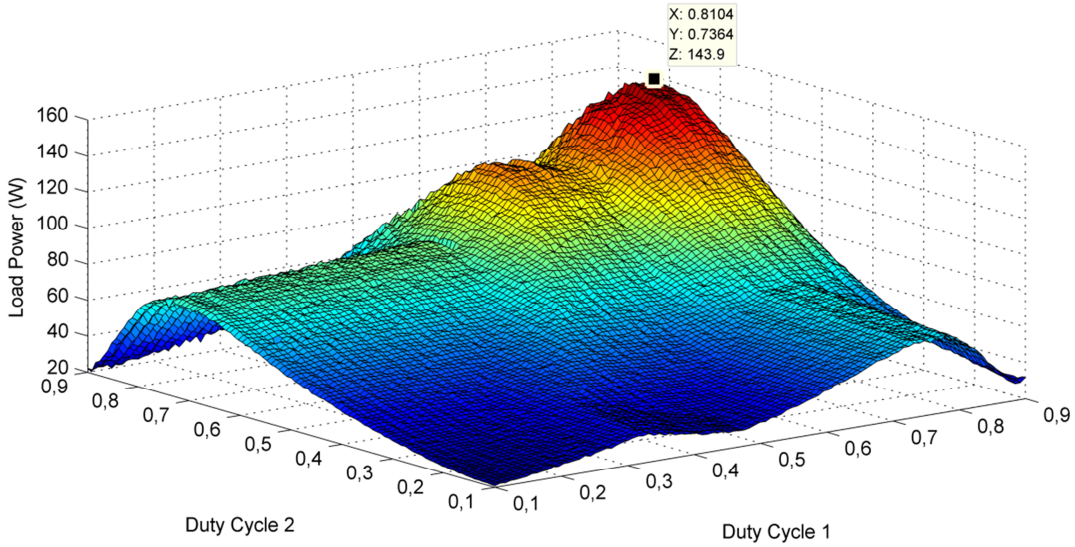
X: 0.8104
Y: 0.7364
Z: 143.9
Load Power (W)
160
140
120
100
80
60
40
20
0,9
0,8
0,7
0,6
0,5
0,4
0,3
0,2
0,1
Duty Cycle 2
0,1
0,2
0,3
0,4
0,5
0,6
0,7
0,8
0,9
Duty Cycle 1

(b)

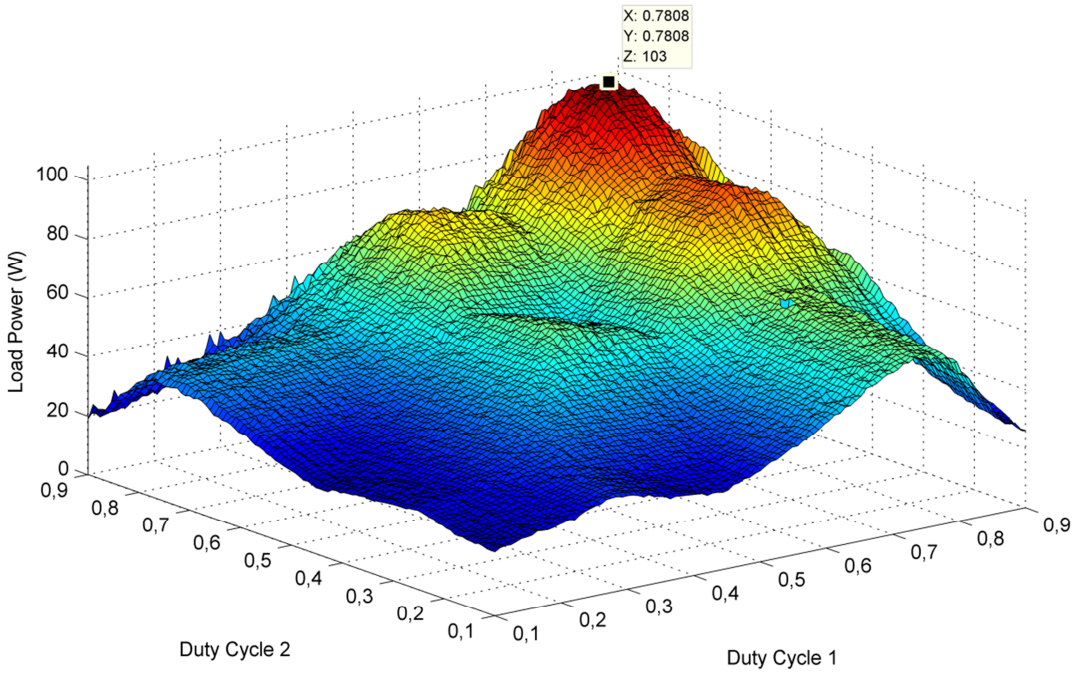

(c)

Figure 5.23: Considered shading patterns.

5.3.2.1. Power Tracking with various shading patterns:

The ability of the proposed algorithm to track the global maximum power point in both cases static and dynamic, two tests are carried out:

In the first one, the PV generator is subject to uniform irradiance profile (SP1), shown in figure (5.23-a). Figure (5.24) shows the dynamic responses of the load voltage and the load current. In addition to the load current and voltage, the load power and the duty cycle of each converter are stored in the internal memory of the DSP board, and then are plotted using Matlab environment as shown in figure (5.25). According to the output power plot, the steady state value is around 219 W which perfectly matches the power given in figure (5.23-a).

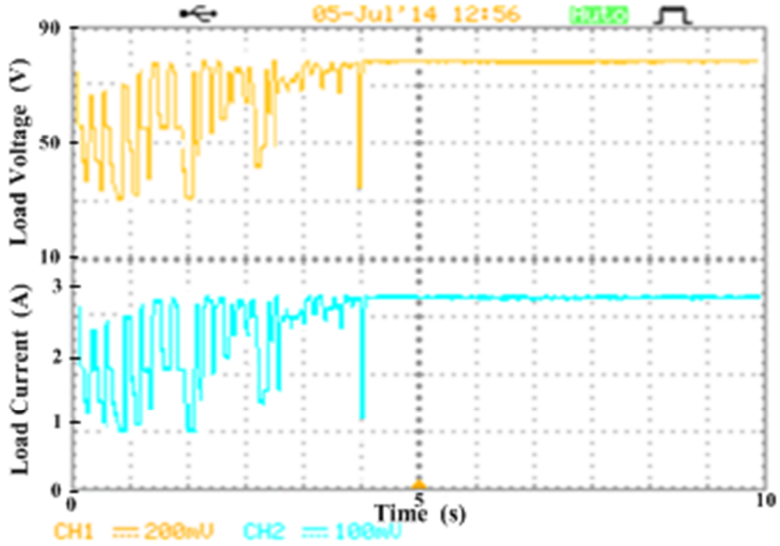

Figure 5.24: Load voltage and current dynamic responses under uniform insolation condition.

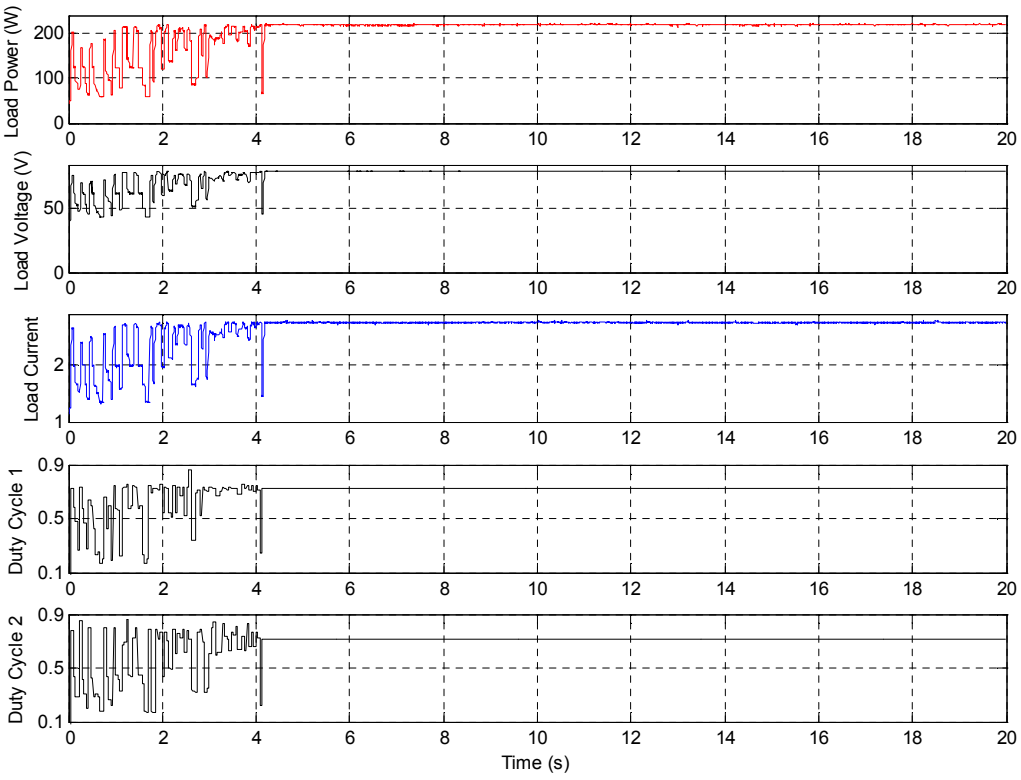

Figure 5.25: Collected DSP data under uniform insolation condition.

In the second test, the PV generator is subject to uniform irradiance until 20s. At this instant a part of the PV generator is intentionally shaded (pattern (SP3) shown in figure (5.23-c)). The output power, the load current, the output voltage and the

corresponding duty cycles are shown in figure (5.26). The obtained results show the good the performance of the ABC algorithm to track the global maximum power point in both situations; uniform irradiance and partially shaded conditions.

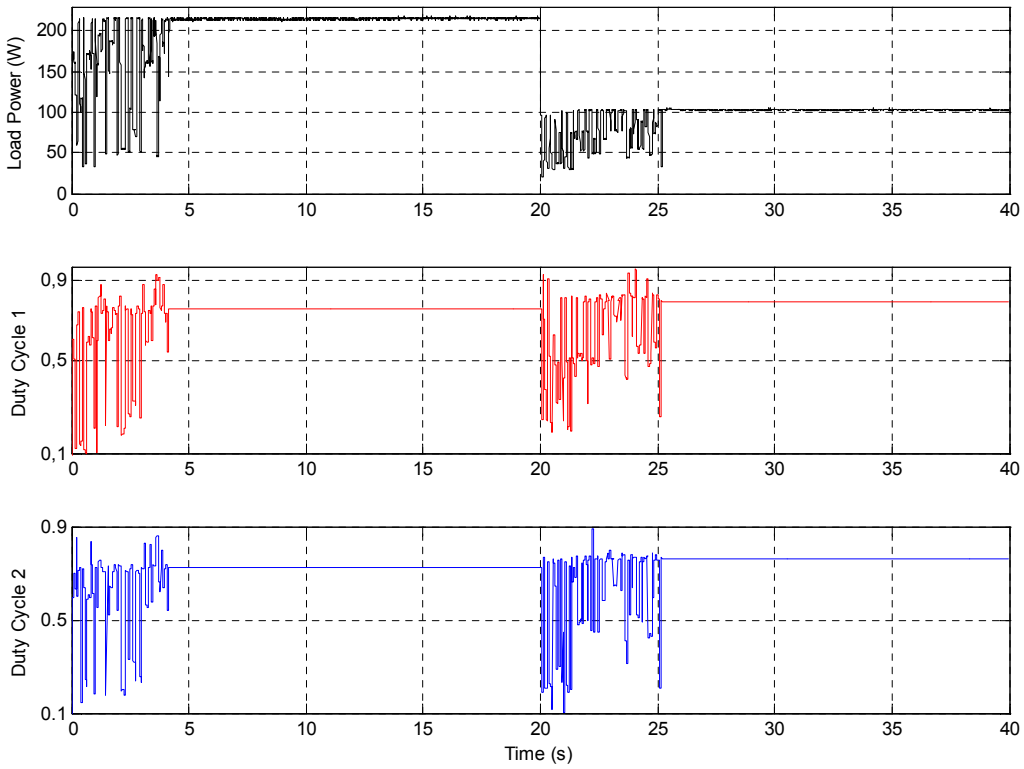

Figure 5.26: Behavior of the new MPPT algorithm before and during the occurence of partial shadow.

5.3.2.2. Comparison with the PSO-based approach:

In this experiment a comparison between the proposed ABC-based MPPT and the PSO-based MPPT is carried out under the three shading patterns presented above. In this comparison, both MPPT algorithms are executed, for each pattern, 200 times. The obtained results, given in Table 5.2, confirm the good performance of the ABC-based MPPT, especially in terms of number of successful convergence.

Table 5.2: Comparison between the ABC and the PSO based MPPT algorithms under different shading patterns.

Pattern N°/ Algorithm		Number of successful convergence (%)	Accuracy (%)	Average convergence cycle
SP1	ABC	98.50	99.17	14.1
	PSO	98.00	98.43	11.9
SP2	ABC	96.50	98.25	13.5
	PSO	88.50	98.32	10.8
SP3	ABC	94.50	98.64	12.4
	PSO	73.50	97.81	10.3

5.4. Conclusion:

The performance of the developed ABC-based MPPT approaches, that are dedicated to the control of one-dimensional and multidimensional PV systems, was experimentally assessed. The feasibility and the effectiveness of the proposed algorithms were investigated by considering various shading patterns. The experimental results have shown that, compared to the PSO-based MPPT, the recent popularly used technique, the proposed ABC-based MPPT algorithm has provided good performance. However, a slight difference between the convergence speed of the ABC based-MPPT algorithm and that of the PSO based-MPPT algorithm has been observed.

CONCLUSION

The main objective of the present doctoral thesis was the development of efficient control algorithms for power converters used in grid connected photovoltaic systems allowing efficiency enhancement while meeting international standards.

The overall efficiency of the grid connected photovoltaic system depends on both MPPT stage and inverter stage controllers. MPPT stage efficiency can be enhanced by using a adequate algorithm capable of extracting the true maximum power available at the output terminals of the PV array whatever weather conditions and surrounding obstacles while efficiency enhancement of the inverter stage can be achieved with an appropriate control algorithm ensuring low total harmonic distortion and near unity power factor operation.

Regarding MPPT stage, we focused on swarm intelligence based algorithm especially on bee colony algorithm. This choice was based on the result of numerous comparative studies between ABC algorithm and several other swarm-intelligence-based algorithms such as particle swarm optimization and ant colony optimisation. The comparative results have clearly indicated that ABC performances are better or at least similar to the performances of these algorithms. Moreover, they were found to be more attractive in term of computation efficiency, better solutions accuracy and simpler than other algorithms.

Two MPPT structures based on artificial bee colony algorithm were deeply investigated and studied, namely: one-dimensional and multidimensional PV systems. Performance of these MPPT structures have been evaluated and compared with P&O algorithm, belonging to conventional MPPT techniques, and PSO belonging to global search based MPPT techniques. The obtained simulation results are promising, as the convergence rate of the proposed algorithm is globally superior than the existing methods. However, a slight difference between the convergence speed of ABC based-MPPT algorithm and that of PSO based-MPPT algorithm has been observed. In fact, ABC based-MPPT algorithm has slow convergence speed toward the global maximum power point than PSO based-

MPPT algorithm. Experimental verification of the two proposed MPPT structures based on ABC algorithm has been conducted and compared against PSO based MPPT techniques. Experimental results were in good agreement with simulations results.

To deal with power quality problems, an improved and efficient version of the well-known deadbeat control algorithm suitable for DSP-based platform implementation has been proposed. In this thesis, single phase current controlled voltage source inverter topology with L and LCL filter has been investigated to derive the control strategy. In the proposed enhanced dead beat algorithm, a simple linear prediction model has been used to compute the future values of all required state variables for computing the expected pulse width duration. Thus, phase shift problem, total harmonic distortion and power factor have been significantly improved.

In addition to the evaluation of each of the proposed algorithms independently, a computer simulation of the complete single phase grid connected PV system, incorporating the developed and the auxiliary controllers, was carried out to assess the operation of the whole system under the proposed the algorithms. The obtained results have confirmed the good control performance of the proposed algorithms and the agreement with international standards.

In our point of view, solving the MPPT problem using soft computing techniques is very promising where lot of opportunities for enhancements and improvements are feasible. Within the frame of this work, two ABC-based MPPT algorithms have been developed. Despite their good performances, further enhancements, with respect to the convergence time, could be obtained using more efficient version of the ABC algorithm or other new soft computing algorithm.

Finally, although a DSP based bench test was considered to evaluate the two proposed MPPT approaches, an experimental implementation of the overall grid connected system, including auxiliary controllers, are still necessary to further evaluate the proposed control strategies in a real grid-connected system environment.

PUBLICATIONS AND CONFERENCES

1- A. Benyoucef, K. Kara, A. Chouder, S. Silvestre. Prediction-based Deadbeat Control for Grid-connected Inverter with L-filter and LCL-filter. Electric Power Components and Systems. 42-12 (2014) 1266-77.

Abstract—In this article, an improved deadbeat control algorithm suitable for digital signal processor-based circuit implementation is proposed. The control algorithmallows the derivation of a nearly sine wave output current with a fixed switching frequency of a current-controlled voltage source inverter. Two low-pass output filters con-figurations are considered in this study: a simple inductance filter and an LCL-filter. By taking advantage of prior knowledge of the state variables' shape, the improved deadbeat control algorithm is based on a simple prediction model to derive the expected duty cy-cle needed to switch on and off the power switches. The control study of the grid-connected inverter with L and LCL output filters has been considered using a co-simulation approach with (Powersim Inc., Rockville, Maryland, USA) andMATLAB software (TheMath-Works, Natick, Massachusetts, USA). The obtained results show the improvement of both shape quality and tracking accuracy of the out-put current quantified by low ripple content and a nearly unity power factor.

2- A. Benyoucef, A. Chouder, K. Kara, S. Silvestre, O. Ait sahed. Artificial bee colony based algorithm for maximum power point tracking (MPPT) for PV systems operating under partial shaded conditions. Applied Soft Computing. 32 (2015) 38-48.

Abstract— Artificial bee colony (ABC) algorithm has several characteristics that make it more attractive than other bio-inspired methods. Particularly, it is simple, it uses fewer control parameters and its convergence is independent of the initial conditions. In this paper, a novel artificial bee colony based maximum power point tracking algorithm (MPPT) is proposed. The developed algorithm, does not allow only overcom-ing the common drawback of the conventional MPPT methods, but it gives a simple and a robust MPPT scheme. A co-simulation methodology, combining Matlab/SimulinkTM and Cadence/Pspice TM , is used to verify the effectiveness of the proposed method and compare its performance, under dynamic weather conditions, with that of the Particle Swarm Optimization (PSO) based MPPT algorithm. Moreover, a lab-oratory setup has been realized and used to experimentally validate the proposed ABC-based MPPT algorithm. Simulation and experimental results have shown the satisfactory performance of the proposed approach.

3- O. Ait sahed, K. Kara, A. Benyoucef. Artificial bee colony-based predictive control for non-linear systems. Transactions of the Institute of Measurement and Control. (2014).

Abstract— In this paper, a new approach for the implementation of non-linear predictive control is proposed using fuzzy modelling and the artificial bee colony (ABC) algorithm. The main difficulty relevant to the implementation of non-linear predictive control techniques is obtaining, in real time, accurate solu-tions to the optimization problem. The aim of this work is to derive a simple and efficient algorithm that can solve the non-linear optimization problem with minimal computational time; this allows the real-time feasibility of the control algorithm to be ensured. Indeed, to deal with the problem of slow and premature convergence of the ABC algorithm, a new enhanced version of this algorithm is proposed. In this version, to improve the convergence speed, the initial population is generated using a chaotic map and a modified update equation is used. Furthermore, to avoid the premature conver-gence of the ABC algorithm, a new expression for the limit parameter, which allows an increase in the exploratory capabilities of the algorithm, is pro-posed. The modified ABC algorithm allows accurate solutions for the optimization problem of non-linear predictive control with low computational burden to be obtained. First, a statistical analysis of the convergence of the ABC improved version, using some well-known benchmark functions, is pre-sented and compared with that of other ABC algorithm versions. Then, to assess the efficiency and the performance of the proposed control algo-rithm, control of a continuous stirred tank rector model is considered. To demonstrate further the effectiveness of the proposed controller, a comparative study, using several meta-heuristic algorithms, is carried out.

4- O. Ait sahed, K. Kara, A. Benyoucef, M. Hadjili. A new artificial bee colony algorithm for numerical optimization. 3rd International Conference on Control, Engineering & Information Technology (CEIT), vol., no., pp.1-6, 25-27 May 2015.

Abstract— In this paper a new variant of the artificial bee colony algorithm is proposed. It is a known fact that any good optimization algorithm requires a good balance between exploring and exploiting prominent regions of the search space. To this end, several modifications of the artificial bee colony basic algorithm are introduced in the proposed version. The efficiency of the algorithm is evaluated against four other variants of the ABC algorithm using ten standard numerical benchmark functions. The obtained results show that the proposed algorithm has good performances.

APPENDIX A

LIST OF ABBREVIATIONS

ABC:	Artificial bee colony
AC :	Alternative current
ACO :	Ant colony optimization
ANN :	Artificial Neural Network
BL :	Bridge-linked configuration
CC-VCI :	Current controlled voltage controlled inverter
CCA:	Constant current adjustment
CCI :	Current controlled inverter
CCM :	Continuous Conduction Mode
BCM:	Boundary conduction mode
c-Si :	Crystalline silicon
CSI :	Current source inverter
DC :	Direct current
DCM:	Discontinuous Conduction Mode
DE :	Differential Evolution
EC:	Evolutionary computation
EMC :	Electromagnetic compatibility
GA:	Genetic algorithm
Gmpp	Global maximum power point
HC:	Hill climbing
I-V:	Current-voltage characteristic
Lmpp :	Local maximum power point
IEC:	International Electrotechnical Commission
IEEE :	Institute of Electrical and Electronics Engineers
MPC :	Model predictive control

MPP : Maximum power point

MPPT : Maximum power point tracking

NDZ: Non-detection zone

NOCT : Nominal operation cell temperature

P-V: Power-voltage characteristic

P&O : Perturb and observe technique

PCA : Proportional current adjustment

PCC : Point of common coupling

PF : Power factor

PI Proportional integral controller

PLL : Phase-locked loop

PR Proportional resonant controller

PSO : Particle swarm optimization

PV : Photovoltaic

PVG : Photovoltaic generator

Ppv : Hybrid Mode Spectral Domain

QSG : Quadrature signal generator

RC Repetitive controller

SI: Swarm intelligence

SP : Series-parallel configuration

SRE: Standard reference environment

STD: Standard test conditions

TCT: Total-crossed-tied configuration

THD: Total harmonic distortion

VCI : Voltage controlled inverter

VSI : Voltage source inverter

WT: Wavelet transform

APPENDIX B

LIST OF SYMBOLS

C_1/C_2 :	Acceleration coefficients
C_{DC} :	DC link capacitor
d:	Duty cycle
E_g:	Band-gap energy
G :	Irradiance intensity
G_{best} :	Global best position
G_{ref} :	Irradiance intensity at standard test conditions
I_0 :	Reverse saturation current
$I_{o,ref}$:	Nominal saturation current
I_{mpp}:	Current at maximum power point
$I_{sc,ref}$:	Short-circuit current at standard test conditions
I_{PH}:	Photocurrent
I_{sc} :	Short-circuit current
k:	Boltzmann constant
K_i:	Integral gain
K_p :	proportional gain
n:	Diode ideality factor
N_p :	Number of parallel cells
N_s :	Number of series cells
$P_{i\text{-}best}$:	Personal best position
P_{mpp} :	Power at maximum power point
P_{pv} :	Power of the PVG
q:	Charge of electron
R_s :	Series resistance
R_{sh}:	Parallel resistance

T:	Solar cell temperature
T_{ref} :	Temperature at standard test conditions
U_d :	DC bus voltage
v:	Velocity
$V_{oc\ ref}$:	Solar cell open-circuit voltage at reference condition
V_{grid} :	Grid voltage
V_{mpp}:	Voltage at maximum power point
V_{nom}:	Nominal viltage
V_{oc} :	Open-circuit voltage
V_t :	Thermal voltage
ω:	Inertia weight
ω_{grid}:	Grid pulsation
ΔU_d :	DC bus voltage ripple
μ_{Isc}:	Solar cell short-circuit temperature coefficient

APPENDIX C

BOOST CONVERTER

A boost converter (step-up converter) is a power converter with an output DC voltage greater than its input DC voltage. It is a class of switching-mode power supply (SMPS). A simple boost converter consists of an inductor L_{boost}, a controlled switch *S* and a diode *D*, filters made of a capacitors are normally added to the output and the input of the converter to reduce voltage ripples (see figure (C.1)).

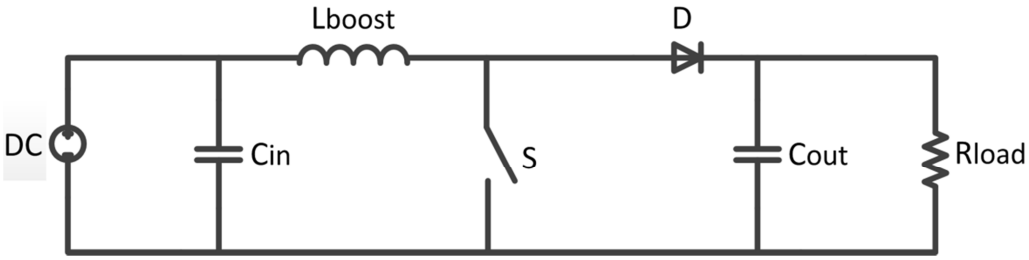

Figure C.1: Boost converter schematic.

The operation of a boost converter is to boost or step-up a certain input voltage to a higher level, at the same time the boost converter steps-down the current as a natural result of the energy conservation principle, which implies that power, being the product of voltage and current, must be conserved.

C.1. Modes of operation:

The operation of the boost converter is essentially based on the inductor charge and discharge. When an inductor is charged, it behaves like a load as it absorbs energy. On the other hand, when it is discharged, it behaves as an energy source. The fundamental idea behind the boost effect is the fact that the inductor's voltage during a discharging process depends only on the rate of change of its current with respect to time, and this voltage is independent of the source voltage by which the inductor was charged. This independency gives the possibility of having an output voltage greater than the input voltage.

The Boost converter circuit operation can be divided into two phases. Phase 1 begins when the switch *S* is turned on at $t=T_{on}$ as shown in figure (C.2-a). The input current which rises flows through inductor L_{boost} and switch *S*. During this mode, energy is stored in the inductor. Phase 2 begins when the switch is turned off at $t=T_{off}$, the energy stored in the inductor is released through the diode to the output Load, as shown in Figure (C.2-b).

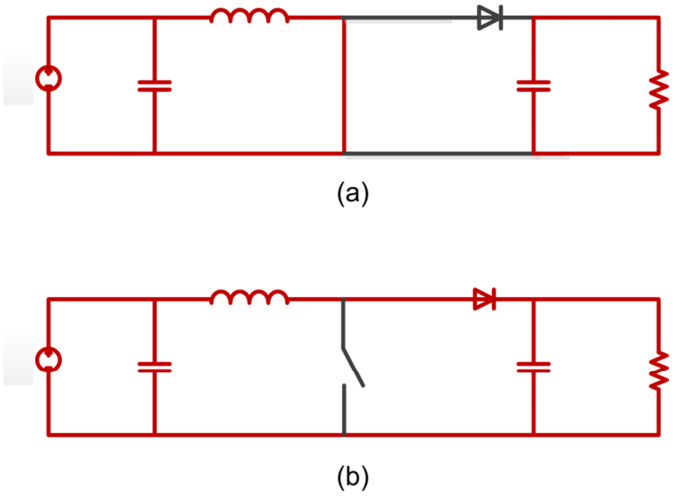

Figure C.2: The two operation phases of a boost converter, depending on the state of the switch *S*.

The boost converter as all others DC-DC converters has two fundamentally different modes of operation: Continuous-Conduction Mode (CCM) and Discontinuous-Conduction Mode (DCM). The boost converter and its control are designed based on both modes of operation. In the Continuous Conduction mode, the inductor current flows continuously that is the inductor current is always above zero throughout the switching period as shown in figure (C.3).

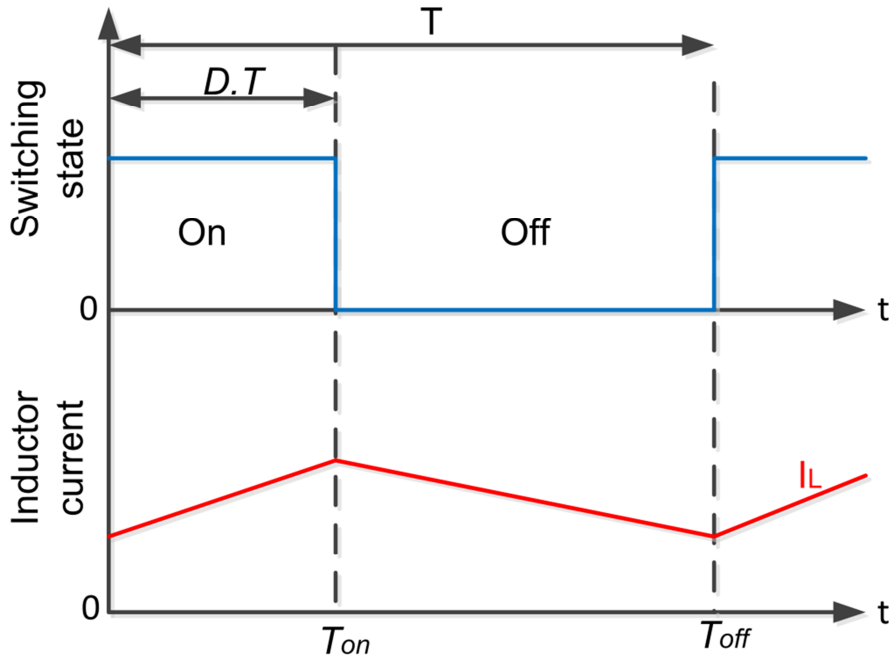

Figure C.3: Waveforms of current and voltage in a boost converter operating in continuous mode.

In the Discontinuous Conduction Mode, the inductor current is discontinuous, that is inductor current reaches zero before the end of each switching period, as shown in figure (C.4).

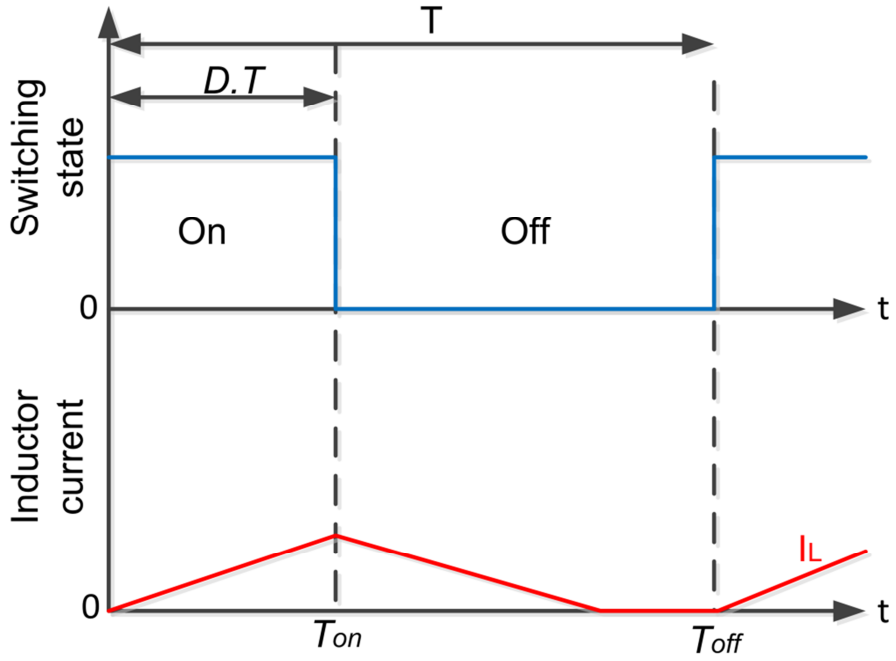

Figure C.4: Waveforms of current and voltage in a boost converter operating in discontinuous mode.

The advantages of CCM over DCM include the DC conversion ratio is independent of the load, which makes DC analysis of converters operating in CCM easier. While operating in DCM, the output voltage depends on the load and the duty ratio of the switch, which makes DC analysis of converters operating in DCM more complicated. Also, to deliver the same power in DCM as in CCM, the peak currents are higher, resulting in greater losses in the conduction paths leads to reduced efficiency and higher peak current can also cause switch stress and greater input and output current ripple that adversely affects EMC noise issues.

In the following, the electrical analysis is dictated by the choice of operating the converter "boost" in continuous conduction mode (CCM) and under the below assumptions:

- The circuit is operating in the steady state.
- The components are ideal.

C.2. Electrical circuit analysis:

C.2.1 Current flows through the inductor:

During the On-state, the switch *S* is closed, which makes the input voltage V_{in} appear across the inductor, which causes a change in current I_L flowing through the inductor during a time period *t* to be as in (C.1):

$$\frac{dI_L}{dt} = \frac{V_L}{L} = \frac{V_{in}}{L} \tag{C.1}$$

By integrating the two parts of the equality, we find that:

$$I_{L1}(t) = \frac{V_{in}}{L} t + I_{L\min} \tag{C.2}$$

We can see that $I_L(t)$ has a positive slope, which proves that in this phase, the inductor is charging.

At the end of the On-state, the increase of I_L is therefore:

$$\Delta I_{L\,on} = \frac{1}{L}\int_0^{DT} V_{in} dt = \frac{DT}{L} V_{in} \tag{C.3}$$

D is the duty cycle. It represents the fraction of the commutation period T during which the switch is on. Therefore D ranges between 0 (S is never on) and 1 (S is always on).

During the Off-state, the switch S is open, so the inductor current flows through the load. If we consider zero voltage drop in the diode, and a capacitor large enough for its voltage to remain constant, the evolution of I_L is:

$$\frac{dI_L}{dt} = \frac{V_{in} - V_{out}}{L} \tag{C.4}$$

By integrating the two parts of the equality, we find that:

$$I_{L2}(t) = \frac{V_{in} - V_{out}}{L} t + I_{L\max} \tag{C.5}$$

In the case of boost converter V_{out} is always greater than V_{in}. Thus, $I_L(t)$ has a negative slope, which proves that in this phase, the inductor is discharging.

Therefore, the variation of I_L during the Off-period is:

$$\Delta I_{L\,off} = \int_0^{(1-D)T} T \frac{(V_{in} - V_{out})dt}{L} = \frac{(V_{in} - V_{out})(1-D)T}{L} \tag{C.6}$$

It should be noted that during the two conduction phases (on/off), I_L varies (increases/decreases) in a ΔIL bandwidth around a mean value $I_{Lmean} = I_{in}$. See figure (C.5).

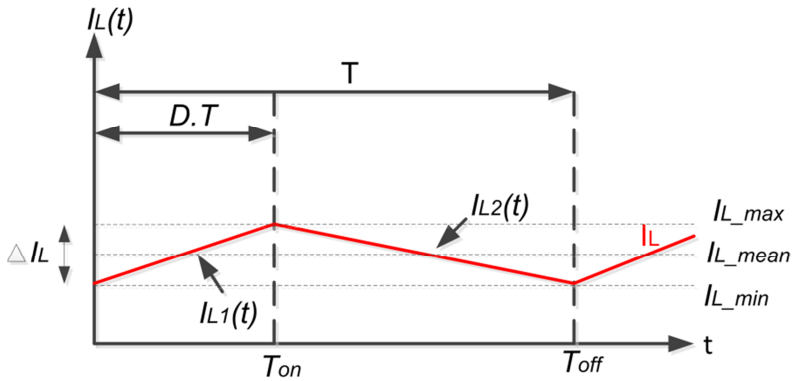

Figure C.5: Inductor's current variation.

C.2.2 Current flows through the Diode:

During the On-state, the switch *S* is closed, the diode becomes reverse-biased and the average current passing through it is zero.

$$I_D(t) = 0 \tag{C.7}$$

During the Off-state, the switch *S* is open. According to the circuit diagram in figure (C.2-b) and according to the Kirchhoff's circuit law, we can write:

$$I_D(t) = I_{L2}(t) = \frac{V_{in} - V_{out}}{L} t + I_{L\max} \tag{C.8}$$

C.2.3 Current flows through the switch:

During the On-state, the switch *S* is closed, and if we assume that the switching resistance R_{DS_ON} is zero. The current flows through the switch can be given by:

$$I_s(t) = I_{L1}(t) = \frac{V_{in}}{L} t + I_{L\min} \tag{C.9}$$

During the Off-state, the switch *S* is open, and if we assume that the switching resistance R_{DS_Off} is infinite. The current flows through the switch can be given by:

$$I_s(t) = 0 \tag{C.10}$$

C.2.4 Current flows through the input capacitor:

During the On-state, the switch *S* is closed. According to the circuit diagram in figure (C.2-a) and according to the Kirchhoff's circuit law, the current flows through the input capacitor can be given by:

$$I_{Cin}(t) = I_{in} - I_{L1}(t) = I_{L\_mean} - I_{L1}(t) \tag{C.11}$$

Following the same reasoning as that adopted during the On-state. During the Off-state, the current flows through the switch can be given by:

$$I_{Cin}(t) = I_{in} - I_{L2}(t) = I_{L\_mean} - I_{L2}(t) \tag{C.12}$$

C.2.5 Current flows through the output capacitor:

Referring to the diagram in Figure (C.2-a), it is clearly shown that the output capacitor feeds the load R_L during the On-state with a constant current I_{out} given by:

$$I_{Cout}(t) = I_{out}(t) = \frac{V_{out}}{R_{load}} \tag{C.13}$$

During the Off-state, the output capacitor is connected to the source supply via the inductor L. According to the Kirchhoff's circuit law, the current flows through the output capacitor can be given by:

$$I_{Cout}(t) = I_{L2}(t) - I_{out}$$

Thus,

$$I_{Cout}(t) = \frac{V_{in} - V_{out}}{L} t + I_{L\max} - \frac{V_{out}}{R_{load}} \tag{C.14}$$

C.2.6 Boost converter's gain:

As we consider that the converter operates in steady-state conditions, the amount of energy stored in each of its components has to be the same at the beginning and at the end of a commutation cycle. In particular, the energy stored in the inductor is given by (C.15).

$$E = \frac{1}{2} L I_L^{\,2} \tag{C.15}$$

Therefore, the inductor current has to be the same at the beginning and the end of the commutation cycle. This can be written as:

$$\Delta I_{L\,on} + \Delta I_{L\,off} = 0 \tag{C.16}$$

Substituting $\Delta I_{L\,on}$ and $\Delta I_{L\,off}$ by their expressions yields:

$$\Delta I_{L\,on} + \Delta I_{L\,off} = \frac{DT}{L} V_{in} + \frac{(V_{in} - V_{out})(1-D)T}{L} = 0 \tag{C.17}$$

This can be written as:

$$\frac{V_{out}}{V_{in}} = \frac{1}{1-D} \tag{C.18}$$

This in turns reveals the duty cycle to be:

$$D = 1 - \frac{V_{in}}{V_{out}} \tag{C.19}$$

From the expression (C.18) it can be seen that the output voltage is always higher than the input voltage (as the duty cycle goes from 0 to 1), and that it increases with D, theoretically to infinity as D approaches 1.

APPENDIX D

BOOST CONVERTERS DESIGN

In this appendix, boost converters considered in chapter II and IV will be designed.

D.1 Design of the boost converter considered in the second chapter:

In the following, we will design a boost converter interfacing between a PV generator of *160W* and a resistive load of 100Ω. The block diagram of the considered system is shown in figure (2.6). Table D.1 summarize electrical characteristics of the considered PV generator that consist of two series modules BP SX80.

Table D.1: electrical characteristics of the considered photovoltaic generator.

Open circuit voltage V_{OC_STC}	42 V
Short circuit current I_{SC_STC}	5.17 A
Maximum power P_{MAX_STC}	160 W
Voltage at maximum power V_{MAX_STC}	33.6 V
Current at maximum power I_{MAX_STC}	4.75 A

D.1.1 Switching:

To reduce the size of the inductor, the Boost converter will be switched at a high frequency. A switching frequency of $F_s = 20\ kHz$ will be used.

D.1.2 Voltage rating:

The input voltage is a function of the temperature, and in a practical calculation, the voltage variation with temperature of a string consisting of N_S cells in series , is often calculated by using equation (D.1).

$$\begin{aligned} V_{OC\_\max} &= -2.310^{-3} N_s (T_{\min} - T_{STC}) + V_{oc\_STC} \\ V_{OC\_\min} &= -2.310^{-3} N_s (T_{\max} - T_{STC}) + V_{oc\_STC} \end{aligned} \quad (D.1)$$

Assuming the temperature of the cells can vary from -30 °C to 60 °C, and the number of cells in series per string is N_S=36x2=72 , the open circuit voltage range is:

$$V_{OC\_\max} = -2.310^{-3}72(-30-25)+42 = 51.1\ V$$
$$V_{OC\_\min} = -2.310^{-3}72(60-25)+42 = 36.2\ V \quad \text{(D.2)}$$

This is the maximum and minimum voltages at open circuit, and the converter should be able to handle the maximum open circuit voltage even though it is not the normal operating voltage at MPP. So the maximum operating voltage of the boost converter becomes:

$$V_{pv\_\max} = V_{oc\_\max} = 51.1\ V \quad \text{(D.3)}$$

The boost converter supplies a resistive load of $Rload = 100\Omega$, and the maximum power of the photovoltaic generator is $P_{\max} = 160\ W$. Thus, the maximum output voltage is given by:

$$V_{out\_\max} = \sqrt{P_{pv\_\max} R_{load}} = \sqrt{160 \times 100} = 126.5\ V \quad \text{(D.4)}$$

D.1.3 Current rating:

Since the converter will operate in continuous conduction mode (CCM), a lower current limit must be set. It is desired to have a large operating range of the converter, and thus a low limit, but at the same time it is desired to keep the boost inductor as small as possible, and thus a higher limit. So a minimum input current limit of $\Delta I_L / 2$ is therefore used, and the maximum input current is equal the short circuit current of the PV generator. With the ripple inductor current is chosen to be $\Delta I_L = 10\% \times I_{sc} = 0.5A$. Giving an operating range of:

$$0.25\ A \le I_{pv} \le 5.17\ A \quad \text{(D.5)}$$

The maximum input current is equal to the maximum current delivered by the PV generator. Thus, the maximum input current is given by:

$$I_{in\_\max} = I_{SC\_STC} = 5.17A \quad \text{(D.6)}$$

The maximum output current is given by:

$$I_{out\_\max} = \frac{V_{out\_\max}}{R_{load}} = \frac{126.5}{100} = 1.26A \quad \text{(D.7)}$$

D.1.4 Duty cycle limits:

In order to find the MPP in different situations, a large search space is needed. Thus, the chosen duty cycle limits are:

$$D_{\min} = 0.05$$
$$D_{\max} = 0.95 \tag{D.5}$$

D.1.5 Boost inductor:

When the photovoltaic generator feeds a resistive load via a Boost converter, the indicator of this latter is designated by following the two complementary conditions given below:

$$L_{boost} \geq \max\left(\frac{(1-D)^2.D.R_L}{2.F_s}\right) \tag{D.6}$$

$$L_{boost} \geq L_{\min} = \frac{V_{pv}.D}{\Delta I_L.F_s} \tag{D.7}$$

This latter condition is very important, because the inductor current ripple considerably affects the operating point of the PV generator.

As seen from the equation(D.6), the only variable is the duty cycle *d*. In the figure below the boost inductor is shown as a function of the duty cycle.

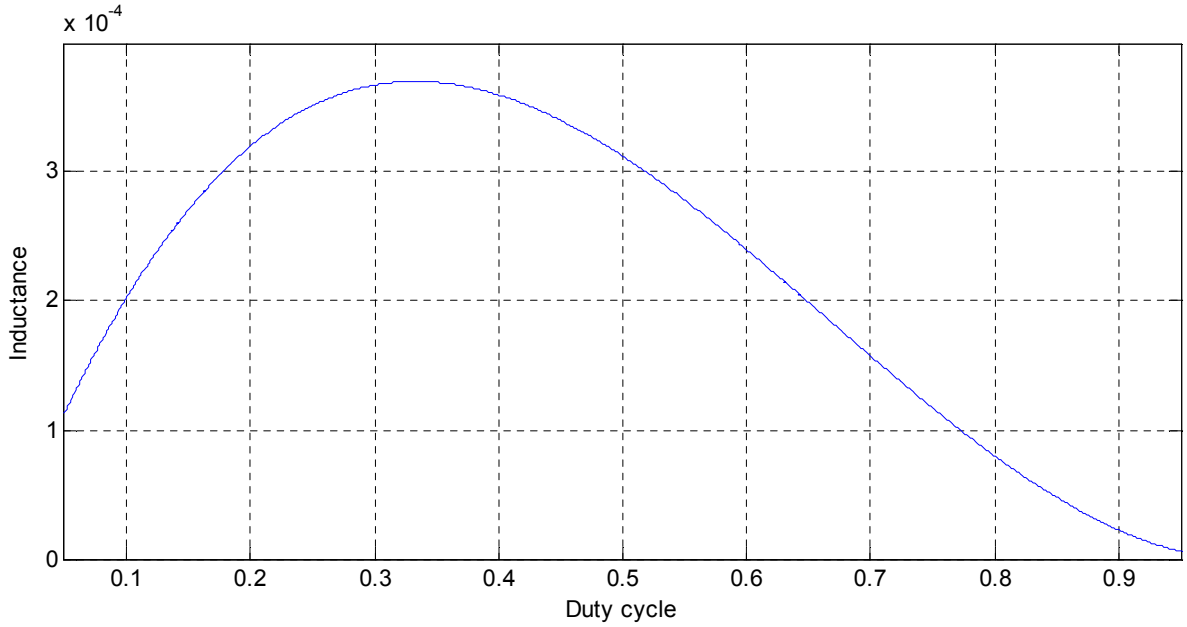

Figure D.1: Boost inductor as a function of the duty cycle.

Taking the value of the duty cycle in which the first condition is at its maximal value, and replacing it in the second condition with $V_{pv} = V_{pv\_max}$, the value of the minimum inductance is:

$$L_{\min} = \frac{51.1 \times 1/3}{0.5 \times 20000} = 1.7mH \tag{D.8}$$

We have chosen:

$$L_{boost} = 2mH \tag{D.9}$$

D.1.6 Input capacitor:

The PV panel can be seen as a current source, and it is needful to convert it to a voltage source by adding a capacitor in parallel. In this way the capacitor will handle the ripple current from the boost inductor, smooth the current from the PV generator, and keep the PV generator voltage ripple at a minimum.

On the basis of equations (C.11) and (C.12), figure below shows the charge quantity exchanged by the input capacitor C_{in} during a switching period T.

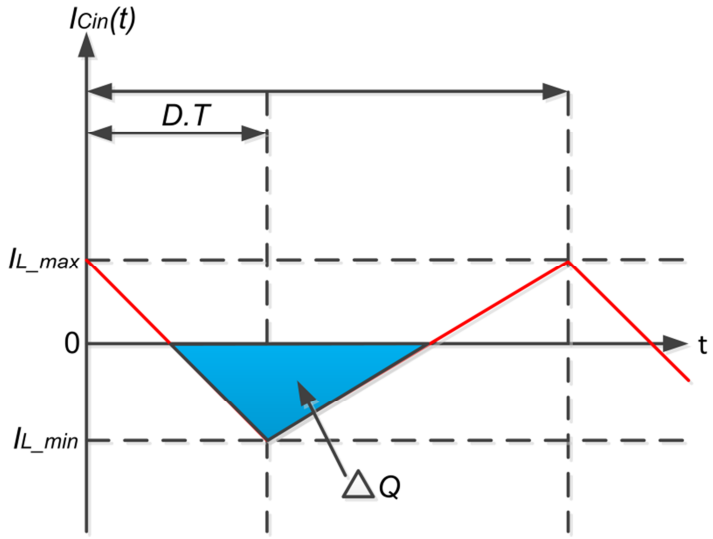

Figure D.2: Input capacitor charge behaviour during one switching period.

ΔQ is the triangle area, which is given by:

$$\Delta Q = \frac{1}{2}\frac{T}{2}\frac{\Delta I_L}{2} = \frac{\Delta I_L}{8F_s} \tag{D.10}$$

In addition, charge-voltage relationship of a capacitor is given by:

$$\Delta Q = C\,\Delta V \tag{D.11}$$

Combining (D.10) and (D.11), and choosing $\Delta V_{in} = 1\% V_{pv\_\max} = 0.51V$, the minimum value of the input capacitor is given by:

$$C_{in\_\min} = \frac{\Delta I_L}{8\Delta V_{in} F_s} = \frac{0.51}{8 \times 0.5 \times 20000} = 6.25 \times 10^{-6}\, F \tag{D.12}$$

We have chosen:

$$C_{in} = 220uF \tag{D.13}$$

D.1.7 Output capacitor:

To size the output capacitor, we will follow the same reasoning as that used for the input capacitor.

On the basis of equations (C.13) and (C.14), figure below shows the charge quantity exchanged by the output capacitor C_{out} during a switching period T.

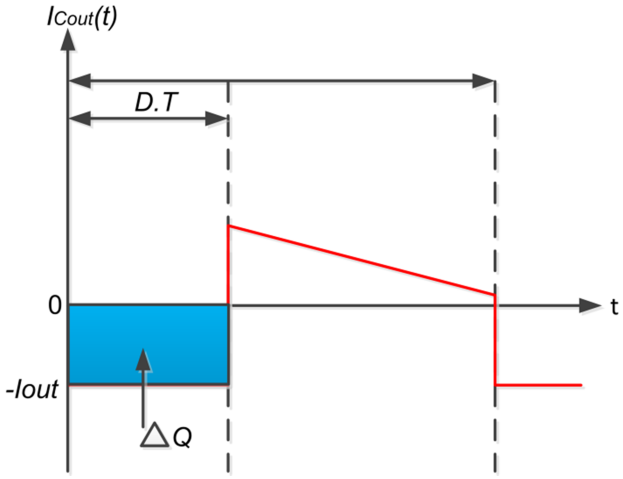

Figure D.3: Output capacitor charge behaviour during one switching period.

ΔQ is the square area, which is given by:

$$\Delta Q = D.T.I_{out} \tag{D.14}$$

Combining this latter equation with equation (D.11), we can found the minimal output capacitor expression:

$$C_{out\_\min} = \frac{D_{\max}.I_{out\_\max}}{\Delta V_{out} F_s} \tag{D.15}$$

For:

The maximum duty cycle $D_{\max} = 0.95$

The maximal output current $I_{out\_\max} = 1.26\,A$

The output voltage ripple $\Delta V_{out} = 1\% V_{out\_\max} = 1.26V$

$$C_{out\_\min} = \frac{0.95 \times 1.26}{1.26 \times 20000} = 47.5 \times 10^{-6}\,F \qquad \text{(D.16)}$$

We have chosen:

$$C_{out} = 220uF \qquad \text{(D.17)}$$

D.2 Design of the boost converter considered in the fourth chapter:

In the following, a boost converter interfacing between a PV generator of *1.92kW* and a grid connected inverter will be designed. The block diagram of the considered system is shown in figure (4.24). Table D.2 summarize electrical characteristics of the considered PV generator that consist of two strings in parallel and each string has 12 modules BP SX80.

Table D.2: electrical characteristics the considered photovoltaic generator.

Open circuit voltage V_{OC_STC}	252 V
Short circuit current I_{SC_STC}	10.34 A
Maximum power P_{MAX_STC}	1.92 kW
Voltage at maximum power V_{MAX_STC}	201.6 V
Current at maximum power I_{MAX_STC}	9.5 A

D.2.1 Switching:

To reduce the size of the inductor, the Boost converter will be switched at a high frequency. A switching frequency of $F_s = 50\ kHz$ will be used.

D.2.2 Voltage rating:

The input voltage is a function of the temperature, and in a practical calculation, the voltage variation with temperature of a string consisting of N_S cells in series , is often calculated by using equation (D.1).

Assuming the temperature of the cells can vary from -30 °C to 60 °C, and the number of cells in series per string is N_S=36x12=432 , the open circuit voltage range is:

$$V_{OC\_\max} = -2.310^{-3}432(-30-25)+252 = 306.6\ V$$
$$V_{OC\_\min} = -2.310^{-3}432(60-25)+252 = 217.2\ V \quad \text{(D.18)}$$

This is the maximum and minimum voltages at open circuit, and the converter should be able to handle the maximum open circuit voltage even though it is not the normal operating voltage at MPP. So the maximum operating voltage of the boost converter becomes:

$$V_{pv\_\max} = V_{oc\_\max} = 306.6\ V \quad \text{(D.19)}$$

The inverter will be connected to a single-phase 220Vrms grid, and in order to ensure a power flow from PV side to grid side, the DC bus voltage (U_d) must be higher than the peak value of the grid voltage (V_{grid_rms}). Based on this the needed, the DC-link voltage can be calculated based on the equation (1.14).

$$U_d \geq \sqrt{2} * 220 + 10\% * 220 = 333.12\ V \quad \text{(D.20)}$$

We have chosen the DC bus voltage to be $U_d = 400V$.

D.2.3 Current rating:

Since the converter will operate in continuous conduction mode (CCM), a lower current limit must be set. It is desired to have a large operating range of the converter, and thus a low limit, but at the same time it is desired to keep the boost inductor as small as possible, and thus a higher limit. So a minimum input current limit of $\Delta I_L / 2$ is therefore used, and the maximum input current is equal the short circuit current of the PV generator. With the ripple inductor current is chosen to be $\Delta I_L = 5\% \times I_{sc} = 0.5A$. Giving an operating range of:

$$I_{pv} = [0.25\ A,\ 10.34\ A] \quad \text{(D.21)}$$

D.2.4 Duty cycle limits:

In order to find the MPP in different situation a large search space is needed. Thus, the chosen duty cycle limits are:

$$d_{\min} = 0.1$$
$$d_{\max} = 0.9 \qquad \text{(D.22)}$$

D.2.5 Boost inductor:

The following equation is a good estimation for the right inductor:

$$L_{boost} \geq L_{\min} = \frac{V_{PV}(U_d - V_{pv})}{\Delta I_L . F_s . U_d} \qquad \text{(D.23)}$$

As seen from the equation, the only variable is the PV voltage. In the figure below the boost inductor is shown as a function of the PV voltage.

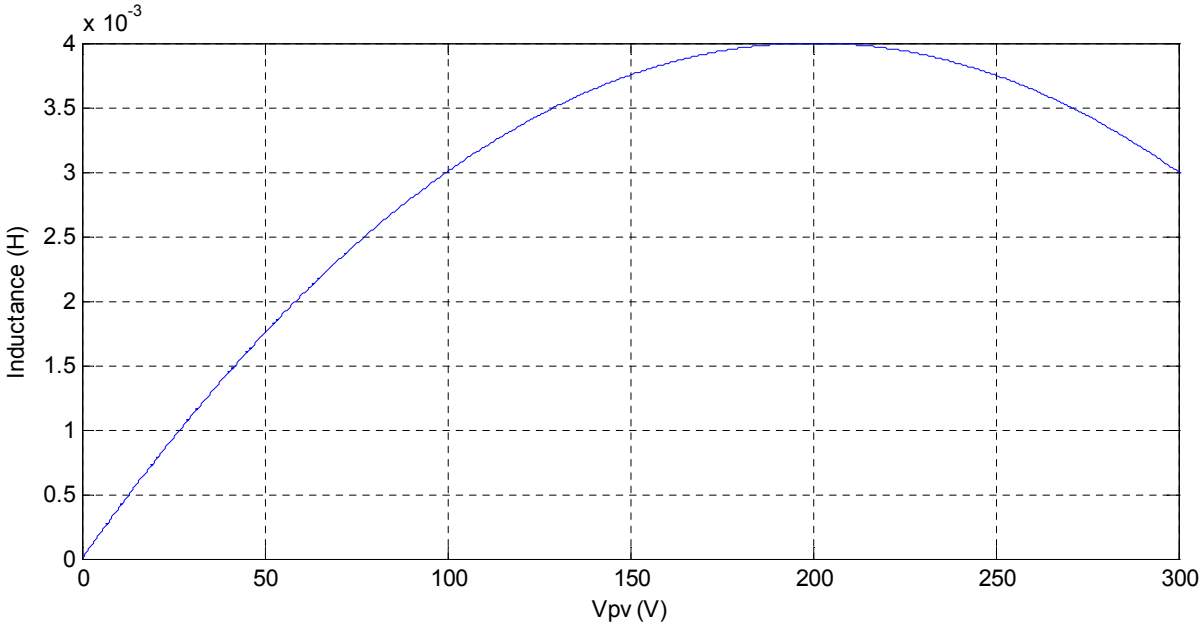

Figure D.4: Boost inductor as a function of the PV voltage.

It can be shown that the minimum inductance value to be chosen is $L_{\min} = 4\ mH$.

We have chosen:

$$L_{boost} = 5mH \qquad \text{(D.24)}$$

D.2.6 Input capacitor:

Following the same reasoning as that used in section (D.1.6), the minimal input capacitor value can be given as following:

$$C_{in\_\min} = \frac{\Delta I_L}{8\Delta V_{in} F_s} = \frac{0.5}{8 \times 3 \times 50000} = 41.6 \times 10^{-6} F \quad \text{(D.25)}$$

We have chosen:

$$C_{in} = 220uF \quad \text{(D.26)}$$

D.2.7 DC link capacitor:

Figure below shows the charge quantity exchanged by the DC-link capacitor C_{DC}.

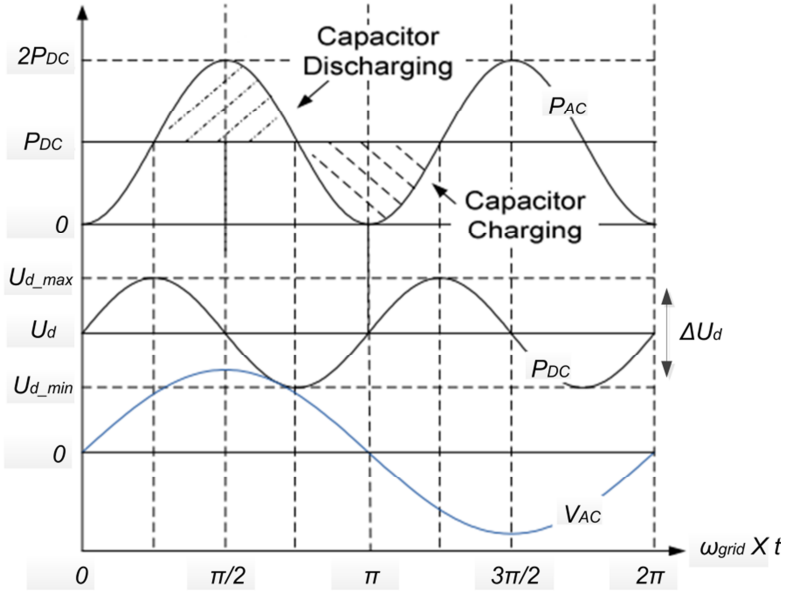

Figure D.5: DC link capacitor charge behaviour.

In unity power factor operation of PV inverter, the voltage and the current expressions at inverter output are given by:

$$\begin{aligned} V_{grid} &= \sqrt{2} V_{grid\_rms} \sin(\omega_{grid} t) \\ V_{injected} &= \sqrt{2} I_{injected\_rms} \sin(\omega_{grid} t) \end{aligned} \quad \text{(D.27)}$$

So, the instantaneous output power of the inverter can be expressed as following:

$$P_{AC} = 2 V_{grid\_rms} I_{injected\_rms} \sin^2(\omega_{grid} t) \quad \text{(D.28)}$$

Applying a simple trigonometric identity yields a new form of (D.28):

$$P_{AC} = V_{grid\_rms} I_{injected\_rms} - V_{grid\_rms} I_{injected\_rms} \cos(2\omega_{grid} t) \quad \text{(D.29)}$$

If losses are neglected, the average output power of the inverter is equal to the generated PV power, therefore the output power can be expressed as:

$$P_{AC} = P_{pv} - P_{PV}\cos(2\omega_{grid}t) \tag{D.30}$$

The net power into or out of the DC bus (DC link capacitor) is described by:

$$P_{Bus} = P_{pv} - P_{AC} \tag{D.31}$$

Combining (D.30) and (D.31) yields the instantaneous DC bus power that the capacitor will need to sink or source every half cycle:

$$P_{Bus} = P_{PV}\cos(2\omega_{grid}t) \tag{D.32}$$

Integrating (D.32) for one half cycle ($\pi/4$ to $3\pi/4$) and setting it equal to the expression for energy stored in a capacitor given by (D.11), rearranging the result, the equation to size the input capacitor is expressed as:

$$C_{DC} = \frac{P_{pv}}{2\times\omega_{grid}\times U_d\times\Delta U_d} \tag{D.33}$$

So, for P_{pv}=1.92kW, U_d=400V and $\Delta U_d = 1\%U_d$, the DC bus capacitor value is given by:

$$C_{DC} = \frac{1920}{2\times 6.28\times 50\times 400\times 4} = 1.91\times 10^{-3} F \tag{D.34}$$

We have chosen:

$$C_{DC} = 3mF \tag{D.35}$$

APPENDIX E

L-FILTER AND LCL-FILTER MODELS AND DESIGN PROCEDURES

This appendix addresses the mathematical model and the design procedure of the L (inductive) filter and the LCL (inductive-capacitive-inductive) filter for single-phase full bridge grid connected inverters.

E.1 Filters model:

In this section the state-space models and the transfer functions of the considered filters are obtained, given that the parasitic resistances are neglected.

E.1.1 L-filter model:

According to figures (3.1 and 3.2-a), the output current is related to the output voltage of the inverter and the utility grid voltage by the following equation:

$$L\frac{dI_L(t)}{dt} = U_0(t) - U_{grid}(t) \tag{E.1}$$

where L is the filter inductance, $I_L(t)$ is the current in inductance L (the injected current), $U_{grid}(t)$ is the grid voltage, and $U_0(t)$ is the inverter output voltage.

The transfer function from U_0 to I_L, $\frac{I_L}{U_0}$ is given by:

$$G_L(s) = \frac{I_L}{U_0} = \frac{1}{L.s} \tag{E.2}$$

E.1.2 LCL-filter model:

The bloc diagram of a grid connected inverter through an LCL filter is shown in figures (3.1 and 3.2-b). Define $I_{L1}(t)$ as the current through the inductor L_1, $I_{L2}(t)$ as the current through the inductor L_2 (the injected current), and $V_C(t)$ as the voltage across the capacitor C. Then the model of the system is given by:

$$L_1\frac{dI_{L1}(t)}{dt} = U_0(t) - V_c(t) \tag{E.3}$$

$$L_2\frac{dI_{L2}(t)}{dt} = V_C(t) - U_{grid}(t) \tag{E.4}$$

$$C\frac{dV_C(t)}{dt} = I_{L1}(t) - I_{L2}(t) \tag{E.5}$$

The transfer function from U_0 to I_{L2}, $\frac{I_{L2}}{U_0}$ is given by:

$$G_{LCL}(s) = \frac{I_{L2}}{U_0} = \frac{L_1}{L_1.L_2.C.s^3 + (L_1 + L_2).s} \tag{E.6}$$

The resonant frequency is:

$$\omega_{res} = \sqrt{\frac{L_1 + L_2}{L_1 L_2 C}} \tag{E.7}$$

E.2 Filters design:

E.2.1 L-filter design:

The selection for the *L* inductor of figure (3.2-a) can be done in terms of the desired current ripple at the switching frequency:

$$L = \frac{U_d}{8.\Delta I_{L\_\max}.F_s} \tag{E.8}$$

Where F_s is the switching frequency (Hz) of the inverter, U_d is the DC-link voltage and ΔI_{L_max} is the maximum ripple magnitude percentage (2.5% - 25%).

E.2.2 LCL-filter design:

There are some limits on the parameter values when designing a LCL-filter, such as:

- The capacitance is limited by the reactive power factor.

- The resonant frequency ω_{res} should be in range: $10\omega_g \le \omega_{res} \le \frac{\omega_s}{2}$ to avoid resonance problems, where ω_g is the utility frequency (rad/s) and ω_s is the switching frequency (rad/s).

The total filter inductance can be calculated by considering the maximum current ripple using equation (E.8).

By adding a capacitor, the total filter inductance is divided into two parts: the inverter-side inductance *L1* and grid-side inductance *L2*. These inductance values have the following relationship:

$$L_1 = aL_2 \tag{E.9}$$

where *a* is the inductance index (*a*≥1).

The filter capacitance *C* can be determined by considering the reactive power absorbed in filter capacitor as following:

$$C = \frac{Q_c}{\omega_g U_{grid}^2} = \alpha \frac{\mathrm{P}_{rated}}{\omega_g U_{grid}^2} \tag{E.10}$$

where Q_c is the reactive power absorbed by filter capacitor, P_{rated} is the rated power and α is the reactive power factor normally less than 10%.

E.3 Design of filters considered in the third and the fourth chapter:

In the following, we will design inverters output filters used in the third and the fourth chapter. In which the DC bus voltage is set to *400v*, and in order to decrease the lower harmonic content, a high switching frequency will be applied. It also reduces the size of the capacitive and inductive filters components, and enables faster response of the controller. A switching frequency of *10kHz* will be used.

E.3.1 Design of inverter output filters considered in the third chapter:

In the following, the Inverter output filters will be designed for a rating power of *2.2kW*.

A. L-filter:

For *Ud=400v*, *Fs=10kHz,Irate=10A* and using a *2.5%* of the rated current for the current ripple, because it is considered as an acceptable value in terms of inductor size and current ripple.

The L-filter inductor value can be calculated using equation (E.8) as follow:

$$L = \frac{400}{8 \times 0.025 \times 10 \times 10000} = 15mH \tag{E.11}$$

B. LCL-filter:

Using the same reasoning as that used to calculate the L-filter inductor value, the total filter inductor value is equal to 15mH. Thus, the total filter inductance is divided into two parts: the inverter-side inductance *L1* and grid-side inductance *L2* using equation (E.9) for *a=2*:

$$\begin{aligned} L_1 &= 10mH \\ L_2 &= 5mH \end{aligned} \tag{E.12}$$

Thus, the filter capacitor value can be determined by considering the reactive power factor $\alpha = 5\%$ using equation (E.10) as following:

$$C = 0.05 \frac{2200}{2 \times \pi \times 50 \times 220^2} = 7.23uF \quad \text{(E.13)}$$

E.3.1 Design of the LCL-filter considered in the fourth chapter:

The total peak power of the photovoltaic generator used in the fourth chapter simulations is 1.92kW, so the LCL-filter used in the third chapter simulation is oversized. Therefore no further calculations will be made, and the same LCL-filter configuration as that used in the third chapter will be used in fourth chapter simulations.

REFERENCES

[1] Renewables 2013 global status report., in: Renewable Energy Policy Network for the 21st Century, Paris, 2013.

[2] T.K. Ghosh, M.A. Prelas, Energy Resources and Systems, Springer Dordrecht Heidelberg London New York, 2011.

[3] N.S. Lewis, Powering the planet, MRS bulletin, 32 (2007) 808-820.

[4] L. Castaner, S. Silvestre, Modelling Photovoltaic Systems Using PSpice, Wiley, 2003.

[5] K. Ishaque, Z. Salam, H. Taheri, Syafaruddin, Modeling and simulation of photovoltaic (PV) system during partial shading based on a two-diode model, Simulation Modelling Practice and Theory, 19 (2011) 1613-1626.

[6] Z. Salam, J. Ahmed, B.S. Merugu, The application of soft computing methods for MPPT of PV system: A technological and status review, Applied Energy, 107 (2013) 135-148.

[7] A. Benyoucef, K. Kara, A. Chouder, S. Silvestre, Prediction-based Deadbeat Control for Grid-connected Inverter with L-filter and LCL-filter, Electric Power Components and Systems, 42 (2014) 1266-1277.

[8] H. Mathieu, Physique des semiconducteurs et des composants électroniques, Dunod, 2009.

[9] E. Lorenzo, Solar electricity: Engineering of Photovoltaic systems, PROGENSA, 1994.

[10] T. Markvart, Solar electricity, 2nd edition ed., Wiley, 1999.

[11] f.i.f.s.e.s. ISE, Photovoltaics Report, in, 2014.

[12] C.E. Backus, Solar Cells, IEEE Press, 1976.

[13] J. Nelson, The Physics of Solar Cells, Imperial College Press, 2003.

[14] Z. Salameh, Chapter 2 - Photovoltaic, in: Z. Salameh (Ed.) Renewable Energy System Design, Academic Press, Boston, 2014, pp. 33-113.

[15] T. Markvart, Light harvesting for quantum solar energy conversion, Progress in Quantum Electronics, 24 (2000) 107-186.

[16] U. Eicker, Solar Technologies for Buildings, Wiley, New York, 2003.

[17] F. Lasnier, Photovoltaic engineering handbook, CRC Press, 1990.

[18] L. El Chaar, Chapter 3 - Photovoltaic System Conversion, in: M.H. Rashid (Ed.) Alternative Energy in Power Electronics, Butterworth-Heinemann, Boston, 2011, pp. 155-175.

[19] H.-L. Tsai, C.-S. Tu, Y.-J. Su, Development of Genereralize Photovoltaic Model Using MATALB/SIMULINK, in: Proceedings of the World Congress on Engineering and Computer Science, San Francisco,USA, 2008.

[20] P. Trinuruk, C. Sorapipatana, D. Chenvidhya, Estimating operating cell temperature of BIPV modules in Thailand, Renewable Energy, 34 (2009) 2515-2523.

[21] I.E. Commission, Crystalline Silicon Terrestrial Photovoltaic (PV) Modules: Design Qualification and Type Approval, 2002.

[22] M.C. Alonso García, J.L. Balenzategui, Estimation of photovoltaic module yearly temperature and performance based on Nominal Operation Cell Temperature calculations, Renewable Energy, 29 (2004) 1997-2010.

[23] L. Castaner, S. Silvestre, Modelling Photovoltaic Systems Using Pspice, J. Wiley, 2002.

[24] A. Woyte, J. Nijs, R. Belmans, Partial shadowing of photovoltaic arrays with different system configurations: literature review and field test results, Solar Energy, 74 (2003) 217-233.

[25] Y. Liu, Advanced control of photovoltaic converters, in, University of Leicester, England, April 2009.
[26] S. Daraban, D. Petreus, C. Morel, A novel MPPT (maximum power point tracking) algorithm based on a modified genetic algorithm specialized on tracking the global maximum power point in photovoltaic systems affected by partial shading, Energy, 74 (2014) 374-388.
[27] T. Esram, P.L. Chapman, Comparison of Photovoltaic Array Maximum Power Point Tracking Techniques, IEEE Transactions on Energy Conversion, 22 (2007) 439-449.
[28] C.V. Nayar, S.M. Islam, H. Dehbonei, K. Tan, H. Sharma, Chapter 1 - Power Electronics for Renewable Energy Sources, in: M.H. Rashid (Ed.) Alternative Energy in Power Electronics, Butterworth-Heinemann, Boston, 2011, pp. 1-79.
[29] O.C. Onar, A. Khaligh, Chapter 2 - Energy Sources, in: M.H. Rashid (Ed.) Alternative Energy in Power Electronics, Butterworth-Heinemann, Boston, 2015, pp. 81-154.
[30] D.C. Martins, Analysis of a Three-Phase Grid-Connected PV Power System Using a Modified Dual-Stage Inverter, ISRN Renewable Energy, 2013 (2013) 18.
[31] I. Colak, E. Kabalci, R. Bayindir, Review of multilevel voltage source inverter topologies and control schemes, Energy Conversion and Management, 52 (2011) 1114-1128.
[32] A.S. Khalifa, E.F. El-Saadany, Control of three phase grid-connected photovoltaic arrays with open loop maximum power point tracking, in: Power and Energy Society General Meeting, 2011 IEEE, 2011, pp. 1-8.
[33] P.P. Dash, M. Kazerani, Dynamic Modeling and Performance Analysis of a Grid-Connected Current-Source Inverter-Based Photovoltaic System, IEEE Transactions on Sustainable Energy, 2 (2011) 443-450.
[34] A. VanderMeulen, J. Maurin, Current source inverter vs. Voltage source inverter topology, Technical Data TD02004004E, Eaton, (2010).
[35] H.B. Massawe, Grid Connected Photovoltaic Systems with SmartGrid functionality, in: Department of Electric Power Engineering, Norwegian University of Science and Technology, 2013.
[36] J. Schonberger, A single phase multi-string PV inverter with minimal bus capacitance, in: Power Electronics and Applications, 13th IEEE European Conference, 2009, pp. 1-10.
[37] B.A. Johnson, Modeling and analysis of a PV grid-tied smart inverters support functions, in, California State University, 2013.
[38] N. Mohan, T.M. Undeland, Power electronics: converters, applications, and design, John Wiley & Sons, 2007.
[39] I. Glasner, J. Appelbaum, Advantage of boost vs. buck topology for maximum power point tracker in photovoltaic systems, in: Electrical and Electronics Engineers in Israel, 1996., Nineteenth Convention of, 1996, pp. 355-358.
[40] S.O. Simonsen, Development of a Grid Connected PV System for Laboratory Use, in: Department of Electric Power Engineering, Norwegian University of Science and Technology, 2009.
[41] J. Bauer, Single Phase Voltage Source Inverter Photovoltaic Application, Acta Polytechnica, 50 (2010).
[42] S.V. Araujo, A. Engler, B. Sahan, F. Antunes, LCL filter design for grid-connected NPC inverters in offshore wind turbines, in: Power Electronics, 7th IEEE Internatonal Conference, 2007, pp. 1133-1138.
[43] O. Godswill, O.A. Okiemute, I.K. Charles, Design of a Photovoltaic Grid-Connected DC-AC Inverter, International Journal of Emerging trends in Engineering and Development, 4 (2012) 1-16.

[44] K.H. Ahmed, S.J. Finney, B.W. Williams, Passive Filter Design for Three-Phase Inverter Interfacing in Distributed Generation, Electrical Power Quality and Utilization, 13 (2007) 49-58.
[45] B. Majhi, Analysis of Single-Phase SPWM Inverter, in: Department of Electrical Engineering, National Institute of Technology, Rourkela, 2012.
[46] S.E. Evju, Fundamentals of Grid Connected Photo-Voltaic Power Electronic Converter Design, in: Department of Electrical Power Engineering, Norwegian University of Science and Technology, 2007.
[47] T.C.Y. Wang, Y. Zhihong, S. Gautam, Y. Xiaoming, Output filter design for a grid-interconnected three-phase inverter, in: Power Electronics Specialist Conference, 2003. PESC '03. 2003 IEEE 34th Annual, 2003, pp. 779-784 vol.772.
[48] IEEE Standard for Interconnecting Distributed Resources with Electric Power Systems, IEEE Std 1547-2003, (2003) 1-28.
[49] IEC 61727 standard: Photovoltaic (PV) systems – Characteristics of the utility interface, in, 2004.
[50] IEEE Recommended Practice for Utility Interface of Photovoltaic (PV) Systems, IEEE Std 929-2000, (2000) i.
[51] S.V. Araujo, P. Zacharias, B. Sahan, Novel grid-connected non-isolated converters for photovoltaic systems with grounded generator, in: Power Electronics Specialists Conference, 2008. PESC 2008. IEEE, 2008, pp. 58-65.
[52] X. Yaosuo, C. Liuchen, K. Sren Baekhj, J. Bordonau, T. Shimizu, Topologies of single-phase inverters for small distributed power generators: an overview, IEEE Transactions on Power Electronics, 19 (2004) 1305-1314.
[53] S.B. Kjaer, J.K. Pedersen, F. Blaabjerg, A review of single-phase grid-connected inverters for photovoltaic modules, IEEE Transactions on Industry Applications, 41 (2005) 1292-1306.
[54] R. Teodorescu, M. Liserre, P. Rodriguez, Grid converters for photovoltaic and wind power systems, John Wiley & Sons, 2011.
[55] N.A. Kamarzaman, C.W. Tan, A comprehensive review of maximum power point tracking algorithms for photovoltaic systems, Renewable and Sustainable Energy Reviews, 37 (2014) 585-598.
[56] G.M. Hans, Solar cell and test circuit Patent US3, 350, 635, (1967).
[57] J.D. Hartman, Power conditioning system, Patent US3, 384, 806, (1968).
[58] T.O. Paine, Maximum Power Point Tracker, National Aeronautics and Space Administration, NASA, Patent US3, 566, 143, (1969).
[59] H. Yongji, L. Deheng, A new method for optimal output of a solar cell array, in: Industrial Electronics, 1992., Proceedings of the IEEE International Symposium on, 1992, pp. 456-459 vol.451.
[60] D.P. Hohm, M.E. Ropp, Comparative study of maximum power point tracking algorithms using an experimental, programmable, maximum power point tracking test bed, in: Photovoltaic Specialists Conference, 2000. Conference Record of the Twenty-Eighth IEEE, 2000, pp. 1699-1702.
[61] K.H. Hussein, I. Muta, T. Hoshino, M. Osakada, Maximum photovoltaic power tracking: an algorithm for rapidly changing atmospheric conditions, Generation, Transmission and Distribution, IEE Proceedings-, 142 (1995) 59-64.
[62] L. MacIsaac, A. Knox, Improved maximum power point tracking algorithm for photovoltaic systems, in: International Conference on Renewable Energies and Power Quality ICREPQ, 2010.

[63] M. El-Shibini, H. Rakha, Maximum power point tracking technique, in: Electrotechnical Conference, 1989. Proceedings.'Integrating Research, Industry and Education in Energy and Communication Engineering', MELECON'89., Mediterranean, IEEE, 1989, pp. 21-24.
[64] J.D.v.W. J.J. Schoeman, A simplified maximal power controller for terrestrial photovoltaic panel arrays, in: IEEE Power Electronics Specialists Conference. PESC '82 Record. , New York, 1982, pp. 361–367.
[65] H. GW, B. HM, C.I. CH, Experimental tests of open-loop maximumpower-point tracking techniques for photovoltaic arrays. , Solar Cells, 13 (1984) 185-195.
[66] H. Patel, V. Agarwal, Maximum Power Point Tracking Scheme for PV Systems Operating Under Partially Shaded Conditions, IEEE Transactions on Industrial Electronics, 55 (2008) 1689-1698.
[67] T. Kok Soon, S. Mekhilef, Modified Incremental Conductance Algorithm for Photovoltaic System Under Partial Shading Conditions and Load Variation, IEEE Transactions on Industrial Electronics, 61 (2014) 5384-5392.
[68] X. Weidong, W.G. Dunford, A modified adaptive hill climbing MPPT method for photovoltaic power systems, in: Power Electronics Specialists Conference, 2004. PESC 04. 2004 IEEE 35th Annual, 2004, pp. 1957-1963 Vol.1953.
[69] M. Pedemonte, S. Nesmachnow, H. Cancela, A survey on parallel ant colony optimization, Applied Soft Computing, 11 (2011) 5181-5197.
[70] S. Gupta, S. Bhardwaj, P.K. Bhatia, A reminiscent study of nature inspired computation, International Journal of Advances in Engineering & Technology, 1 (2011) 117-125.
[71] K. Ishaque, Z. Salam, Syafaruddin, A comprehensive MATLAB Simulink PV system simulator with partial shading capability based on two-diode model, Solar Energy, 85 (2011) 2217-2227.
[72] M. Veerachary, N. Yadaiah, ANN based peak power tracking for PV supplied DC motors, Solar Energy, 69 (2000) 343-350.
[73] X. Jinbang, S. Anwen, Y. Cheng, R. Wenpei, Y. Xuan, ANN Based on IncCond Algorithm for MPP Tracker, in: Bio-Inspired Computing: Theories and Applications (BIC-TA), Sixth IEEE International Conference, 2011, pp. 129-134.
[74] A. Messai, A. Mellit, A. Guessoum, S.A. Kalogirou, Maximum power point tracking using a GA optimized fuzzy logic controller and its FPGA implementation, Solar Energy, 85 (2011) 265-277.
[75] H. Taheri, Z. Salam, K. Ishaque, Syafaruddin, A novel Maximum Power Point tracking control of photovoltaic system under partial and rapidly fluctuating shadow conditions using Differential Evolution, in: Industrial Electronics & Applications (ISIEA), 2010 IEEE Symposium on, 2010, pp. 82-87.
[76] A.K. Qin, V.L. Huang, P.N. Suganthan, Differential Evolution Algorithm With Strategy Adaptation for Global Numerical Optimization, IEEE Transactions on Evolutionary Computation, 13 (2009) 398-417.
[77] D. Karaboga, An idea based on honey bee swarm for numerical optimization. TECHNICAL REPORT-TR06, in, Erciyes University, Engineering faculty, computer engineering department, 2005.
[78] F. Valdez, P. Melin, O. Castillo, A survey on nature-inspired optimization algorithms with fuzzy logic for dynamic parameter adaptation, Expert Systems with Applications, 41 (2014) 6459-6466.
[79] F. Qiang, T. Nan, A Complex-Method-Based PSO Algorithm for the Maximum Power Point Tracking in Photovoltaic System, in: Information Technology and Computer Science (ITCS), Second IEEE International Conference, 2010, pp. 134-137.

[80] L. Yi-Hwa, H. Shyh-Ching, H. Jia-Wei, L. Wen-Cheng, A Particle Swarm Optimization-Based Maximum Power Point Tracking Algorithm for PV Systems Operating Under Partially Shaded Conditions, IEEE Transactions on Energy Conversion, 27 (2012) 1027-1035.
[81] H. Renaudineau, A. Houari, J.P. Martin, S. Pierfederici, F. Meibody-Tabar, B. Gerardin, A new approach in tracking maximum power under partially shaded conditions with consideration of converter losses, Solar Energy, 85 (2011) 2580-2588.
[82] N. Tat Luat, L. Kay-Soon, A Global Maximum Power Point Tracking Scheme Employing diresct search algorithm for Photovoltaic Systems, IEEE Transactions on Industrial Electronics, 57 (2010) 3456-3467.
[83] A. Bouilouta, A. Mellit, S.A. Kalogirou, New MPPT method for stand-alone photovoltaic systems operating under partially shaded conditions, Energy, 55 (2013) 1172-1185.
[84] G. Velasco-Quesada, F. Guinjoan-Gispert, R. Pique-Lopez, M. Roman-Lumbreras, A. Conesa-Roca, Electrical PV Array Reconfiguration Strategy for Energy Extraction Improvement in Grid-Connected PV Systems, IEEE Transactions on Industrial Electronics, 56 (2009) 4319-4331.
[85] K. Kobayashi, I. Takano, Y. Sawada, A study of a two stage maximum power point tracking control of a photovoltaic system under partially shaded insolation conditions, Solar Energy Materials and Solar Cells, 90 (2006) 2975-2988.
[86] G.R. Walker, J.C. Pierce, PhotoVoltaic DC-DC Module Integrated Converter for Novel Cascaded and Bypass Grid Connection Topologies — Design and Optimisation, in: Power Electronics Specialists Conference, 2006. PESC '06. 37th IEEE, 2006, pp. 1-7.
[87] N.D. Kaushika, N.K. Gautam, Energy yield simulations of interconnected solar PV arrays, IEEE Transactions on Energy Conversion, 18 (2003) 127-134.
[88] E. Karatepe, M. Boztepe, M. Çolak, Development of a suitable model for characterizing photovoltaic arrays with shaded solar cells, Solar Energy, 81 (2007) 977-992.
[89] H. Ghoddami, A. Yazdani, A Single-Stage Three-Phase Photovoltaic System With Enhanced Maximum Power Point Tracking Capability and Increased Power Rating, IEEE Transactions on Power Delivery, 26 (2011) 1017-1029.
[90] N. Femia, G. Lisi, G. Petrone, G. Spagnuolo, M. Vitelli, Distributed Maximum Power Point Tracking of Photovoltaic Arrays: Novel Approach and System Analysis, IEEE Transactions on Industrial Electronics, 55 (2008) 2610-2621.
[91] C. Yaow-Ming, W. Hsu-Chin, C. Yung-Chu, DC bus regulation strategy for grid-connected PV power generation system, IEEE International Conference on Sustainable Energy Technologies,2008, pp. 437-442.
[92] A. Abedini, A. Nasiri, An Improved Adaptive Filter for Voltage and Current Reference Extraction, in: Power Electronics and Motion Control Conference, 2006. IPEMC 2006. CES/IEEE 5th International, 2006, pp. 1-5.
[93] G. Wenjie, L. Fei, T. Zheng, Nonlinear PI control for three-phase PWM AC-DC converter, in: Industrial Electronics Society, 2005. IECON 2005. 31st Annual Conference of IEEE, 2005, pp. 5 pp.
[94] S. Buso, P. Mattavelli, Digital control in power electronics, 2006.
[95] C.N.m. Ho, V.S.P. Cheung, H.S.H. Chung, Constant-Frequency Hysteresis Current Control of Grid-Connected VSI Without Bandwidth Control, IEEE Transactions on Power Electronics, 24 (2009) 2484-2495.
[96] J. Irwin, M.P. Kazmierkowski, R. Krishnan, F. Blaabjerg, Control in power electronics: selected problems, Academic press, 2002.
[97] D.N. Zmood, D.G. Holmes, Stationary frame current regulation of PWM inverters with zero steady-state error, IEEE Transactions on Power Electronics, 18 (2003) 814-822.

[98] R. Teodorescu, F. Blaabjerg, Proportional-resonant controllers. A new breed of controllers suitable for grid-connected voltage-source converters, in: The 9 th International Conference on Optimization of Electrical and Electronic Equipments, Optim 2004, 2004, pp. 9-14.
[99] R. Pavlanin, P. Spanik, B. Dobrucky, Comparison of Multi-Resonant-and Hysteresis Band Controllers used in Current Control Loop of Shunt Active Power Filter, Renewable energy & power quality journal-ISSN, (2012).
[100] M. Monfared, A simplified control strategy for single-phase UPS inverters, Bulletin of the Polish Academy of Sciences Technical Sciences, 62 (2014) 367-373.
[101] Z. Keliang, L. Kay-Soon, W. Yigang, L. Fang-Lin, Z. Bin, Zero-phase odd-harmonic repetitive controller for a single-phase PWM inverter, IEEE Transactions on Power Electronics, 21 (2006) 193-201.
[102] S. Chen, Y.M. Lai, S.C. Tan, C.K. Tse, Analysis and design of repetitive controller for harmonic elimination in PWM voltage source inverter systems, Power Electronics, IET, 1 (2008) 497-506.
[103] Z. Keliang, W. Danwei, Z. Bin, W. Yigang, Plug-In Dual-Mode-Structure Repetitive Controller for CVCF PWM Inverters, IEEE Transactions on Industrial Electronics, 56 (2009) 784-791.
[104] H. Akagi, Y. Kanazawa, A. Nabae, Instantaneous Reactive Power Compensators Comprising Switching Devices without Energy Storage Components, IEEE Transactions on Industry Applications, 20 (1984) 625-630.
[105] K. Hyosung, H. Akagi, The instantaneous power theory on the rotating p-q-r reference frames, in: Power Electronics and Drive Systems IEEE Conference , 1999, pp. 422-427 vol.421.
[106] B.P. McGrath, D.G. Holmes, J.J.H. Galloway, Power converter line synchronization using a discrete Fourier transform (DFT) based on a variable sample rate, IEEE Transactions on Power Electronics, 20 (2005) 877-884.
[107] A. Pigazo, V.M. Moreno, Discrete Wavelet Transforms for Synchronization of Power Converters Connected to Electrical Grids, DISCRETE WAVELET TRANSFORMS □ THEORY AND APPLICATIONS, (2011) 215.
[108] H. Guan-Chyun, J.C. Hung, Phase-locked loop techniques. A survey, IEEE Transactions on Industrial Electronics, 43 (1996) 609-615.
[109] Sa, x, V. ez, Marti, A. n, M. Rizo, A. Rodriguez, E.J. Bueno, A. Hernandez, A. Miron, FPGA implementation of grid synchronization algorithms based on DSC, DSOGI_QSG and PLL for distributed power generation systems, in: Industrial Electronics (ISIE), 2010 IEEE International Symposium on, 2010, pp. 2765-2770.
[110] Y. Han, L. Xu, M.M. Khan, G. Yao, L.-D. Zhou, C. Chen, A novel synchronization scheme for grid-connected converters by using adaptive linear optimal filter based PLL (ALOF–PLL), Simulation Modelling Practice and Theory, 17 (2009) 1299-1345.
[111] S. Evju, Fundamentals of grid connected photovoltaic power electronic converter design, Ph.D. dissertation, Department of Electrical Power Engineering, Norwegian University of Science and Technology, (2007).
[112] J. Thornycroft, T. Markvart, Chapter IIC-1 - Grid Connection of PV Generators: Technical and Regulatory Issues, in: A. McEvoy, T. Markvart, L. Castañer (Eds.) Practical Handbook of Photovoltaics (Second Edition), Academic Press, Boston, 2012, pp. 779-803.
[113] W. Bower, M. Ropp, Evaluation of islanding detection methods for utilityinteractive inverters in photovoltaic systems, in: Sandia report, SAND2002-3591., 2002.
[114] M.A. Eltawil, Z. Zhao, Grid-connected photovoltaic power systems: Technical and potential problems—A review, Renewable and Sustainable Energy Reviews, 14 (2010) 112-129.

[115] K.N.E. Ku Ahmad, J. Selvaraj, N.A. Rahim, A review of the islanding detection methods in grid-connected PV inverters, Renewable and Sustainable Energy Reviews, 21 (2013) 756-766.
[116] H. Zeineldin, J. Kirtley, A simple technique for islanding detection with negligible non-detection zone, in: Power & Energy Society General Meeting, 2009. PES '09. IEEE, 2009, pp. 1-1.
[117] S. Syamsuddin, N.A. Rahim, Krismadinata, J. Selvaraj, Implementation of TMS320F2812 in islanding detection for Photovoltaic Grid Connected Inverter, in: Technical Postgraduates (TECHPOS), 2009 International Conference for, 2009, pp. 1-5.
[118] J. Young-Hyok, J. Doo-Yong, K. Jun-Gu, K. Jae-Hyung, L. Tae-Won, W. Chung-Yuen, A Real Maximum Power Point Tracking Method for Mismatching Compensation in PV Array Under Partially Shaded Conditions, IEEE Transactions on Power Electronics, 26 (2011) 1001-1009.
[119] P.E. Kakosimos, A.G. Kladas, Implementation of photovoltaic array MPPT through fixed step predictive control technique, Renewable Energy, 36 (2011) 2508-2514.
[120] K. Ishaque, Z. Salam, A. Shamsudin, M. Amjad, A direct control based maximum power point tracking method for photovoltaic system under partial shading conditions using particle swarm optimization algorithm, Applied Energy, 99 (2012) 414-422.
[121] M. Miyatake, M. Veerachary, F. Toriumi, N. Fujii, H. Ko, Maximum Power Point Tracking of Multiple Photovoltaic Arrays: A PSO Approach, IEEE Transactions on Aerospace and Electronic Systems, 47 (2011) 367-380.
[122] F. Keyrouz, S. Georges, Efficient multidimensional Maximum Power Point Tracking using Bayesian fusion, in: Electric Power and Energy Conversion Systems (EPECS), 2nd IEEE International Conference, 2011, pp. 1-5.
[123] L.L. Jiang, D.L. Maskell, J.C. Patra, A novel ant colony optimization-based maximum power point tracking for photovoltaic systems under partially shaded conditions, Energy and Buildings, 58 (2013) 227-236.
[124] O. Wasynezuk, Dynamic Behavior of a Class of Photovoltaic Power Systems, IEEE Transactions on Power Apparatus and Systems, 102 (1983) 3031-3037.
[125] T. Chee Wei, T.C. Green, C.A. Hernandez-Aramburo, A current-mode controlled maximum power point tracking converter for building integrated photovoltaics, in: Power Electronics and Applications, IEEE European Conference, 2007, pp. 1-10.
[126] E. Koutroulis, K. Kalaitzakis, N.C. Voulgaris, Development of a microcontroller-based, photovoltaic maximum power point tracking control system, IEEE Transactions on Power Electronics, 16 (2001) 46-54.
[127] M.G. Villalva, E. Ruppert F, Analysis and simulation of the P&O MPPT algorithm using a linearized PV array model, in: Industrial Electronics, 2009. IECON '09. 35th Annual Conference of IEEE, 2009, pp. 231-236.
[128] L. Yupeng, X. Dongwei, H. Zhanning, MPPT of a PV system based on the particle swarm optimization, in: Electric Utility Deregulation and Restructuring and Power Technologies (DRPT), 4th IEEE International Conference, 2011, pp. 1094-1096.
[129] M. Miyatake, F. Toriumi, T. Endo, N. Fujii, A Novel maximum power point tracker controlling several converters connected to photovoltaic arrays with particle swarm optimization technique, in: Power Electronics and Applications, IEEE European Conference, 2007, pp. 1-10.
[130] L. Chun-Liang, L. Yi-Feng, H. Jia-Wei, L. Yi-Hua, A PSO-based MPPT algorithm for photovoltaic systems subject to inhomogeneous insolation, in: Soft Computing and Intelligent Systems (SCIS) and 13th International Symposium on Advanced Intelligent Systems (ISIS), 6th IEEE International Conference, 2012, pp. 721-726.
[131] A. Banharnsakun, T. Achalakul, B. Sirinaovakul, The best-so-far selection in Artificial Bee Colony algorithm, Applied Soft Computing, 11 (2011) 2888-2901.

[132] S.-M. Chen, A. Sarosh, Y.-F. Dong, Simulated annealing based artificial bee colony algorithm for global numerical optimization, Applied Mathematics and Computation, 219 (2012) 3575-3589.
[133] D. Karaboga, S. Okdem, C. Ozturk, Cluster based wireless sensor network routing using artificial bee colony algorithm, Wireless Networks, 18 (2012) 847-860.
[134] S. Samanta, S. Chakraborty, Parametric optimization of some non-traditional machining processes using artificial bee colony algorithm, Engineering Applications of Artificial Intelligence, 24 (2011) 946-957.
[135] W.-f. Gao, S.-y. Liu, A modified artificial bee colony algorithm, Computers & Operations Research, 39 (2012) 687-697.
[136] F. Kang, J. Li, Q. Xu, Structural inverse analysis by hybrid simplex artificial bee colony algorithms, Computers & Structures, 87 (2009) 861-870.
[137] A. Singh, An artificial bee colony algorithm for the leaf-constrained minimum spanning tree problem, Applied Soft Computing, 9 (2009) 625-631.
[138] E. Cuevas, F. Sención, D. Zaldivar, M. Pérez-Cisneros, H. Sossa, A multi-threshold segmentation approach based on Artificial Bee Colony optimization, Applied Intelligence, 37 (2012) 321-336.
[139] U. Kılıç, K. Ayan, Optimizing power flow of AC–DC power systems using artificial bee colony algorithm, International Journal of Electrical Power & Energy Systems, 53 (2013) 592-602.
[140] A.F. Mohamed, M.M. Elarini, A.M. Othman, A new technique based on Artificial Bee Colony Algorithm for optimal sizing of stand-alone photovoltaic system, Journal of Advanced Research, 5 (2014) 397-408.
[141] O.A. Sahed, K. Kara, A. Benyoucef, Artificial bee colony-based predictive control for non-linear systems, Transactions of the Institute of Measurement and Control, (2014).
[142] E. Cuevas, D. Zaldívar, M. Pérez-Cisneros, H. Sossa, V. Osuna, Block matching algorithm for motion estimation based on Artificial Bee Colony (ABC), Applied Soft Computing, 13 (2013) 3047-3059.
[143] A. Şencan Şahin, B. Kılıç, U. Kılıç, Design and economic optimization of shell and tube heat exchangers using Artificial Bee Colony (ABC) algorithm, Energy Conversion and Management, 52 (2011) 3356-3362.
[144] V. Tereshko, Reaction-diffusion model of a honeybee colony's foraging behaviour, in: Proceedings of the 6th international conference on parallel problem solving from nature, Springer-Verlag, London, UK, 2000, pp. 807-816.
[145] V. Tereshko, T. Lee, How information mapping patterns determine foraging behaviour of a honeybee colony, Open Systems and Information Dynamics, 9 (2002) 181–193.
[146] V. Tereshko, A. Loengarov, Collective decision-making in honeybee foraging dynamics, Computing and Information Systems Journal, 9 (2005) 1-7.
[147] N. Femia, G. Petrone, G. Spagnuolo, M. Vitelli, Optimizing sampling rate of P&O MPPT technique, in: Power Electronics Specialists Conference, 2004. PESC 04. 2004 IEEE 35th Annual, 2004, pp. 1945-1949 Vol.1943.
[148] K. Fekete, Z. Klaic, L. Majdandzic, Expansion of the residential photovoltaic systems and its harmonic impact on the distribution grid, Renewable Energy, 43 (2012) 140-148.
[149] M. Calais, J. Myrzik, T. Spooner, V.G. Agelidis, Inverters for single-phase grid connected photovoltaic systems-an overview, in: Power Electronics Specialists Conference, 2002. pesc 02. 2002 IEEE 33rd Annual, 2002, pp. 1995-2000.
[150] P. Cortes, M.P. Kazmierkowski, R.M. Kennel, D.E. Quevedo, J. Rodriguez, Predictive Control in Power Electronics and Drives, IEEE Transactions on Industrial Electronics, 55 (2008) 4312-4324.

[151] R. Kennel, A. Linder, Predictive control of inverter supplied electrical drives, in: Power Electronics Specialists Conference, 2000. PESC 00. 2000 IEEE 31st Annual, 2000, pp. 761-766 vol.762.
[152] E. Shimada, K. Aoki, T. Komiyama, T. Yokoyama, Implementation of deadbeat control for single phase utility interactive inverter using FPGA based hardware controller, in: Power Electronics and Applications, IEEE European Conference, 2005, pp. 10 pp.-P.10.
[153] T. Yokoyama, S. Simogata, M. Horiuchi, T. Ide, Instantaneous deadbeat control for single phase and three phase PWM inverter using FPGA based hardware controller, in: IEEE 35th Power Electron. Spec. Conf, 2004, pp. 3–6.
[154] N. Uemura, T. Yokoyama, Current control method using voltage deadbeat control for single phase utility interactive inverter, in: Telecommunications Energy Conference, 2003. INTELEC '03. The 25th International, 2003, pp. 40-45.
[155] G.K. Hung, C.C. Chang, C.L. Chen, Analysis and implementation of a delay-compensated deadbeat current controller for solar inverters, Circuits, Devices and Systems, IEE Proceedings -, 148 (2001) 279-286.
[156] P. Yang, N. Chen, S. Liu, Research on the improved current deadbeat control algorithm of photovoltaic grid-connected inverter, in: Power Electronics Systems and Applications (PESA), 4th IEEE International Conference, 2011, pp. 1-3.
[157] M. Mengchao, L. Peng, L. Botao, Study on deadbeat control strategy for grid-connected distributed generation system, in: Electric Utility Deregulation and Restructuring and Power Technologies, Third IEEE International Conference, 2008, pp. 2553-2557.
[158] H. Junping, Y. Lei, W. Xuesong, W. Jian, Research on Deadbeat Control of a Three-level Grid- connected Inverter Based on αβ Transform, Procedia Engineering, 23 (2011) 397-402.
[159] Q. Zeng, L. Chang, P. Song, SVPWM-based current controller with grid harmonic compensation for three-phase grid-connected VSI, in: Power Electronics Specialists Conference, 2004. PESC 04. 2004 IEEE 35th Annual, 2004, pp. 2494-2500 Vol.2494.
[160] A.J. Sguarezi Filho, E. Ruppert, A deadbeat active and reactive power control for doubly fed induction generator, Electric Power Components and Systems, 38 (2010) 592-602.
[161] B. Zhihua, W. Zongchen, Z. Shibing, A predictive deadbeat control in shunt active power filter, in: IEEE Wireless Communications and Signal Processing, Nanjing, China, 2011, pp. 9-11.
[162] O. Kukrer, H. Komurcugil, Deadbeat control method for single-phase UPS inverters with compensation of computation delay, Electric Power Applications, IEE Proceedings -, 146 (1999) 123-128.
[163] J.W. Kho, J.Y. Jang, K.B. Lee, Disturbance observer-based deadbeat control for single-phase UPS inverters, in: SICE 2003 Annual Conference, 2003, pp. 1206-1210 Vol.1202.
[164] K. Nishida, M. Rukonuzzman, M. Nakaoka, Advanced current control implementation with robust deadbeat algorithm for shunt single-phase voltage-source type active power filter, Electric Power Applications, IEE Proceedings -, 151 (2004) 283-288.
[165] C. Guang-Da, S. Yi-Zhou, H. Mian-Hua, A Predictive Current Regulator Using Linear Neural Networks For Three-phase Voltage Source PWM-Inverter, in: Neural Networks and Brain, IEEE International Conference, 2005, pp. 793-798.
[166] B. Jianrong, and Longya, X., An effective deadbeat fuzzy algorithm for current regulation in stationary reference frame, in:

IEEE Power Electronics in Transportation,

Dearborn, MI, 24–25 1996, pp. 151–157.
[167] S.S. Haykin, Adaptive Filter Theory, 4th ed., Upper Saddle River, NJ: Prentice Hall, Chap. 6, pp. 241–290, 2002.

[168] D. Holmes, D. Martin, Implementation of a direct digital predictive current controller for single and three phase voltage source inverters, in: Industry Applications Conference, 1996. Thirty-First IAS Annual Meeting, IAS'96., Conference Record of the 1996 IEEE, IEEE, 1996, pp. 906-913.
[169] Y. Yang, F. Blaabjerg, Synchronization in single-phase grid-connected photovoltaic systems under grid faults, in: Power Electronics for Distributed Generation Systems (PEDG), 2012 3rd IEEE International Symposium on, 2012, pp. 476-482.
[170] S. Golestan, M. Monfared, F.D. Freijedo, J.M. Guerrero, Design and Tuning of a Modified Power-Based PLL for Single-Phase Grid-Connected Power Conditioning Systems, IEEE Transactions on Power Electronics, 27 (2012) 3639-3650.
[171] b. nadjib, special autom, http://www.specialautom.net/trans-deuxieme-ordre.htm, in, 2014.
[172] B. Messner, Control Tutorials for MATLAB and Simulink, http://ctms.engin.umich.edu/CTMS/index.php?example=Introduction&section=SystemAnalysis, in, 2012.
[173] A. Nicastri, A. Nagliero, Comparison and evaluation of the PLL techniques for the design of the grid-connected inverter systems, in: Industrial Electronics (ISIE), 2010 IEEE International Symposium on, 2010, pp. 3865-3870.
[174] S.M. Silva, B.M. Lopes, B.J.C. Filho, R.P. Campana, W.C. Bosventura, Performance evaluation of PLL algorithms for single-phase grid-connected systems, in: Industry Applications Conference, 2004. 39th IAS Annual Meeting. Conference Record of the 2004 IEEE, 2004, pp. 2259-2263 vol.2254.
[175] M. Cacciato, A. Consoli, V. Crisafulli, G. Scarcella, G. Scelba, Robustness evaluation of phase-locked loop algorithms for single-phase distributed generation systems, in: Power Electronics Electrical Drives Automation and Motion (SPEEDAM), 2010 International Symposium on, 2010, pp. 914-919.
[176] A. Gupta, A. Porippireddi, V.U. Srinivasa, A. Sharma, M. Kadam, Comparative Study of Single Phase PLL Algorithms for Grid Synchronization Applications, International Journal of Electronics & Communication Technology, 3 (2012) 237-245.
[177] K. De Brabandere, T. Loix, K. Engelen, B. Bolsens, J. Van den Keybus, J. Driesen, R. Belmans, Design and Operation of a Phase-Locked Loop with Kalman Estimator-Based Filter for Single-Phase Applications, in: IEEE Industrial Electronics, 32nd IEEE Annual Conference, 2006, pp. 525-530.
[178] A. Chaoui, J.P. Gaubert, F. Krim, L. Rambault, IP Controlled Three-Phase Shunt Active Power Filter for Power Improvement Quality, in: IEEE Industrial Electronics, 32nd IEEE Annual Conference, 2006, pp. 2384-2389.
[179] C. Hanju, V. Trung-Kien, Comparative analysis of low-pass output filter for single-phase grid-connected Photovoltaic inverter, in: Applied Power Electronics Conference and Exposition (APEC), 2010 Twenty-Fifth Annual IEEE, 2010, pp. 1659-1665.
[180] M. Yingram, S. Premrudeepreechacharn, Investigation of relationship between voltage and nondetection zone of OUV/OUF of local islanding detection techniques, Journal of Clean Energy Technologies, 2 (2014) 299-304.
[181] Y. Zhihong, A. Kolwalkar, Y. Zhang, D. Pengwei, R. Walling, Evaluation of anti-islanding schemes based on nondetection zone concept, IEEE Transactions on Power Electronics, 19 (2004) 1171-1176.
[182] A. Kwasinski, EE462L, Spring 2014 DC–DC Boost Converter, in, University of Texas at Austin, 2014.
[183] M.H. Rashid, Power electronics: circuits, devices, and applications, Pearson Education India, 2003.

[184] LEM, LV25-P, datasheet, in, 2012.
[185] P. Horowitz, W. Hill, The art of electronics, Cambridge Univ. Press, 1989.